Understanding the influence of water absorption and fibre architecture on matrix dominated properties of carbon fibre reinforced composites

Faisel Almudaihesh (BEng, MSc)

A thesis submitted in partial fulfilment for
the degree of Doctor of Philosophy

Mechanics, Materials and Advanced Manufacturing
School of Engineering

June 2021

Abstract

The increased demand for and usage of Carbon Fibre Reinforced Polymers (CFRP) composites in many industries across sectors such as in aerospace, automotive and marine applications require further scientific attention leading to greater understanding of these materials which are expected to operate for long periods under harsh environments.

This thesis discusses a key parameter 'fibre architecture' and shows that it plays a major role in the performance of CFRP composites when subjected to water absorption. Unidirectional (UD), and 2D woven (plain and twill weaves) of CFRP specimens were immersed in water. An investigation on the directional moisture diffusion coefficients of this materials has been conducted with the use of Fick's law in order to obtain comparative diffusion coefficient values. UD material showed higher diffusion coefficients by up to 21.56% as compared with their 2D woven equivalents.

The mechanical properties dominated by the condition of the matrix and interfacial regions such as compression, shear, and impact resistance were assessed for un-aged and aged specimens. A reduction in strength was observed for all aged specimens. However, the observed reduction in strength varies depending on both the fibre architecture used and the specific load case. The largest effect on properties was observed in unidirectional materials, which leads to the recommendation that less conservative safety factors could be used for woven fibre architectures.

Further work was undertaken to understand the effect of gradually increasing water absorption on interlaminar strength of UD materials, as this is the material that experiences greatest reduction in short beam strength (SBS). This work used Acoustic Emission (AE), optical strain measurements and microscopy to provide an assessment of the gradual change in failure mechanisms due to the degradation of a polymer's structure with increasing water absorption. The SBS values decreased as immersion times were increased; the decrease was significant at longer immersion times (up to 24.47%). Failures evolved from a single shear delamination at low immersion times to more complex crushing, intralaminar cracking and multiple delaminations at long exposure times, suggesting that the true SBS was not determined at long exposure times. AE data supports this and was able to distinguish different material behaviours prior to final fracture for un-aged and aged specimens, and this was further validated using optical measurements and microscopy.

Key words: Water absorption, fibre architecture, water ingress mechanism, water diffusion, interfacial condition, mechanical properties, fracture behaviour, Acoustic Emission, and optical measurement.

Acknowledgments

I would like to take this opportunity to express my greatest gratitude to the excellent supervision team I worked with throughout this project, Dr Mark Eaton, Professor Rhys Pullin, and Professor Karen Holford. No words can express the amount of technical and academic research skills I gained throughout this project under their support, encouragement, and supervision.

I must also thank all my colleagues at the Cardiff University Tribology and Performance of Machines, Structures and Materials Group along with all technician staff at the School of Engineering for their friendship and assistance throughout this project.

I am also grateful to all Cardiff University departments and schools that I have come across throughout this project and somehow contributed in my work from all aspects including research office, IT, admissions, and finance.

Table of Contents

Abstract i

Acknowledgments iii

Abbreviation List ix

1 Introduction 1

1.1 Aims and objectives 1

1.2 Novelty statement 2

1.3 Published outputs 3

1.4 Thesis organisation 3

2 Literature Review 5

2.1 Composite materials background 5

2.2 CFRP structures 11

2.3 Moisture absorption in CFRP composites 16

2.3.1 Epoxy resin and the phenomena of hydrolysis and plasticisation in composites 16

2.3.2 Damage mechanism from a fibrous/polymeric structure prospective 19

2.3.3 The effect of water absorption on the ‘glass transition temperature’ in epoxy resin composites 21

2.3.4 Experimental studies 24

2.3.5 Moisture diffusion, novel theories for water intake into composite materials (Fick’s law and others)........28

2.4 The effects of hydrothermal aging on the properties of CFRP composites 38

2.4.1 Effects of accelerated aging on CFRP composites........38

2.4.2 Hydrothermal effects on the mechanical properties of CFRP composites....40

2.4.3 Effects of constituent contents of CFRP composites........42

2.4.4 The importance of the interface between fibres and resin in the sizing process and its effect on water absorption........43

2.5 Monitoring and evaluation for assessing damage in composite materials........47

2.5.1 Microscopy........47

2.5.2 Non-Destructive Testing (NDT) using ultrasonic scans for polymeric composite materials........52

2.5.3 Optical measurements........56

2.5.4 Characterising polymeric composites using Acoustic Emission........58

2.6 Literature review summary and the gap of knowledge........63

3 Materials and Methods........66

3.1 Introduction........66

3.2 Materials and fabrication........66

3.2.1 Materials........66

3.2.2 Fabrication........67

3.3 Constituent contents 70

3.4 Moisture absorption 75

3.4.1 Water uptake 75

3.4.2 Diffusion coefficients 77

3.5 Compressive characterisation 78

3.6 Shear characterisation 82

3.7 Impact damage characterisation 84

3.8 Microscopic imaging 88

3.9 C-scanning 88

3.10 Scanning Electron Microscopy 89

3.11 Optical measurement 90

3.12 Acoustic Emission 91

4 Moisture Absorption in Unidirectional and 2D woven CFRP Composites 94

4.1 Introduction 94

4.2 Methods 95

4.2.1 Sample geometry 95

4.2.2 Water uptake 97

4.2.3 Water diffusion 97

4.3 Results and discussion 102

4.3.1 Constituent contents 102

4.3.2 Water uptake 102

4.3.3 Water diffusion 119

4.4 Conclusions 131

5 Effects of Moisture Absorption on the Mechanical Properties of Unidirectional and 2D Woven CFRP Composites 133

5.1 Introduction 133

5.2 Methods 133

5.3 Results and discussion 133

5.4 Conclusions 144

6 An assessment of the effect of progressive water absorption on the interlaminar strength of unidirectional CFRP using Acoustic Emission 145

6.1 Introduction 145

6.2 Methods 146

6.2.1 Materials and testing 146

6.2.2 Optical measurement and AE approach 147

6.3 Results and discussions 149

6.4 Conclusion 172

7 Summary of Conclusions and Future Recommendations 174

7.1 Summary of conclusions 174

7.2 Future recommendations 177

References 179

Appendices..205

Appendix A (data sheets) 205

Appendix B (all water absorption testing data) 210

Appendix C (all individual mechanical properties data)..218

Appendix D (all AE data)..228

Abbreviation List

AE	Acoustic Emission
BVID	Barely Visible Impact Damage
CFRP	Carbon Fibre Reinforced Polymers
CLC	Combined Loading Compression
D	Diffusions Coefficient
IDR	Impact Damage Resistance
ILSS	Interlaminar Shear Strength
J	Joules
SBS	Short-beam Strength
SEM	Scanning Electron Microscopy
Tg	Glass Transition Temperature
UD	Unidirectional
V_{air}	Void Volume Fraction
V_f	Fibre Volume Fraction
VID	Visible Impact Damage
V_m	Matrix Volume Fraction
VSG	Video Strain Gauge

1 Introduction

1.1 Aims and objectives

The high demands for lighter materials with high strength and stiffness to weight ratios operating in moist conditions has led to intensive research in understanding the performance of Carbon Fibre Reinforced Polymers (CFRP) after water absorption (Takeda et al. 2014). This becomes of particular concerns in industries where products are designed to perform for long life service with ideally minimal maintenance such as in marine, aerospace, automotive, energy, and civil engineering structures. Therefore, further investigations towards a better understanding are essential to produce safe and reliable designs (Shen and S. Springer 1976; Shenoi, R A and Wellicome 1993; Luke et al. 2002; Baley et al. 2004; Alam et al. 2018). This thesis aims at studying the influence of water absorption and fibre architecture on matrix dominated properties of CFRP, to propose safer selections of CFRP parameters for applications operating in moist environments.

The key objectives are:

- Investigate the role of water uptake in CFRP composites with the focus on the influence of fibre architecture on the directional diffusion
- Study the role of fibre architecture on matrix dominated properties and the consequential damage mechanism of CFRP composites following water absorption
- Study of the effect of progressive water content on the interlaminar failure of CFRP composites with the use of non-destructive testing techniques

1.2 Novelty statement

The thesis focuses on understanding the effects of hydrothermal aging on the properties of CFRP composites. The key areas of novelty are:

- The development of a new experimental approach to investigate the directional diffusion of CFRP composites with the use of Fick's law to compare water diffusion in three fibre architectures: unidirectional (UD), plain, and twill
- A study of the role of fibre architecture in the reduction of matrix dominant properties in CFRP composites with like for like epoxy resin. It is shown that after water absorption, the optimum material/design for an application may not be the most intuitive choice based on un-aged properties. Under compressive failures, the most linear fibres (the UD), showed a reduction of 14.6% after ageing, followed by the twill (the fibre architecture is more linear than plain) reduced by 7.5% whereas plain only reduced by 1.3%. Care is therefore should be taken in selecting materials and applying safety factors for application operating in moist conditions
- Investigate the effect of progressive water absorption on the interlaminar strength of UD CFRP (the most used form of fibre architecture) with the use of short-beam strength (SBS) test. It is shown that the failure mode of CFRP specimens changes with increasing exposure time to water. Multiple delaminations triggered by compressive failure are seen after longer exposure times and this failure does not represent true interlaminar shear failure. Therefore, the true interlaminar strength after water absorption might be higher than these values suggested by the SBS tests and often reported in literature

1.3 Published outputs

- Almudaihesh, F., Holford, K., Pullin, R., & Eaton, M. (2021). A comparison study of moisture diffusion in unidirectional and 2D woven carbon/epoxy composites. Polymer Composites, 1.
- Almudaihesh, F., Grigg, S., Holford, K., Pullin, R., & Eaton, M. (2021). An assessment of the effect of progressive water absorption on the interlaminar strength of unidirectional carbon/epoxy composites using Acoustic Emission. Sensors, 21(13), 4351.
- Grigg, S., Almudaihesh, F., Roberts, M, K., Pullin. (2021). Impact monitoring of CFRP composites with acoustic emission and laser Doppler vibrometry. Engineering Research Express 3(1), p. 015012.
- Almudaihesh, F., Holford, K., Pullin, R., & Eaton, M. (2020). The influence of water absorption on unidirectional and 2D woven CFRP composites and their mechanical performance. Composites Part B, 182.
- Almudaihesh, F., Alfaris, H., Sangha, P., Pullin, R. and Eaton, M. (2021). Understanding the role of graphene on the moisture absorption in graphene/polymer nanocomposites. IOP Conference Series: Materials Science and Engineering 1024(1), p. 012006.
- Almudaihesh, F., Grigg, S., Pullin, R., Holford, K., & Eaton, M. (2019). The influence of water absorption on the damage mechanism of unidirectional and 2D woven CFRP. Melbourne: Twenty-Second International Conference on Composite Materials (ICCM22).
- Almudaihesh, F., Pullin, R., Holford, K. & Eaton, M. (2018). The effects of fibre architecture on water absorption induced degradation in CFRP laminates (follow up results). Southampton: BSSM 13th International Conference on Advances in Experimental Mechanics.
- Almudaihesh, F., Pullin, R., Holford, K., & Eaton, M. (2018). The effects of fibre architecture on water absorption induced degradation in CFRP laminates. Athens: 18th European Conference on Composite Materials (ECCM18).

1.4 Thesis organisation

This chapter outlines the aims and objectives along with the contribution observed from the published outputs as a result of this work. Chapter 2 is a literature review covering the previous work carried out within the field and an understanding of the key issues. Chapter 3 covers all the testing methods used in this thesis (Chapters 4 to 6). Chapter 4 investigates the water absorption of UD and 2D woven CFRP, Chapter 5 studies the consequential reduction on matrix dominated properties of UD and 2D woven CFRP caused by the hydrothermal aging, and Chapter 6 further demonstrates the gradual influence of hydrothermal aging on the interlaminar strength of UD CFRP. Chapter 7 highlights the summary of the thesis, conclusions and potential future work. Finally, the appendices include the additional information and data regarding the materials used in this study, the water absorption individual results, and the individual mechanical properties for reference.

2 Literature Review

2.1 Composite materials background

Composites are simply defined as ‘materials that combine two or more substances with different distinct phases’. Structural composites in particular have played a large role in many recent applications, such as in aerospace, automotive, marine, and energy industries (Barbero 2017). Fibrous composites mainly include two significant materials whose properties reinforce each other (Herakovich 1998). These being the fibres and the polymer matrix, where each provide specific contributions to the composites properties.

The first phase is fibres; they can be simply defined as ‘the strength guard for fibrous composites’. In addition, to the main function that fibres provide in fibrous composites, such as high strength and stiffness, they are light compared with other engineering materials like steel and aluminium. Their excellent strength and stiffness to weight ratio makes fibrous composites an attractive material for engineers. The fibres in fibrous composites have been in use by engineers since the 1930s. In the late 1950s, fibres were developed with higher levels of performance, demonstrating significant increases in structural properties of stiffness-divided-by-density and strength-divided-by-density. Thus, fibres exhibiting these advanced features, which were first introduced in 1959, are known as advanced fibres. Fibre types used for advanced composites vary. Each type provides specific features and can be continuous or chopped (Herakovich 1998). Table 1 presents the main fibre types, highlighting their properties (Herakovich 1998; Vasiliev and Morozov 2007).

Table 1: Types of fibres found in fibrous polymeric composites.

<table>
<tr><th>Fibre type</th><th colspan="2">Origin</th><th>Comment</th></tr>
<tr><td>Glass fibre</td><td colspan="2">Molten glass is pulled at 1300°C through dies with dimensions between 0.8 to 3.0mm in diameter with further high speed stretching to 3–19 µm diameter.</td><td>First type of fibre used in fabric composites.
Not generally considered to be an advanced fibre because of its comparatively low modulus. However, it is one of the most significant types due to its high specific strength and low cost.</td></tr>
<tr><td>Quartz fibre</td><td colspan="2">High speed stretching at a temperature of about 2200°C by quartz rods of fused quartz crystals or sand.</td><td>Higher thermal resistance than glass fibre due to the high viscosity of molten quartz but requires more complicated procedure for manufacturing.</td></tr>
<tr><td>Basalt fibre</td><td colspan="2">Made of molten basalt rocks. Less complexity in manufacturing, relatively similar method to glass fibre.</td><td>Provides lower capability in performance. Thus, it is not used in applications that require high performance i.e. the aerospace industry.</td></tr>
<tr><td>Carbon fibre</td><td colspan="2">Made by pyrolysis using two types of fibre, PAN-based and pitch-based.
PAN-based is Polyacrylonitrile (PAN) which is stressed/ stretched and heated at a temperature of 400°C (stabilisation). Stage two is where non-carbonate filaments are detached or transformed to carbon at a temperature of 900°C (carbonisation).
For pitch-based fibres, organic filaments are made in a similar manner to that of glass fibres, with molten petroleum or coal pitch going through the stages of carbonisation and graphitisation (a subsequent stage to introduce graphite fibre).</td><td>More than 50 types of carbon fibre exist. Mainly categorised based on their strength, modulus, cost, and the process of fibre advancement.</td></tr>
<tr><td>Graphite fibre</td><td colspan="2">Starts with the same stages as carbon fibre but a subsequent stage is added, referred to as graphitisation, to be graphitised under heat treatment at a temperature of about 2800°C.</td><td>Usually referred to as carbon fibre. The only difference between graphite fibre and carbon fibre is that in graphite fibre the carbon content exceeds 99% compared with 80-95% in standard carbon fibre.</td></tr>
<tr><td>Boron</td><td colspan="2">Boron fibres have a larger diameter in comparison to other fibres 100–200 µm. This is due to the manufacturing process. The process requires a chemical vapour deposition of boron onto 12µm diameter tungsten or carbon fibre (core).</td><td>The first advanced fibre developed for use in applications after Talley introduced it in 1959.</td></tr>
<tr><td>Aramid fibre</td><td colspan="2">Aramid is an organic fibre. Initially extruded from a liquid crystalline of corresponding polymer in sulphuric acid, in addition to a subsequent washing in a cold-water bath, followed by stretching at high temperature.</td><td>Can be used as an additional material to other advanced fibres as a reinforcing element. Aramid fibre has the advantage of low thermal conductivity, providing good heat insulation, with the capability of maintaining shape under heat. Moreover, it has better water resistance than inorganic fibres but lower creep resistance.</td></tr>
<tr><td>Silicon carbide (SiC) fibre</td><td colspan="2">A common ceramic fibre type deposited on a tungsten or carbon fibre (core) by gas mixture of silanes and hydrogen reaction. Relatively thin fibres, 8–12µm diameter can be made by polycarbon-silane (pyrolysis of polymeric) fibres at 1400°C temperature.</td><td>Has the advantage of a very high melting temperature (about 2600°C). Less reduction in strength compared to other fibres when operating in hot conditions.</td></tr>
<tr><td>Alumina fibre</td><td colspan="2">Sintering of fibres extruded from viscous alumina slurry.</td><td>Similar properties to SiC fibre but with lower melting temperature at 2000°C.</td></tr>
<tr><td>Boron carbide fibre</td><td colspan="2">Obtained by two possible reaction processes. First, it can be a result of carbon fibre with a mixture of hydrogen and boron chloride at about 1800°C. Second, a reaction of cellulosic fibres soaked with boric acid solution.</td><td>Very high thermal resistance at 2300°C</td></tr>
<tr><td rowspan="12">Natural fibres</td><td colspan="3">Natural fibres are those which are not modified, are purely obtained from nature, and have lower strength and stiffness than man-made fibres. They vary in terms of mechanical properties and diameter size. The following are some of the common natural fibres.</td></tr>
<tr><td>*Natural fibre name*</td><td>*Diameter in µm*</td><td>*Ultimate tensile stress in MPa*</td></tr>
<tr><td>Spider silk</td><td>*4*</td><td>*1750*</td></tr>
<tr><td>Wood</td><td>15 to 20</td><td>160</td></tr>
<tr><td>Jute</td><td>10 to 50</td><td>580</td></tr>
<tr><td>Natural silk</td><td>15</td><td>400</td></tr>
<tr><td>Asbestos</td><td>02</td><td>1700</td></tr>
<tr><td>Cotton</td><td>15</td><td>540</td></tr>
<tr><td>Bamboo</td><td>15</td><td>550</td></tr>
<tr><td>Bagasse</td><td>25</td><td>180</td></tr>
<tr><td>Rice</td><td>5 to 15</td><td>100</td></tr>
<tr><td>Wool</td><td>75</td><td>170</td></tr>
<tr><td>Metal fibres</td><td colspan="3">Thin wires made of metal-based materials such as steel, tungsten, molybdenum, titanium, and beryllium.</td></tr>
</table>

The second phase is matrices. Many types of matrices can be used in composites such as polymers, metals, and ceramics. Each type provides certain specifications and requires certain processes when used. More recently, polymeric matrices are becoming a main element in advanced composites, due to their mechanical properties, ease of processing, and low costs. The role of the polymeric matrix includes the bonding of fibres together, whilst transmitting stress between them. Polymeric matrices play a significant role in stress diffusion within a composite, leading to lower stress concentrations on an individual fibre, yarn, or tow. Composite properties are often limited by the properties of the polymer matrix. For example, in fibre-polymer matrix composites, fibres have relatively high temperature resistance; unlike polymers, where the glass transition temperature is significantly lower than fibres, in addition to being more brittle at lower temperatures which therefore results in temperature operation limitation (Bogdanovic and Pastore 1996). Additionally, most failure mechanisms originate with matrix failure, highlighting the importance of polymers in strength and damage resistance (Vasiliev and Morozov 2007). Polymeric matrix materials also have the advantage of certain properties that provide a significant input within fibrous composites on top of adhesion. For example, low matrix liquid viscosity, in addition to good fibre surface wettability, is a significant feature that allows the matrix to squeeze between the fibres, especially in more complex fibre structures. Relatively high viscosity is then obtained after a proper cure process, which is important in order to allow the matrix liquid to retain and combine with the fibres (Vasiliev and Morozov 2007). Polymeric materials are divided into two main types. The first type is thermoset, which is the most commonly used in advanced composites, and the second is thermoplastic. The primary difference between the two is that thermoset is a material that strengthens when heated, but cannot be remoulded or heated after the initial forming, while thermoplastics can be reheated, remoulded, and cooled as necessary without causing any chemical changes (Herakovich 1998). Both types are presented in Table 2 and Table 3, with further examples and performance details (Bogdanovic and Pastore 1996; Herakovich 1998; Duann et al. 2004; Vasiliev and Morozov 2007; Broughton 2012).

Table 2: Types of thermoset polymers found in fibrous polemic composites (Bogdanovic and Pastore 1996; Herakovich 1998; Duann et al. 2004; Vasiliev and Morozov 2007; Broughton 2012).

Thermoset materials	Notes	Ultimate tensile stress UTS (MPa)	Modulus E (GPa)
Epoxy	Mainly glycidyl ethers and amines. Relatively better moisture resistance when compared to other thermoset materials. Significantly lower shrinkage on curing process. Cure temperature up to 175°C and glass transition temperature varies from 60°C to 200°C.	60-90	2.4-4.2
Polyester	Generally made by a dibasic organic acid and dihydric alcohol. Glass transition temperature is aproxiamtely 80°C. Cure temperature can go up to 240°C.	30-70	2.8-3.8
Phenol-formaldehyde	Glass transition temperature is 60-75°C and cure temperature 135 to 180°C.	40-70	7-11
Organosilicon	Really high temperature resistance thermoset materials with up to 400°C cure temperature and glass transition temperature of 250°C to 300°C.	25-50	6.8-10
Polyimide	Another higher use in temperature for a thermoset material with 300°C to 400°C cure temperature and about 250°C glass transition temperature.	55-110	3.2
Bismaleimide	Similar to organosilicon and polyimide in cure and operating temperatures.	80	4.2

Table 3: Types of thermoplastic polymers found in fibrous polymeric composites (Bogdanovic and Pastore 1996; Herakovich 1998; Duann et al. 2004; Vasiliev and Morozov 2007; Broughton 2012).

Thermoplastic materials	Glass transition temperature (°C)	UTS (Mpa)	E (GPa)
Polyethylene	ranges about 128°C	20-45	6-8.5
Polystyrene	approximately 100°C	35-45	30
Teflon	-	15-35	3.5
Nylon	70°C	80	2.8
Polyester (PC)	150 °C	60	2.5
Polysulfone (PSU)	190°C	70	2.7
Polyamide-imide (PAI)	270°C	90-190	2.8-4.4
Polyetheretherketone (PEEK)	140°C	90-100	3.1-3.8
Polyphenylene sulphide (PPS)	90°C	80	3.5
Polylactic Acid (PLA)	65°C	50	3.5

For the purposes of this study, *continuous* Carbon Fibre Reinforced *thermoset epoxy* Polymer (CFRP) is the dominant material that will be investigated, due to its high demand in recent engineering applications (Alam et al. 2018).

2.2 CFRP structures

Continuous CFRP exists in different forms. Initially, the raw combination of carbon fibres and matrix materials can be manually built by the wet lay-up process. They can also be in the form of prepreg, where specific fibre weight fraction and matrix weight fraction are built and stored in rolls, and where the manufacturing process for an application can be carried out without the need to combine both materials during the lay-up process. Prepregs are widely used in engineering applications, due to the accurately controlled resin content and chemistry within the composite structure. Along with fibre orientation, the accurately controlled amounts of constituent contents can further maximise the quasi-isotropic properties by achieving the exact amount needed, based on the application requirements (Meredith et al. 2015). However, it is relatively more complicated to add additional materials to the composites when they are already in the form of prepreg, specifically adding certain elements to the fibres or the matrix (for instance, adding graphene). These continuous CFRPs can be produced in a variety of structures, such as unidirectional lamina, and woven fabrics (Herakovich 1998).

Unidirectional lamina is the basic form of continuous fibre composites. Simply, one ply/layer contains continuous fibres in one direction. The ply can be in the form of prepreg tape, which contains fibres and matrix, or other fabrication methods can be used, such as filament winding, pultrusion, or Resin Transfer Moulding (RTM). The mechanical properties of unidirectional lamina are significantly dependent on the fibre direction in relation to an applied load. The greatest variance in properties is seen when the load is parallel (longitudinal), compared with perpendicular (transverse), to the fibres (Herakovich 1998).

In woven fabrics, the fibres are formed in different architectures, angles, and directions within one layer. Woven fabrics can be defined as yarns of weft and warp fibres forming a specific design for specific properties. A braiding system is used to form the woven fabrics and can be expressed as a system that involves two or more yarns intertwined with each other at certain angles, without overlapping or twisted around one and other. This system has the advantage of having many fibre architectures assembled to form a structure. An example of one form is ‘biaxial’, in which two yarns are crossing over and under each other at a ±45 degrees weave angles, producing different woven structures such as twill weave, plain weave, satin weave, and basket weave. Another form is ‘triaxial’, in which there is a third set of yarns are added on the axial direction, achieving a multi-directional ‘off-axis’ and unidirectional ‘axial’ reinforcement in one layer. This can be used to achieve a quasi-isotropic balance in one single layer. Both biaxial and triaxial are referred to as 2D woven structures as fibres are predominately in the in-plane direction, whereas 3D woven also exist to utilise the fibre performance constructed from yarns and tows arranged into complex three-dimensional structures, created from a 3D weaving process (Pastore and Gowayed 2008; Schwartz 2008; Xiao et al. 2019). Figure 1 presents the primary configurations and designs of 2D and 3D woven fabrics (Pastore and Gowayed 2008; Schwartz 2008; Xiao et al. 2019).

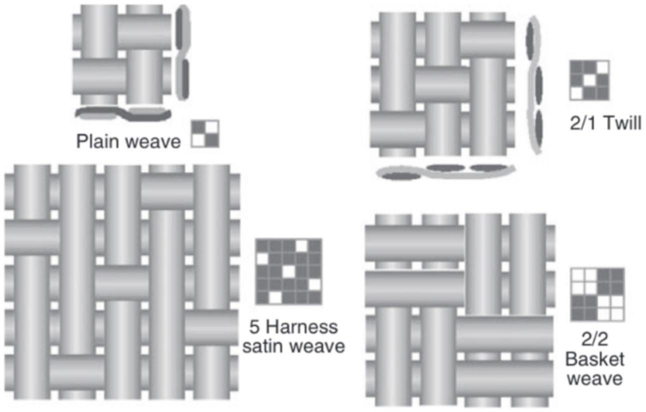

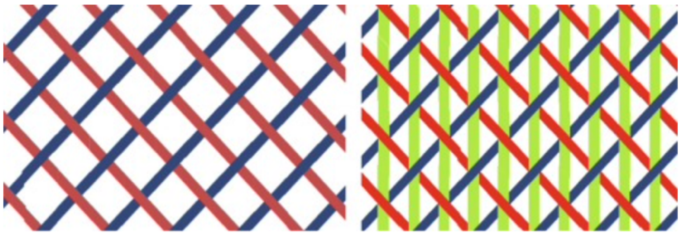

A biaxial braid A triaxial braid

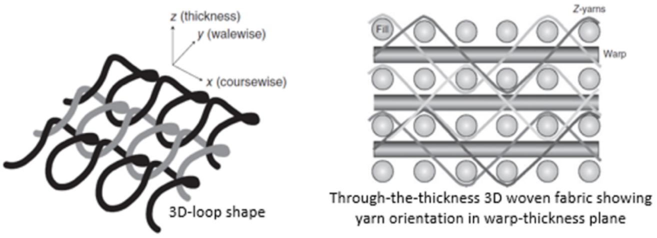

Figure 1: 2D and 3D woven fabric examples (Pastore and Gowayed 2008; Schwartz 2008; Xiao et al. 2019).

Laminates are formed by staking layers of unidirectional or 2D woven fabric, or a combination of both fibre architectures. The laminates are made to form specific properties based on thickness, orientations, or staking sequence of individual layers (Vasiliev and Morozov 2007). These laminates are presented in the form of codes. These codes present the staking sequence of each layer; that is, to present the orientation and the number of layers in the laminate. Table 4 presents examples of layer staking sequences and their corresponding code used in ASTM D6507-19.

Table 4: Fibre Reinforcement Orientation Codes for Composite Materials.

Example	Full laminate stack	Code
Six unidirectional layers at 0° (six layers in total)	[0°/0°/0°/0°/0°/0°]	$[0_6]$
Three unidirectional layers at +45° and three unidirectional layers at -45° (six layers in total)	[45°/45°/45°/-45°/-45°/-45°]	$[45_3/-45_3]$
One unidirectional layer at +45° and one unidirectional layer at -45°, symmetric (four layers in total)	[45°/-45°/-45°/45°]	$[45/-45]_s$
One unidirectional layer at 0°, one unidirectional layer at +45°, and one unidirectional layer at 90°, symmetric (six layers in total)	[0°/45°/90°/90°/45°/0°]	$[0/45/90]_s$
Three woven layers at (0/90)° and three woven layers at (45/-45)° (six layers in total)	[(0/90)°/(0/90)°/(0/90)°/(45/-45)°/(45/-45)°/(45/-45)°]	$[(0/90)_3/(45/-45)_3]$
One woven layer at (0/90)° and one woven layer at (45/-45)°, symmetric (four layers in total)	[(0/90)°/(45/-45)°/(45/-45)°/ (0/90)°]	$[(0/90)/(45/-45)]_s$
One woven layer at (0/90)° and one unidirectional layer at 45°, symmetric (four layers in total)	[(0/90)°/45°/45°/(0/90)°]	$[(0/90)/45]_s$

The complicated structure of CFRP composites and complicated failure mechanisms are distinct features of the material, which generally includes several structural defects and failure types. Figure 2 highlights the potential defects, along with the failure terms of CFRP composites that will be referred to several times within this thesis (Herakovich

1998; Campbell 2004; Vasiliev and Morozov 2007; Silberschmidt 2016). These illustrations are presented through a simple structure of [0°/90°] laminates.

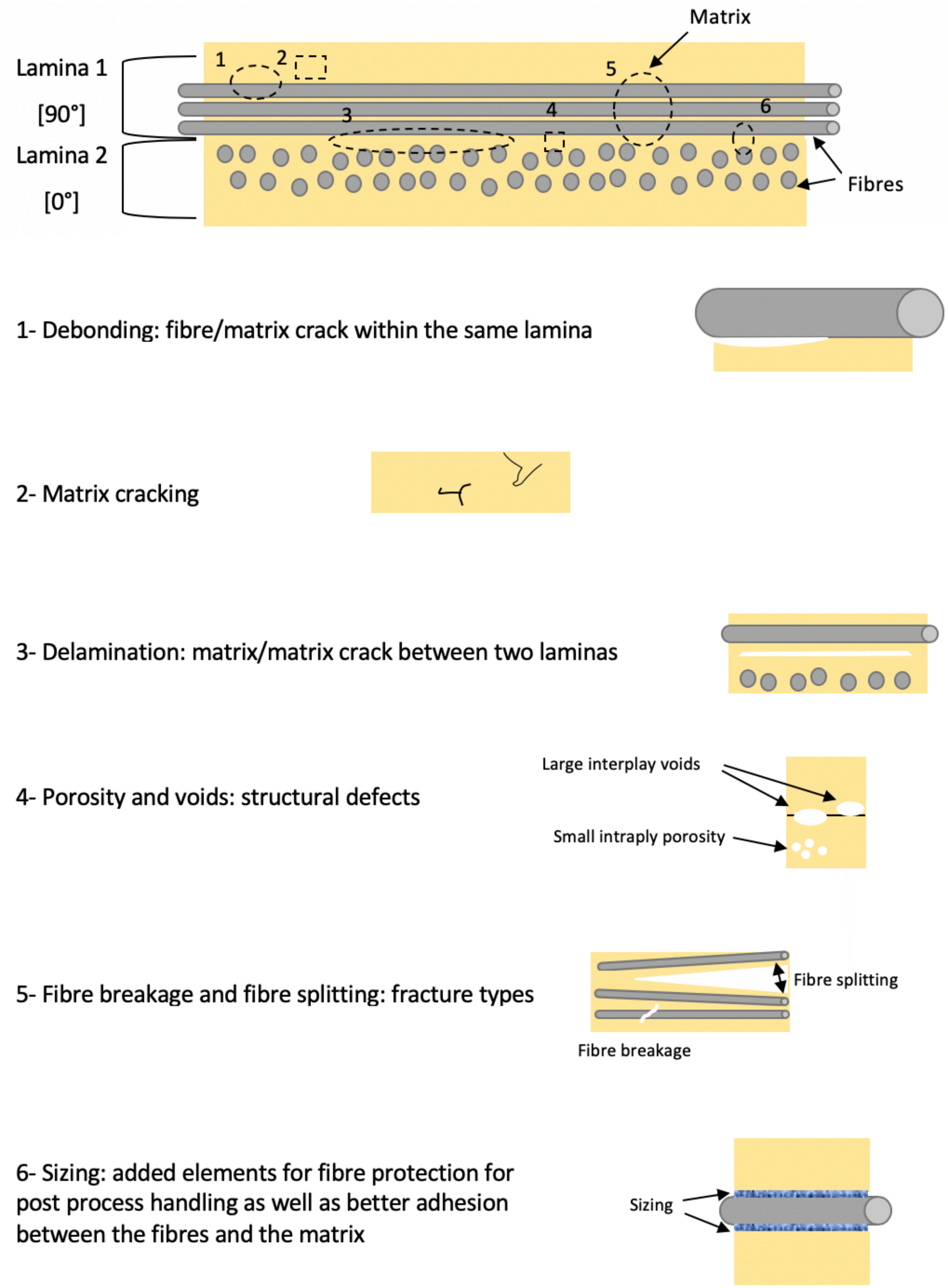

Figure 2: CFRP general structure and failure terms (Herakovich 1998; Campbell 2004; Vasiliev and Morozov 2007; Silberschmidt 2016).

2.3 Moisture absorption in CFRP composites

2.3.1 Epoxy resin and the phenomena of hydrolysis and plasticisation in composites

The performance of CFRP composites can be limited in real life applications due to degradation or ageing caused by processes taking place in a moisture-based or harsh environment, particularly within polymers (Frigione and Lettieri 2018). The absorbed water can cause reversible and/or irreversible changes in the physical and chemical properties of the material (Cauich-Cupul et al. 2011a; Zafar et al. 2012; Pérez-Pacheco et al. 2013; Saeed et al. 2014; Grammatikos et al. 2015; Cysne Barbosa et al. 2017; Capiel et al. 2018) because polymers in composite materials chemically react with water. Epoxy resins have the ability to absorb substantial amounts of moisture and are commonly used in structural applications. These reactions are triggered by the polar groups in the material and are caused by the replacement of ester groups with alcohol and carboxyl acids that attract water molecules, leading to plasticisation (Capiel et al. 2018). Plasticisation is the swelling of the membranous structure of polymers due to sorption of a penetrant in a polymer matrix. The penetrant can be either carbon dioxide or water in addition to a range of linear hydrocarbons and aromatics. This process generally yields an increase in the fractional free volume of the membrane, resulting in the diffusion of all the gas species via the membrane. This is followed by an increase in permeability and loss of selectivity. For example, the plasticisation of BTEX aromatics at 200–1,000 ppm can reduce the membrane’s selectivity by 30%–50% (Kentish 2011). However, the ageing of membranes is essentially the reverse of plasticisation – compaction of membranous structures over time, resulting in loss of fractional free volume. This results in loss of permeability with increased selectivity (Kentish 2011). Plasticisation effects also decrease the glass transition temperature (T_g) of composite materials (Chateauminois et al. 1995). These physico-chemical changes affect both diffusion and hydrolysis kinetics. It is the hydrolysis of the reactive groups, present in a polymer's structure, that causes the detrimental degradation. Hydrolysis is a chemical decomposition process in which the dissolution of organic substances takes place by water (Asmatulu et al. 2014). Hydrolysis causes chain scission, which decreases a polymers' crosslink density (Capiel et al. 2018). Moreover, chemical scissions due to hydrolytic degradation occur on the same elastically active chain. This results in relatively low molecular weight species that have the tendency to leave the polymer network through lixiviation (Capiel et al. 2017; Capiel et al. 2018). This process results not only in global degradation but also in chemical and structural changes that turn into a complicated diffusion-reaction coupled phenomena (Capiel et al. 2017; Capiel et al. 2018). The absorption processes of epoxy resins can be complicated and often reveal various anomalies in the mass uptake. It has been found that part of the absorbed water is present as free molecules in the micro-voids of the network; alternatively, it is involved in physical interactions with the polymer chains or other water molecules (Azwa et al. 2013). The rest of the water molecules are involved in hydrolysis reactions within the material (Capiel et al. 2017). Therefore, the total absorbed water cannot be considered an indication of a unique ageing process since it has different effects on the polymeric constituent. It is necessary to examine the absorption of moisture molecules, with the subsequent evolution of properties, in terms of swelling. For this purpose, spectroscopy techniques, such as the Nuclear Magnetic Resonance (NMR) and Fourier Transform Infrared (FTIR) are used (El Yagoubi et al. 2015). Generally, water absorbed into composite materials after their immersion in water is categorised as two types: free water and bound water. Free water is transported into a polymer via microcracks, whereas bound water is dispersed in the polymer matrix and attaches to the polymer's polar groups, Figure 3 (Chang et al. 2020).

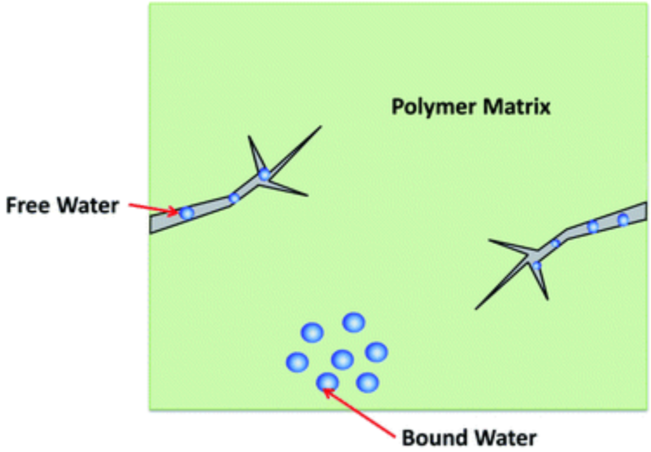

Figure 3: The transport of water into the polymer through different routes (Chang et al. 2020).

Knowledge of the mechanisms that drive moisture absorption, as well as the influence of dimensions, temperature and relative humidity, is important when the long-term properties of the composite are of interest (Sales et al. 2017). It is crucial to understand the three common methods of moisture absorption by polymeric composite materials, namely: diffusion process, capillary actions and transport of water molecules. The diffusion process takes place inside the micro gaps between polymer chains (Karmaker 1997; Espert et al. 2004). The capillary process occurs in the empty spaces between the fibre-matrix interfaces. These spaces within the interfaces are produced during the manufacturing process, particularly when the reinforcement's impregnation into the matrix is incomplete. The transport of water through microcracks is the most important mechanism that leads to the ultimate debonding of the fibre-matrix (Spragg et al. 1996; Cauich-Cupul et al. 2011a; Muñoz and García-Manrique 2015).

The study of the interaction of polymers with water at the molecular level is very important because water intake determines a material's mechanical properties at the macroscopic level (Sales et al. 2017) and any moisture absorption by polymeric composite materials can result in permanent damage to the matrix and interface (El Yagoubi et al. 2015). This ingress of water molecules is significant if the polymer-based structure is immersed in water, salt or alkaline-based solutions because this leads to a reduction in stiffness, strength and the resin's glass transition temperature (T_g) due to plasticisation effects (Cauich-Cupul et al. 2011a; Zafar et al. 2012; Pérez-Pacheco et al. 2013; Saeed et al. 2014; Kafodya et al. 2015; Cysne Barbosa et al. 2017; Frigione and Lettieri 2018).

2.3.2 Damage mechanism from a fibrous/polymeric structure prospective

Polymers are known to degrade in moist environments by reacting with water in a hydrolysis process which affects their mechanical performance (Masoumi and Valipour 2016). The influence of water ingress on fibrous-polymer composites varies based on temperatures and water type, such as seawater or demineralised water (Davies et al. 2017). Higher temperatures are known to have more influence in accelerating the moisture absorption and degradation process in polymers (Grammatikos et al. 2016; Cysne Barbosa et al. 2017). This can also lead to significant changes in the overall intrinsic structural performance and failure mechanisms of CFRP (Selzer 1997; Saito and

Kimpara 2009; Kim and Takemura 2011; Pérez-Pacheco et al. 2013; Kafodya et al. 2015; Korkees et al. 2018c; Zhang et al. 2019).

In the case of thermoset polymers, it has been known for some time that the matrix and fibre-matrix interface dominated properties are most affected by moisture absorption. Selzer (1997) showed that for unidirectional carbon fibre reinforced epoxies, transverse, compression and interlaminar fracture properties reduced significantly following moisture absorption, whereas no discernible change was observed in fibre direction tensile properties. This corresponds to the accepted mechanisms of moisture absorption in CFRP laminates, which starts with free water molecules at the surface, travelling through surface micro-cracks and voids (Figure 4 (stage I-III)). This leads to hydrolysis, which has a plasticising effect, leading to a reduction in properties. When water molecules reach the fibre-matrix interface, the resultant degradation leads to the reduction of stress transfer (Zafar et al. 2012; Pérez-Pacheco et al. 2013) (Figure 4, Stage IV). Ultimately, debonding can occur as the polymer continues to degrade (Ray 2006; Vasiliev and Morozov 2007; Dao et al. 2010) (Figure 4, Stage V). This process is dependent on time, temperature, fibre architecture, layup, fibre volume fraction, void content, polymer type, fibre sizing or surface treatment, water type, and contact area (Costa et al. 2006; Ray 2006; Zafar et al. 2012; Pérez-Pacheco et al. 2013; Sethi and Ray 2015; Davies et al. 2017). However, the extent to which each of these factors affects the final properties of a composite is not clear. The variety of constituent materials, hydrothermal conditioning, and properties measured in the current literature makes it challenging to draw consistent conclusions.

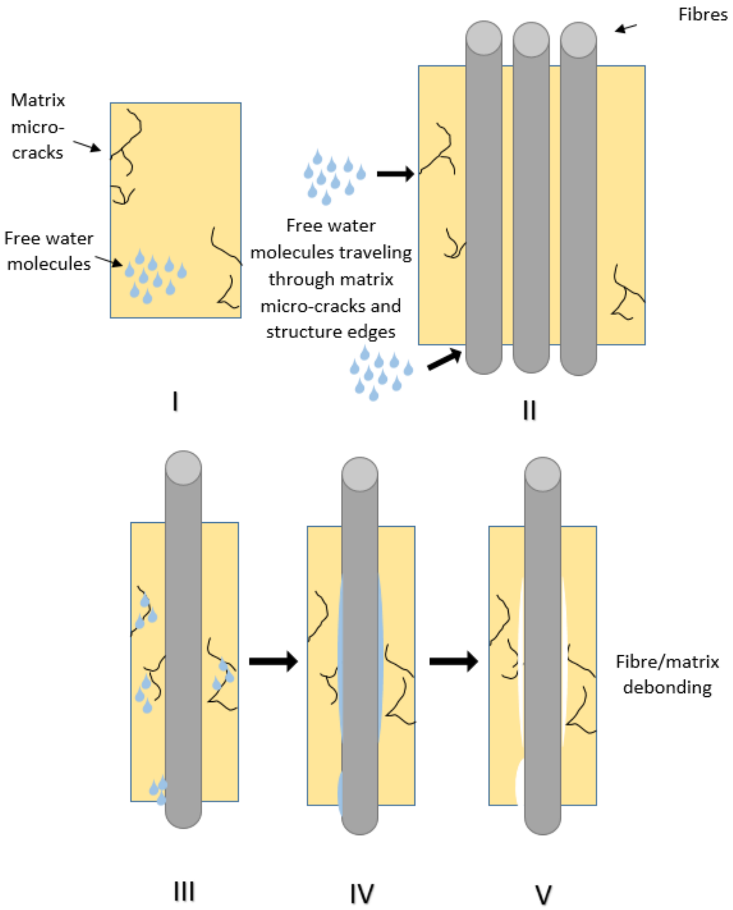

Figure 4: Water ingress mechanism in fibrous reinforced polymers composites.

2.3.3 The effect of water absorption on the 'glass transition temperature' in epoxy resin composites

Composite materials are exposed to a variety of environmental conditions; hence, the knowledge of mechanisms such as liquid diffusion, degradation and performance retention is critical. The epoxy resin has a high affinity to moisture, and the absorption of moisture takes place at a rapid rate at high temperatures, which can cause the polymer to swell, plasticise and lose properties over time (Otaluka et al. 2015). The plasticisation process is the phenomenon observed when the polymers are immersed in water. In composites, the moisture absorbed results in a decrease in the glass transition temperature (T_g) due to plasticisation. The swelling produced as a result of this process increases the volume of the composite material and adversely affects the T_g of the material (Chateauminois et al. 1995; Chang et al. 2020). Generally, the extent to which T_g varies is directly proportional to the water absorption rate in the polymeric material. This is due to the breakdown of the hydrogen and the Van der Waal's forces by the water molecules, which further results in an increase in the chain segment mobility (Chang et al. 2020). The presence of hydroxyl groups in the epoxy-based composites that form from the ring-opening polymerisation makes the polymer susceptible to water absorption. This water content instantly causes the polymer to lose its strength when compared to dry conditions (Dutta 2008). The water absorption by the epoxy network can lower the value of T_g by more than 50°C (Chateauminois et al. 1995). The effects of absorption is even worse when the water temperature is near or above the value of T_g whereby the water effects can lead to a disastrous failure. The water absorbed acts as a plasticiser and lowers the T_g of the epoxy resin as a function of the quantity of water absorbed. For a fully cured system, the effects can be reversible. However, heating at elevated temperatures along with water absorption leads to an irreversible degradation (Johncock and Tudgey 1986). This results in the tensile strength of the epoxy to reduce from 40% to 75%. Alternatively, when more crosslinks are present in the polymeric structure, the drop in the T_g is less, which results in a lesser reduction in the tensile strength. For epoxy-based composites, anhydrides are used for curing, which allows the epoxy polymers to have better properties at temperatures slightly above T_g (Dutta 2008).

It has been observed that water can have two effects on the network of polymers depending on its concentration. At the start of the hygrothermal process, the water absorbed can cause a relaxation in the residual stresses along with an acceleration in the additional crosslinking. The change in these properties increases the mechanical properties. The value of T_g is the most important factor in revealing the material's degradation level. The more flexible the polymeric chains, the lower the value of T_g. The decrease in the value of T_g is attributed to plasticisation and deterioration (chain scission), while the increase in the value of T_g indicates a crosslinking of the polymeric chains alongside an embrittlement of the composite. Therefore, the degradation of the mechanical properties is mainly due to the plasticisation and deterioration of the epoxy resin (Krauklis et al. 2018). In order to predict the reduction in the value of T_g due to plasticisation effects on a molecular basis, two approaches have been adopted. The first is the 'free volume' approach, which was introduced to understand the dependence of the composites on the value of T_g and the viscosity in the polymer-diluent systems. In this method, both the diluent and the 'free volume' of the polymer are considered to be additive. This means that the value of T_g of a polymer can be reduced by mixing with a liquid that contains more free volume than that of the undiluted polymer. This approach was first transposed to epoxy-water systems by Chateauminois et al. (1995). The second approach involves the 'configurational entropy theory' of glass formation to predict the compositional dependence of the glass transition temperature for binary mixtures obeying the 'regular solutions' laws (Chateauminois et al. 1995). The water absorbed by an epoxy-based composite reduces the glass transition temperature due to plasticisation of the polymeric network. This effect also leads to the deterioration of the mechanical performance of the composite material. The other mechanical properties, such as the compressive strength and the intra-laminar/inter-laminar shear strength, are also significantly affected by the absorbed moisture at higher temperatures. This can also cause inter-laminar damage or a delamination in the epoxy-carbon composites (Sales et al. 2017).

2.3.4 Experimental studies

Generally, it has been found that moisture can diffuse easily and rapidly into polymers in the early stages, followed by a slow, gradual increase in the second stage, until equilibrium is reached, and the material is saturated. This equilibrium stage is influenced by the geometry of the materials, where longer periods are expected in larger structures, of up to months or years, prior to saturation (Korkees et al. 2018a). Accelerated aging is therefore implemented in many investigations (Brown et al. 1995). This means aging the materials in severe conditions provokes degradation, subsequently reducing aging times to a more realistic timescales of an investigation (Grammatikos et al. 2016). The kinetics of moisture absorption start almost immediately on contact with the environment within the surface layers (Korkees et al. 2018c).

Grammatikos et al. (2015) carried out an experimental study on the moisture uptake characteristics of a pultruded fibre (E-glass) reinforced polymer (isophthalic polyester) PFRP flat sheet, subjected to hot/wet aging. The experiment included exposing samples of varying geometry to distilled water at 25°C, 40°C, 60°C, and 80°C for a period of 224 days. The geometric aspects for each water temperature were square samples of 40 x 40 mm^2, 80 x 80 mm^2, and 200 x 200 mm^2 and all cut from the same sheet, 6.4 mm in thickness. The concluding observations in their experimental approach included that the initial rate of moisture uptake increased with rising immersion temperature. None of the samples of any geometry, of those exposed to 25°C, and 40°C, had reached the moisture saturation state after 224 days; whereas, all samples exposed to 60°C and 80°C reached saturation after about 140 days and 40 days, respectively. Figure 5 summarises the water uptake results of this study (Grammatikos et al. 2015). A dominant factor that is seen to influence the moisture uptake percentage is the total surface area to volume ratio. The higher the ratio is, the higher the moisture uptake percentage is observed along the immersion time axis. The study concluded with a graphical representation of the change in moisture uptake on an FRP material over a prolonged time period, dividing the characteristic curve into three distinct stages (presented in Figure 6). Stage (I) is where moisture uptake and material decomposition are competing until the condition of moisture saturation is reached (Grammatikos et al. 2015). During this stage, the moisture uptake is greater than the mass loss. In stage (II), moisture uptake has reached a maximum, or its rate of increase is equal, or less than, the rate of mass loss into the immersion solution (Grammatikos et al. 2015). In stage (III), the decomposition rate is dominant (to establish actual mass loss, an aged sample can be dried) (Grammatikos et al. 2015).

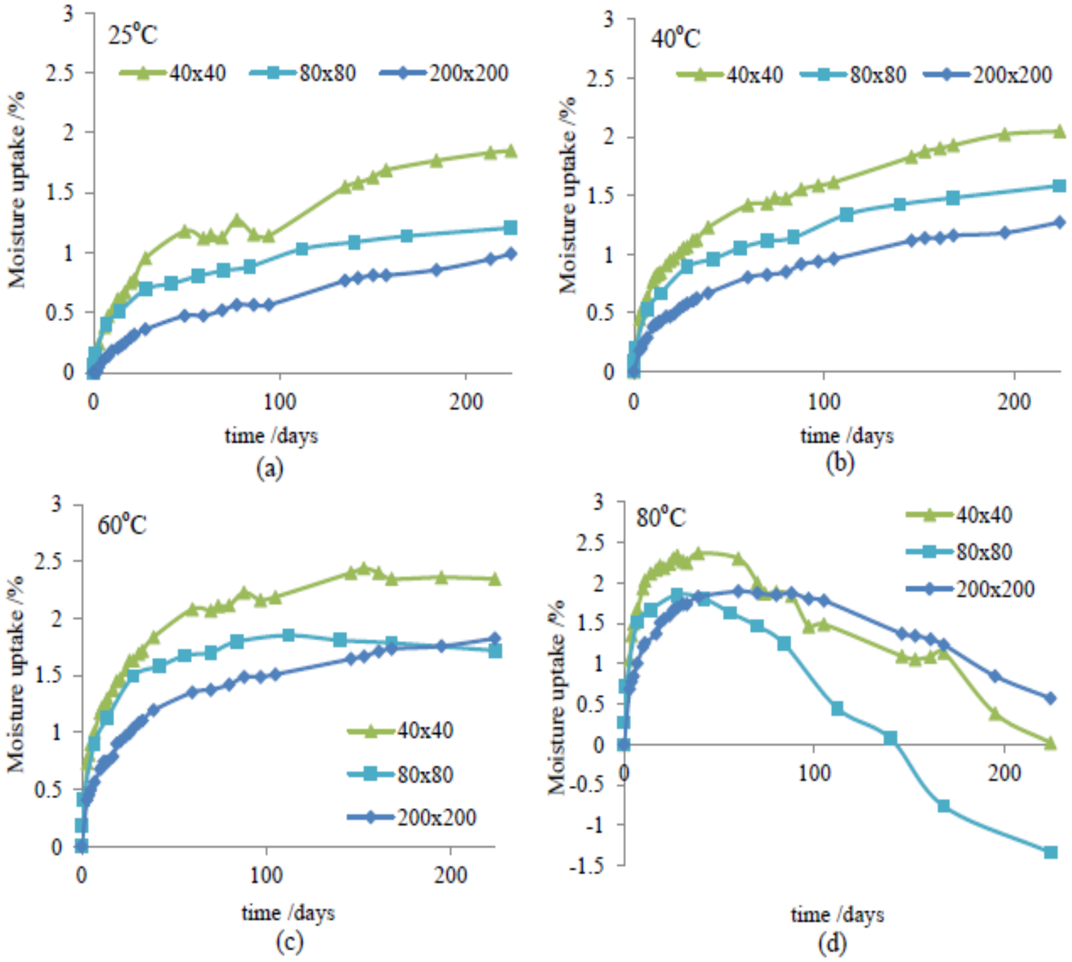

Figure 5: Percentage of mass change versus time: (a) 25°C; (b) 40°C; (c) 60°C; (d) 80°C (Grammatikos et al., 2015)

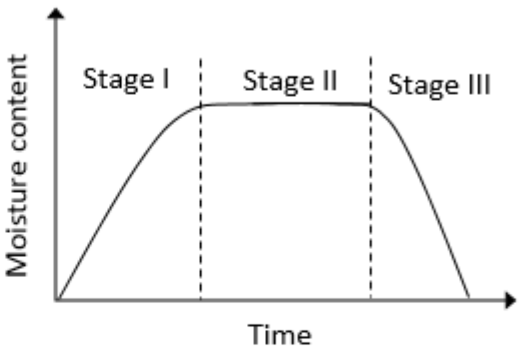

Figure 6: Schematic configuration of a moisture uptake curve as function of time observed from (Grammatikos et al., 2015).

Korkees et al. (2018c) investigated the long-term water uptake behaviour (more than 3.7 years) and mechanisms of CFRP composites. Unidirectional, ±45° (symmetrical) lay-up, and epoxy samples were used in their study and immersed in 23°C, 40°C, 60°C, 70°C, and 80°C distilled water, with other samples exposed to the different relative humidities of 45%, 60%, 85%, and 100% at 70°C. Figure 7 shows the maximum moisture saturation contents observed in their study. The values confirm that the moisture content is a function of the resin content. Furthermore, the values demonstrated the dependency of maximum moisture contents on the experimental condition in terms of temperature and relative humidity (Korkees et al. 2018c). The authors believe that the water solubility into epoxy resins and their composites might be expected to increase with temperature, because the free volume of the epoxy resin increases with temperature, allowing more water to diffuse into this additional volume (Korkees et al. 2018c).

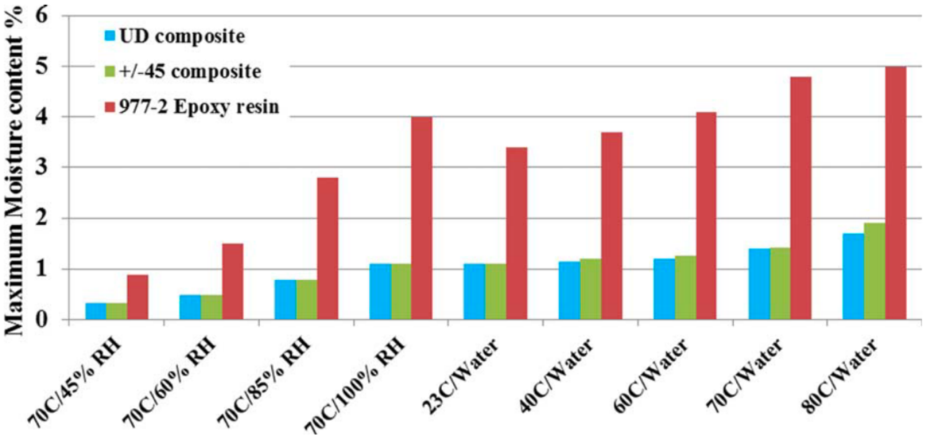

Figure 7: The maximum moisture contents observed in the Korkees et al. (2018c) study.

2.3.5 Moisture diffusion, novel theories for water intake into composite materials (Fick's law and others)

In terms of efficiency, water absorption is a critical factor when it comes to composite materials. This is due to the fact that the water absorption can be used as an indication of the adhesion between the fibres and the matrix. As a result, most researchers attempted to decrease the water absorption rate in order to increase the adhesion between the fibres and the matrix (Megiatto et al. 2010). A study by Imoisili and Jen (2020) investigated the potassium permanganate ($KMnO_4$) treated plantain (*Musa Paradisical*) fibres reinforced epoxy bio-composites to determine how the water absorption varies with the treatment of the fibres. Untreated, and treated fibres with 0.025%, 0.05%, and 0.1% $KMnO_4$ – acetone solution for a period of 3 minutes each were tested. From the results of this study, it was concluded that potassium permanganate significantly affects the composite's water absorption characteristics. From the results shown in Figure 8, it is evident that the treatment of fibres improved the water resistance, and this is characterised by the reduced weight gain. However, when 0.1% treatment was used (i.e. the K3 sample), the weight gain significantly increased due to the damage of the fibres, which allowed more water to penetrate into the composite (Imoisili and Jen 2020).

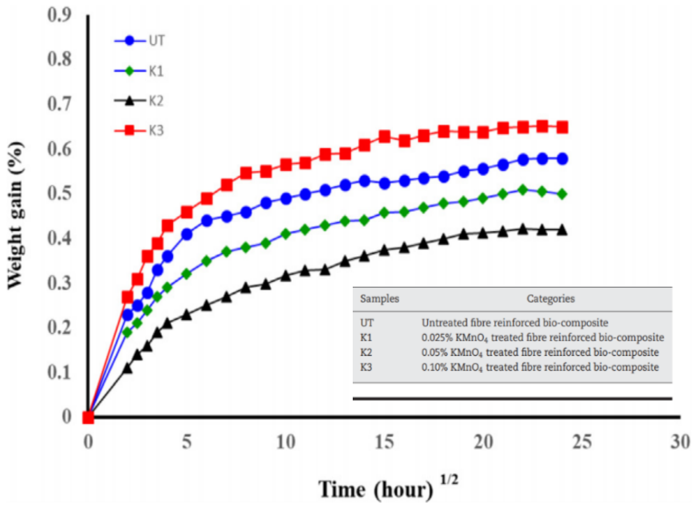

Figure 8: The water absorption properties of the treated and untreated fibres (Imoisili and Jen 2020).

The study describes the mechanism of water absorption using diffusion theories. The authors suggest that there are various diffusion mechanisms taking place during the process of water absorption. It states that these diffusion mechanisms are somewhat unusual and do not obey Fick's law until the water intake upsurges with the square root of time, and thereafter, progressively reduces to the equilibrium plateau. After this point, the equilibrium plateau tends to reduce with time according to Equation 1:

$$\frac{M_t}{M_s} = Kt^n \tag{1}$$

where M_t is the moisture at time t; M_s is the moisture at equilibrium; K is the contact coefficient between the sample and the water; and n is the sorption process. This equation describes the separation of the various diffusion mechanisms. In other words, when n is equal to 0.5, the sorption process follows Fick's law. If the n value is equal to 1 or higher, it indicates that the sorption process is not following Fick's law, and this applies to n values between 0.5 and 1. Water absorption has been found to be one of the significant reasons for the damage of the fibre matrix interfaces (Lahouari et al. 2013). As stated in this investigation, most of the water absorption models were fundamentally based on Fick's law. However, there seem to be some additional models that have been used by other researchers in addition to Fick's law (Mrad et al. 2018). These models do not necessarily deviate from the fundamental mechanics related to Fick's law, but some exceptions can be found within the literature. In this regard, Melo et al. (2018) confirmed that several methods can be employed to describe and simulate the water absorption other than Fick's law. Such models include the Jacob's–Jones model, the Time–Variable Mass Diffusivity model and the Langmuir model (Melo et al. 2018). The Jacob's–Jones model assumes that the material has distinct phases with different sorption properties. In addition, the chemical bonds that may be formed between the polymer and the water molecules have been ignored in this model. On the other hand, the Time–Variable Mass Diffusivity model suggests, as its name implies, that water diffusion increases with time. Furthermore, the Langmuir model takes an additional step by describing the moisture as consisting of two major components, the free state and the bound state, each of which influences the water absorption to a certain level. In addition, Kahraman and Al-Harthi (2005) have proposed another model that deviates from Fick's law to describe the moisture sorption of aluminium-powder-filled epoxy. They carried out investigations in two different environments, namely water and NaCl aqueous solutions. It was observed that the adhesives adsorb a larger amount of water upon exposure to distilled water than when exposed to different NaCl solutions, as shown in Figure 9 (Kahraman and Al-Harthi 2005). The moisture diffusion rate in the adhesive immersed in a test solution is, however, proportional to the salt concentration of the solution. Also, the addition of aluminium filler into epoxy decreases the total amount of water intake at saturation.

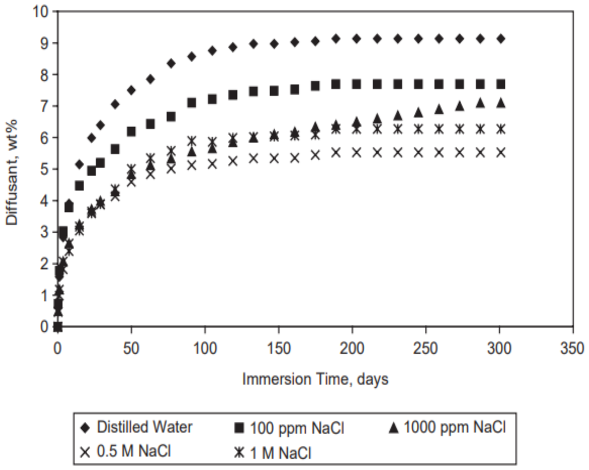

Figure 9: The observed diffusion water intake in different solutions (Kahraman and Al-Harthi 2005).

In the same study, Kahraman and Al-Harthi developed a simplified sorption model. This was based on the fact that the observation is more straightforward when the diffusion coefficient is constant. In such scenarios, the sorption experiment would be linear. The simplified model is given as in Equation 2:

$$\frac{M_t}{M_\infty} = 4\left(\frac{Dt}{\pi l^2}\right)^{1/2} \tag{2}$$

where M_t is the amount of diffusant; M_∞ is the equilibrium sorption; D is the diffusion coefficient; *t* is the time; and *l* is the thin film thickness. Furthermore, Kahraman and Al-Harthi stated that when the diffusion is a function of concentration, Fick's law cannot express the sorption dynamics or its derivation from the law. However, Tsenoglou et al. (2006) stated that the water absorption takes place within a composite interfacial zone in the polymer's region. The authors also defined the diffusion coefficient (D) in terms of volume fractions such that in Equation 3 (Tsenoglou et al. 2006):

$$D = D_0 e^{-1/f} = D_0 \exp\left(\frac{-1}{V_{P}f_{P}+V_{F}f_{i}}\right) \tag{3}$$

where D_0 is the pre-exponential coefficient; the term (V_P f_P) is the free volume corresponding to the polymer; and the term ($V_F f_i$) is the free volume of interfacial origin.

From literature, Fick's theory is found to be frequently reported in modelling the moisture uptake process due to its suitability in determining moisture diffusion coefficient (Surathi and Karbhari 2006; Grammatikos et al. 2015) as compared with other theoretical approaches (Carter and Kibler 1978; Wong and Broutman 1985; Surathi and Karbhari 2006). Bulk diffusion, D, from Fick's second law of diffusion, as postulated for composite materials, and the theoretical change in mass, M, of composite materials from water immersion, are given in Equation (4) and (5), respectively (Crank 1975; Shen and S. Springer 1976).

$$D = \pi\left(\frac{h}{4M_\infty}\right)^2\left(\frac{M_2-M_1}{\sqrt{t_2}-\sqrt{t_1}}\right)^2\left(1+\frac{h}{L}+\frac{h}{w}\right)^{-2} \tag{4}$$

$$M = \left[1-\frac{8}{\pi^2}exp\left(-\pi^2\frac{Dt}{h^2}\right)\right]M_\infty \tag{5}$$

M_1 and M_2 are the moisture contents at times t_1 and t_2, respectively; h is the distance into thickness; L is the composite length; w is the composite width; t is time; and M_∞ is the maximum change in mass.

Several fundamental parameters would affect the diffusion coefficient in polymeric composites and mainly attributed to temperature where a small change in the temperature can cause a large change in the rate of diffusion (Surathi and Karbhari 2006). Other factors can also include the chemical structure of the polymer, including the imperfections such as microcracks, and the degree of cross-linking (Crank 1975). The diffusion coefficient also depends on internal structure of CFRP composites such as the interphase region preceding the matrix/fibre interface where the polymer chains are pinned, the fibre/interface, fibre itself (i.e. diameter, and architecture), and the fibre volume fraction (Rao et al. 1984a; Rao et al. 1984b). Further complications can also be introduced to those affecting parameters, such as the use of fibre sizing, the fibre surface roughness, the microstructure of constituent contents, and the presence of structural defects (Rao et al. 1984a; Rao et al. 1984b; Alam et al. 2018).

Arnold et al. (2013) carried out a study to determine the directional moisture diffusion coefficient of UD CFRP under 23°C, 40°C, and 70°C water immersion by using full 3D Fickian solution analysis. Diffusivity across the fibres and through the thickness were 40%, and 13% of that found along the fibres, respectively. The study also compared the diffusion of unreinforced resin (matrix only specimens) with ‘along the fibre’ diffusion and the results showed slightly lower diffusion rates for the unreinforced resin, indicating some effects from the fibre interface and interphase regions (Arnold et al.

2013). Arao et al. (2008) compared the diffusivities of UD, quasi-isotropic laminate, and woven fabric for CFRP composites by producing two geometries of specimens for each form, in order to allow calculation of the directional diffusion coefficients. The first geometry is a rod with a square cross-section to measure the dimensional change and mass change, and the other geometry is a thin specimen (50mm by 50mm and 1mm in thickness) to achieve a saturation state at shorter exposure times (Arao et al. 2008). Table 5 summarises the comparison results observed in their study (Arao et al. 2008). It is worth noting that Arao et al.'s study involved different material suppliers for each CFRP form used, that varied in the carbon fibre type as well as the epoxy; therefore, the results are to only compare the directional diffusivities case in each form and comparison of diffusivity values across materials should only be done with caution. D_x refers to along the fibre direction, D_y is across the fibre, and D_z is through the thickness (Figure 10) ($D_x = D_y$ in quasi-isotropic laminate and woven fabric due to their symmetrical structure in both direction) (Arao et al. 2008).

Table 5: Comparison of diffusivities (Arao et al., 2008).

Material	Diffusivities D_x (mm^2/h)	Diffusivities D_y (mm^2/h)	Diffusivities D_z (mm^2/h)
UD	0.00555	0.00244	0.00131
Quasi-isotropic laminate	0.00459	0.00459	0.00133
Woven fabric	0.00482	0.00482	0.00227

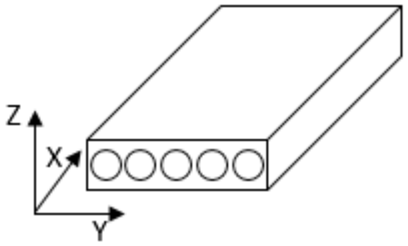

Figure 10: Directional configuration.

Grammatikos et al. (2015) studied the directional diffusion coefficients for PFRP at 60°C. To achieve this, samples were prepared in a way that exposed an opposing pair of edge surfaces that are perpendicular to the direction of moisture uptake being characterised. A <1 mm epoxy layer and an aluminium tape layer of ≈30µm thickness were applied to the four non-exposed surfaces to act as a barrier to moisture (Grammatikos et al. 2015). This test configuration was believed to make a negligible amount of moisture absorbed by the epoxy layer and aluminium tape volumes (Post et al. 2009). The results of this study are summarised in Table 6 (Grammatikos et al. 2015). The study also employed the 3D diffusion approximation initially reported by Shen and S. Springer (1976) where the linear part of the moisture sorption curve can be used to approximate a three-dimensional behaviour by using Equation (6).

$$D = D_z\left(\frac{h}{l}\sqrt{\frac{D_y}{D_z}} + \frac{h}{w}\sqrt{\frac{D_x}{D_z}} + 1\right)^2 \tag{6}$$

where D is the bulk moisture diffusion (observed from Equation (4)), h is the thickness of the specimen, l is the length, and w is the width, D_x, D_y, and D_z are the directional configuration (Figure 10).

For the same materials and water temperature but with additional data observed from different rectangular fully exposed samples in Grammatikos et al. (2015) study, the results are surmised in Table 7 for the directional diffusion coefficients. The study concluded that the differences in D values between the two methods can be attributed to the differences in test methodology, as well as the assumptions involved in the mathematical and experimental approximation employed for their determination since the principle on which they applied features different geometrical aspect rations (Grammatikos et al. 2015).

Table 6: Directional diffusion coefficients for the PFRP 6.4 mm flat sheet material (Grammatikos et al., 2015).

Material	D_x (x 10^{-6} mm^2/s)	D_y (x 10^{-6} mm^2/s)	D_z (x 10^{-6} mm^2/s)
PFRP	9.26	7.04	1.85

Table 7: Directional diffusion coefficients using the 3D approximation from Shen and S. Springer (1976) (Grammatikos et al., 2015).

Material	D_x (x 10^{-6} mm^2/s)	D_y (x 10^{-6} mm^2/s)	D_z (x 10^{-6} mm^2/s)
PFRP	44.8	5.26	0.55

Zafar et al. (2012) investigated the long-term effects of moisture on CFRP composites in seawater and demineralised water at ambient temperature. Pure epoxy and composite specimens were exposed for up to 300 days. In the case of pure epoxy specimens, initially the specimens gained moisture linearly and reached their saturation with equilibrium moisture content of 1.79% and 2.03% after 40 days of immersion in seawater and demineralised water, respectively (Zafar et al. 2012). For the composite specimens, a sharper linear increase in the moisture absorption curves was observed as compared with the pure epoxy specimens. After a sharp linear increase in the moisture absorption curves, the composite specimens reached their equilibrium moisture contents of 2.18% and 2.31% slowly, after 57 days, for the seawater and demineralised water, respectively (Zafar et al. 2012). The bulk diffusion coefficients (x10^{-14} m^2/s) were 7.89, 8.4, 11.9, and 12.6 for pure epoxy specimens in seawater, pure epoxy specimens in demineralised water, composite specimens in seawater, composite specimens in demineralised water, respectively (Zafar et al. 2012). The authors believe that the equilibrium moisture content and diffusion coefficient values for composites specimens were higher due to the imperfect interface between the fibre and matrix. Therefore, the moisture transport in the composite specimens is also governed by capillary transport into the gaps at the interfacial regions (Zafar et al. 2012). The study suggested that the observed higher moisture contents found in those specimens exposed to demineralised water, compared with their equivalents in seawater, was due to the presence of salt in the seawater, which reduces the activity of the water molecules because salt particles are less readily absorbed (Zafar et al. 2012). The accumulation of salt particles on the surface of the specimens could inhibit the water absorption, the concentration of salt particles in the seawater inside the epoxy specimen is less than that in the surrounding seawater, which would result in a creation of an osmotic pressure that acts against the water absorption (Zafar et al. 2012). Therefore, the equilibrium moisture is lower for the specimens in the seawater as compared with the specimens in demineralised water (Zafar et al. 2012).

2.4 The effects of hydrothermal aging on the properties of CFRP composites

2.4.1 Effects of accelerated aging on CFRP composites

Elevated immersion temperatures are used to accelerate the aging process of moisture absorption in CFRP composites (Alam et al. 2018). Both water and temperature individually affect the chemical physics and mechanical properties of CFRP. Combining the two parameters (water and temperature) to hydrothermally condition would eventually further complicate the condition. Carbon fibres are more resistant to higher temperatures compared with the polymers in CFRP composites. Generally, carbon fibres start to decompose at temperatures of about 350°C where physical pits and holes start to form on the surface and increase with the rise in temperature (Feih et al. 2009; Tranchard et al. 2017). This temperature is unlikely to be conducted at hydrothermal aging levels, it is however important to understand the role of temperature on the polymeric and interfacial components of the CFRP composites before they are combined with water in a hydrothermal condition for more realistic performance predictions when elevated temperatures are applied in accelerated aging conditions.

Higher temperatures are known to increase molecular mobility and reduce the load-carrying capability of polymers, as clearly evidenced by the stress-strain curve illustrated in Figure 11 (Le Gac et al. 2017). Increasing the temperature of polymers leads to glassy or semi-crystalline domains within the structure becoming more amorphous, resulting in a viscous response to load. Thus, a rubbery state is reached as the Tg is surpassed, which eventually eliminates the ability of polymers to store energy, while their flow characteristics increase (Cao et al. 2009).

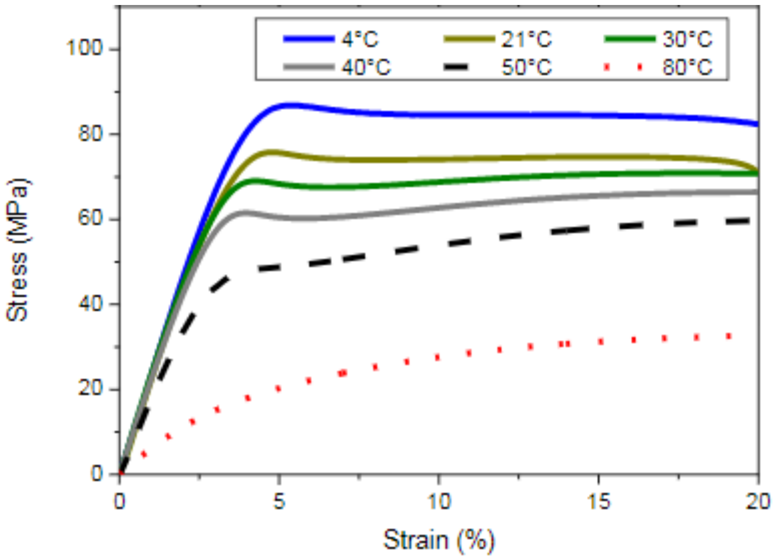

Figure 11: Effect of testing temperature on tensile behaviour of polyamide 6 (Le Gac et al., 2017).

At elevated temperatures, polymers lose their ability to transfer load through their composite structure, which in turn, influences the overall mechanical properties of the CFRP composite. A study by Cao et al. (2009) demonstrated a 33% decrease in the tensile strength of CFRP sheets with an increase in temperature up to the Tg, with a little further variation in strengths observed at temperatures above the Tg. Cree et al. (2015) also reported loss of up to about 50% and 20% of tensile strength and tensile modulus respectively at elevated temperatures (up to 200°C) as compared with the tensile properties observed under an ambient temperature. The loss in tensile strength and modulus at elevated temperatures was correlated to the softening of the polymer and load transfer capability from fibre to fibre. In addition, the failure of tensile bond strength between two laminates observed in their study was due to polymer resin matrix degradation when exposed to high temperatures (Cree et al. 2015). The observed greater reduction in tensile strength compared with the tensile modulus is attributed to the fact that the tensile strength is more influenced by the matrix properties (Cree et al. 2015). In contrast, the modulus is more dependent on the fibre properties but the increase in temperature results in an increase in the loss of fibre to fibre interaction due to matrix softening (Cree et al. 2015). Peters and Anderson (1989) studied the influence of matrix fracture strain and interface strength on cross-ply CFRP laminate ($0/90_4/0$) in a temperature range of -100°C to +100°C. The study showed a correlation of that with the increase in the fracture strain. A reduction on the interfacial strength is observed through the input of temperature (Peters and Andersen 1989). This suggests that with elevated temperatures, there is an increase in the probability of interfacial failure, as opposed to interlaminar failure (matrix dominated) (Peters and Andersen 1989).

In a hydrothermal aging condition, the immersion temperature vary between 'ambient' to those that are ultimately based on the Tg of the composite matrix, where Bank et al. (1995) suggests that temperatures lower than the polymer's Tg by 20°C are more likely to avoid the secondary degradation mechanism (excessive unwanted degradation). This degradation mechanism activates when the temperature is near, or exceeds, Tg (Bank et al. 1995; Maxwell et al. 2005; Hunkley and Connell 2012).

2.4.2 Hydrothermal effects on the mechanical properties of CFRP composites

Many researchers have studied the influence of moisture absorption on the mechanical properties of CFRP materials with unidirectional fibre architectures. A general trend for reductions in matrix/interface dominated properties is observed. A consistent and significant loss of interlaminar strength is seen by researchers with reductions in short beam strength (SBS) of 26% (Kafodya et al. 2015), 22-25% depending on sizing (Pérez-

Pacheco et al. 2013) and 29% (Almeida et al. 2016) observed in $[0]_n$ carbon fibre-epoxy laminates. More cracks were observed in $[\pm45]_{4s}$ CFRP after one month of water immersion in tap water at 50 °C with a small variation in the SBS between un-aged and aged specimens, whereas the $[90/0]_{4s}$ CFRP specimens showed a reduction of 20% in the SBS after one month of water immersion under the same conditions (Meng et al. 2015). A 15% reduction in mode II fracture toughness was also observed by Selzer (1997) during end-notched flexural tests of $[0]_n$ laminates. Significant losses in compression properties were also reported in the case of $[0]_n$ carbon fibre-epoxy laminates, with reductions of 26-33% depending on matrix system used (Selzer 1997), and 19% (Almeida et al. 2016). A loss in compression strength was also observed in quasi-isotropic layups with UD fibre architectures, with reductions varying from 10-30% depending on layup used (Cheng et al. 2011). This was shown to increase further, up to 50%, in the presence of through-thickness stitching.

However, in cases where differing fibre architectures are considered, the same reductions in properties are not always seen. A study considered hydrothermal effects on plain weave fibre architectures with quasi-isotropic layups, and showed that the compressive strengths reduced by only 6% (Kawai et al. 2013). Saito and Kimpara (2009) considered hydrothermal effects on compression after impact (CAI) strength and post-impact fatigue (R=-1) performance of a plain weave (T300-3K) fibre architecture and a multi-axial knitted fabric (T700-12k, consisting of UD layers with through-thickness stitching). Moisture absorption had little influence on the CAI strength for either material. Neither did it influence the post-impact fatigue (PIF) performance of the woven material, whereas, on the multi-axial knitted fabric, moisture absorption had a significant influence on the PIF performance, reducing cycles to failure by 1–2 orders of magnitude (Saito and Kimpara 2009). This suggests that the fibre architecture parameter can have a significant influence on the residual strength of materials exposed to moist environments, and that observed reductions, and therefore appropriate safety factors, can vary for each material and each property. This has important implications in the design of composite components and structures, particularly where minimising weight is a priority.

2.4.3 Effects of constituent contents of CFRP composites

The internal nature of CFRP composites structure can be described by parameters such as fibre volume fraction, matrix volume fraction, and void volume fraction. These parameters will influence the moisture and diffusivity behaviour of water molecules in a composite (Wright 1981). Bao and Yee (2002) studied moisture diffusion and hygrothermal aging on bismaleimide matrix carbon fibre composites. Their findings showed that neat resin exhibited similar two-stage diffusion behaviour to the composites, suggesting that the moisture diffusion in the composite is a matrix dominated process (Bao and Yee 2002). The model used in their study consisted of two independent diffusion processes with very different diffusivities, correlating the fast process to be due to cure-induced voids and cracks in the composites, whereas, the slow process is intrinsic diffusion in the matrix (Bao and Yee 2002). Karbhari and Xian (2009) reported that the ratios of longitudinal to transverse diffusivity of desorption indicate a decrease when there is an increase in the initial temperature of immersion in de-ionised water for high fibre volume fraction in pultruded, unidirectional, carbon/epoxy composites. The authors compared their values with other papers and reported significant increases as compared with those values observed for lower fibre volume fraction composites (Karbhari and Xian 2009). This was attributed to high levels of fibre loading, with local areas of fibre-to-fibre contact (Kondo and Taki 1982; Karbhari and Xian 2009).

2.4.4 The importance of the interface between fibres and resin in the sizing process and its effect on water absorption

The literature clearly states that the characteristics of the interface between the resin and the reinforcement carbon fibres play a vital role in terms of adhesion, and mechanical and thermal stability (Ladizesky and Ward 1983). The strong chemical interaction between the resin and the reinforcing material provides a good adhesion quality as well as enhanced mechanical and thermal properties. A study by Liu et al. (2015) investigated and reviewed the interfacial characteristics of CFRP materials. The study emphasised that the interface between the carbon fibres and the resin is the most critical factor in the performance of the final product. Furthermore, it thoroughly discussed the important interface characteristics related to CFRPs, such as the characterisation of the interface, control measures and the modification approaches, and it used surface characterisation techniques, including the X-ray photoelectron (XPS), Atomic Force Microscope (AFM) and X-ray diffraction XRD, for the analysis (Liu et al. 2015). The study concluded that the performance of a product can be further enhanced by introducing nano-materials to the entire composite structure, as shown in Figure 12. To illustrate this phenomenon, a nano-phase polymer matrix or a nanostructure-based interface can be applied to the interface region. The study also shows that the interface of a reinforced composite plays an essential role in its mechanical stability and adhesion.

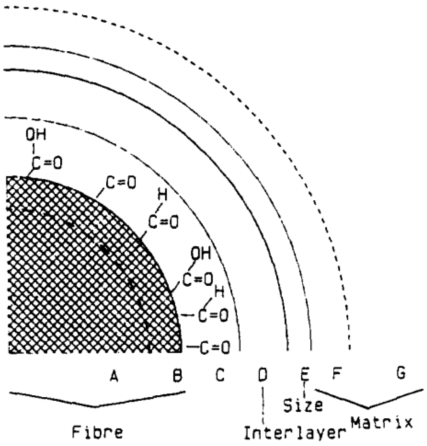

Figure 12: The various zones of the interface region (Hughes 1991).

Another study carried out by González and LLorca (2007) confirmed that the fibre-resin interface properties could easily manipulate the micro-mechanical properties; they conducted a computational simulation study to obtain such a conclusion. The relationship between the induced stresses and the fibre-resin interface was investigated by implementing computational micromechanics studies (González and LLorca 2007). When the stress-strain curves developed by altering the interface, properties were studied, it was observed that significant differences in the micro-mechanical properties were achieved. In other words, by adjusting the surface properties at the interface, the micro-mechanical properties can be altered. These findings confirm the outcomes of previous studies, which identified that the micro-mechanical properties can be enhanced by changing the interface bonding characteristics. Moreover, it can be concluded that mechanical failures are expected when the quality of the bonding at the interface is not maintained to a certain level. A literature study indicated that the mechanical properties can be easily affected by making the CFRPs more versatile

(Hughes 1991). In this context, if the high-stress properties need to be enhanced, it is a pre-requisite to introduce additives to the matrix. However, there is the risk of deteriorating the transverse properties of the material. For this reason, the enhancement of the surface bonding characteristics might be the most suitable approach in enhancing the CRFP's mechanical properties. In the same study, Hughes (1991) recommended adding silanes into the carbon fibre-resin interface to improve the mechanical properties of the material. Another study conducted by Buxton and Baillie (1994) showed that the quality of the interface bonding is affected by other factors in addition to the internal factors such as the resin type, hardener and curing time or the external factors such as humidity and temperature. The other influential factors include the interface between the fibre and resin, which is considered a critical factor that determines the bulk properties of polymeric composites (Buxton and Baillie 1994).

Furthermore, sizing is another critical factor when it comes to the quality of CFRP materials as this process controls several properties, such as the water absorption, thermal stability and flexural strength (Ren et al. 2006). In this regard, Ren (2006) investigated this effect by altering the properties of the sizing epoxy of a composite material. A high modulus carbon fibre reinforced polymer was used in their study, and the water absorption of the composite material was investigated. The water absorption rate was plotted as a function of the boiling time, as shown in Figure 13. In this figure, the M40J and the BADCy refer to the composite material under investigation, whereas the E51 & E20 are the sizing epoxy resins. The water absorption measurements were carried out as follows: (1) specimens were placed under the temperature condition of 100°C to let the specimen reach asymptotic value, W_0; (2) after the high-temperature treatment, the specimens were placed in boiling water; (3) after the boiling water treatment, the weight of each specimen was measured (W_t). It is clear from the displayed results that the 10wt% E51 sized material composite shows the lowest water absorption rate, which is favourable. The authors further concluded that an interfacial layer produced by sizing the fibres decreases the water permeability, which is beneficial for most applications.

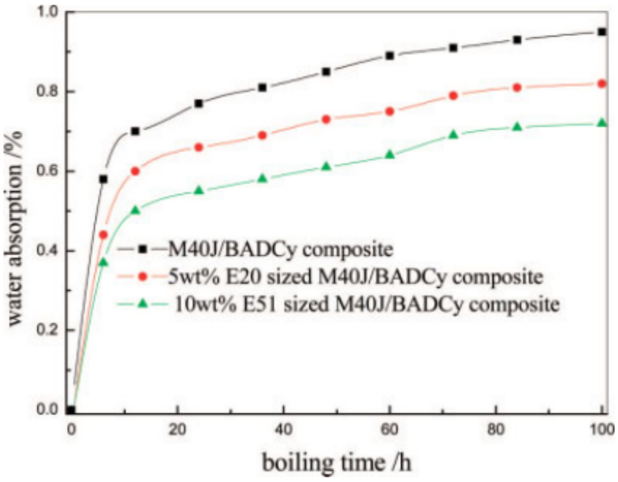

Figure 13: The water absorption rate as a function of the boiling time (Ren et al. 2006).

2.5 Monitoring and evaluation for assessing damage in composite materials

2.5.1 Microscopy

The complex structures of CFRP composites require a further understanding of their failure criteria. Microscopy is an essential tool from which the failure modes and the structure condition in CFRP composites are sighted. It is also easier to analyse and correlate to their potential cause of initiation and growth. Meng et al. (2015) investigated the effects of hygrothermal stress on the failure of CFRP composites with the use of tap water and seawater. The interface conditions of the samples are illustrated in Figure 14 with the use of Scanning Electron Microscopy (SEM). In the dry samples, the epoxy was still attached to the carbon fibre, whereas the aged samples showed that the epoxy became porous after immersion in tap water; and the surface, after immersion in seawater, indicated that the adhesion of epoxy on carbon fibre had deteriorated (Meng et al. 2015). A comparative microscope image of dry and seawater-immersed samples is presented in Figure 15, after SBS test for UD CFRP (Meng et al. 2015). A larger number of micro cracks were found in the optical microscope analysis for aged samples, particularly after seawater immersion (Meng et al. 2015). Dell'Anno and Lees (2012) looked at the effect of water immersion on the flexural performance of low-cost liquid resin-infused carbon fabric composites. The authors argued that the adoption of different resin/fabric combinations does not trigger any substantial change in the flexural strength of dry composites. The microscopic analysis of failed coupons and of coupons under bending load suggests that the failure mechanism in flexure configuration is connected more to fibre buckling and tensile failure than to resin/fibre adhesion (Figure 16). Such a fibre-dominated mechanism results in an almost equivalent performance of all selected systems (Dell'Anno and Lees 2012). Sun et al. (2011) reported the morphology of carbon fibre/bismaleimide composites in Figure 17; showing that the surface of fibres is smooth, with only a slight amount of resin adhered on the surface in the wet specimens; and the dominating deformation mechanism is debonding because of hydrothermal aging. Furthermore, the authors reported that the differences between dry and wet samples are that the matrix in wet samples b, d, and f of Figure 17 is in the form of granules or powder, due to matrix plasticization; whereas, a, c, and e of Figure 17 exhibit shear-band, further demonstrating that dry samples differ in their failure modes with different SBS values (Sun et al. 2011).

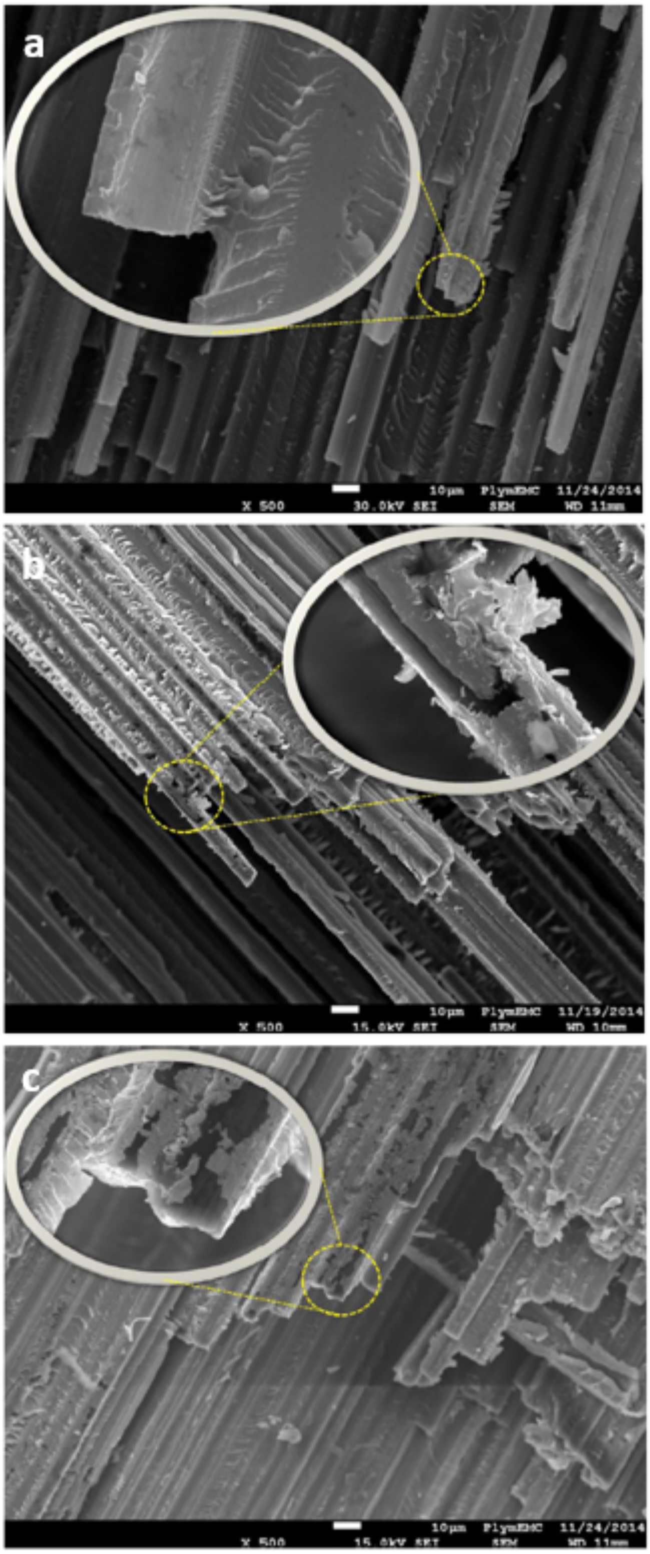

Figure 14: SEM images of; (a) dry, (b) after tap water immersion, (c) after seawater immersion (Meng et al. 2015).

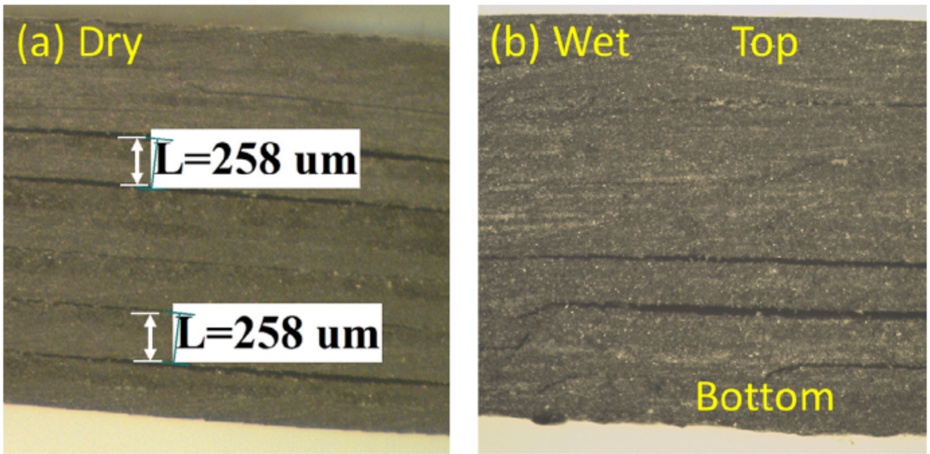

Figure 15: Failure mode observed after SBS test (Meng et al., 2015).

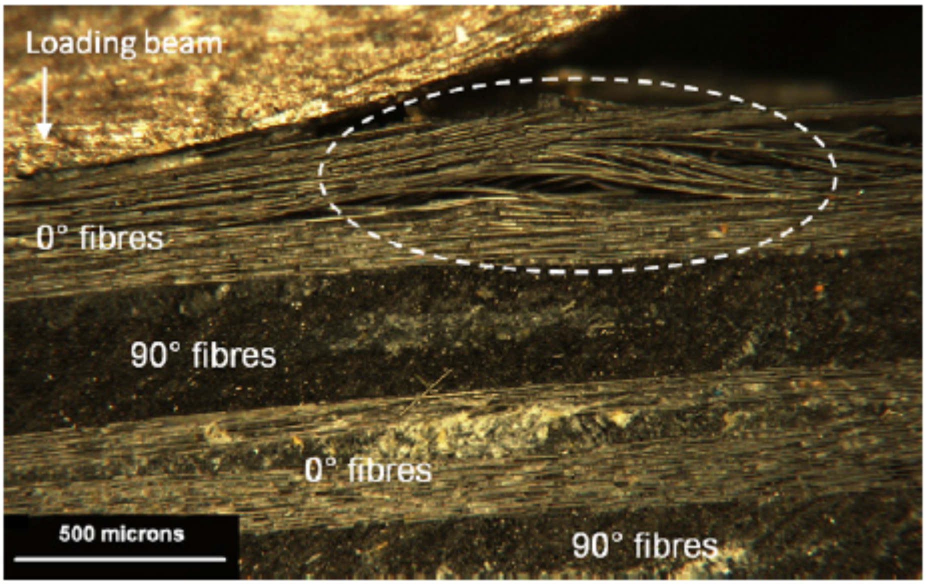

Figure 16: Detail of loaded portion of flexural samples at the onset of failure with buckling fibres in the dashed circle (Dell'Anno and Lees. 2012).

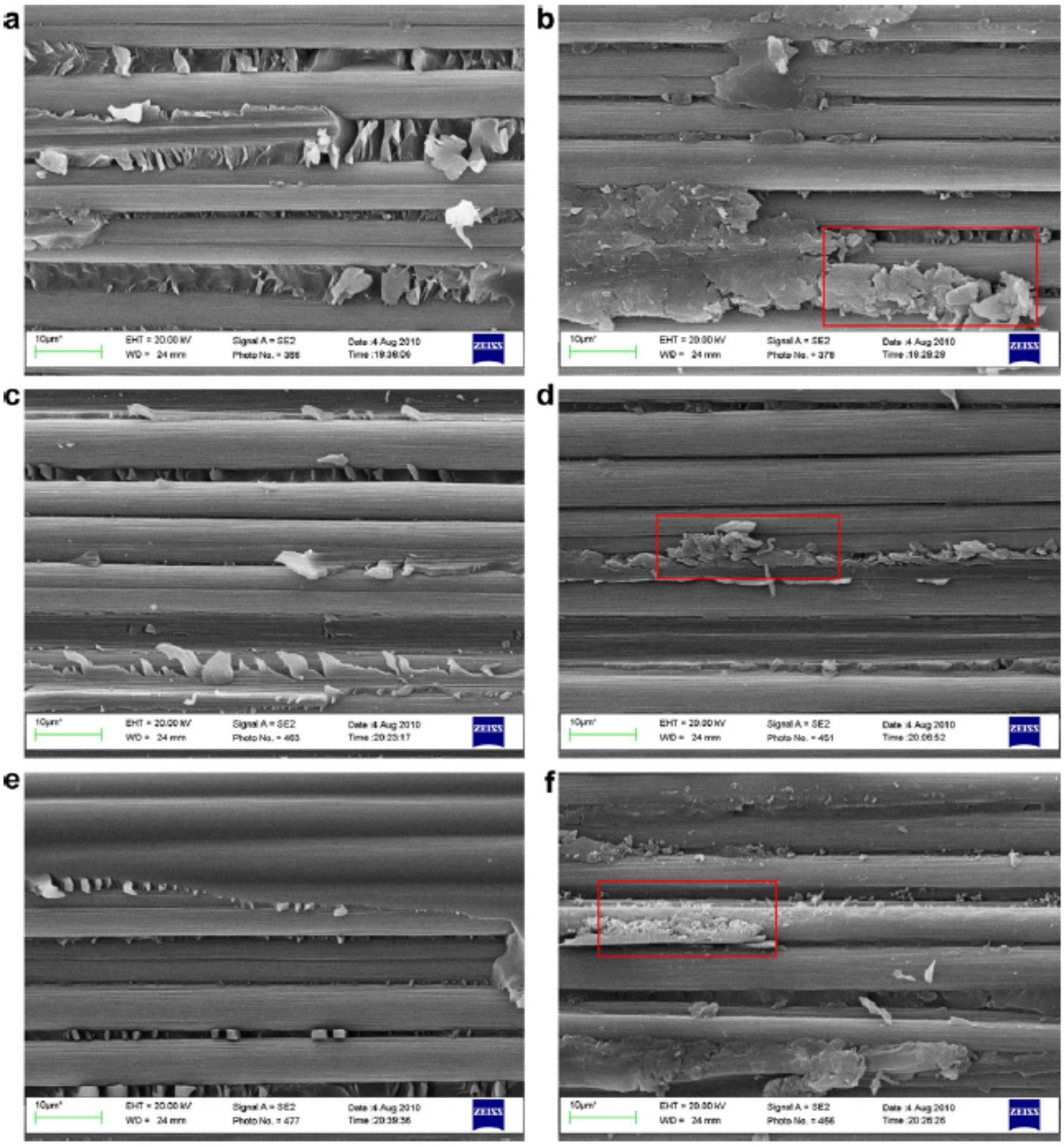

Figure 17: SEM images of (a)14_1dry, (b) 14_1wet, (c) 14_2dry, (d) 14_2wet, (e) 14_3dry, and (f) 14_3wet. '14_1wet' means putting the specimens into the humidity chamber and immersed in distilled water at 71°C for 14 days, and '14_1dry' means drying the '14_1wet' in a desiccator at 85 °C until a constant weight was obtained. '14_2wet' means putting the '14_1dry' into the humidity chamber and immersed in distilled water at 71°C for 14 days. '14_2dry' means drying the '14_2wet' in a desiccator at 85°C until a constant weight was obtained. By analogy, 14_3 have similar means (Sun et al. 2011).

2.5.2 Non-Destructive Testing (NDT) using ultrasonic scans for polymeric composite materials

The evaluation of delamination damage in composites is important but often challenging, particularly in CFRP composite due to the separation of individual layers usually invisible on the surface, making visual inspection impossible. Ultrasonic Testing (UT) can be employed for the assessment of internal damage/delamination without altering or interfering with the material's internal properties (Campbell 2004). Several UT techniques are used for the examination of composite structures where short pulses of ultrasound (a few microseconds) are passed into the composite materials and detected after having interrogated the structure. These techniques include pulse-echo, through transmission, back-scattering, acousto-ultrasonics and ultrasonic spectroscopy (Zhang and Richardson 2011). The ultrasonic pulse-echo technique is one of the most common NDT methods used for finding flaws in composite structures (Marsh 2002; Wróbel and Pawlak 2007; Kersemans et al. 2018; Arhamnamazi et al. 2019). It involves the detection of echoes produced when an ultrasonic pulse is reflected from a discontinuity or an interface within the sample. This technique contains three primary methods A-scan, B-scan and C-scan. In the A-scan method (where A referrer to Amplitude), a short impulse is generated into the object and echoes are displayed as a function of time. During the A-scan, the probe is held stationary at a certain position at the surface of the sample and one-dimensional information is obtained. On the other hand, the B-scan method (where B refers to Brightness) involves moving the probe horizontally along the surface of the sample. This method displays two-dimensional information with each echo is represented as dots on the voltage-penetration depth plot which is different to the A-scan which displays the results as ‘spikes or amplitudes’ on the voltage-penetration depth plot. The C-scan (also known as time-motion scan) combines the features of both A and B-scans. In this method, the probe is held stationary as in the A-scan and echoes appear as dots as in the B-scan (Zhang and Richardson 2011). The ultrasonic pulse-echo technique is summarised in Figure 18. In general, the pulse-echo method has the advantage of allowing flaws to be sized and located in the direction of the ultrasonic beam within the composites. This also allows the depth of flaws to be determined as well as their location along the scanning axes (Zhang and Richardson 2011). On the other hand, there is a time period approximately equal to the pulse length during which the probe cannot detect signals because it is either emitting a pulse or reverberating, this is refereed as the dead zone. Therefore, there is a region near the probe in which defects cannot be detected (Zhang and Richardson 2011). This problem can be limited by using a shorter pulse, immersion testing, a stand-off probe, or employing a twin crystal probe. A twin crystal probe has two transducers slightly angled toward each other, one dedicated to emitting and the other dedicated to receiving. A similar problem occurs when attempting to resolve defects very near the from surface of the component. The solution here may be to increase the frequency and thereby shorten the pulse length, or scan from the other side of the specimen (Zhang and Richardson 2011).

Overall, the C-scan, in particular, is the most widely used method for polymeric composites when it comes to a plane view of a specimen representing the reconstruction of internal damage (Hasiotis et al. 2007). Papa et al (2021) carried out C-scan reconstruction of low velocity impacted specimens to determine delamination in glass fibres/epoxy and glass fibres/vinylester highlighting the role of resin used. The authors reported significant problems in the glass fibres/vinylester panels due to the particular kind of resin. When the epoxy resin was used, the damage image was revealed brighter and more defined allowing more information to be obtained in regard to the dynamic behaviour (Papa et al. 2021). Kersemans et al. (2018) evaluated three NDT techniques namely, ultrasonic C-scan, local defect resonance, and lock-in infrared thermography in reflection to detect and assess damage in CFRP composites. The authors concluded their study by stating that the overall C-scan data gives the best indication of lateral defect size, and depth even for those samples with barely visible impact damage (Kersemans et al. 2018).

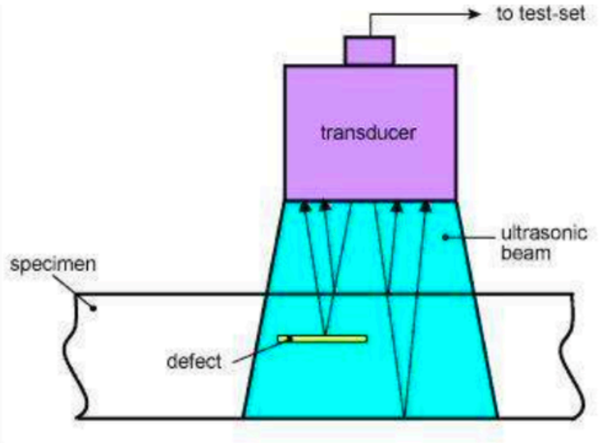

Immersion pulse-echo test with submerged specimen

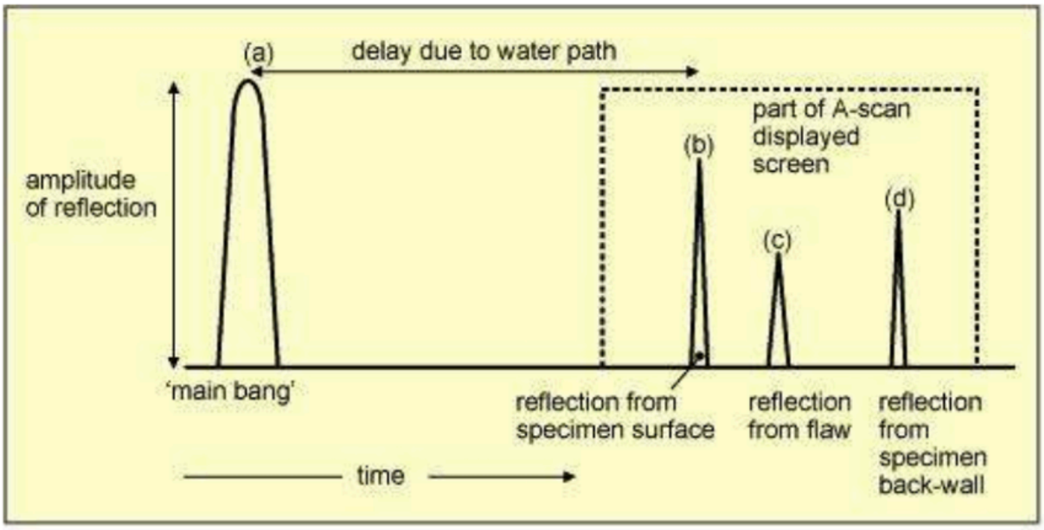

Diagrammatic A-scan display for a typical pulse-echo immersion test

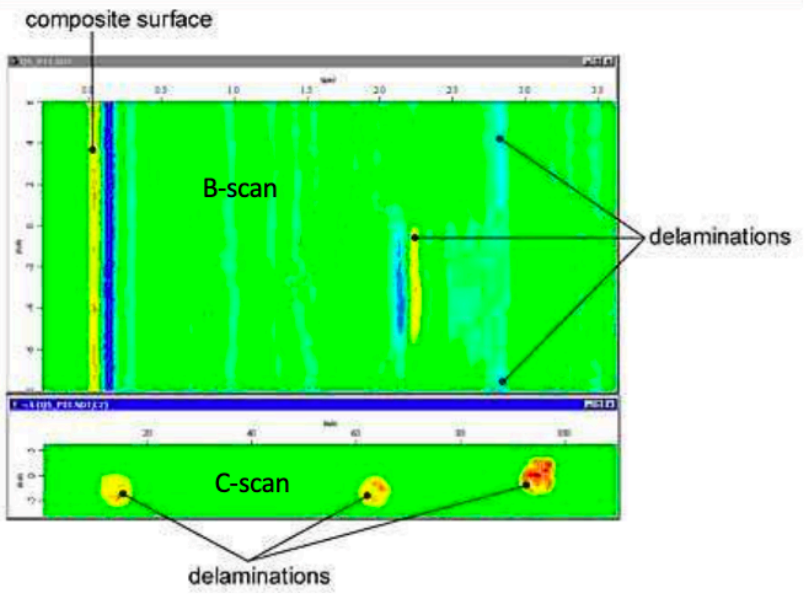

Ultrasonic image of delamination in CFRP B and C scans

Figure 18: Ultrasonic pulse-echo test with summary of A, B, and C scans gathered from (Zhang and Richardson 2011).

2.5.3 Optical measurements

Digital Image Correlation (DIC) is an optical measurement technique originally developed by researcher at the University of South Carolina in the early 1980s (Peters and Ranson 1982). The technique is now commonly used in materials testing and characterisation with a range of commercial systems available. The technique is used to measure full-field in plane and 3 dimensional (with 3D/2 camera system) displacements and strains on the surface of the specimen subjected to driven force and can be used to characterise a wide range of materials and gain greater understanding of their mechanical performance (Schreier et al. 2009). Unlike the traditional photoelastic coatings and foil crack gauges which require physical attachment to the structure, DIC uses static images of a structure’s surface and digitally automated pattern recognition to determine the surface’s displacement and subsequently strain (McCrory 2016). The nature of DIC also allows the use of technology alongside with other techniques such as Acoustic Emission (AE) without detrimentally affecting one another (Pullin et al. 2010; Carmi et al. 2015).

Recent studies on moisture absorption effects on fibrous composites in general, have led to a promising potential use of optical measurements to better understand and distinguish the fracture behaviour of healthy and aged composite materials. For instance, Perrier et al. (2017) carried out a study on the influence of water absorption on the damage behaviour of single hemp yarn/epoxy resin composites with the use of DIC. The experimental results, illustrated in Figure 19, show an increase in the measured strain after water aging when tested with a micro tensile tester, the stress values correspond to the applied stress levels, and the strains correspond to the longitudinal strain values measured by DIC. The colour contours (Figure 19) are showing the full-field strain with each image representing a different applied stress (Perrier et al. 2016; Perrier et al. 2017). Fard et al. (2019) used the DIC system as part of a study to characterise the interlaminar fracture modes I, II, I – II in CFRP composites under hygrothermal effects. The authors concluded the study by declaring the use of DIC to be an effective system that is believed to have reduced the errors in calculation of energy due to extra compliance and crack positing (Fard et al. 2019).

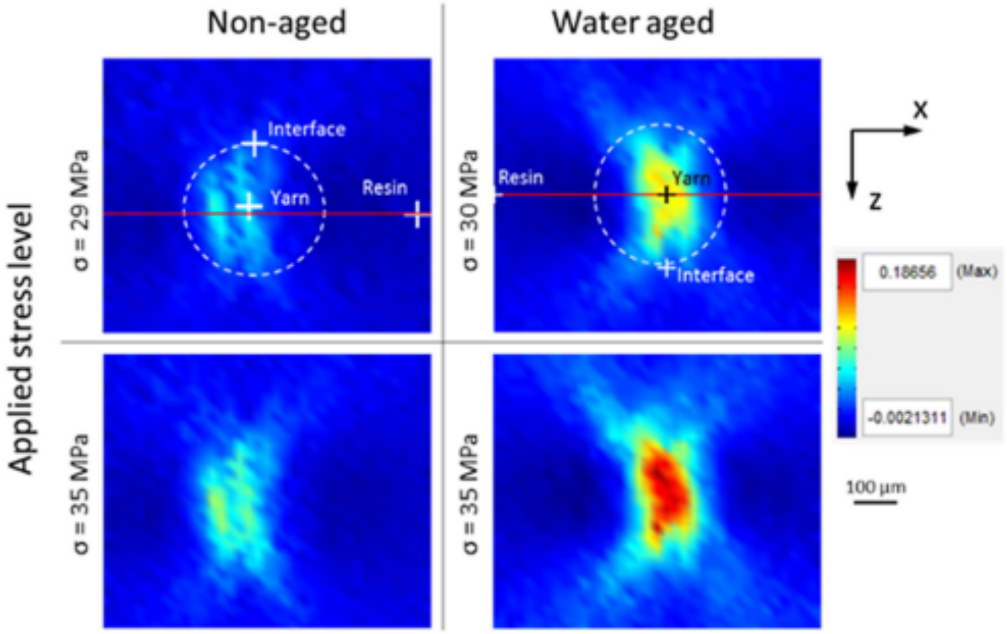

Figure 19: The stress values correspond to the applied stress levels, and the strains correspond to the longitudinal strain values measured by DIC. The colour contours are showing the full-field strain with each image representing a different applied stress (Perrier et al., 2017).

2.5.4 Characterising polymeric composites using Acoustic Emission

The elastic energy that is released when a given material is deformed is classified as Acoustic Emission (AE). For a material that is subjected to a certain level of stress, the crack growth or the plastic deformation areas form surfaces which release energy, as shown in Figure 20 (ASTM 1989). Piezoelectric transducers are used to detect and harness the elastic waves that are propagated along the material's surface. The range of frequencies used in the AE technique varies approximately between 10 kHz to 1 MHz (Miller and McIntire 1987). In recent years, technological advancements have made it possible to use computers to improve acquisition rates and processing power. The AE method is slightly different from the other non-destructive counterparts: in AE tests the material has to be exposed to stress conditions, whilst in other methods, structures are examined under static conditions, i.e. at rest (Miller et al. 2005).

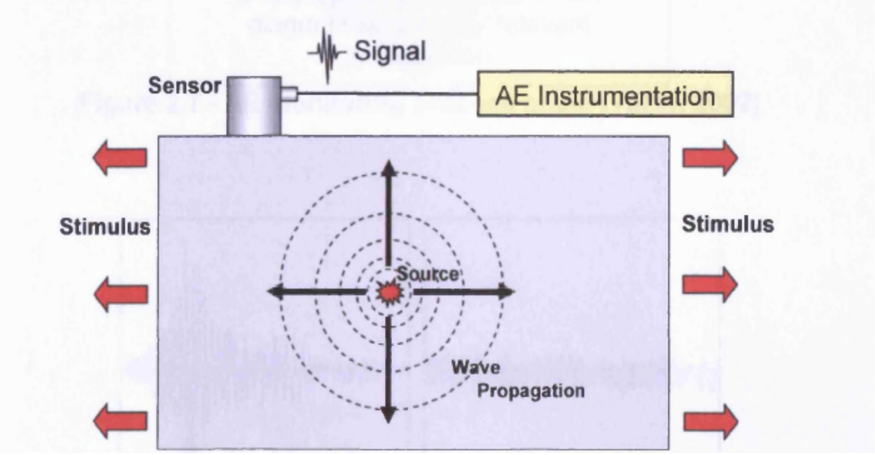

Figure 20: The AE working principle (ASTM 1989).

Most polymers tend to display a certain level of heterogeneity. This makes the identification and damage evaluation processes in such materials quite complex. However, recent research has made it possible to qualitatively find the correct interpretation of amplitude distribution, damage mechanisms, noise and friction. The absolute values of the AE set values vary as a result of the material differences and geometric impacts, such as reflection, attenuation or dispersion. It is sufficient to use the results obtained from the AE technique to interpret the differences in micro-failure mechanisms. It is necessary to use data from other characterisation methods to provide an overall interpretation of the material's behaviour in such applications (Ríos-Soberanis 2011). The field of materials research is the single major field where the AE technique is used. AE play a key role in finding where the damage initiation begins by making the right estimations. The nature of damage mechanisms, along with the failure rate under the influence of the material's loading or crack propagation, in different media can be fulfilled with AE techniques. The understanding of the obtained data from specified applications is essential in the area of pressure vessels, aircraft construction and the use of polymer-based composites (Ríos-Soberanis 2011). The AE results produce two types of signals, namely transient and continuous signals. Continuous signals are characterised by the frequency and amplitude variation of a signal of infinite length. Continuous AE can be obtained in friction, leakage or flow noise. The discrete signals that have a start and an endpoint are known as transient signals. These signals are commonly used in structural testing applications and are capable of providing information on the crack growth and/or fractures, Figure 21 shows the difference between transient and continuous AE. In this context, fibre failure, matrix micro-cracking, delamination and fibre pullout are the main applications of the AE technique (Eaton 2007).

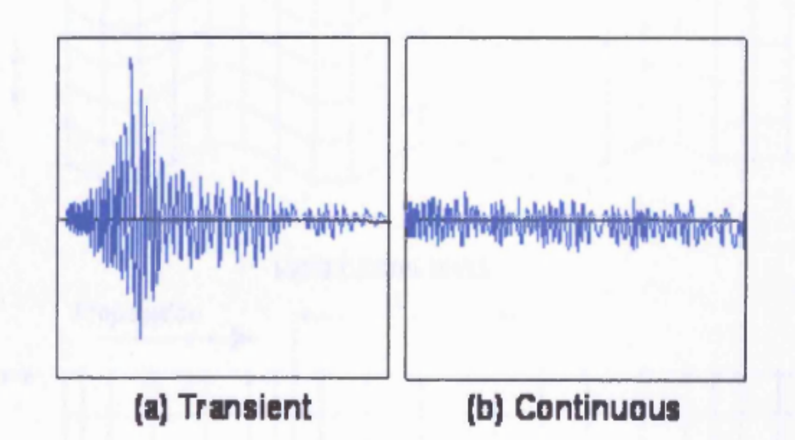

Figure 21: An illustration of the transient and continuous waves in AE (Eaton 2007).

The propagation of acoustic waves in a solid media is a complex problem that is further discussed in these references (Rindorf 1981; Pollock 1986; Gorman and Prosser 1990). The elastic waves travel through an infinite medium in either a particle motion that is perpendicular to the direction of propagation or a particle motion with localised compression and refraction that is parallel to the direction of propagation. In either option, by introducing a boundary-like surface, longitudinal and transverse waves combine to make a Rayleigh wave. In a case where the propagation medium is bonded between any two surfaces, Lamb waves are produced since the bulk waves couple at the surfaces and result in two surface modes (Eaton 2007). A reduction of the signal's amplitude with the increasing travel distance is known as 'attenuation'. The origins of a signal attenuation can be attributed to geometric spreading where a wave that is generated by a given point source possesses a finite amount of energy and has to be distributed over a large wavefront in order to facilitate propagation. For a two-dimensional plate structure, the reduction in amplitude is inversely proportional to the square root of the propagation distance. Attenuation may also result from internal friction. The elastic wave energy degrades in the form of heat energy and is dependent on the type of material. The internal friction effects are more severe in polymers compared to metals. The amplitude trend exponentially reduces by increasing the distance, while the associated losses as a result of internal friction increase with frequency (Miller et al. 2005). The dispersion of waves results in a spread of the short pulses as propagation occurs, and this, therefore, results in an amplitude loss. The attenuation rate is affected by the dispersion of waves along with the bandwidth and the dispersion curve gradient of the waves (Eaton 2007). An illustration of the AE method on a tensile sample made of CFRP is shown in Figure 22 alongside the stages involved in the test using this technique.

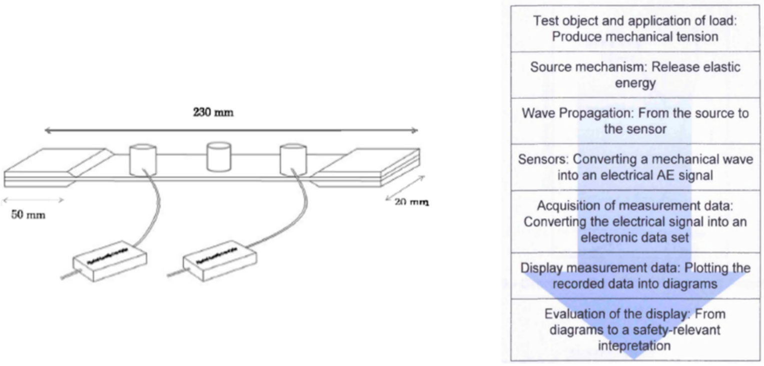

Figure 22: (Left) the AE test being carried on a material under tension, (Ríos-Soberanis 2011); and (right) a summary of the test monitoring chain (Eaton 2007).

Many researchers have attributed various AE parameters to the characteristics of composite materials in order to gain a deeper insight into the damage mechanism (Kumosa 1987; de Groot et al. 1995; Zhuang and Yan 2005; Liu et al. 2012; Pérez-Pacheco et al. 2013; Liu et al. 2017). Kumosa (1987) reported that AE can be used to distinguish between different types of damage in glass fibre reinforced polymers (GFRP). Kumosa stated that high-amplitude events are associated with fibre fractures, whereas low amplitude events are associated with matrix cracking. de Groot (1995) used AE frequency distribution to identify damage mechanisms in CFRP. The signals analysed ranged from 50 to 600 kHz and were distinguished as being released from four special types of failure. By using different types of specimen it was concluded that matrix cracking released frequencies between 90 and 180 kHz, fibre failure frequencies above 300 kHz, debonding frequencies between 240 and 310 kHz and pull-out frequencies between 180 and 240 kHz (de Groot et al. 1995). Pérez-Pacheco et al. (2013) used the AE (duration versus amplitude) under tensile tests to study CFRP composite behaviour after the fibre/matrix interface was exposed to moisture. The authors correlated physical failure mechanism with AE response (duration versus amplitude), as shown in Table 8.

Table 8: Correlation between the physical damage and the fracture mechanism detected with the AE technique (Pérez-Pacheco et al. 2013).

Duration	Amplitude		
	Low (35–40 dB)	Medium (40–80 dB)	Large (80–100 dB)
Low (<1,000 μs)	Onset matrix microcrack	Propagation of matrix microcrack	-
Medium (between 1,000 and 10,000 μs)	-	Interfacial adhesion failure	Fibre breakage
Large (>10,000 μs)	-	-	Propagation of macrocrack associated to delamination

2.6 Literature review summary and the gap of knowledge

The increased use of CFRP composites in applications operating in moist environments is a fact; therefore, understanding the role of water absorption on the fracture behaviour of matrix dominant properties, namely impact, compressive and interlaminar shear strength in CFRP composites is crucial due to their large dependency on the polymeric constituents of the composite (Hull 1994). This leads to the fact that moisture conditions will most likely result in changes on the mechanical performance of the material (Alam et al. 2018). Many researchers have investigated the role of water absorption on CFRP composites in terms of directional diffusivities, and the matrix dominant properties on CFRP composites particularly with the focus on one fibre architecture (Saito and Kimpara 2009; Cheng et al. 2011; Arnold et al. 2013; Kawai et al. 2013; Pérez-Pacheco et al. 2013; Grammatikos et al. 2015; Kafodya et al. 2015; Almeida et al. 2016; Grammatikos et al. 2016; Meng et al. 2016; Cysne Barbosa et al. 2017; Korkees et al. 2018a; Liu et al. 2018). From the reviewed literature it is evident that the key parameter, fibre architecture, is not fully explored. This PhD investigates the role of fibre architecture for the same materials on the water absorption ingress mechanism by studying their directional diffusivities, and somewhat more importantly the consequential reduction in strength that corresponds to each architecture and their fracture behaviour. It is also found that the interlaminar shear strength is often a limiting factor of fibrous-polymeric composites (Chandrasekaran et al. 2011). The in-plane properties of the laminate depend primarily on the fibres whereas the out-of-plane (through the thickness) properties such as SBS, historically referred as interlaminar shear strength (ILSS) depend largely on the polymeric constituents of the composite

(Hull 1994). The interfacial fibre-matrix properties are also a key factor due to the fact that load on the composite is transferred from the matrix to the fibres through the interface; hence fibre-matrix interfacial shear strength can affect the toughness and strength of the composite (Dirand et al. 1996; Zhang 2000). Therefore, moisture conditions will most likely result in changes on the mechanical properties of the matrix and/or the interfacial properties between the fibres and the matrix (Alam et al. 2018). A number of researchers reported a consistent and significant loss of SBS values in CFRP specimens after water absorption (Kafodya et al. 2015; Meng et al. 2015; Cysne Barbosa et al. 2017). There are still gaps in understanding the fracture behaviour under the SBS test particularly after aging. For instance, Cysne Barbosa et al. (2017) reported that there was a drop in CFRP composites' SBS values after water absorption and the aged specimens showed a sharp drop in applied load from the load-versus-displacement graphs, followed by its further increase until the final failure is observed. The authors suggested that this behaviour to the potential formation of microcracks in the composites. Therefore, this PhD further investigates this behaviour and studies the evolution of damage mechanisms in CFRP material following water immersion for increasing durations. It focuses on the matrix dominated property of interlaminar strength; additionally, examination of load history, in-test fracture imaging and representative AE features provided a detailed understanding of the change in failure behaviours that occur. This reflects on the understanding of the effects of gradual water absorption on the delamination resistance of fibrous/polymeric composites. It also explains, from a micro-scale perspective, the fracture mechanism observed prior to final fracture and provides an overall evaluation of the SBS testing method with the use of non-destructive test (NDT) techniques.

3 Materials and Methods

3.1 Introduction

This chapter highlights the main methods and techniques applied in this study and documents the materials, their fabrication and post process along with the testing procedures applied in this study.

3.2 Materials and fabrication

3.2.1 Materials

In this work, three versions of CFRP prepreg with different fibre architectures were used. The UD, Plain weave and 2x2 twill weave fibre architectures used in this study were chosen due to their current high usage in aerospace, energy, and automotive industries (Hexcel 2013). All were manufactured by SK Chemicals using Skyflex K51 Epoxy resin to avoid the influence of using different matrix type (the glass transition temperature (t_g) for K51, from Dynamic Mechanical Analysis (DMA) in accordance with ASTM D7028, is 122.83°C). The specification of each prepreg variant used were: 15k Unidirectional (UD), Pyrofil TR50S high strength carbon fibre 200gsm with 33% resin content; 3k plain weave, Pyrofil TR30S high strength carbon fibre 198gsm with 40% resin content; and 2x2 3k twill weave, Pyrofil TR30S high strength carbon fibre 198gsm with 40% resin content. Fibres sizing levels were 1.0% and 1.2% for Pyrofil TR50S and Pyrofil TR30S, respectively. All carbon fibres featured the same filament diameter of 7um, the same yield of (1000 mg/m for 15K and 200 mg/m for 3K), and the same tensile modulus of 235GPa. The tensile strength, elongation to failure, and density were slightly different with 4.90GPa, 2.1%, and 1.82g/cm^3 for Pyrofil TR50S, respectively, and 4.12GPa, 1.8%, and 1.79 g/cm^3, for Pyrofil TR30S, respectively. The materials technical details are attached in Appendix A.

3.2.2 Fabrication

The use of hand lay-up process and bagging followed by an autoclave cure was implemented in this work in line with the materials supplier specifications. Prior to the autoclave cure, a lay-up process is required. This involves placing the prepreg layers manually with the required stacking sequences until the required thickness or number of plys are achieved. This process can introduce trapped air within the structure particularly with larger thicknesses. Removing trapped air and managing ply flatness alignments is achieved by introducing debulking operations during the lay-up process. The debulking operations are mainly based on the geometry and thickness of the part. Typical debulking operations are carried out every 3 to 5 plies for 5 to 15 minutes of vacuum pressure at room temperature. An autoclave is sometimes used if hot debulking is required where in some cases the tool will not fit together unless the bulk factor is reduced to near final dimension tolerances and this can only be achieved by introducing high temperature to the debulking operations. Controversy exists particularly over the merits of debulking (Campbell 2004). A constant number or a logical manner must be applied between each debulking operation. For instance, a number of 24 plies will either be debulked at 4 plies per operation or at 6 plies per operation if the cost is to be reduced (Campbell 2004).

Generally, autoclaves are intensively used in the fabrication of the composites in many industries. It is in fact of a particular interest of those industries that require high quality finish products as the process provide high quality products with significant low rates of voids compared to other fabrication methods due to the procedure of heat and pressure applied through the cure cycle (Zhang et al. 2017). In this study, all materials were cured with the same cure cycle, as recommended by the material supplier, using an autoclave presented in Figure 23 under two dwells, 30 minutes at 80°C temperature and 5 bar pressure followed by 60 minutes at 125°C temperature and 5 bar pressure as illustrated in Figure 24. Large panels (the panel size for each CFRP panel produced is detailed in their relevant section) were manufactured for each test with required stacking sequences (the vacuum bagging preparations for each CFRP panel produced in this study prior to autoclave curing is detailed in their relevant section). The specimens were then cut into the desired specimen dimensions using a diamond blade (using Acmitaly cutting machine, model ACM BS 740). For specimen's tolerances and edge finishes, a rotor polishing machine by Struers model Knuth-Rotor-3 with silicon carbide grinding paper grit 320 was used. All panels were c-scanned to ensure manufacturing quality and edges were inspected after cutting with the use of microscopic imaging detailed in (3.8 Microscopic imaging) to monitor and prevent any unnecessary damages which can be caused by the cutting process.

Figure 23: Autoclave image used in the fabrication process.

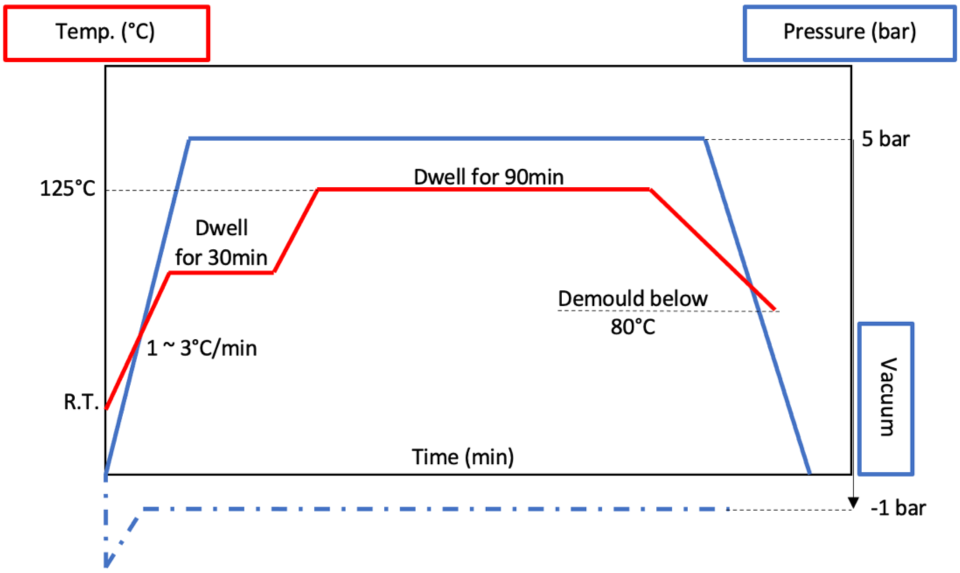

Figure 24: Cure cycle used for this study.

3.3 Constituent contents

Several techniques are used to determine the constituent contents of fibrous composites which are already standardised such as in ASTM D3171-15. Two methods are stated in ASTM D3171-15 in which they determine the constituent content of composites materials. The first method mainly involves a physical removal of the matrix leaving the reinforcement therefore allowing a measurement of the reinforcement as well as the void content. Method 2 on the other hand is only applicable to laminate materials with known fibre areal weight. This allows the calculation of reinforcement or matrix content by volume or weight assuming no presence of void volume.

Method 1 can be carried out by removing the matrix through digestion, ignition, or carbonisation. Eight techniques are used for this method:

- Matrix digestion using nitric acid
- Matrix digestion using sulfuric acid/hydrogen peroxide
- Matrix digestion using ethylene glycol/potassium hydroxide
- Matrix digestion using sodium hydroxide
- Matrix digestion using hydrochloric acid
- Matrix digestion with nitric acid in a microwave oven
- Matrix burnoff in a muffle furnace
- Matrix carbonisation in a nitrogen-purging furnace

The use of matrix digestion (method 1) was implemented in this work to excrementally determine the constituent contents including the void volumes (which can play a significant role on the water uptake) for the specimens used in this study. This was carried out by using 60ml nitric acid for each specimen at 80°C for six hours. The carbon fibres were then filtered into pre-weighed sintered glass filters under a vacuum of better than 17 kPa. The carbon fibres were cleaned with demineralised water at least three times and a final acetone wash to help improve drying times. This was followed by one hour oven drying at 100°C. The carbon fibres were then left to cool to room temperature. The weight was then recorded to the nearest 0.0001g using Sartorius LA310S analytical balance. The procedure is highlighted in Figure 25.

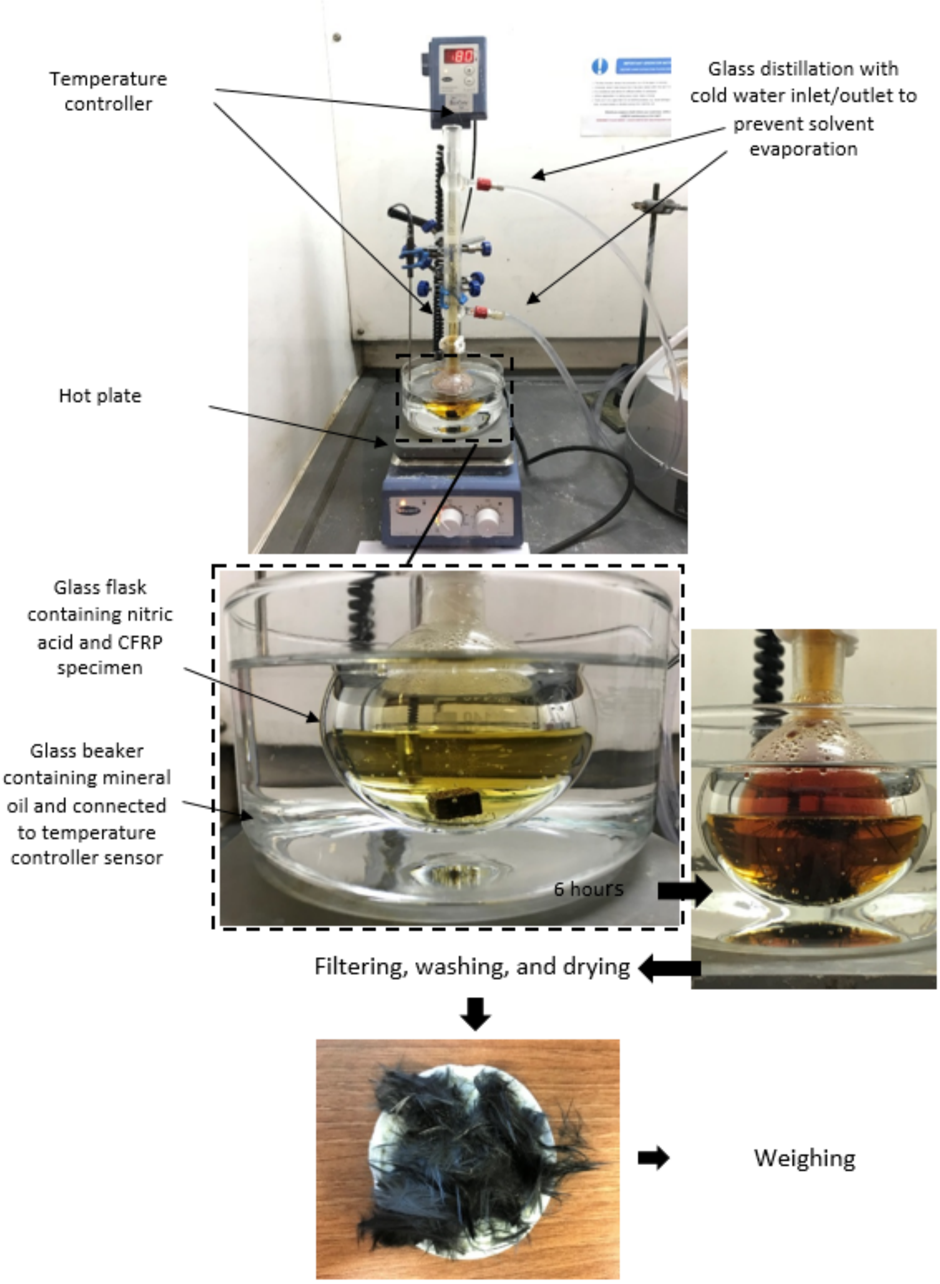

Figure 25: Procedure applied for constituent contents measurements.

Reinforcement volume is determined by using Equation (7)

$$V_r = \left({}^{M_f}/_{Mi} \right) \times 100 \times {}^{P_c}/_{P_r} \tag{7}$$

where:

V_r = reinforcement volume (%)

M_i = initial mass of the specimen (g)

M_f = final mass of the specimen after digestion (g)

P_c = density of the specimen (g/cm^3)

P_r = density of reinforcement (g/cm^3)

Matrix volume is determined by using Equation (8)

$$V_m = \left(M_i - M_f\right)/M_i \times P_c/P_m \times 100 \tag{8}$$

where:

V_m = matrix volume (%)

P_m = density of matrix (g/cm^3)

Void volume is determined by using Equation (9)

$$V_v = 100 - (V_r + V_m) \tag{9}$$

where:

V_v = Void volume (%)

The specimen densities P_c were determined in accordance with ASTM D792-13. This was carried out by determining the mass of a specimen in air and in water recorded to the nearest 0.0001g using Sartorius LA310S analytical balance assembled with YDK 01 Sartorius density kit. The procedure is highlighted in Figure 26.

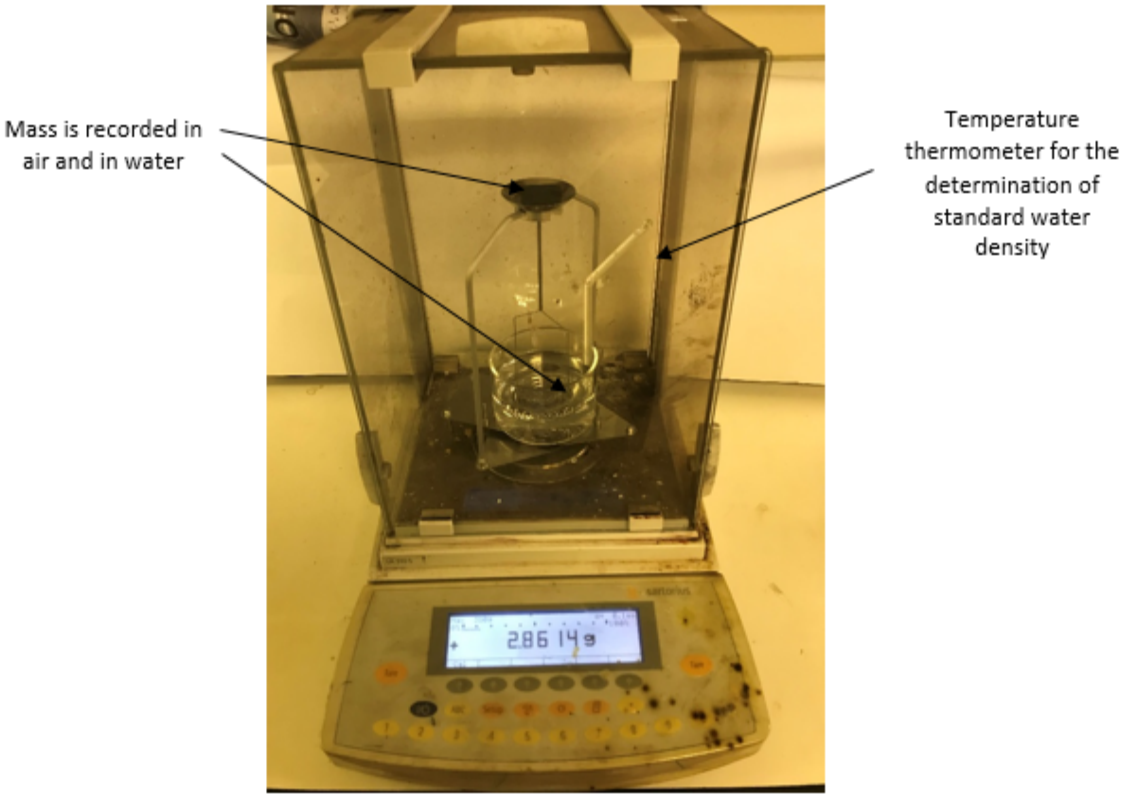

Figure 26: Analytical balance assembled with density kit.

The specimen density is determined by using Equation (10):

$$P_c = \big(a/(a-b)\big) \times water\ density \tag{10}$$

where:

a = specimen mass in air (g)

b = specimen mass in water (g)

3.4 Moisture absorption

3.4.1 Water uptake

Water absorption testing was carried out by the gravimetric method. This was achieved by using non-ambient moisture conditioning in a water immersion tank at a prescribed constant temperature of 70°C for a fixed-time period of 40 days, in accordance with ASTM D5229-14 (condition method of procedure code BWFF). Still natural spring water was used with typical contents values of 48.5mg/l calcium, 5.2mg/l magnesium, 14.0mg/l sodium, 0.8mg/l potassium, 148.0mg/l bicarbonate, 10.7mg/l chloride, 27.6mg/l sulphate, and 4.0mg/l nitrate. An unstirred digital bath (NE2-28D) supplied by Clifton with a sensitivity of ±0.2°C and uniformity of ±0.1°C was used, attached with stainless steel hinged gable lid. The lid is designed to reduce water evaporation maintaining the water levels as illustrated in Figure 27. The specimens were placed in the water bath, which has previously reached the specified steady-state temperature. For weighing records, specimens were individually removed from the water bath, left in a sealed bag until it became to an acceptable temperature for laboratory handling (room temperature), and then removed from bag, surface moisture wiped, mass change measured using analytical balances with accuracy of 0.0001g (using the Sartorius LA310S analytical balance) for specimens with weights of ≥5g but <50g and 0.001g (using Adam Nimbus NBL 623i analytical balance) for specimens that are ≥50g in accordance with ASTM D5229-14, and put back into the water bath. The specimen water content was determined as a percentage change using Equation (11)

$$Mass\ percentage\ change, \% \ = \left(\frac{W_i - W_o}{W_o}\right) \times 100 \qquad (11)$$

where:

W_i = weight of the specimen at each point of the weight recorded during the experiment

W_o = initial weight of the specimen before any contact with water

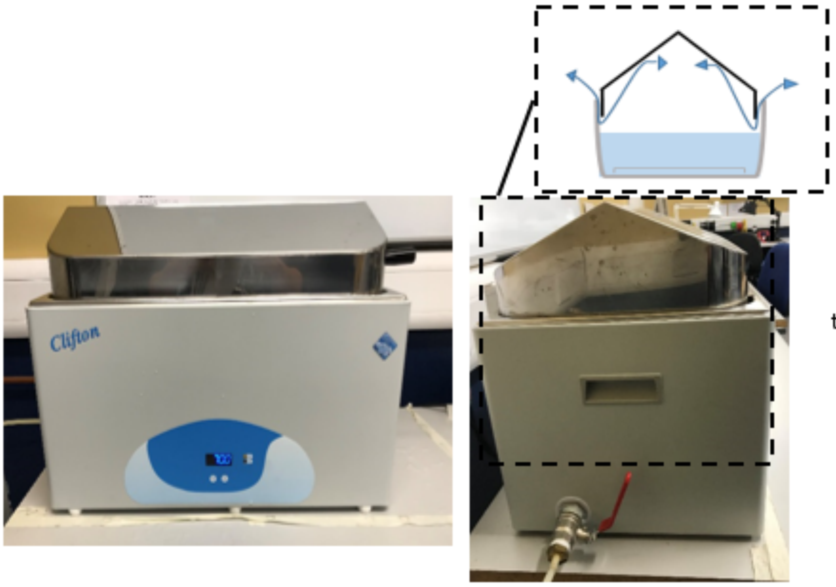

Natural airflow maintained, without sacrificing water temperature stability, and minimum water evaporation

Figure 27: Water absorption experiment set-up.

In part of the experimental moisture conditioning of this thesis, specimens were exposed to 90°C water temperature to further accelerate the aging process for longer duration up to 100 days. Purified water (Type 1) was also used to exclude the effects of natural elements present in the spring water. Further details of these key changes and the motivation behind them are further explained and referenced accordingly in their relevant sections for clearer justification.

3.4.2 Diffusion coefficients

The diffusion coefficients in this work were obtained by employing Fickian theory with the assumption of uniform moisture and temperature conditions throughout the volume using Equation (4) which was initially developed from Fick's transient equation (12) by Crank (Crank 1975).

$$\frac{\partial z}{\partial t} = D\frac{\partial^2 C}{\partial z^2} \tag{12}$$

where:

Z= the distance into the thickness (h) from an exposed surface

C= the concentration of water

D= the bulk diffusion coefficient

The bulk diffusion coefficient refers to a fully exposed specimen. Crank (1975) develops the summation solution to Equation (12) as Equation (13):

$$\frac{M_t}{M_\infty} = 1 - \frac{8}{\pi^2}\sum_{k=0}^{\infty}\frac{1}{(2k+1)^2}exp\left(-\frac{D(2k+1)^2\pi^2 t}{h^2}\right) \tag{13}$$

Equation (13) can be simplified for short and long term time approximation as presented in Equation (14) and Equation (15):

$$\frac{M_t}{M_\infty} = \frac{4}{\pi^2}\sqrt{\frac{Dt}{h^2}\pi^2} \text{ for } \frac{Dt}{h^2} < 0.004 \tag{14}$$

$$\frac{M_t}{M_\infty} = 1 - \frac{8}{\pi^2}\ exp\left(\frac{-Dt}{h^2}\pi^2\right) \text{ for } \frac{Dt}{h^2} > 0.004 \tag{15}$$

D for a statistical homogeneous material can be determined using Equation (4) as long as M∞, and the slope can be established from a gravimetric curve as illustrated in Figure

28. In Equation (4), moisture diffusion is assumed to be one directional (in the thickness direction) and the last dimensional factor of the equation represents the effect of edges where parameters l and w are the length and width of the specimen (Shen and S. Springer 1976).

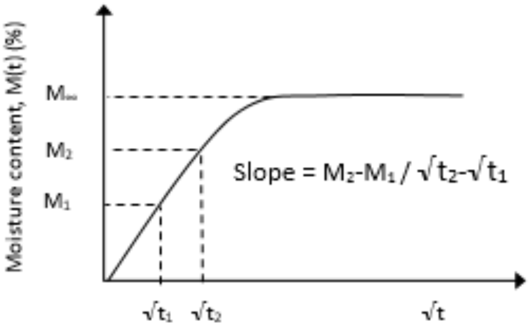

Figure 28: Representative of classical Fickian diffusion three-stage curve for M(t) vs. √t.

3.5 Compressive characterisation

The combined loading compression (CLC) test was used to determine the laminate compressive strength for dry and water-immersed CFRP specimens in accordance with ASTM D 6641-16 as illustrated in Figure 29. Ten specimens were prepared for each fibre architecture (five for dry and five for water-immersed) in order to investigate the influence of water uptake on the compressive properties. All specimens (cut from 220mm by 200mm panel) were 140mm (±0.3mm) long by 13mm width with gauge length of 13mm. Sixteen plies with stacking sequences of $[0/90]_{4S}$ and $[(0/90)]_{16}$ produce thicknesses of 3.1mm and 3.5mm for unidirectional and woven (plain and twill weaves), respectively. The stacking sequences applied were to create an identical distribution of fibre directions between the unidirectional and woven specimens for comparison purposes. For fabrication, the bagging schematic presented in Figure 30 was used where a 1 mm aluminium caul plate covered with nylon inside the vacuum was used to produce smooth surfaces on both sides of the specimens for the fixtures' grips.

The matrix volume fractions and void content for these specimens were obtained by method explained in (Section: 3.3 Constituent contents) based on minimum of three 20mm by 13mm specimens per fibre architecture and cut from the as manufactured panel. An Avery-Denison loading machine with 600kN load cell and two fixed platens was used to apply load to the CLC fixture at a rate of 1.3mm/min. The CLC fixture screws were tightened with a torque of 3.5N-m to hold specimens. The laminate compressive strength was calculated using Equation (16).

$$F_{cu} = \frac{p_f}{w \times h} \tag{16}$$

where:

F_{cu} = laminate compressive strength (MPa)

P_f = maximum load to failure (N)

W = measured specimen gage width (mm)

h = measured specimen gage thickness (mm)

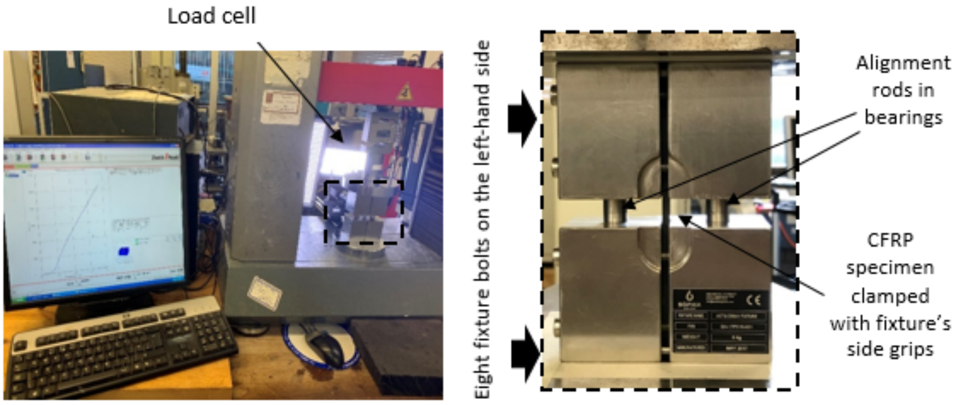

Figure 29: CLC test set-up.

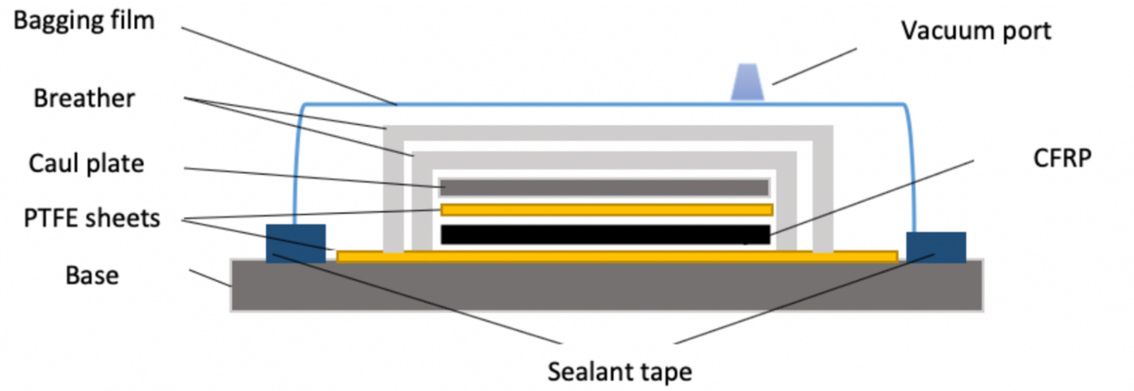

Figure 30: Bagging schematic used to produce CFRP with smooth surfaces.

It is worth highlighting that from trial CLC testing to optimise the test set-up, applying greater than 3.5N-m on the CLC fixture screws when tightened on the specimens for this lay-up sequence and thickness was found to cause excessive gripping leading the specimens to fail in a "through thickness inside grip" failure mode. In addition, less torque than 3.5N-m was found to let the specimens slip while under load leading them to fail in an "end crushing inside grip top" failure mode, noting that both failure modes are not acceptable. Illustrated in Figure 31 are the potential failure modes highlighting the acceptable and not acceptable modes in accordance with ASTM D 6641-16 as given in the list:

1: Transverse shear at grip top (acceptable failure mode)

2: Brooming in middle gage area (acceptable failure mode)

3: Through thickness at grip top (acceptable failure mode)

4: Long splitting in various gage area (acceptable failure mode)

5: Through thickness inside grip (not acceptable failure mode)

6: End crushing inside grip top (not acceptable failure mode)

7: Delamination inside grip top (not acceptable failure mode)

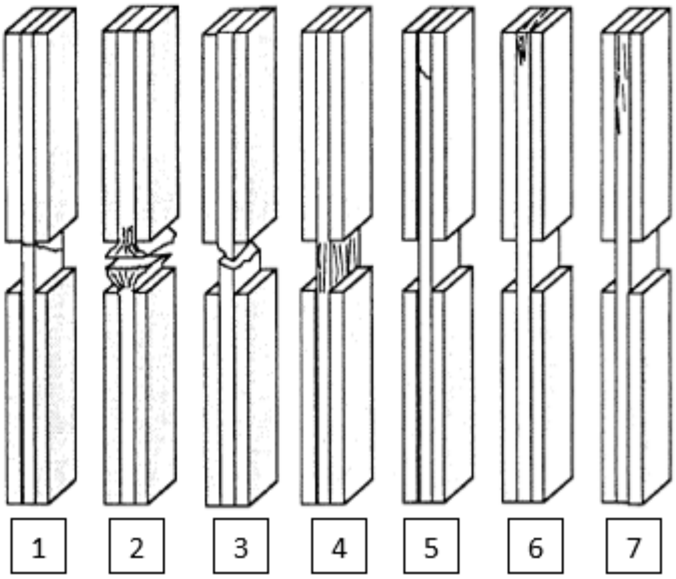

Figure 31: CLC expected failure modes (ASTM D 6641-16).

3.6 Shear characterisation

The interlamiar shear characterisation was fulfilled by employing the short-beam strength test (SBS) using a three-point bending configuration in a Zwick Roell Z050 load machine with 50kN load cell as illustrated in Figure 32. The loading nose was 6mm in diameter, the supports were 3mm in diameter, the span distance was 24mm, and the speed of testing was at a crosshead rate of 1mm/min in accordance with ASTM D2344-16. A minimum of ten specimens were prepared for each fibre architecture (five for dry and five for water-immersed). A 3D printed alignment guide (Figure 32) was designed for the specimens when mounted on the fixture allowing better test repeatability. All specimens were 36mm by 12mm (cut from 110mm by 100mm panel). There were thirty plies with stacking sequences of $[0/90]_{15}$ and $[(0/90)]_{30}$ for unidirectional (5.8 mm thick) and woven (6.4 mm thick), respectively. Debulking operations were applied when making the specimens panels due to their large thicknesses. The debulking process consisted of five minutes vacuum pressure at room temperature for each five plies prior to the main cure cycle. The stacking sequences were selected to create identical distribution of fibre directions between unidirectional and woven specimens for comparison purposes. This is also to simplify the damage mechanism by excluding additional fibre directions and to avoid symmetric plies in the mid plane. For fabrication, the same bagging schematic used for CLC specimens (Figure 30) was used for SBS specimens to produce smooth surfaces on both specimens sides in contact with the fixtures' supports and loading nose. The fibre volume fractions and void content for these specimens were obtained by method explained in (Section: 3.3 Constituent contents) based on a minimum of three 12mm by 10mm specimens per fibre style cut from the as manufactured panel. The short-beam strength was calculated using Equation (17).

$$F_{sbs} = 0.75 \times \frac{P}{b \times h} \tag{17}$$

where:

F_{SBS} = short beam strength (MPa)

P = load observed during the test (N)

b = measured specimen width (mm)

h = measured specimen thickness (mm)

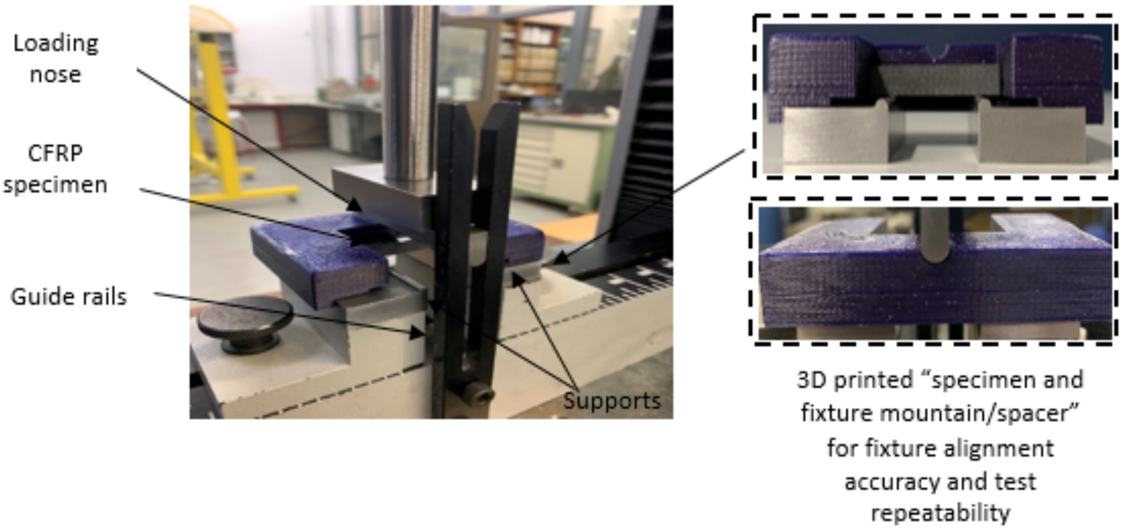

Figure 32: SBS test set-up.

It is worth noting that specimen thicknesses other than those used in this study have led to failure modes that are not representative for interlaminar shear as aimed for in this study. For instance, flexure failure in compression or tension was found in thinner specimens. Additionally, inelastic deformation was reported in thicker specimens. Those failure modes are illustrated in Figure 33 as given in the list:

1: Interlaminar shear (preferred failure mode for this study)

2: Flexure in compression

3: Flexure in tension

4: Inelastic deformation

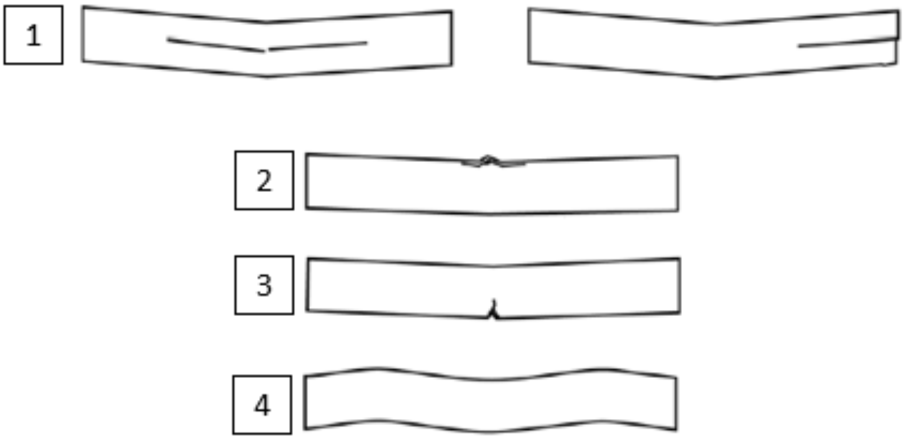

Figure 33: Typical failure mode in the short beam test (ASTM D2344-16).

3.7 Impact damage characterisation

The Impact Damage Resistance (IDR) test was carried out by employing a drop weight test in accordance with ASTM D 7136-15 as illustrated in Figure 34. Fifteen specimens (cut from 700mm by 500mm panel) were prepared for each fibre architecture with dimensions of 150mm (±0.25mm) by 100mm (±0.25mm) and stacking sequences of $[45/0/-45/90]3_s$ and $[(45/-45)/(0/90)]6_s$ for unidirectional (4.8mm thick) and 2D woven (plain 4.8mm thick, and twill 4.8mm thick), respectively. For fabrication, the bagging schematic presented in Figure 35 was applied where the use of perforated release film essential to introduce easier bleed of resin from the bag side direction due to the fact that the CFRP panels for this test in particular were large with further fibre directions in the stacking sequences; therefore, minimum air trapped was desired.

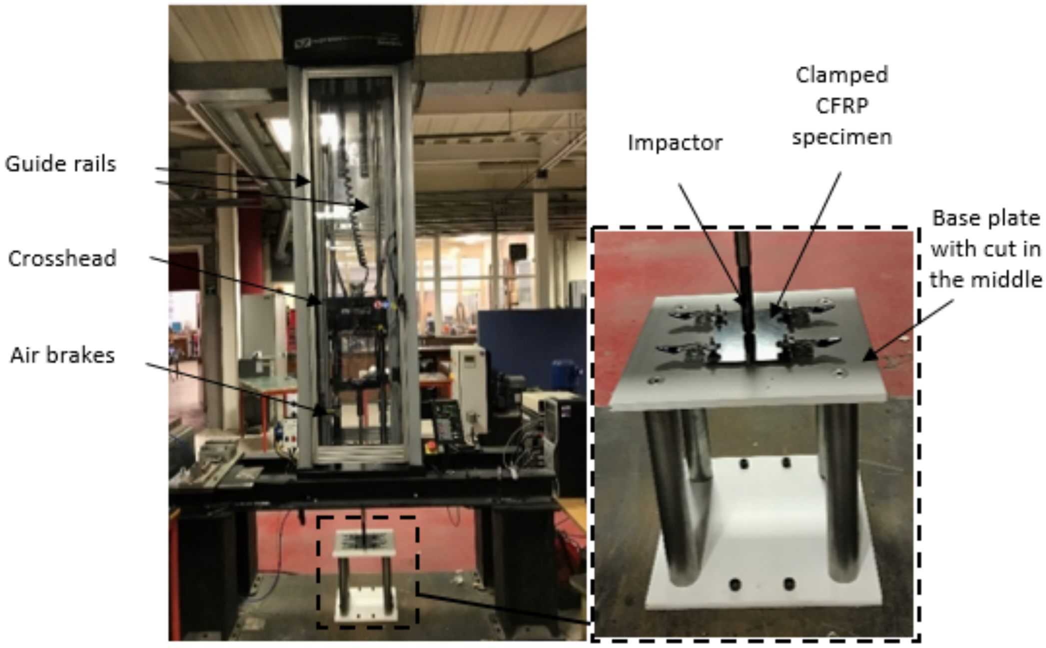

Figure 34: Drop Weight test set-up.

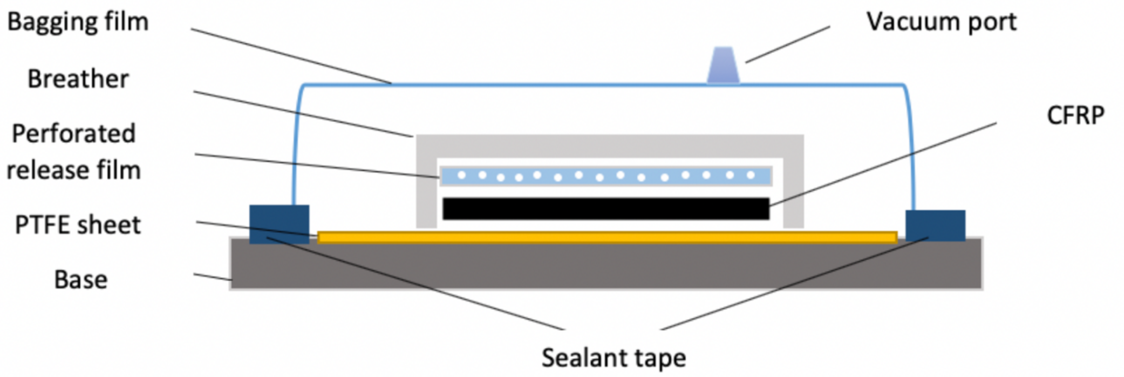

Figure 35: Bagging schematic used for IDR specimens.

The fibre volume fractions and void volumes for the specimens were obtained by method explained in (Section: 3.3 Constituent contents) based on a minimum of three 20mm by 15mm specimens per fibre style cut from the same manufactured panel. To investigate the influence of different levels of impact damage on water uptake, prior to the water absorption experiment 10 specimens of each fibre architecture were impacted, five with an energy of 20J, and 5 with an energy of 70J to represent barely visible impact damage (BVID) and visible impact damage (VID), respectively. The five remaining specimens were left undamaged for comparison with the water uptake of undamaged specimens. The undamaged specimens were then impacted with 70J following the water immersion testing, in order to investigate the influence of moisture absorption on impact resistance. The impact damages were applied using an Instron 9250-HV drop tower, with a 16mm (±0.1) diameter hemispherical impact top and a mass of 5.5kg (±0.25). The drop height was adjusted to achieve the required impact energies.

The external damage was visually inspected whereas the internal damage was inspected by c-scan for internal damage extent measurements. The expected damage modes externally and internally are illustrated in Figure 36 as given in the list:

1: Dent/depression (externals damage)

2: Splits/cracks (externals damage)

3: Combined splits/delamination (externals damage)

4: Combined large cracks with fibre breakage, indentation/puncture (externals damage)

5: Indications of delamination (internal damage)

6: Indications of splits/crack (internal damage)

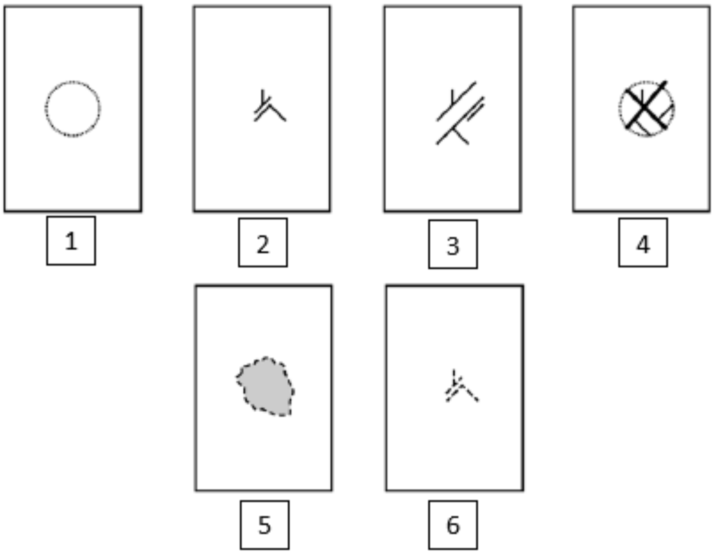

Figure 36: Commonly observed damage modes from out of plane drop weight impact (ASTM D 7136-15).

All impacted specimens were inspected post failure using ultrasound C-scanner with 10MHz probe. The area of damage was achieved using the ‘’-6dB’’ method, for which a drop of 6dB in signal is used to determine the position of a defect edge. The supporting research for this approach was conducted by the National Physical Laboratory (NPL) and is presented in a series of papers (Smith et al. 1998b; SMITH et al. 1998; Smith et al. 1998a; Zeqiri et al. 1998; Zeqiri and Hodnett 1998).

3.8 Microscopic imaging

For microscopic imaging, an Olympus B07 microscope attached with a Moticam 10.0 MP camera illustrated in Figure 37 was used to acquire images. A Leica DM LM microscope was also used in this thesis. The images were then exported using Motic Images Plus 2.0 ML software (for Olympus B07) and using OmniMet Software (for Leica DM LM) attached to the microscopes.

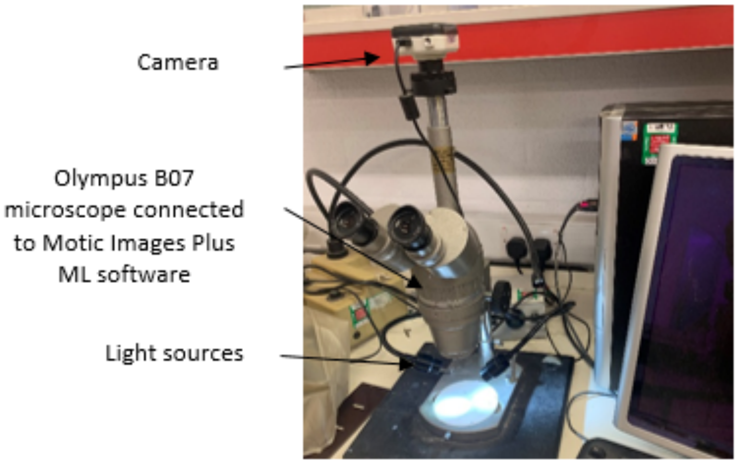

Figure 37: Olympus B07 Microscopic imaging set-up.

3.9 C-scanning

For internal assessment of all CFRP specimens used in this study, a submersion tank ultrasonic c-scanning system supplied by MIDAS NDT Systems Ltd. illustrated in Figure 38 was used. The scan was operated in pulse-receive mode using a 10MHz probe. The data were post processed using ZEUS V3 software and exported as images. The images were then imported to ImageJ to measure the extent of internal damage (Rueden et al. 2017).

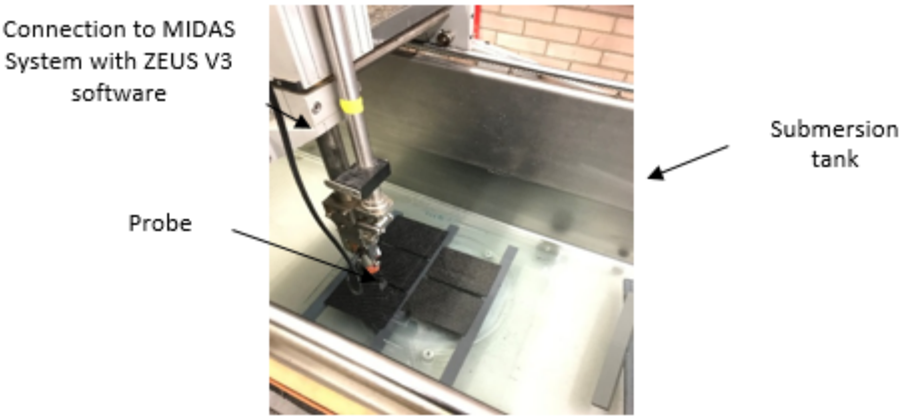

Figure 38: C-scanning Set-up.

3.10 Scanning Electron Microscopy

For the scanning electron microscopy analysis, specimens with dimensions of 3mm by 12mm were cut from the same panel as the SBS specimens. These panels were used due to their high thickness (to capture more areas of the thickness) which was desirable for the SEM analysis. ZEISS Sigma HD illustrated in Figure 39 was adopted to create images of high quality and scrutinise the ageing effects at micro-structural level under different magnification. Prior to SEM imaging, all specimens were oven dried at 50°C for 24 hours. The specimens were then metal coated with 10-15 nm thick layer of gold (90%)-palladium (10%) to enhance the detection resolution by improving the conductivity of the material's surface avoiding charging effects. The data were analysed using ZEISS SmartSEM software.

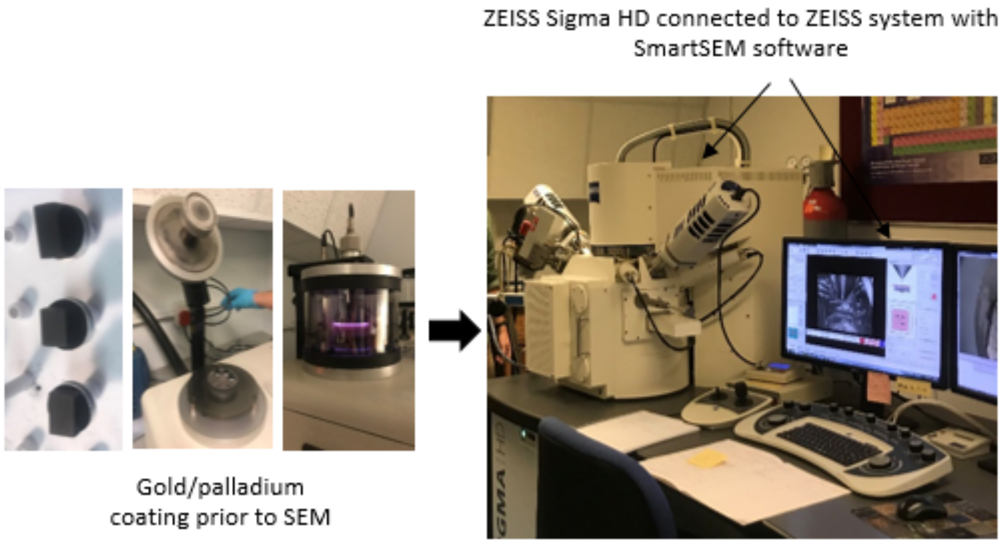

Figure 39: SEM Set-up.

3.11 Optical measurement

An iMetrum Video Strain Gauge (VSG) system illustrated in Figure 40 was used in this study. A 5MPixel IMT-CAM028 camera with IMT-LENS-MT043 material test lenses was used with a field of view of 40x36 mm and a record rate of 2 frames per second. A speckle pattern was applied to all specimens that have been used for the video strain gauge analysis, in-line with iMetrum guidance (Imetrum Limited 2016). This was achieved by spraying the specimens with a light dusting of matt white spray paint (a light layer so that it does not build a thick layer which would eliminate characterising the specimens actual surface) followed by a light dusting spray of matt black paint. This produces a pattern with many light, dark and grey areas for precise target tracking. This allowed the use of iMetrum 2D shear strain map function, which was employed in this study to observe the maximum shear strain (by monitoring the shear optical displacement).

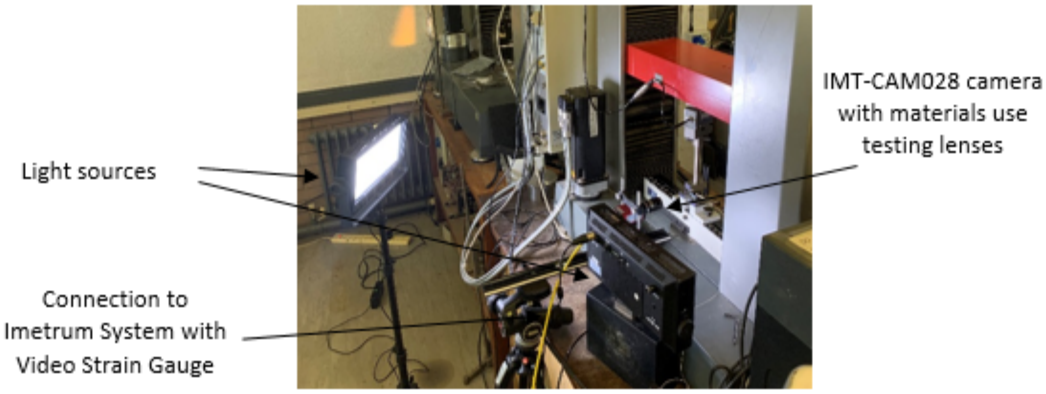

Figure 40: Video Strain Gauge Set-up.

3.12 Acoustic Emission

AE signals were recorded during static testing of SBS samples using a MISTRAS PCI2 AE system. The same PICO sensor was used for each specimen and bonded in the same location, as shown in Figure 41. The sensor type was chosen due to the specimen's small dimension (sensor's technical data is attached in appendix A). The operating frequency range for the PICO sensor is 200-750 kHz. The sensor was mounted to the top surface of the specimen using superglue, which provides physical attachment and acoustic coupling. A MISTRAS 2/4/6 preamplifier with gain set to 40 dB was used with an analogue filter between 20 kHz and 1,200 kHz. The AE system detection threshold was set to 45 dB. The peak detection time (PDT), hit definition time (HDT), hit lockout time (HLT), and max duration were 200 µs, 800 µs, 100 µs and 100 ms, respectively. The progressive growth of damage was monitored by acquiring several parameters from the AE waveforms presented in Figure 42, which were sampled at 40 MHz, these parameters were absolute energy, amplitude, duration and counts (Physical Acoustics Corporation 2004). The peak frequency is also discussed in this thesis. Both load and displacement were also recorded at a rate of 10 Hz and with each hit.

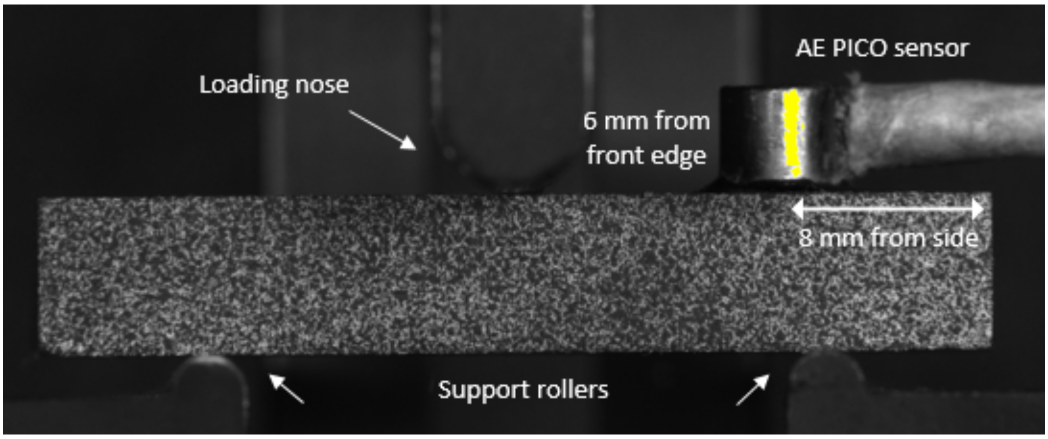

Figure 41: AE Set-up.

The following list describes some of the parameters which can be extracted from the received waveform using commercial MISTRAS AE systems with assistance from (Figure 42)

- **Time of Event** – The time at which the AE signal crosses the threshold
- **Amplitude** – The maximum (positive or negative) amplitude of the AE signal
- **Counts** – The number of times the AE signal crosses the threshold (Positive only)
- **Duration** – The time from when the signal first crosses the threshold, until it last crosses it
- **Rise Time** – The time from when the AE signal first crosses the threshold to its peak value
- **RMS** – The average signal level in volts (root mean squared)
- **Absolute Energy** – The absolute energy of the signal in attoJoules (aJ). This is proportional to the RMS

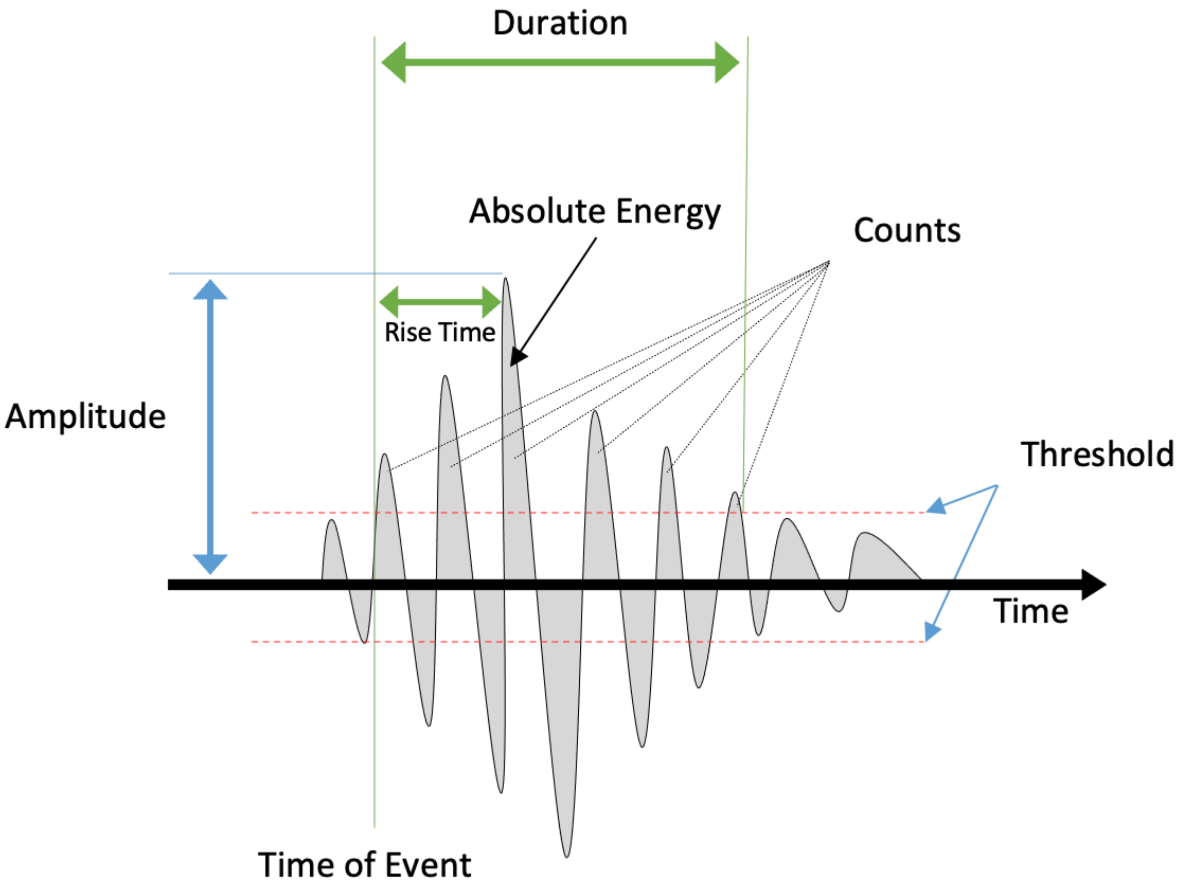

Figure 42: AE waveform features (Physical Acoustics Corporation 2004).

3.13 Conclusions

This chapter has covered the main methods implemented in this study. This involved the materials selection and their fabrication. The procedures used for studying the materials constituent contents have been highlighted along with the moisture absorption, experimental and theoretical approaches. The mechanical properties which are dominantly influenced by the interfacial conditions have been identified and the testing procedures for their assessment have been defined. A range of additional evaluation techniques applied throughout the work have also been outlined, such as microscopic imaging, c-scanning, SEM, VSG, and AE.

4 Moisture Absorption in Unidirectional and 2D woven CFRP Composites

4.1 Introduction

This chapter discusses the influence of moisture on CFRP composites with the focus of the role of a key parameter 'fibre architecture' that is believed to play a major part in the moisture absorption mechanism in CFRP composites. The moisture uptake of unidirectional, plain and twill weave CRFP was monitored in this chapter for different sample geometries based on their mechanical testing standards (compressive strength, interlaminar strength, and impact damage resistance) in order to allow studying the role of moisture on the performance of CFRP composites with different fibre architecture (Almudaihesh et al. 2020). Another set of specimens were also exposed to water absorption in this work to purely calculate their diffusivities by employing Fickian theory allowing a better understanding of the role of fibre architecture on the moisture diffusion mechanism into CFRP structures. The interfacial condition was monitored by Scanning Electron Microscopy (SEM). Some specimens were also exposed to different impact damages prior to water immersion in order to monitor the water absorption behaviour after impact for the different fibre architectures. The following sections in this chapter highlight the methods implemented, the detailed results and their discussions. This study aims at further understanding the role of fibre architecture in the moisture absorption mechanism of CFRP composite.

4.2 Methods

4.2.1 Sample geometry

Different sample geometry selection is considered in accelerated aging based on the aims desired for this study. For those samples that required mechanical testing, this was designed by manufacturing the samples based on their mechanical testing procedures. In addition, exposing some samples in water in order to compare the un-aged ones with their aged equivalents direct from the water experiment to the mechanical testing. This allows testing the specimens immediately after water exposure with no post manufacture processes required, replicating real life scenarios. All SEM samples in this study were not monitored in weight change during water exposure and were only used for SEM analysis at the end of the immersion duration to check the condition of the matrix and interface after aging. Table 9 illustrates the testing matrix for the water experiment specimens based on the related geometrical specifications, fabrication, and layup presented in Chapter 3. The ID presented in Table 9 represents the test associated, followed by the fibre architecture for all samples used for moisture absorption. These set of specimens are exposed to two different conditions; one is for the purpose of studying the mechanical properties after moisture exposure (refereed as water uptake) and the other is for the diffusion coefficient calculations (water diffusion).

Table 9: Test matrix for all water absorption experiments.

ID	Number of specimens	Experiment
CLC UD	Five	Water uptake
CLC plain	Five	
CLC twill	Five	
SBS UD	Five	
SBS plain	Five	
SBS twill	Five	
IDR UD undamaged	Five	
IDR UD 20J damage	Five	
IDR UD 70J damage	Five	
IDR plain undamaged	Five	
IDR plain 20J damage	Five	
IDR plain 70J damage	Five	
IDR twill undamaged	Five	
IDR twill 20J damage	Five	
IDR twill 70J damage	Five	
SEM mechanical UD	One	
SEM mechanical plain	One	
SEM mechanical twill	One	
Bulk diffusion UD	Five	
Bulk diffusion Plain	Five	
Bulk diffusion Twill	Five	
Directional diffusion UD	Five	Water diffusion
Directional diffusion Plain	Five	
Directional diffusion Twill	Five	
SEM diffusion UD	One	
SEM diffusion Plain	One	
SEM diffusion Twill	One	

*All error bars presented in this thesis are standard deviation based on the number of specimens tested in (Table 9) or the number of specimens mentioned in each test (based on their relevant method section)

4.2.2 Water uptake

For this section, the water experiment method used (water type, temperature, and duration) follows section (3.4.1 Water uptake). The water uptake was monitored for those samples that have the same geometry requirements for their mechanical testing CLC, SBS, and IDR, however only the water absorption behaviour is discussed in this Chapter.

4.2.3 Water diffusion

In order to accelerate the aging to reach saturation (maximum moisture absorption) and calculate the diffusivities in accordance to the method detailed in Section (3.4.2 Diffusion coefficients), three parameters were changed; water type, temperature, and duration. The water type used in the samples for diffusion calculation was purified water (type 1) at 90°C for 100 days. This water type was used in order to exclude any potential chemical reaction between the polymers and the mineral containments that can exist in other types of water (i.e. the still natural spring water used in water uptake section) on the interfacial region, which may affect the diffusivity into the structure. The higher water temperature chosen was to accelerate the ageing process and reach saturation within a faster time-scale by increasing the water temperature in order to compare the different diffusivities with the different fibre architecture. In order to also avoid any secondary degradation mechanism in polymers (excessive unwanted degradation) which activates when the temperature is near or exceeds Tg, it is recommended that the temperature is 20°C lower than the polymers Tg (Bank et al. 1995; Maxwell et al. 2005; Hunkley and Connell 2012). The exposure duration was also left until the three different stages of water uptake are observed (mass gain, saturation, and then mass loss) as illustrated in (Figure 6) and more importantly, reaching saturation to allow the calculations of diffusion coefficients. The samples used in this condition are those referred as directional diffusion, and SEM diffusion. The specimens were dried for 24 hours at 30°C in an oven prior to water immersion to make sure they are free from moisture that could be caused by the manufacturing process for a clear diffusion calculation. All specimens were 40mm (±0.3mm) long by 40mm width (±0.3mm). Sixteen plies with stacking sequences of $[0/90]_8$ (for UD) and $[(0/90)]_{16}$ (for woven) produce thicknesses of 3.07mm, 3.54mm, and 3.51 for unidirectional, plain, and twill, respectively. The stacking sequences applied were to create an identical distribution of fibre directions between the unidirectional and woven specimens for comparison purposes. This also allows the assumption that diffusion along the fibre (x-axis) is equal to the diffusion across the fibres (y-axis) in both UD and woven samples (hence, the square shape for the specimens was desired). Smooth surfaces for both sides of the specimens were required in fabrication (Figure 30), due to some specimens being masked from the surfaces for the directional diffusion coefficient calculations. In order to obtain the directional diffusion coefficient for the x-axis and y-axis along with the through- thickness direction (Z-axis), a new experimental approach was used in this study compared with those previously used in the literature. The method included a physical isolation of the two surfaces of each specimen (top and bottom flat surfaces) to stop moisture from penetrating in the (Z-axis) when immersed in water and exposing the four side edges only for each fibre architecture (five specimens for each fibre architecture) to calculate the $D_{x,y}$ (D_x and D_y are assumed to have equal values due to same distribution of fibre directionality in all edges, hence the 0/90 layup and same number of plys for both 0° and 90°). In addition, another five specimens for each fibre architecture were fully exposed in order to obtain the maximum saturation. Figure 43 presents the set up for the fixture used to eliminate the water exposure from the (z-axis) direction, whereas Figure 44 presents the schematic detailing assembly. A neoprene rubber (chloroprene/SBR CQ grade) was added between the toughed glass and the CFRP specimens which is generally used for the purpose of gasket and engineering applications, therefore very resistant to mineral oil, gases, water, UV, ozone, mild chemical, acids. It was essential to add the neoprene rubber to the assembly so the surfaces of the CFRP specimens are submerged into the rubber when the outer toughened glass layers are clamped (at corners and edges of glass) as highlighted in Figure 44 (assuming that the pressure from the clamps is minimal and does not affect water uptake on the $D_{x,y}$ directions). Thus, eliminating the penetration of water from the edges to the surface, allowing the assumption that the z-axes of the specimens have absorbed negligible amount of water.

In summary, the selectively exposed specimens were used to obtain (M_1 at $\sqrt{t_1}$, and M_2 at $\sqrt{t_2}$ from Figure 28) in order to calculate $D_{x,y}$. The fully exposed specimens were used to obtain M_∞ to reach saturation (maximum moisture content) since both the selectively and fully exposed specimens are the same materials and are expected to have the same maximum moisture content. This enables the use of equation (4) excluding the last dimensional factor due to specimens being selectively exposed and assuming Fickian behaviour is present. 96 hours of water immersion for the selectively exposed specimens are believed to be enough to obtain the curve from which the (M_1 at $\sqrt{t_1}$, and M_2 at $\sqrt{t_2}$) values are attained. This duration was also limited by the peel up of the surfaces in contact with the rubber when disassembling the clamps for measurements after longer durations (this process seemed to cause damages on the specimens surface when longer periods applied).

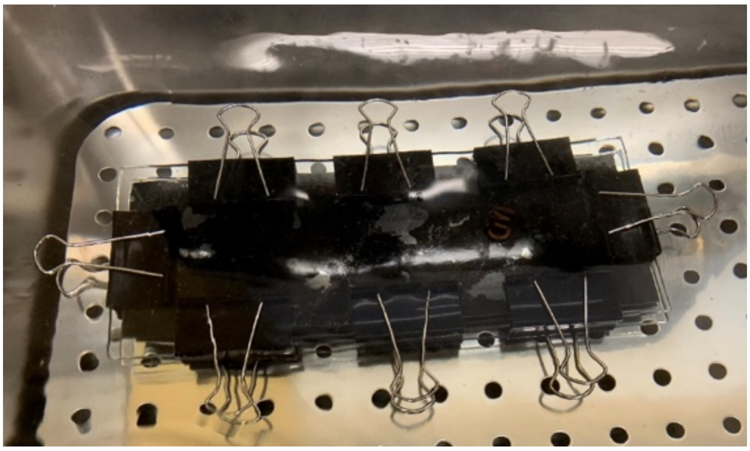

Figure 43: Water diffusion fixture assembly set up.

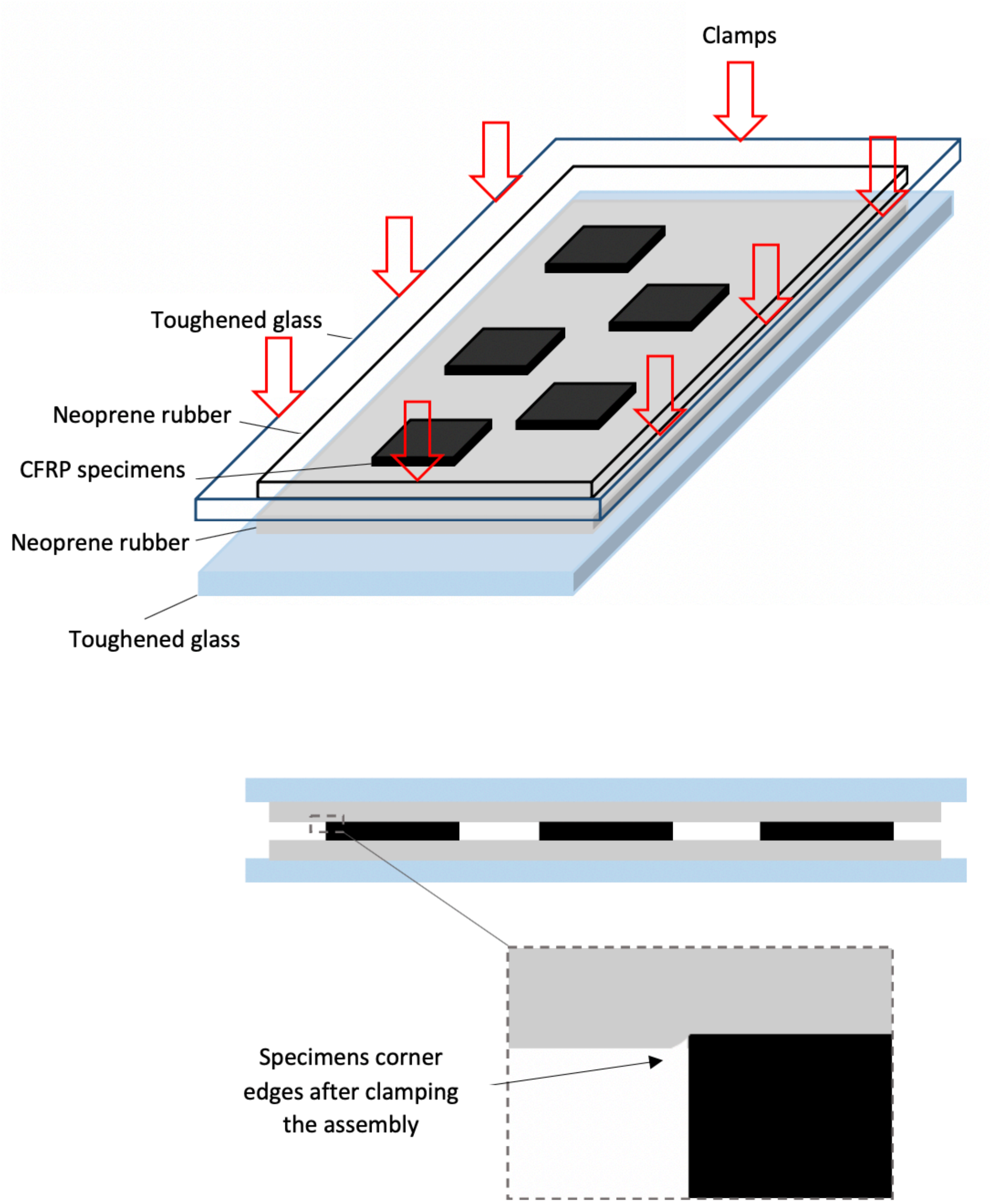

Figure 44: Schematic detailed assembly for water diffusion fixture.

4.3 Results and discussion

4.3.1 Constituent contents

Table 10 presents the constituent contents for all specimens. The matrix volume fraction is similar for the CLC and SBS samples of the same material and as would be expected the woven architectures result in a higher matrix content. The IDR samples exhibit comparatively lower matrix volume fractions, due to the perforated release film used in manufacture, but a trend for higher matrix content in woven architectures is still present. Void contents are seen to be low and, with the exception of the UD IDR sample, are all below 1%, which is in line with aerospace standards (Zhang et al. 2017).

Table 10: Constituent contents.

Specimen Type	V_m (%)			V_{air} (%)		
	UD	Plain	Twill	UD	Plain	Twill
CLC	$41.60^{\pm 0.44}$	$47.47^{\pm 0.19}$	$48.92^{\pm 0.21}$	$0.75^{\pm 0.24}$	$0.38^{\pm 0.08}$	$0.14^{\pm 0.13}$
SBS	$40.55^{\pm 0.73}$	$48.49^{\pm 0.46}$	$47.58^{\pm 0.55}$	$0.86^{\pm 0.29}$	$0.72^{\pm 0.31}$	$0.48^{\pm 0.20}$
IDR	$39.76^{\pm 0.47}$	$43.69^{\pm 0.69}$	$43.91^{\pm 0.16}$	$1.12^{\pm 0.23}$	$0.82^{\pm 0.35}$	$0.83^{\pm 0.29}$

4.3.2 Water uptake

For CLC and SBS specimens, the mass change was measured at the start and end of the water experiment and the results are presented in Figure 45. It is noted that the SBS specimens (unlike the CLC and IDR specimens) had an initial, un-aged, weight that varied between 3.5 to 4g, which is below the minimum of 5g recommended in ASTM D5229-14. The SBS samples have a lower total mass gain in all cases when compared with the CLC samples and this correlates to a larger surface area to volume ratio as seen in Table 11.

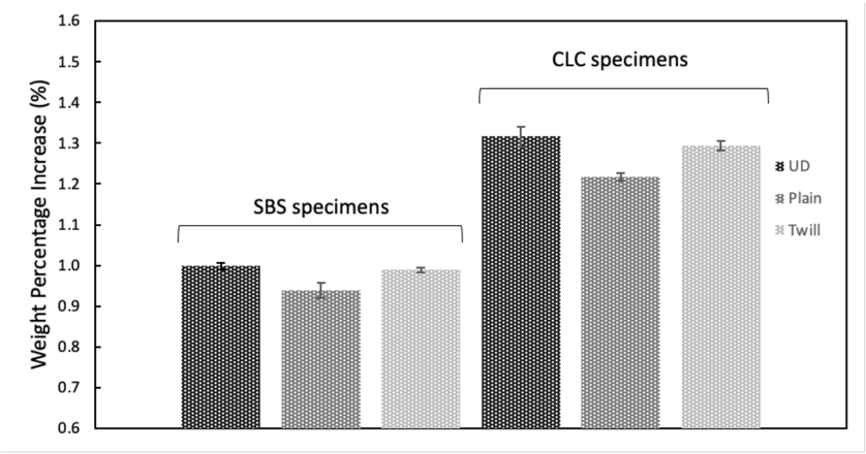

Figure 45: Average weight percentage increase in CLC and SBS specimens.

The total mass gains for the composites vary quite significantly between sample types and smaller variations occur between fibre architectures within each sample type. Plotting the surface area to volume ratio against total mass gain shows a linear correlation with an R^2 value of 0.95 as presented in Figure 46 suggesting that these variations result from geometry and not material differences. When considering the mass gain as a percentage of the matrix only the same correlation is observed, however, mass gain is greater for a given surface area to volume ratio in the UD samples presented in Figure 47. This suggests that diffusion rates are greater in the UD material and this can be correlated to the linearity of the fibre paths, providing direct water ingress into the structure along the fibre matrix interface (Stage IV of Figure 4). In woven architectures, the weave patterns are believed to act as barriers, providing a longer path for moisture ingress along the fibre-matrix interface, theoretically suggested by Choi (Choi et al. 2001). This effect may be exacerbated by the sizing levels, as the UD fibre have a lower sizing level and therefore may allow easier degradation of the fibre matrix interface.

The Scanning Electron Microscope (SEM) images of un-aged UD specimen, shown in Figure 48, presents the fibre-matrix interface of un-aged UD specimen. Figure 49 and Figure 50 show the interface of aged UD specimen. Similar interface conditions are seen for the plain and twill woven architectures as shown by the SEM images (Figures 51-58). It is difficult to observe from these SEM images if the crack corresponds to matrix cracking or a deposition of salt and the crack is on the salt surface. The mineral content attained in the type of water used are believed to have caused the deposition of salts on the surface which was clearly observed from matrix condition in aged specimens compared with their dry equivalents. It is evident that the salt is a key factor in accelerating the plasticisation on polymeric structure causing permanent damage (Cauich-Cupul et al. 2011b; Kafodya et al. 2015). For results comparison, Seo et al. (2017) investigated the salt fog effect on CFRP laminates and compared the SEM results to specimens exposed to non-salt fog as shown in Figure 59 with cracks (shown in red circles) appearing in those samples exposed to salt fog environment. The authors concluded their study with that the exposure to salt fog environments broke the adhesion linkage between resin matrix and carbon fibre (Seo et al. 2017).

Table 11: Summary of water absorption results.

Specimen Type	Total surface/volume ratio			Composites weight increase (%)			Matrix weight increase (%)*		
	UD	Plain	Twill	UD	Plain	Twill	UD	Plain	Twill
CLC	0.82	0.73	0.74	$1.316^{\pm 0.025}$	$1.217^{\pm 0.009}$	$1.294^{\pm 0.011}$	$4.066^{\pm 0.058}$	$3.217^{\pm 0.018}$	$3.314^{\pm 0.018}$
SBS	0.57	0.51	0.53	$0.998^{\pm 0.008}$	$0.938^{\pm 0.018}$	$0.989^{\pm 0.006}$	$3.186^{\pm 0.019}$	$2.380^{\pm 0.036}$	$2.599^{\pm 0.013}$
IDR (0J)	0.47	0.44	0.45	$0.854^{\pm 0.002}$	$0.737^{\pm 0.012}$	$0.724^{\pm 0.002}$	$2.783^{\pm 0.005}$	$2.134^{\pm 0.028}$	$2.084^{\pm 0.005}$
IDR (20J)	0.47	0.44	0.45	$0.892^{\pm 0.002}$	$0.760^{\pm 0.005}$	$0.753^{\pm 0.002}$	$2.903^{\pm 0.007}$	$2.200^{\pm 0.012}$	$2.167^{\pm 0.005}$
IDR (70J)	0.47	0.44	0.45	$0.996^{\pm 0.040}$	$1.095^{\pm 0.029}$	$1.011^{\pm 0.012}$	$3.243^{\pm 0.098}$	$3.170^{\pm 0.064}$	$2.899^{\pm 0.028}$

* The mass change due to moisture absorption as a function of matrix content was achieved by multiplying the resin weight fraction of each specimen by its overall weight and calculating the mass change assuming no moisture effects were observed from the carbon fibres.

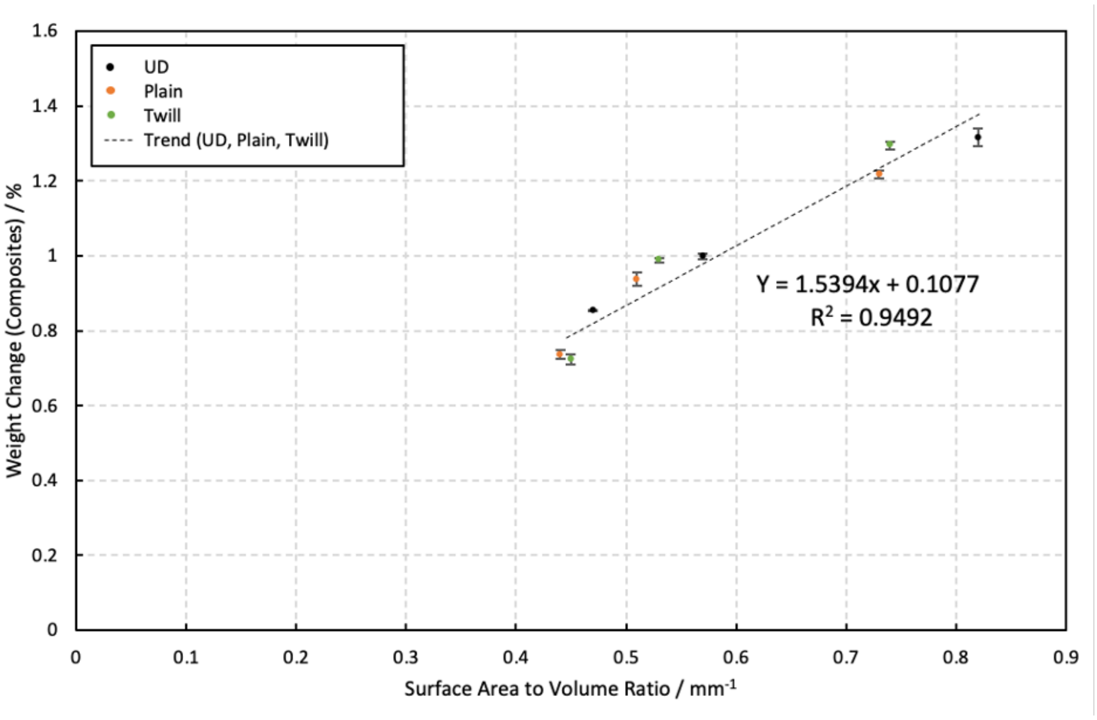

Figure 46: Mass gain versus surface to volume ratio (composite).

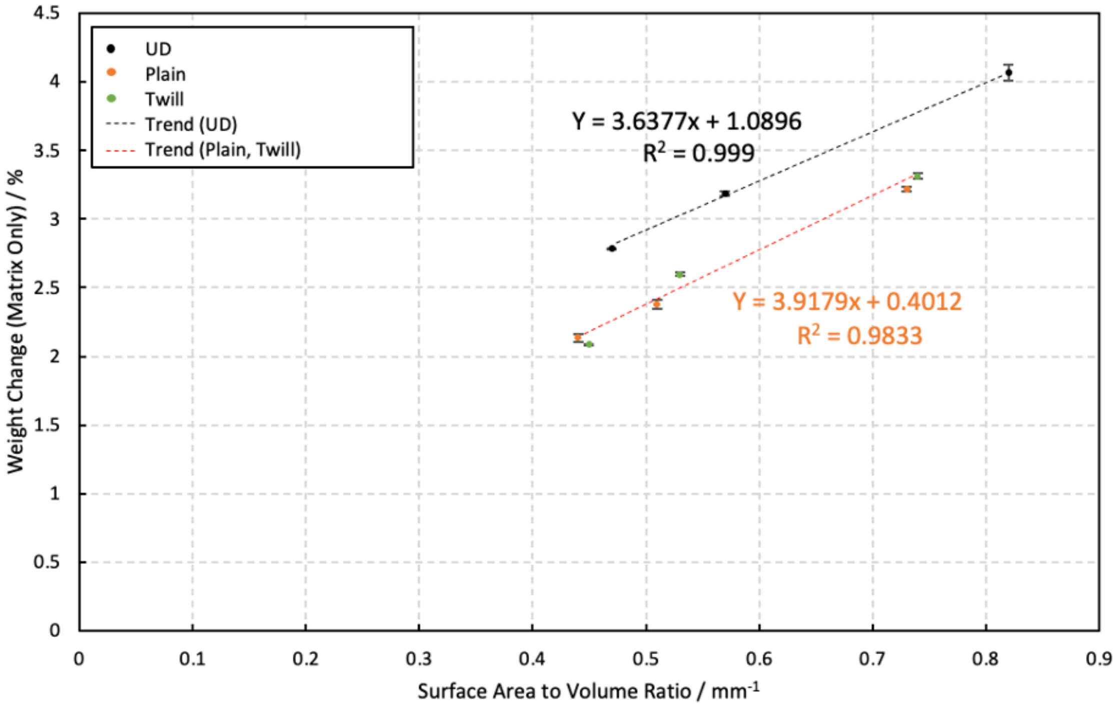

Figure 47: Mass gain versus surface to volume ratio (matrix).

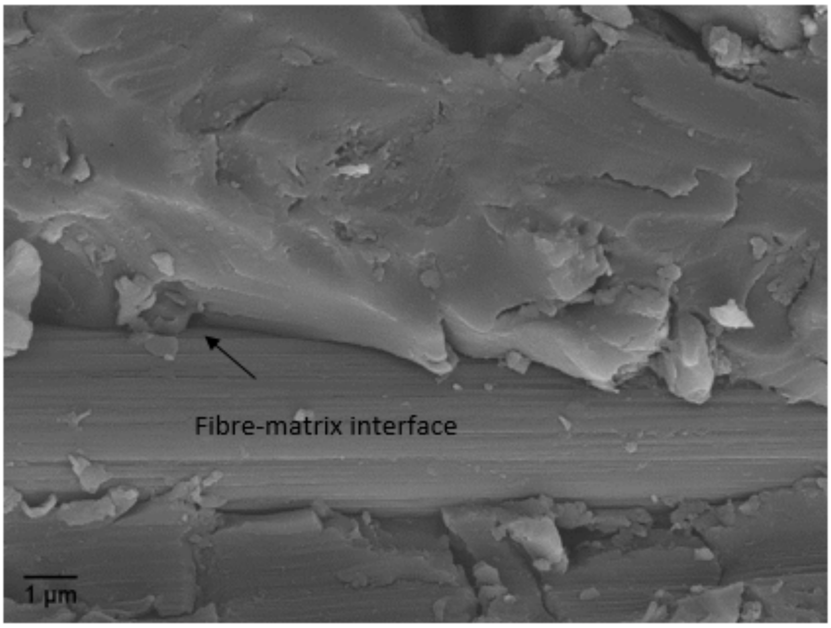

Figure 48: Interface of un-aged UD specimen.

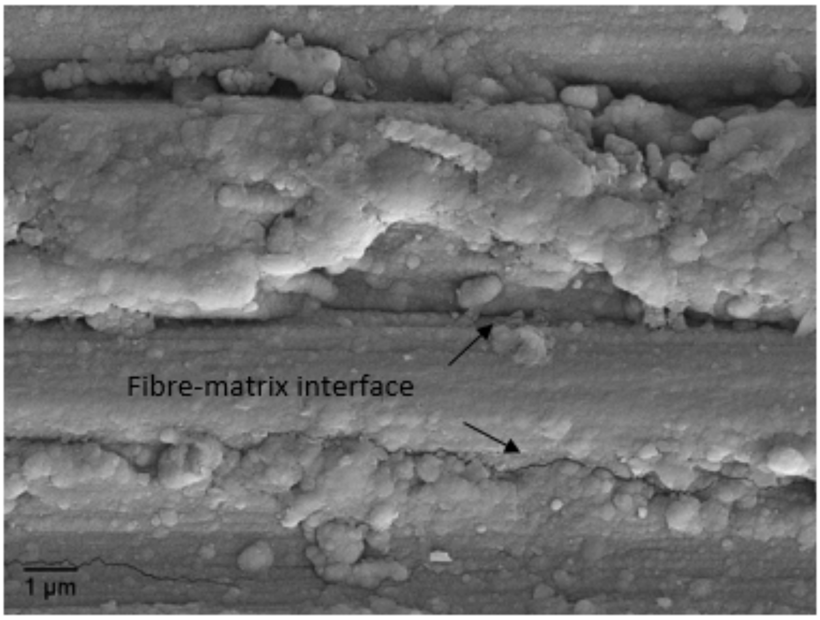

Figure 49: Interface of aged UD specimen.

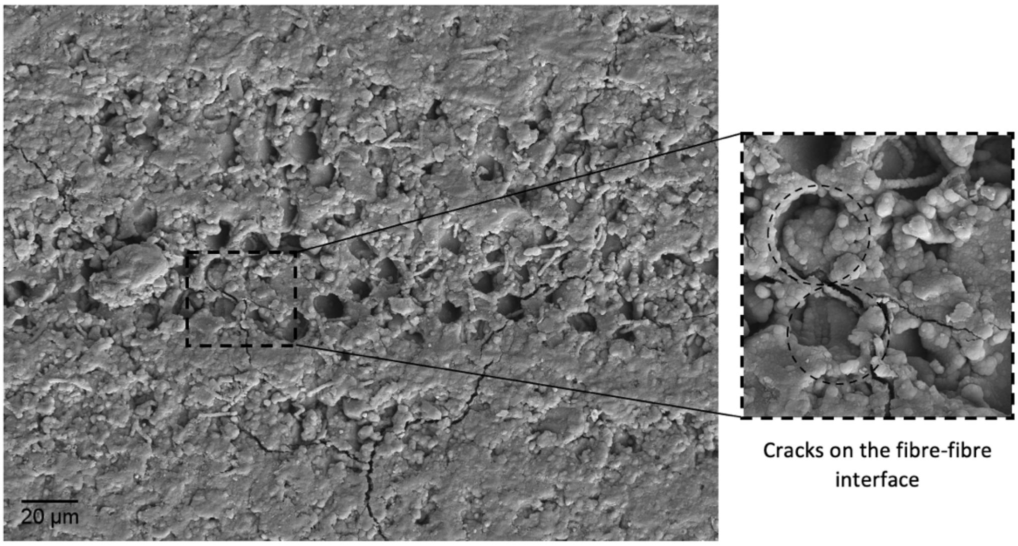

Figure 50: Cracks in aged UD specimen.

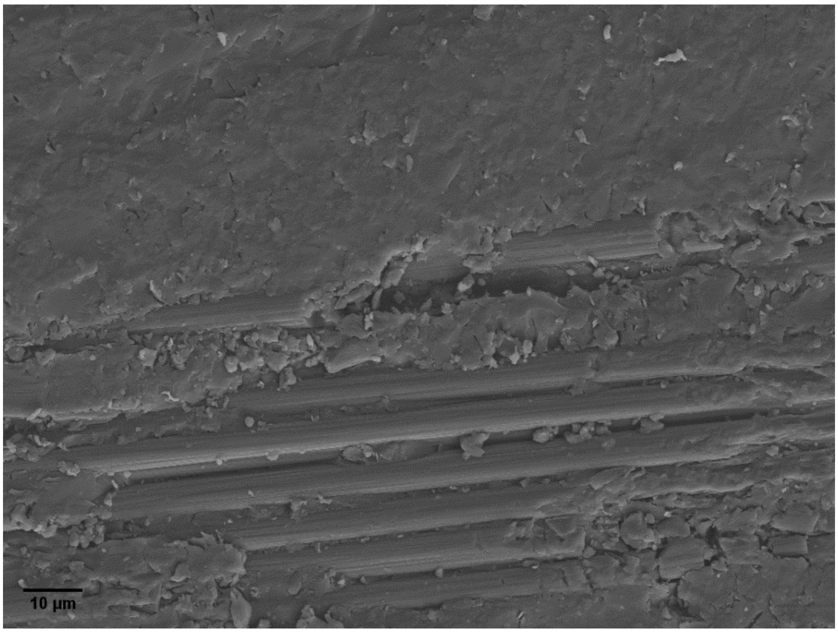

Figure 51: Un-aged plain weave surface.

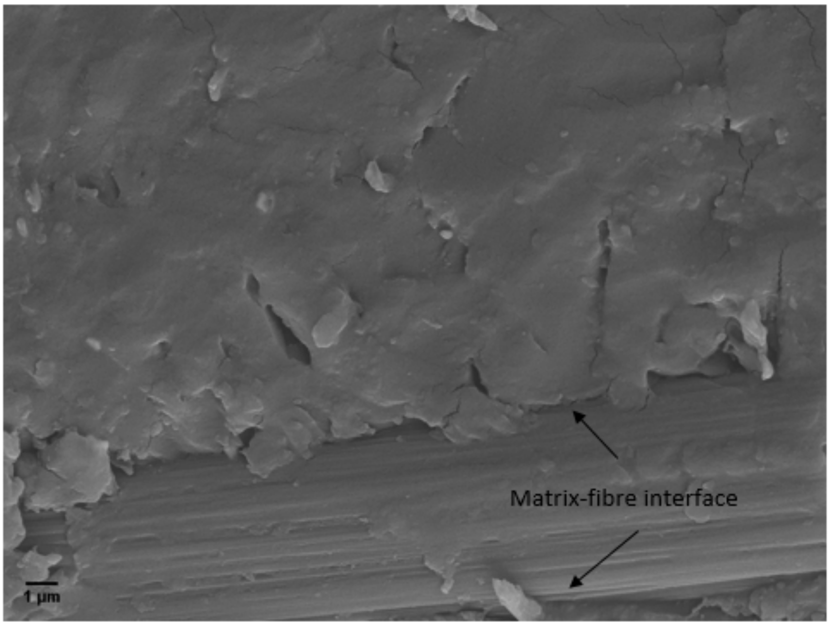

Figure 52: Interface of un-aged plain weave surface.

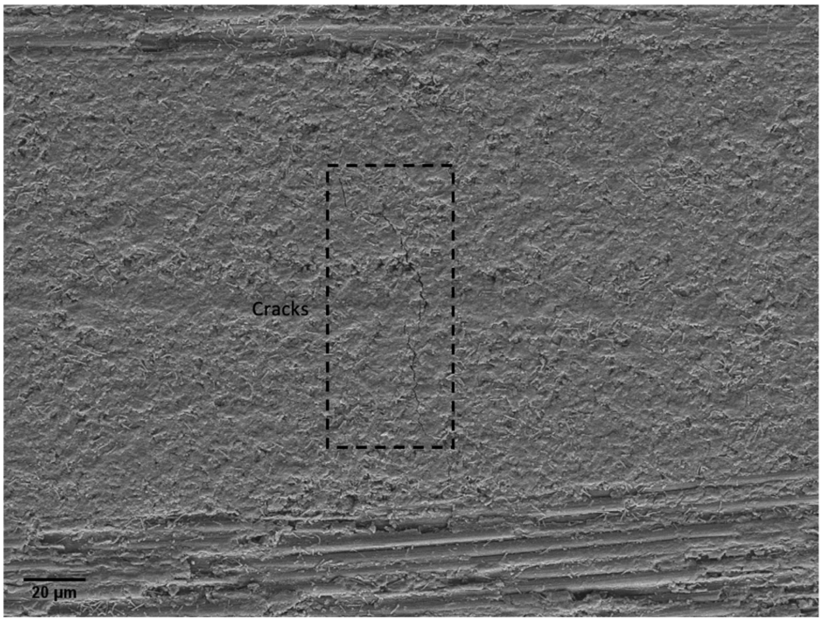

Figure 53: Cracks in aged plain weave surface.

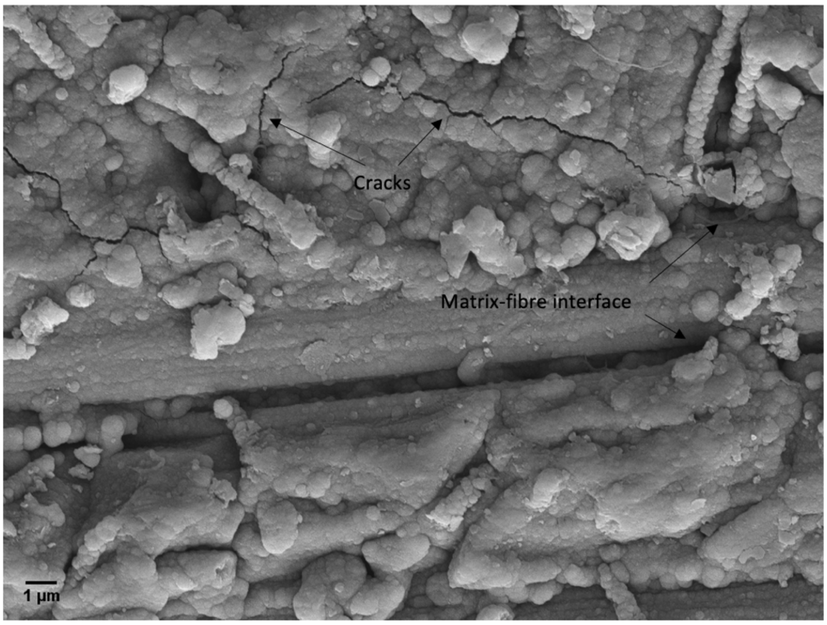

Figure 54: Aged plain weave surface.

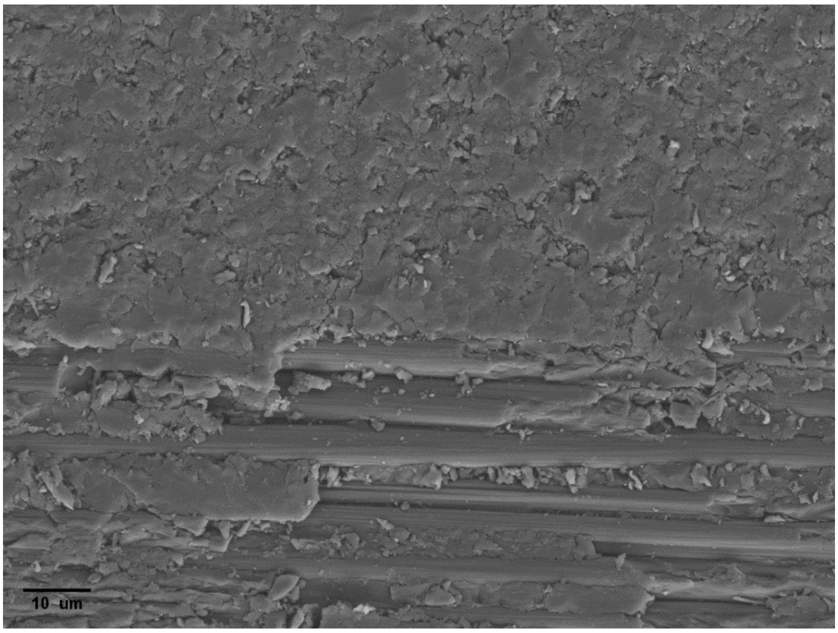

Figure 55: Un-aged twill weave surface.

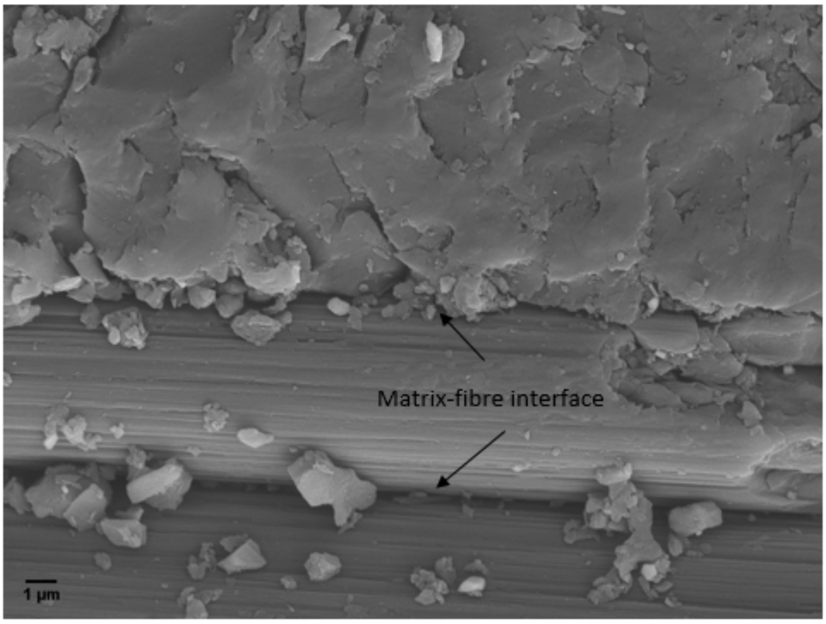

Figure 56: Un-aged twill weave surface.

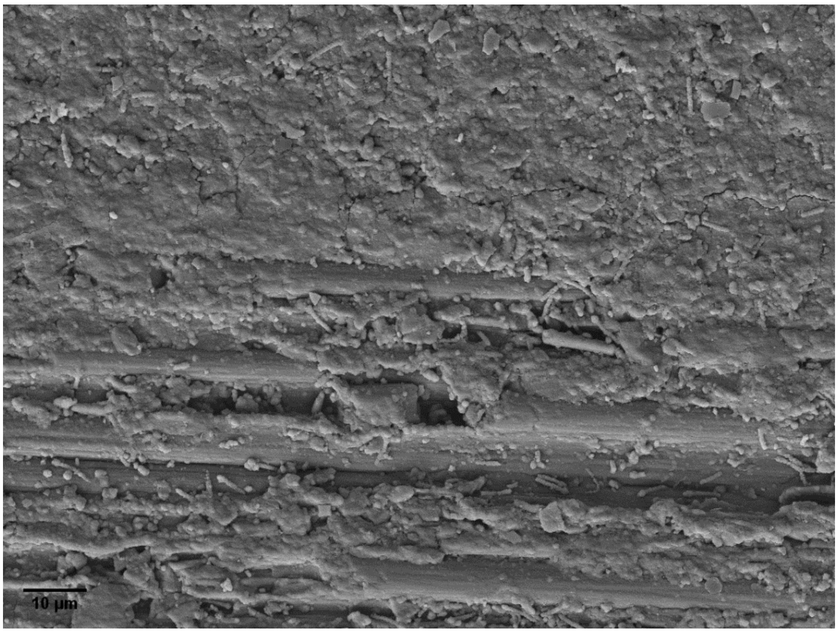

Figure 57: Aged twill weave surface.

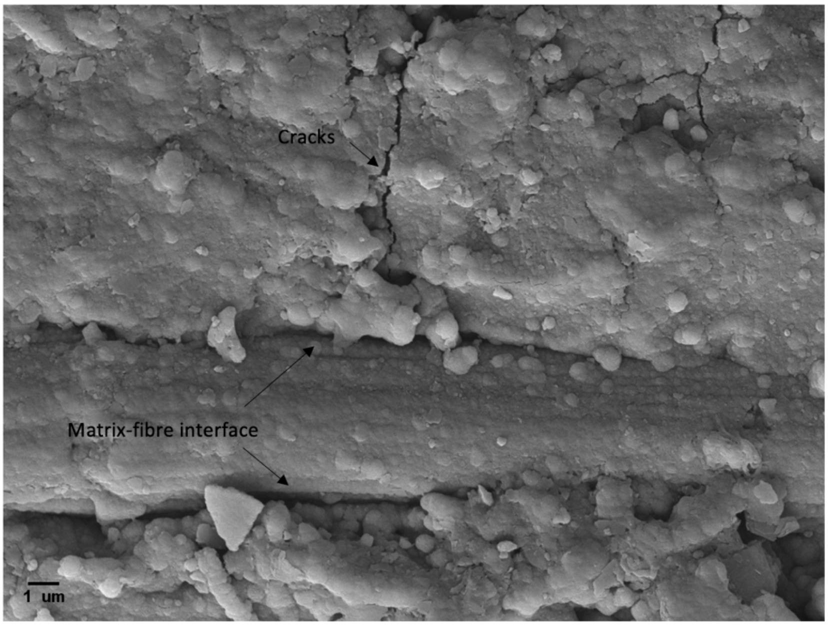

Figure 58: Aged twill weave surface.

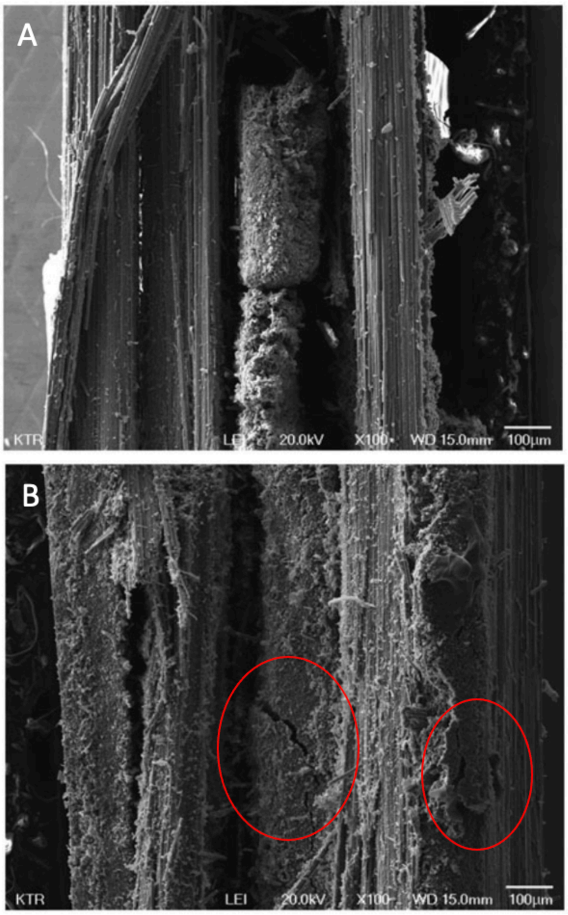

Figure 59: SEM images of (A) non-salt fog exposed CFRP specimen, (B) salt fog exposed CFRP specimen (Seo et al. 2017).

In the case of the IDR specimens, additional mass change measurements were made throughout the water absorption experiment in order to study the influence of impact damage level on moisture uptake. The curves of mass gain versus time for each fibre architecture and damage level are shown in Figure 60. The total percentage mass gain in the undamaged IDR sample is lower, compared with the CLC and the SBS samples, due to their lower surface area to volume ratio (Table 11). Differences in mass gain between the IDR sample types also correlates to the surface area to volume ratio. This correlation remains at the 20J (BVID) damage level but not at the 70J (VID) damage level due to the effects of the increasing damage volume. The larger mass gain seen in the 70J damage level samples shown in Figure 61 results from a higher damage volume but also a larger amount of surface cracking allowing rapid ingress to the damage volume. At lower damage levels (20J) the same trend continues with only marginal increases in total mass gain observed, compared with the undamaged samples. At higher damage levels (70J), a significant increase in total mass gain is seen in all cases with the woven architectures now absorbing more water than the UD material as summarised in Figure 62. The increases in mass uptake with damage level results from the increase in through thickness damage and surface damage. The 70J IDR samples have noticeably more surface damage and therefore allow rapid ingress of moisture into the damaged region. This is clear in Figure 61 where rapid uptake is seen in the first 10 days for the damaged samples. Following this time, the rate of moisture absorption is similar in all cases. The cross-sectional micrographs of the damage induced by 70J impacts are shown in Figure 63 and demonstrates how more significant through thickness damage links to surface cracks in the woven architectures, explaining why the mass gain increases above that of the UD samples at this damage level. The cross-sectional micrographs seen in Figure 64 showing lower through thickness damage induced by 20J impacts to be compared with the 70J impacts seen in (Figure 63).

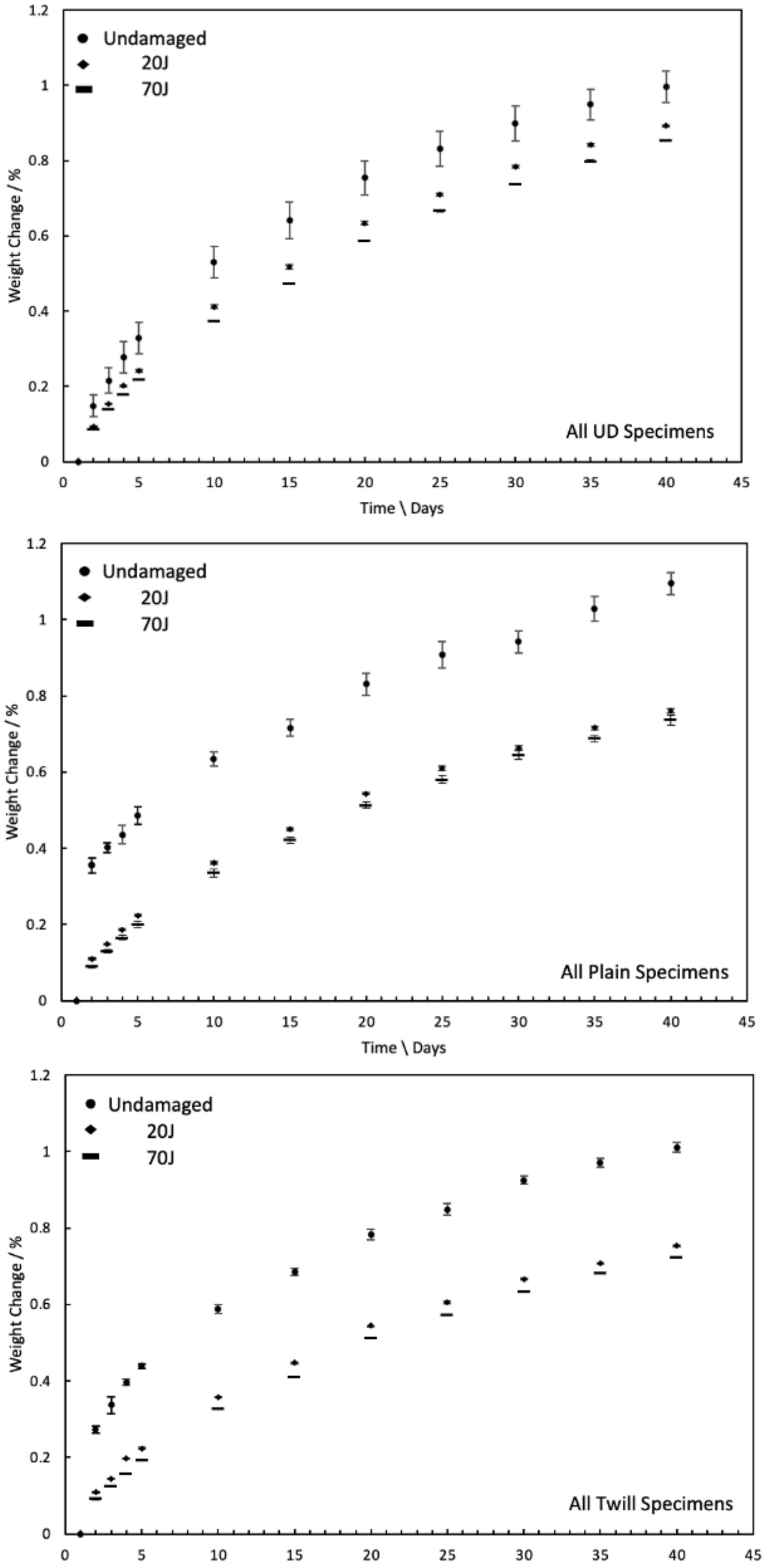

Figure 60: The curves of mass gain versus time for all IDR specimens.

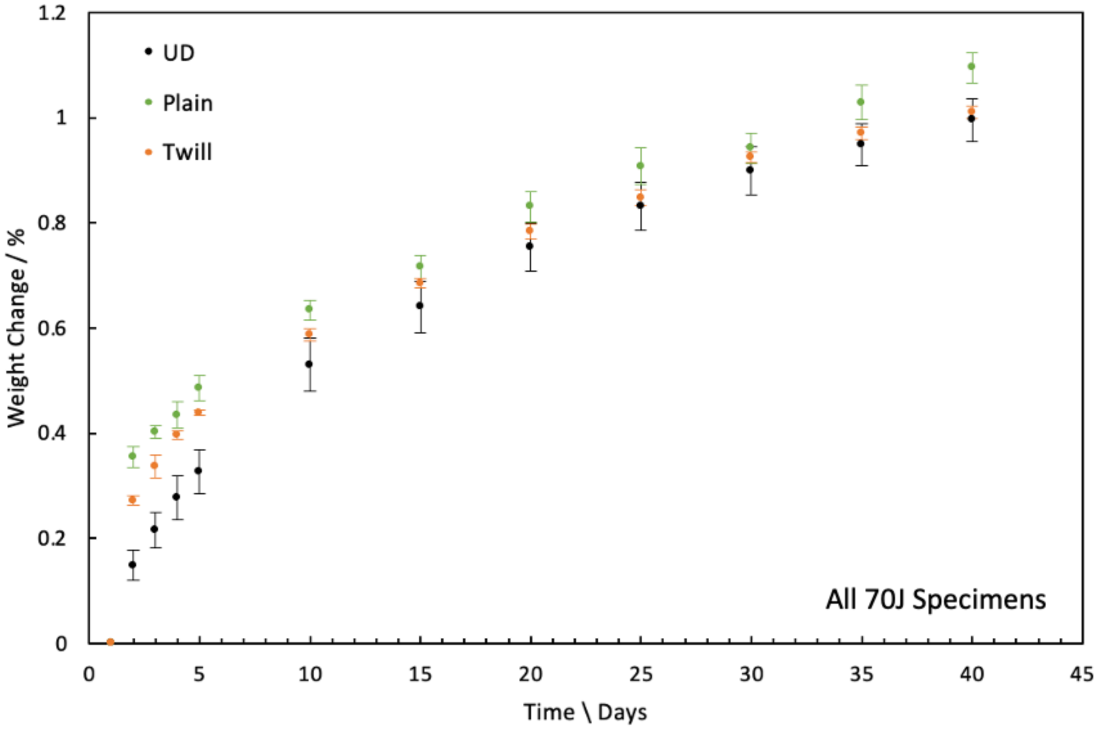

Figure 61: Weight change in the 70J damaged specimens.

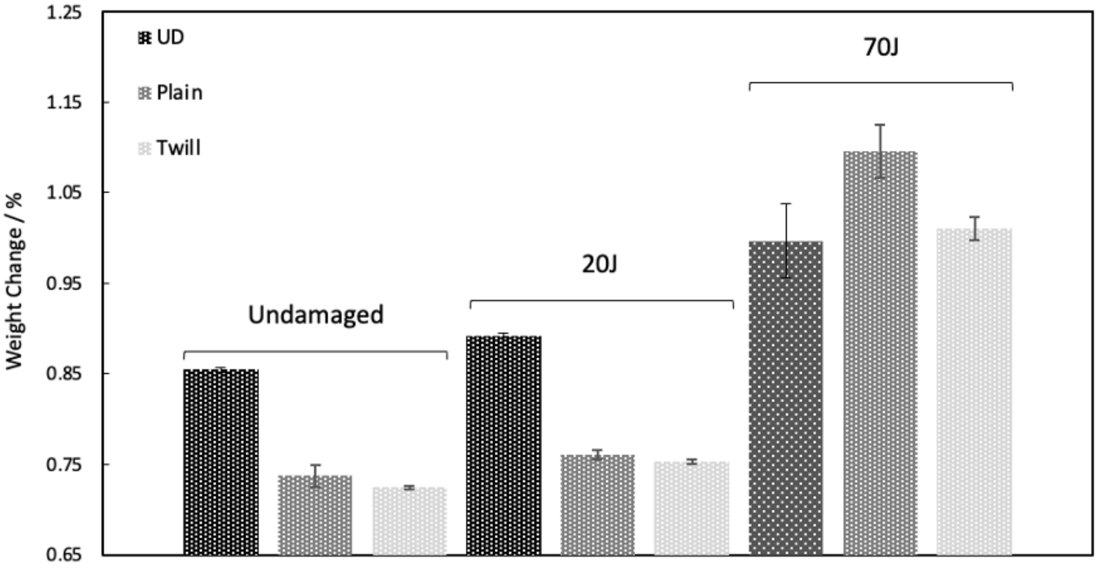

Figure 62: Weight change across all IDR specimen.

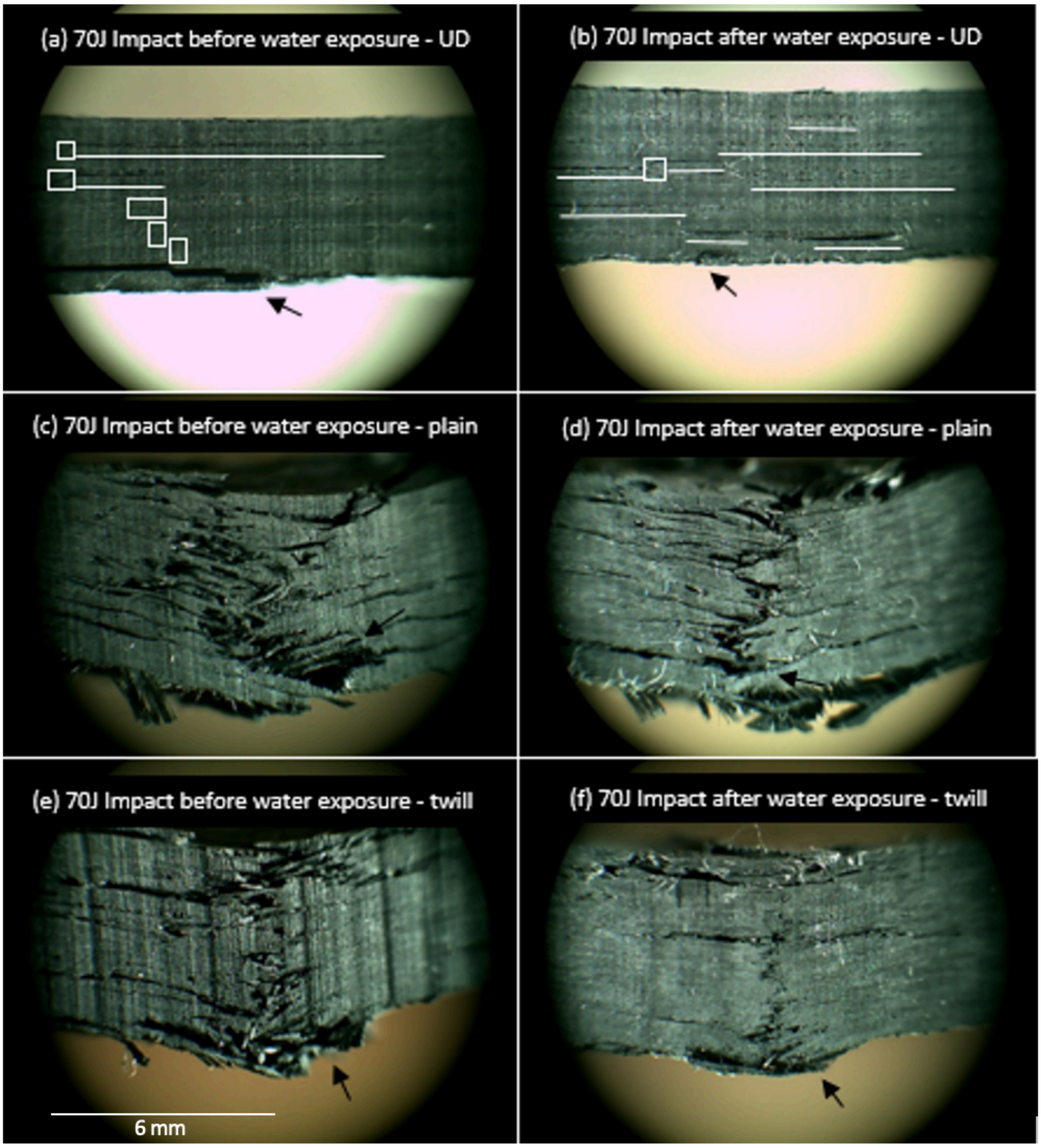

Figure 63: IDR specimens after failure; images are showing the middle section of the specimen's impact damage area.

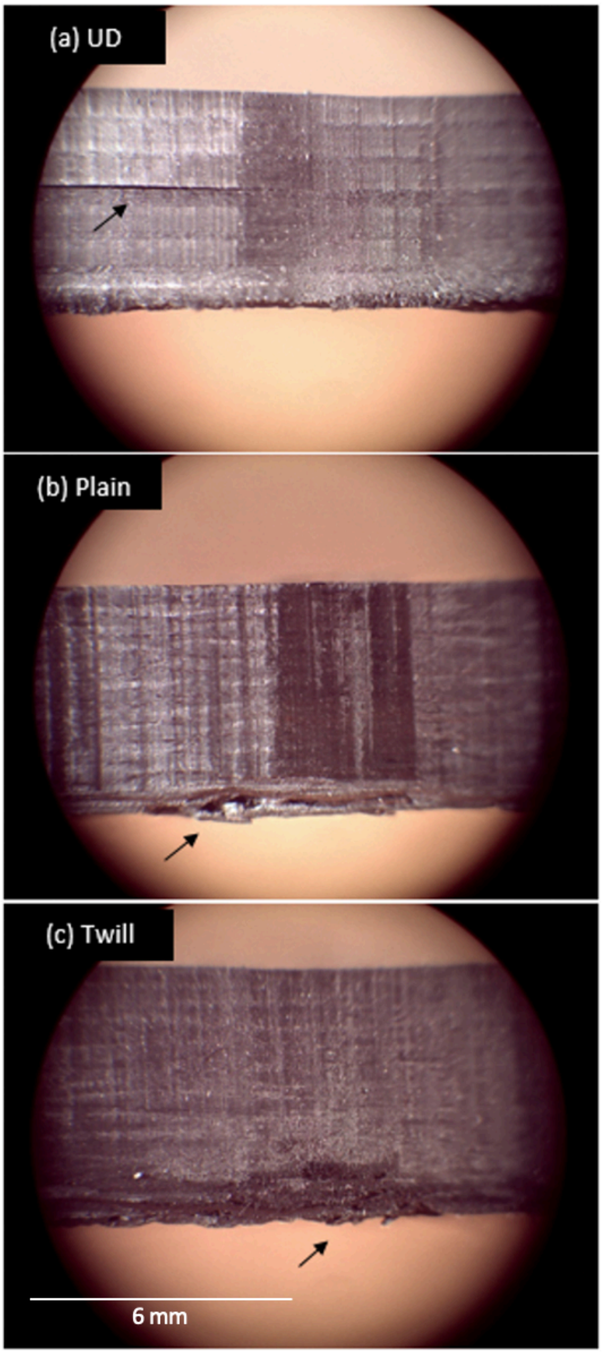

Figure 64: IDR specimens after 20J impact; images are showing the middle section of the specimen’s impact damage area.

4.3.3 Water diffusion

Figure 65 presents the mass change for UD, plain, and twill CFRP composites due to water exposure for 100 days, followed by 15 days of oven drying. It shows that the moisture uptake process follows a classical Fickian trend. The moisture uptake curves (Figure 65) illustrate a gradual moisture uptake at the initial stage until an equilibrium stage (saturation) is reached. The mass change curves then fluctuate with very minimal mass changes (upwards and downwards) indicating at the potential occurrence of degradation mechanisms taking place while moisture uptake continues within the structure (Grammatikos et al. 2015; Korkees et al. 2018b), leading to a fluctuation in mass changes. UD specimens reached a maximum value of mass change after 31 days of water immersion at 90°C. Plain and twill specimens reached their maximum values of mass change after 45, and 43 days of water immersion, respectively, as highlighted in Table 12. It is expected that the woven specimens would take longer times to reach maximum mass change due to higher V_m. However, given the fluctuation in mass observed in the ‘plateau’ region (Figure 65), taking the absolute maximum value of mass gain achieved as the point of saturation is somewhat arbitrary. Instead, the point of saturation has been taken as the point at which the rate of daily mass change becomes less than 1% of the total mass gain (taken as the absolute maximum recorded), with the assumption of that any less than 1% change of the total mass gain is the scatter within the mass measurements (ASTM International, 2014) (with the mass change values being very small at this stage). Figure 66 presents the rate of daily mass change as a percentage of total observed mass gain versus immersion time. In the case where sequential gravimetric measurements are taken more than one day apart the difference is divided by the number of days between measurements (to give a daily rate). This shows that UD and twill specimens reached their saturation stage after 16 days, whereas the plain specimens reached their saturation stage after 20 days. However, given that there were no gravimetric measurements collected between 17-20 days, it is possible that this could have occurred at an earlier point between 17-20 days. Lower masses than that of the original specimens were observed after oven drying (Figure 65) demonstrating that the specimens had reached their maximum moisture uptake (saturation) and subsequently the degradation of the matrix is dominant (Grammatikos et al. 2015).

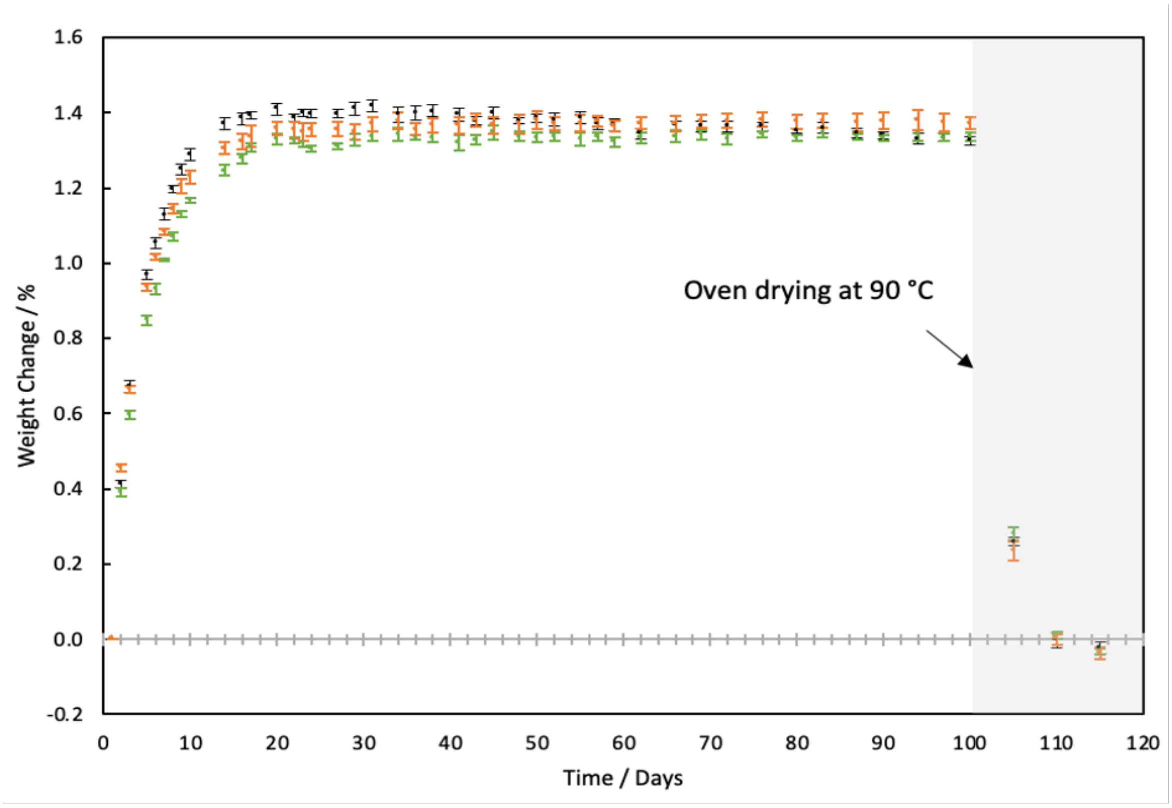

Figure 65: Water uptake for water diffusion experiment.

Table 12: Average mass change data observed for all fully exposed specimens.

Day (hours)	Mass Change (%)			Day (hours)	Mass Change (%)		
	UD	Plain	Twill		UD	Plain	Twill
1 (0)	0.000	0.000	0.000	43 (1008)	1.379	1.327	1.381
2 (24)	0.412	0.390	0.456	45 (1056)	1.400	1.348	1.366
3 (48)	0.672	0.595	0.664	48 (1128)	1.379	1.337	1.369
5 (96)	0.969	0.848	0.936	50 (1176)	1.384	1.335	1.381
6 (120)	1.054	0.931	1.017	52 (1224)	1.381	1.337	1.372
7 (144)	1.129	1.009	1.083	55 (1296)	1.387	1.330	1.371
8 (168)	1.197	1.070	1.144	57 (1344)	1.371	1.337	1.377
9 (192)	1.250	1.132	1.205	59 (1392)	1.368	1.323	1.364
10 (216)	1.289	1.167	1.229	62 (1464)	1.345	1.332	1.372
14 (312)	1.371	1.247	1.306	66 (1560)	1.366	1.337	1.371
16 (360)	1.384	1.278	1.322	69 (1632)	1.363	1.342	1.376
17 (384)	1.392	1.309	1.337	72 (1704)	1.363	1.330	1.379
20 (456)	1.410	1.330	1.359	76 (1800)	1.363	1.342	1.381
22 (504)	1.386	1.325	1.354	80 (1896)	1.352	1.332	1.376
23 (528)	1.400	1.318	1.349	83 (1968)	1.360	1.346	1.379
24 (552)	1.397	1.304	1.354	87 (2064)	1.345	1.337	1.374
27 (624)	1.397	1.311	1.357	90 (2136)	1.339	1.332	1.379
29 (672)	1.410	1.327	1.349	94 (2232)	1.331	1.339	1.381
31 (720)	1.418	1.337	1.369	97 (2304)	1.334	1.335	1.374
34 (792)	1.394	1.342	1.379	100 (2376)	1.326	1.337	1.372
36 (840)	1.400	1.335	1.357	105 ‘oven dried’	0.260	0.281	0.235
38 (888)	1.405	1.334	1.367	110 ‘oven dried’	-0.003	0.009	0.000
41 (960)	1.394	1.320	1.366	115 ‘oven dried’	-0.024	-0.033	-0.037

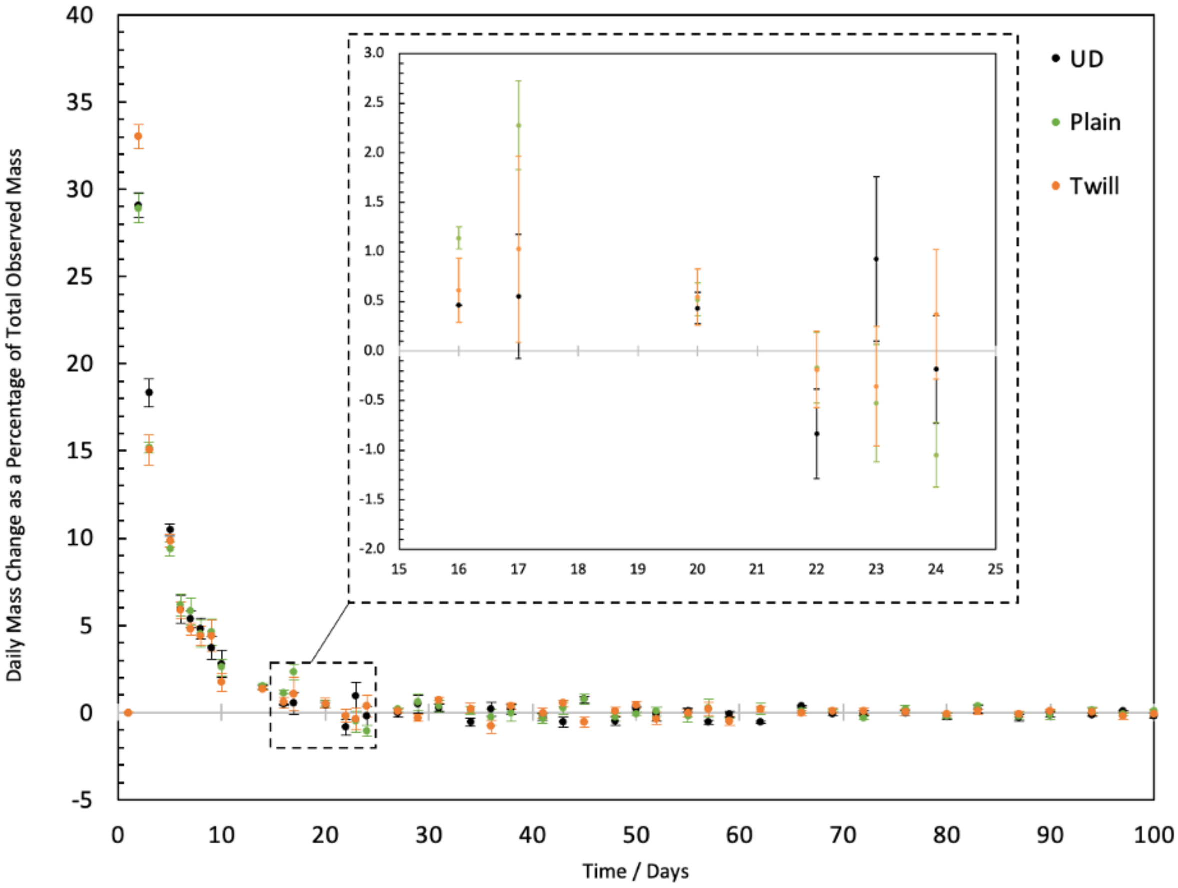

Figure 66: The rate of daily mass change as a percentage of total observed mass gain versus immersion time.

Table 13 presents $\sqrt{t_1}$, $\sqrt{t_2}$, M_1 at $\sqrt{t_1}$, and M_2 at $\sqrt{t_2}$ for the fully exposed specimens and the edges exposed ones.

Table 13: √t1, √t2, M1 at √t1, and M2 at √t2 for fully and edges exposed specimens.

Fibre type	$\sqrt{t_1}$	$\sqrt{t_2}$	Fully Exposed M_1 at $\sqrt{t_1}$	Fully Exposed M_2 at $\sqrt{t_2}$	Edges Exposed M_1 at $\sqrt{t_1}$	Edges Exposed M_2 at $\sqrt{t_2}$
UD (cross-ply)	√24	√96	0.412	0.969	0.381	0.857
Plain	√24	√96	0.39	0.848	0.356	0.792
Twill	√24	√96	0.456	0.936	0.325	0.774

From the observed data in (Table 12 and Table 13) and in order to calculate $D_{x,y}$, equation (4) can be used excluding the last dimensional factor as previously mentioned due to specimens being selectively exposed. The calculation of D_z is also feasible by subtracting M_1 at $\sqrt{t_1}$, and M_2 at $\sqrt{t_2}$ observed for edges exposed specimens from M_1 at $\sqrt{t_1}$, and M_2 at $\sqrt{t_2}$ observed from the fully exposed specimens. Figure 67 presents the directional diffusion coefficients observed in this study.

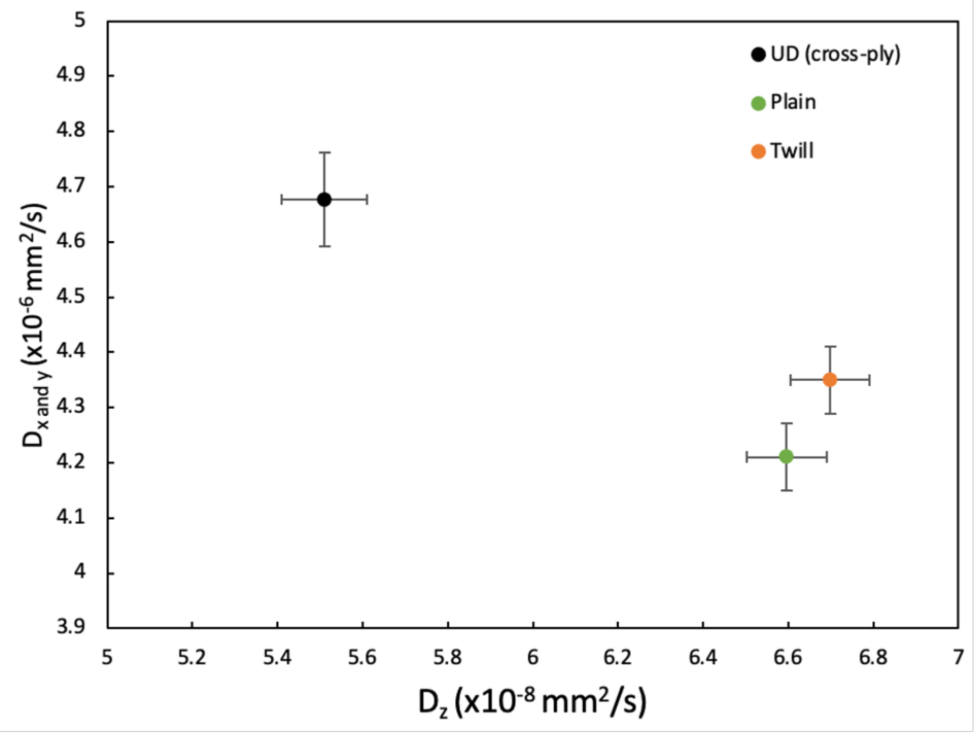

Figure 67: Water diffusion coefficients for UD, plain, and twill.

The trend in the D values suggests that the crimp pattern is playing an essential role in the differences observed. The UD showed 19.69% and 21.56% higher diffusion coefficients in the $D_{x,y}$ direction compared with plain and twill, respectively. This is likely due to a more direct penetration path along the fibre matrix interface as theoretically observed by Choi et al. (2001), and illustrated in Figure 68. UD showed 19.69% and 21.56% higher diffusion coefficients in the $D_{x,Y}$ direction compared with plain and twill, respectively.

The D_z direction is however lower in the UD by 9.98% and 7.01% as compared with plain and twill, respectively. As observed from the literature that the interfacial region is critical in the capillary process (Karmaker 1997; Espert et al. 2004), it is believed that the D_z is higher in the woven samples than the UD sample due to the fact that the weave pattern of the fibres in one ply is allowing easier transfer of water to the neighbouring fibres (through the crimp) allowing a faster water diffusion per ply set in the D_z direction. Unlike the UD where each fibre bundles are uniformly separated by the matrix from the D_z direction.

The SEM images in Figures 69-71 for dry and after 43 days of water immersion in the same moisture condition which show clear evidence of degradation and debonding of the fibre matrix interface, further demonstrating the role of the interfacial region in diffusion. Where the hydrothermal aging induces fibre/matrix interfacial debonding in aged specimens (Karbhari and Xian 2009) and leads to capillary transport, which accelerates diffusion and degradation. This supports the hypothesis that fibre architecture plays an important role in the moisture penetration mechanism of CFRP materials. From these results it is clear that the interfacial region is critical in terms of diffusion rates, this also corresponds to the elements involved in the interfacial region such as the fibre architectures and the fibres sizing. It is crucial to highlight that further investigation using equivalent matrix volume fractions and fibre sizing levels would help to further isolate this effect and clarify its significance. It is also worth highlighting that the SEM images presented in (Figures 69-71) with the type of water being used here is purified water showed no clear evidence of matrix cracking as compared with the SEM images observed in (Figures 48-58) further demonstrating the finding that the mineral content attained in the type of water used for the previous experiment are believed to have caused the deposition of salts and the cracks are conceivably on the surface of the salts.

As observed from literature regarding the use of Fick's law to predict the water ingress in fibrous/polymeric composites, it is well understood that differences in D values can be attributed to the differences in test methodology, as well as the assumptions involved in the mathematical and experimental approximation employed for their determination (Grammatikos et al. 2015). These assumptions are essential for instance in this study to produce D values that allow comparison between the different fibre architectures in order to better understand their behaviour of different fibre architectures. With the use of Fick's law, there are still concerns and limitations in the prediction of moisture into composite materials. For instance, temperature is not part of Fick's law predictions; however, a significant effect on the D values were observed in a study, the higher the temperature, the greater the D obtained (Shi 2007). Therefore, these D values for a specific material are associated with the temperature that they have been exposed to. The microdamage that exist in composite structures is also a concern that is not considered when calculating the D values. It has been reported in other published experiments that the measured diffusivities of carbon epoxy composites with long histories of exposure to sea water or to distilled water are higher by 35%-62% than the expected values. It was claimed that the considerable increase of the diffusivity had caused microdamage in the composites, creating more channels of water penetration (Mazor et al. 1978). In addition, debonding (consequence of material damage) enhances moisture penetration by capillary flow along the interface (Field and Ashbee 1972). As a consequence, a scale transition model accounting for damage occurring in such fibre/epoxy composites is required (Youssef et al. 2009). This leads to the conclusion that the variety of experimental research taking in consideration all the limitation aspects of Fick’s law with key parameters such as geometry, fibre orientation, temperature, and the type of constituent contents (i.e., the reinforcement type, and the polymer type) could support the development of modelling approaches to predict moisture ingress into composite materials.

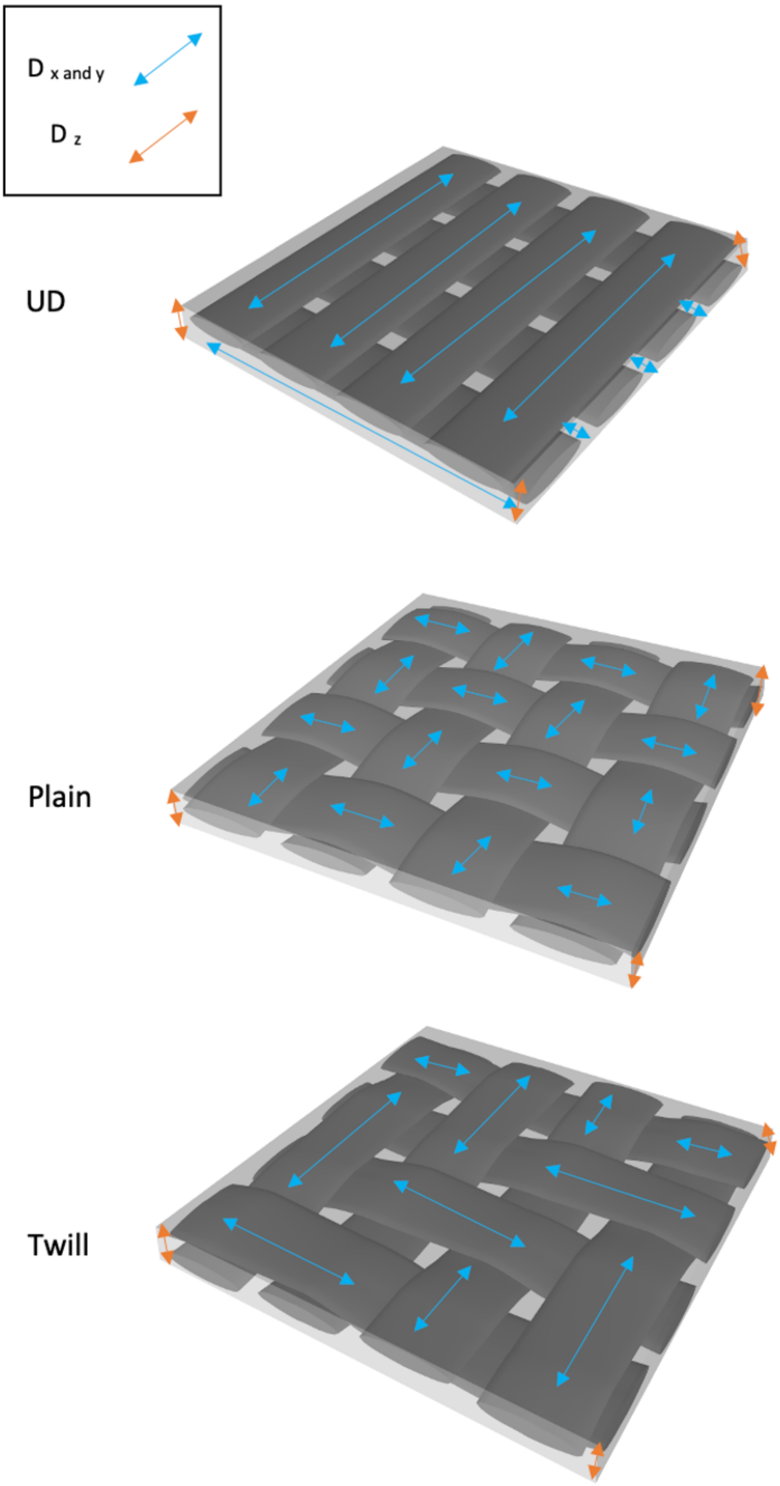

Figure 68: Penetraion paths in different fibre architectures, 3D image was produced using TexGen Software (Brown and Long 2021).

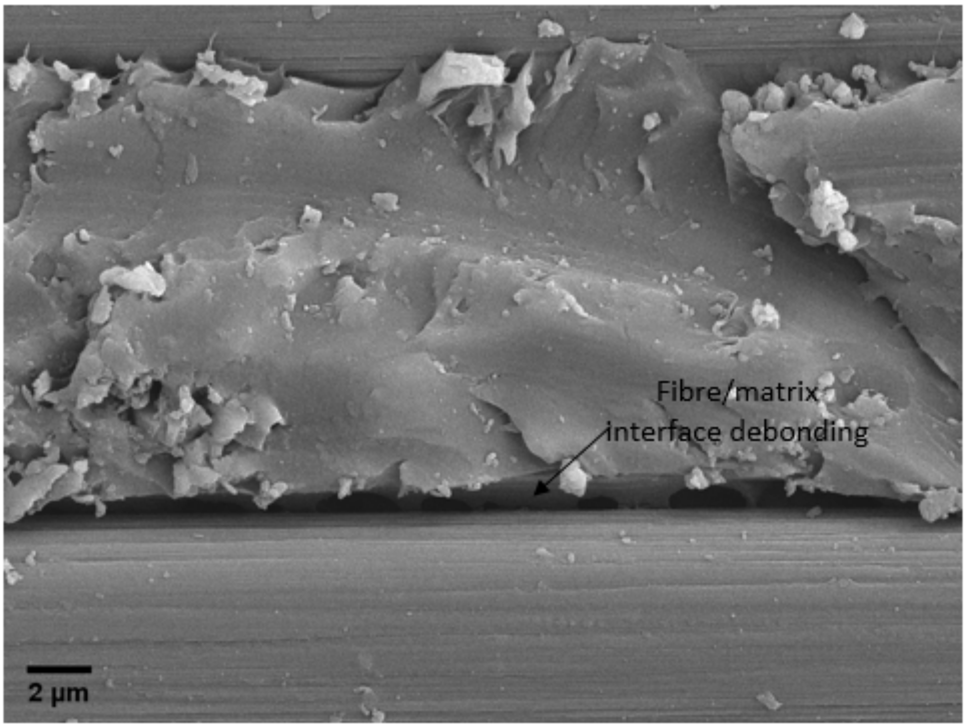

Figure 69: Debonding in a UD specimen after 43 days of water immersion in purified water at 90°C.

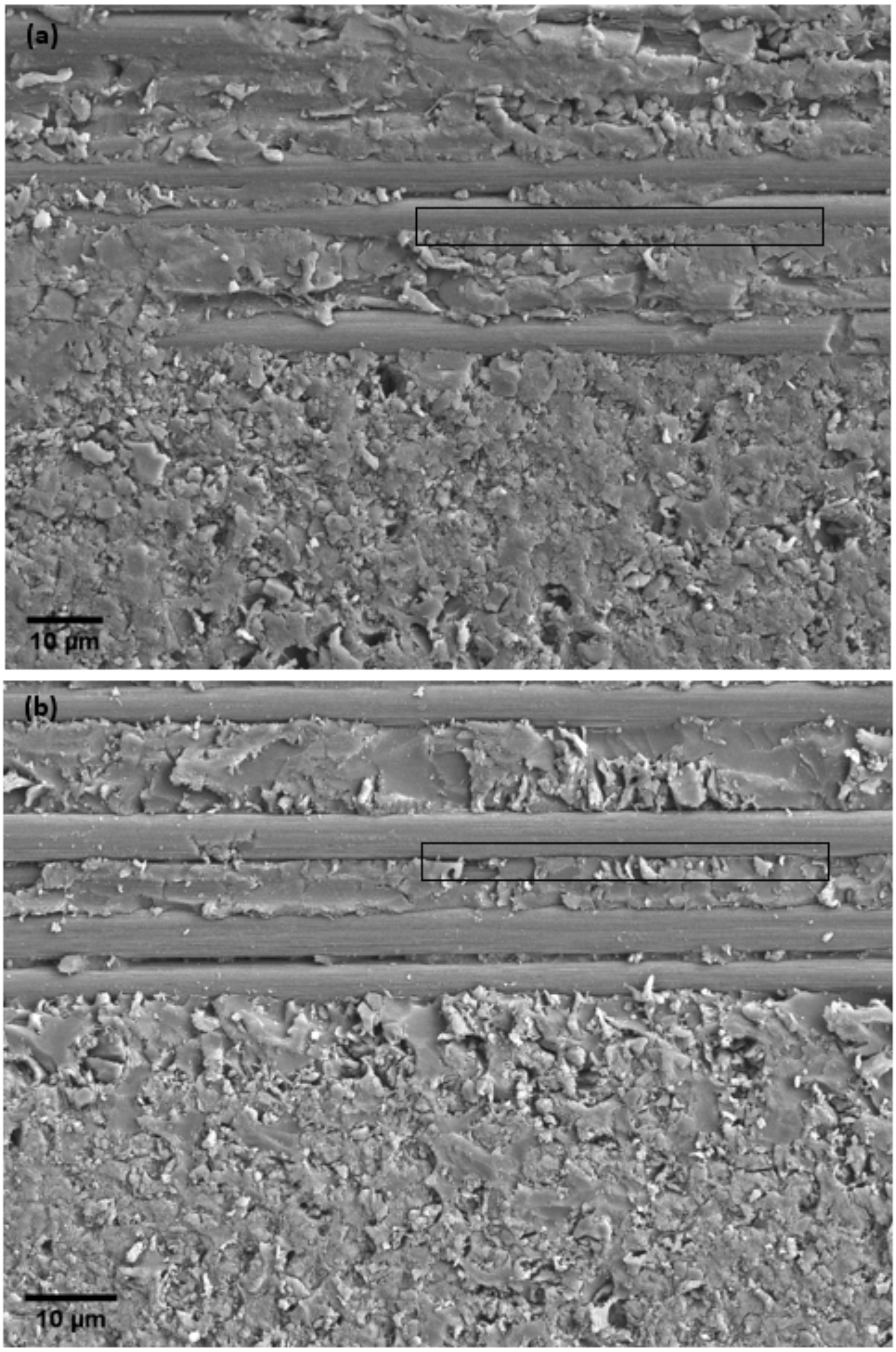

Figure 70: SEM comparison images of; (a) dry, (b) after 43 days of water immersion in purified water at 90°C.

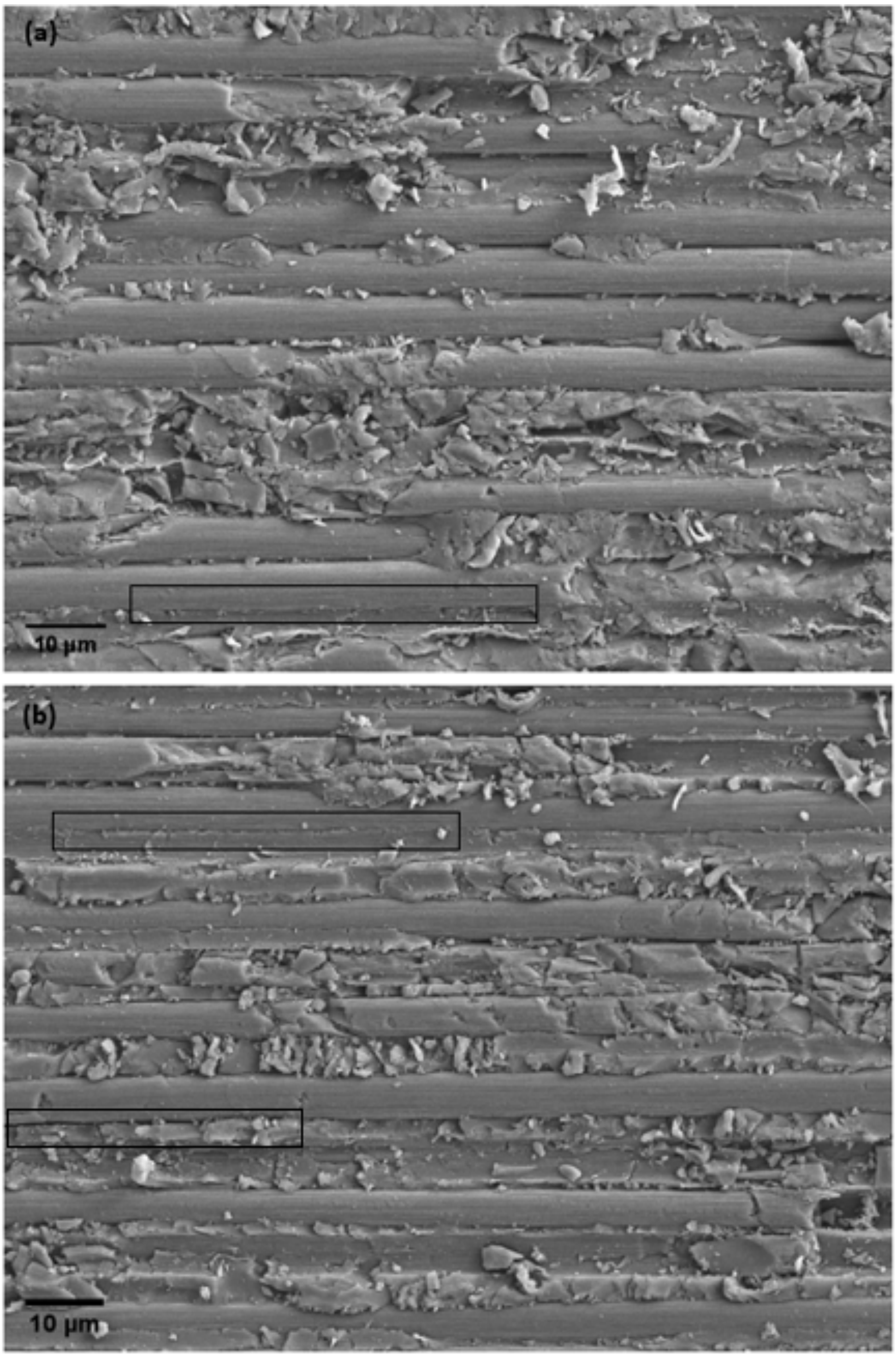

Figure 71: SEM comparison images of a 90° layer; (a) dry, (b) after 43 days of water immersion in purified water at 90°C.

4.4 Conclusions

The moisture absorption behaviour in CFRP composites and the role of fibre architecture in this process have been investigated in this chapter. Unidirectional CFRP showed higher mass change due to water absorption compared with plain and twill weave CFRP composites, this behaviour was correlated to a larger surface area to volume ratio due to the differences in ply thickness and the different geometrical aspects (surface area to volume ratio) between SBS, CLC, and IDR specimens have further demonstrated this finding. The void volume fraction seems to be too small to cause clear influence on the differences in mass change. This suggests that the use of other fabrication methods may increase the void volume, which can result in the moisture behaviour; therefore, it is essential to further understand that to what void content the moisture behaviour remains consistent. The fibre architecture was found to have an essential role on the damage type observed after impact, which therefore influences the water absorption rates. As a result of the greater extent of surface damage and through thickness damage observed at 70J impact energy, 2D woven specimens exceeded the unidirectional specimens' water absorption rates.

An experimental method was also developed to calculate the diffusion coefficients, with the use of Fick's law, to obtain comparative D values for edge ($D_{X,Y}$) and through the thickness (D_z) diffusion between the different fibre architectures in CFRP composites. A clear correlation between crimp pattern and diffusion rate was observed. Higher diffusion coefficients were observed for UD architecture compared with the woven architectures, where a more 'tortuous path' for capillary transport along the woven fibres is believed to slow the water penetration process. UD showed 19.69% and 21.56%

higher diffusion coefficients in the $D_{x,Y}$ direction compared with plain and twill, respectively. The D_z direction is however lower in the UD by 9.98% and 7.01% as compared with plain and twill, respectively.

Even though the UD material featured slightly lower levels of sizing (1% versus 1.2%) and resin content (33% versus 40%) the observed trends are still clear in the woven materials, which had identical constituent properties. The differences in diffusion coefficients are large enough to suggest that the fibre architecture is having a significant influence on moisture penetration mechanisms (particularly considering that the lower matrix volume fraction in the UD material would likely lead to lower moisture uptake). This could prove to be important for mechanical property retention in moist environments and a consideration when selecting materials for use in such environments.

5 Effects of Moisture Absorption on the Mechanical Properties of Unidirectional and 2D Woven CFRP Composites

5.1 Introduction

This study aims at further understanding the consequential reduction in strength that corresponds to each fibre architecture due to moisture absorption. Materials with three different fibre architectures are investigated. Properties with a dependency on matrix and interface properties are investigated, compression, short beam shear, and impact resistance are considered. Clear differences are identified, and the mechanisms are discussed within this chapter (Almudaihesh et al. 2020).

5.2 Methods

For the compression, short beam shear, and impact resistance, the methods in Sections (3.5 Compressive characterisation, 3.6 Shear characterisation, and 3.7 Impact damage characterisation) were applied. This was achieved by mechanically testing the specimens following the water uptake experiment from Chapter 4.

5.3 Results and discussion

The results of compressive strength achieved by CLC testing are presented in Figure 72. In the case of the un-aged samples the UD fibre architecture exhibits the highest strength, followed by the twill weave and then the plain weave. As compressive failures are initiated by microbuckling of the fibres it makes sense that the strength would reduce in this way, because the fibres are misaligned in the woven architectures with the plain weave having the greatest misalignment along with the fact that Pyrofil TR50S

(UD) featured slightly higher tensile strength compared with Pyrofil TR30S (woven). The moisture absorption process in the aged specimens induces plasticisation of the matrix, along with microcracking, which reduces the support of the fibres (Selzer 1997; Vanlandingham et al. 1998; Torres et al. 2000; Li et al. 2003). Hence, a reduction in strength is observed in all aged specimens, however, the magnitude of the reduction varies greatly. The woven architectures exhibit much smaller reductions in strength, because the distorted fibres already have a propensity to buckle, particularly in the case of the plain weave where a negligible reduction (1.34%) is seen. The reduction increases to 7.5% for the twill weave where the straighter fibres rely more on the support of the matrix to resist buckling. The largest reduction is seen in the UD material at 14.6% where the straight fibres require good support of the matrix to carry higher stresses and therefore fail at much lower loads in the aged samples (Gao et al. 2004; Martin 2008; Ma et al. 2014).The occurrence of microbuckling in UD fibres is usually preceded by either local matrix yielding or debonding of the fibre-matrix interface (Agarwal et al. 2006). This correlates to the greater mass gain as a percentage of matrix content observed in the UD samples (Table 11), which suggests either greater plasticisation or interface degradation has occurred and would therefore promote an earlier failure in these samples. The lower level of fibre sizing in the UD samples could also exacerbate this behaviour. Importantly the reduction in strength of the aged UD material is significantly large that it becomes weaker than both of the woven fibre architectures in an aged condition. This has great significance when considering material selection and safety factors for carbon fibre composites operating in moist environments. This corresponds to the observed failure modes in Figure 73 where the relative ease of microbuckling induced failure in the plain weave samples leads to a through thickness crack in the un-aged samples. Conversely significant brooming is seen in the failure for the un-aged UD samples, whereas the twill weave samples exhibit both brooming and through thickness cracking. After aging all samples exhibited significantly less interlaminar cracking / brooming, which corresponds to the increased ductility and toughness of the matrix (Hunkley and Connell 2012). The aged UD samples exhibited mostly through thickness cracking with a significant reduction in the presence of any brooming, due to the premature microbuckling of less well supported fibres. The aged plain weave samples exhibited the same through thickness cracking mechanism. The aged twill weave samples exhibited more through thickness cracking with much less brooming and interlaminar fracture observed. It is noted that all failure modes observed were deemed acceptable in accordance with those reported in ASTM D 6641-16. It is also believed that in the case of woven specimens, the weave pattern is providing a support to the neighbouring plys which indicates to less dependency on the matrix as compared with UD and therefore, less reductions in strength is observed after aging for the woven specimens as compared with UD.

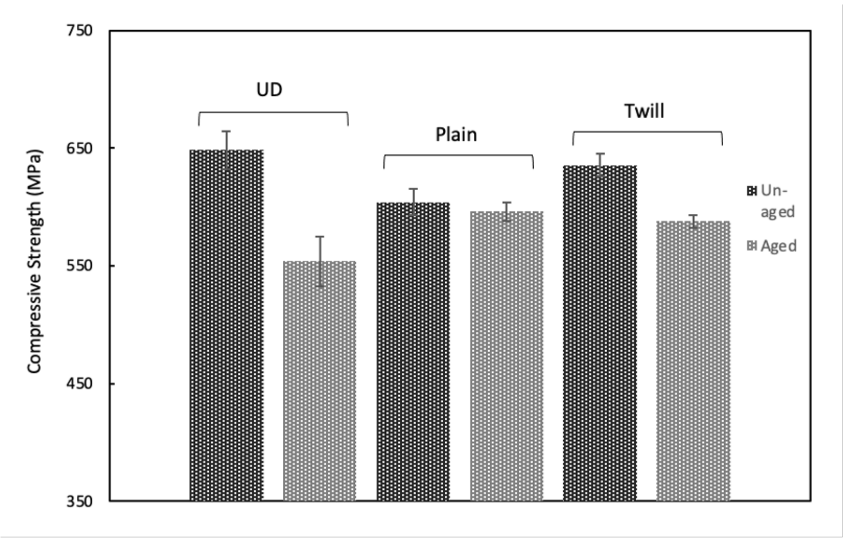

Figure 72: Compressive strength for un-aged and aged CFRP specimens.

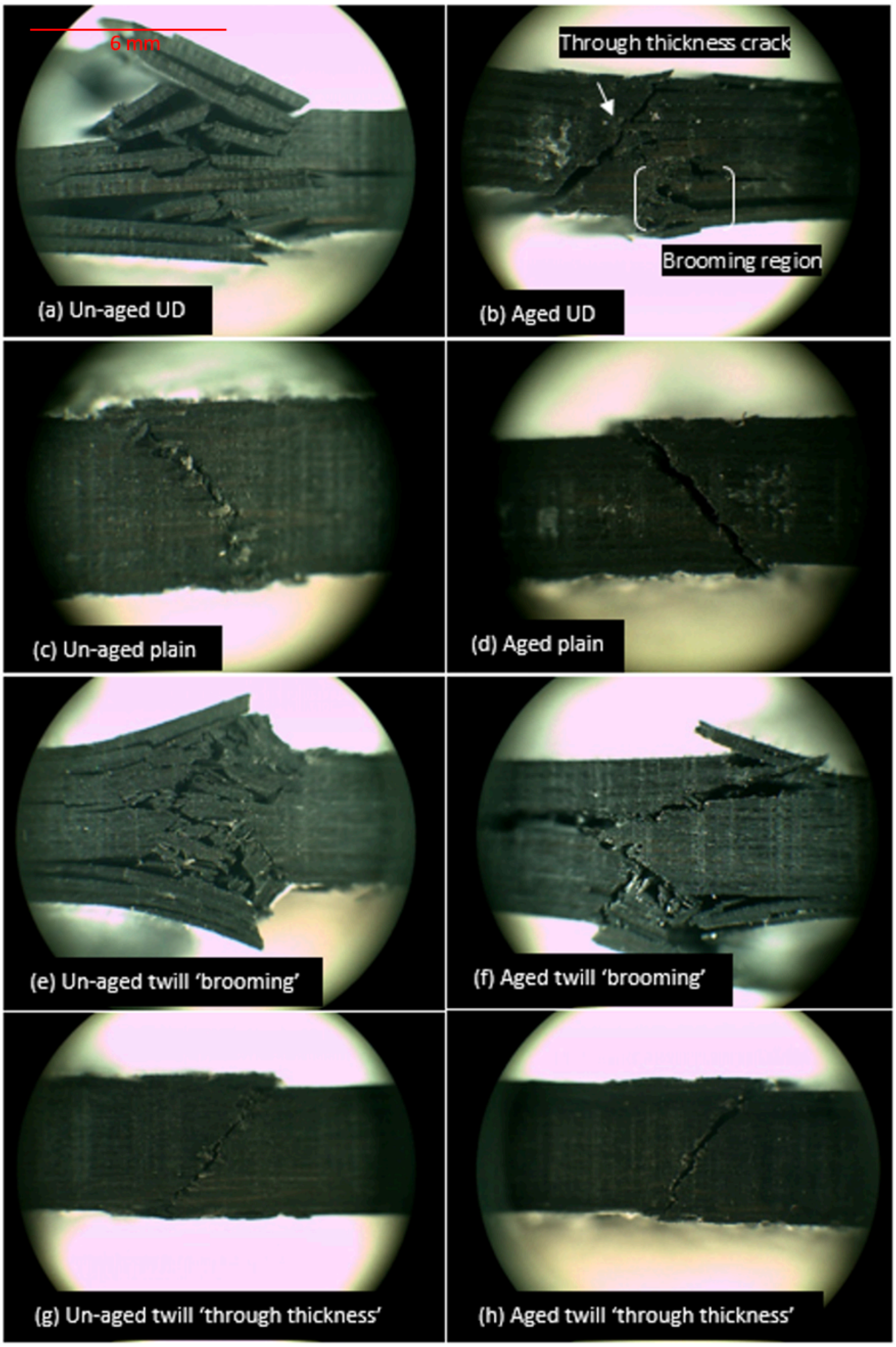

Figure 73: CLC specimens after failure; images are showing the middle section of the specimen's impact damage area.

The short beam shear strength of the materials are presented in Figure 74 where the woven architectures exhibit the highest un-aged strengths, with the through thickness shear stresses that develop from alternating 0,90 layers leading to failure initiation at a lower stress in the UD samples. This type of interlaminar shear failure is dominated by matrix properties and the fibre-matrix interface strength and hence a corresponding reduction in strength is seen in all cases for the aged samples. This results from the degradation of the fibre-matrix interface (seen in the SEM Figures 48-58) allowing the easy initiation and propagation of interlaminar shear cracks. A single delamination along the longitudinal axis and near to the mid-plane was observed for all un-aged UD specimens, with more than one delamination observed in all aged UD specimens as seen in Figure 75. Similar behaviour was observed for woven specimens with a single longitudinal crack near the mid-plane in the middle section of the specimen in the un-aged specimens, with more than one longitudinal crack observed in all aged woven specimen and can be seen in Figure 76 and Figure 77. The longitudinal cracks; however, in woven specimens did not grow into delamination along the longitudinal axis due to the weave structure that eliminated the cracks to grow into delaminations as observed in the UD specimens.

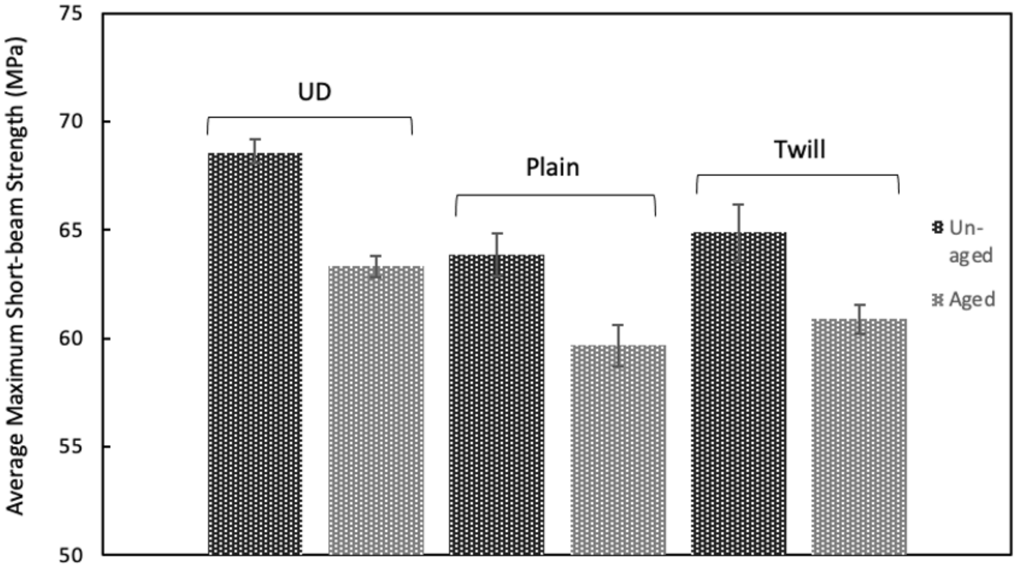

Figure 74: Short-beam properties for un-aged and aged CFRP specimens.

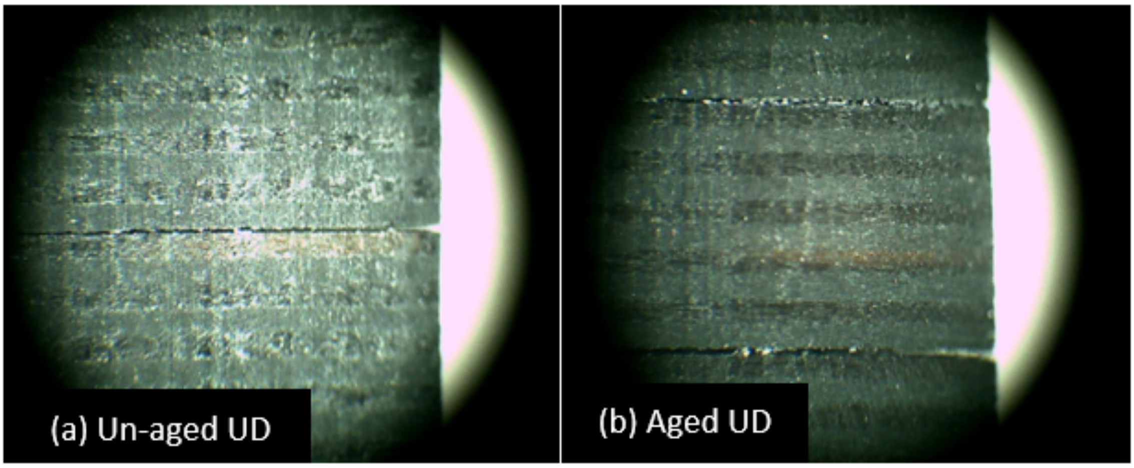

Figure 75: Failure modes of SBS UD specimens, the side edge of the specimens.

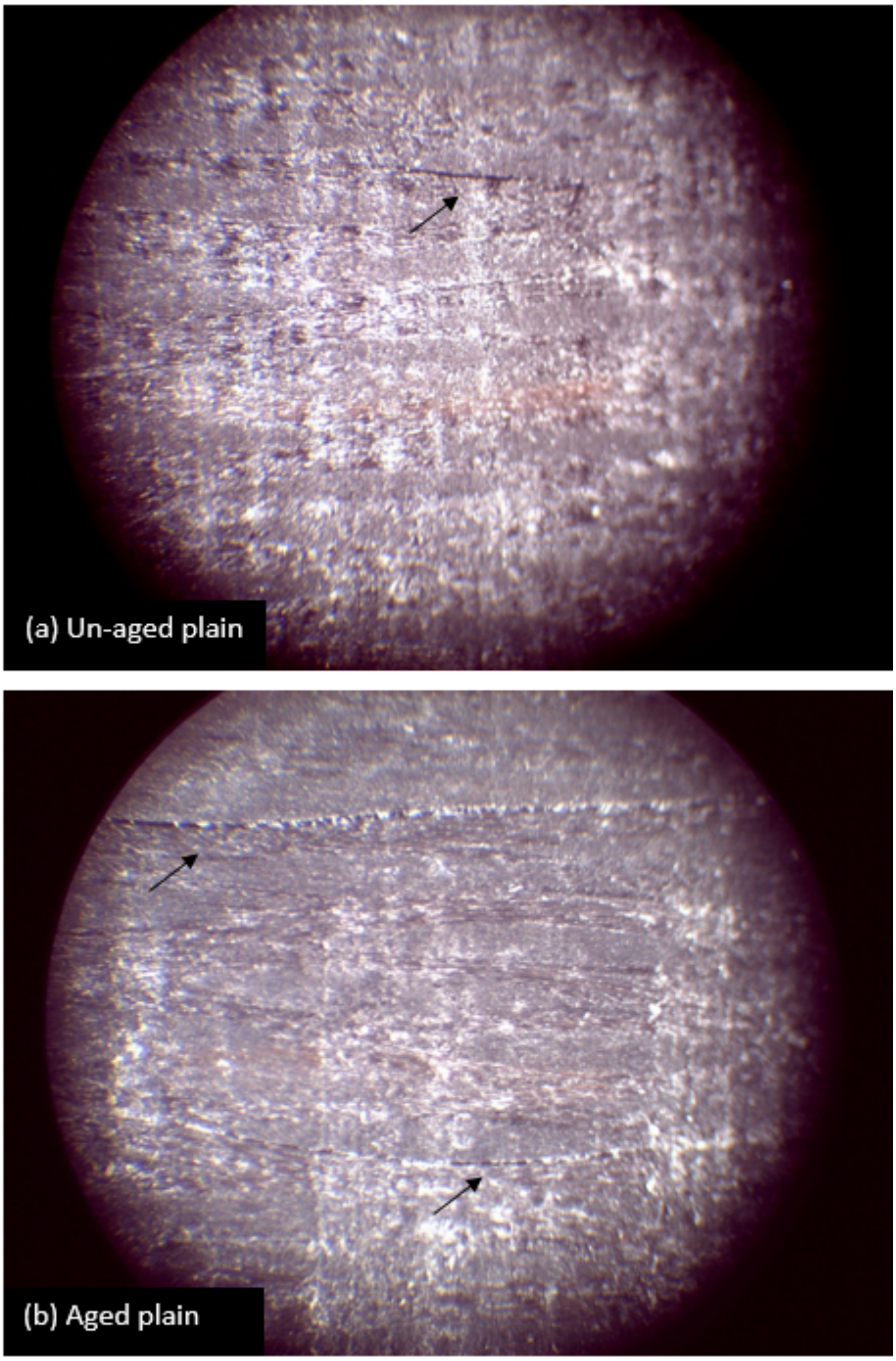

Figure 76: Failure modes of SBS plain specimens, near the mid-plane in the middle section of the specimen.

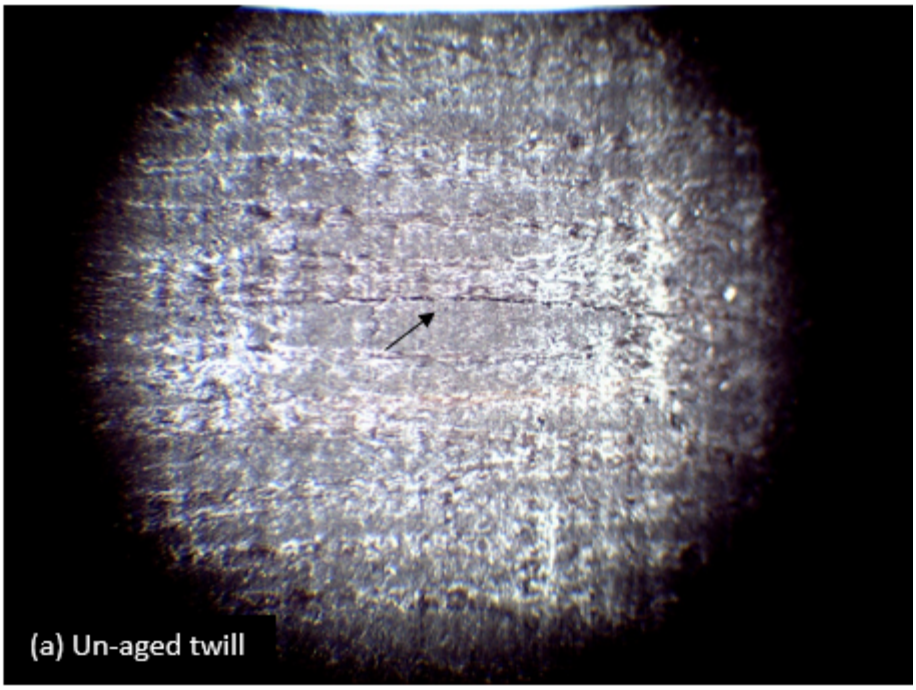

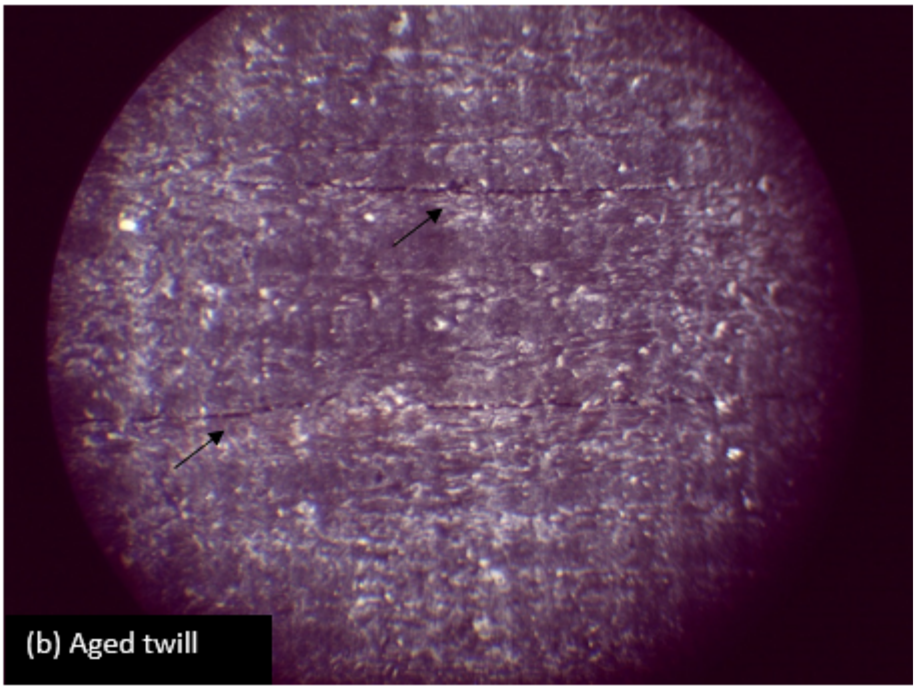

Figure 77: Failure modes of SBS twill specimens, near the mid-plane in the middle section of the specimen.

The influence of moisture absorption on impact damage resistance was investigated by comparison of 70J impacts prior to aging and after aging. Table 14 shows average area of damage determined by ultrasonic C-scanning.

The most linear fibres which is the UD specimens showed the highest area of damage after impact followed by the twill weave which feature a linearity that sits between UD and Plain (Figure 68). It is seen that the average damage area is smaller in aged specimens; however, the changes are very minimal particularly when considering the standard deviations. Therefore, it is difficult to draw conclusions on the fact that the damage area of aged samples is smaller than the dry due to the ductility of the matrix from the observed data. The damage size in woven materials is limited by the extent of longitudinal splitting that can occur in each ply. The woven structure means that long splits cannot form and subsequently grow in to delaminations, as much as they do in UD materials. The cross-sectional micrographs in (Figure 63) show that there is a change in the damage formation in woven materials with fewer interlaminar cracks observed along the through thickness damage (corresponding to increased matrix ductility and toughness). The reduction in interface strength in the aged UD material leads to a greater number of interlaminar cracks (delaminations) that spread over a larger area. This is in agreement with failure observed in the aged SBS UD specimens, demonstrating several longitudinal cracks Figure 75. This further suggests that the woven fibre architectures perform better in an aged condition compared with UD fibres. The smaller damage area observed for woven specimens across all damage levels supports the hypothesis observed in the CLC tests where the weave pattern is providing a support to the neighbouring plys even in stress transfers which also in return translated to larger through thickness damage for woven specimens (Figure 63).

Table 14: The average damage area observed from C-scan images (images presented in Appendix B)

Impact Type	Damage Area (mm^2)		
	UD	Plain	Twill
20J before water immersion	$1478.2^{\pm 32.9}$	$370^{\pm 15.4}$	$816^{\pm 59.0}$
70J before water immersion	$6336.4^{\pm 287.3}$	$798^{\pm 125.4}$	$1067.8^{\pm 24.8}$
70J after water immersion	$6320.4^{\pm 226.8}$	$688^{\pm 26.9}$	$1005.6^{\pm 66.8}$

5.4 Conclusions

The role of fibre architecture in the loss of mechanical properties by environmental degradation has been investigated for carbon fibre reinforced epoxy materials. Whilst the degradation process only takes place in the matrix, the fibre architecture has been shown to influences how failure occurs and how the failure mechanisms change when the matrix degrades. This affects the residual strength of the materials and is therefore a key parameter for materials performance in moist environments. More significant reductions in the mechanical properties were observed in UD specimens after aging, when compared with woven equivalents. In particular, the loss of compressive strength in aged UD materials is large enough (14.6% compared with 1.3% and 7.5% for the plain and twill architectures, respectively) that its residual strength was below that of both woven architectures. This coupled with the lower un-aged interlaminar strength that suffered a larger percentage reduction of 7.8% compared with 6.7%, and 6.5% for plain and twill architectures, respectively, means the UD architecture also demonstrated less resistance to impact damage.

It is feasible then, that under exposure to moist environments in matrix dominant properties, a material with a woven fibre architecture might outperform a UD material, which is often considered superior. In fact, the UD was superior only in the un-aged condition in this work. This highlights that a better understanding of the role of fibre architecture in the failure of aged CFRP materials is needed and that care should be taken in selecting materials and applying safety factors for such applications. Designers should also bear in mind that the optimum material/design for an application may not be the most intuitive choice based on un-aged properties.

6 An assessment of the effect of progressive water absorption on the interlaminar strength of unidirectional CFRP using Acoustic Emission

6.1 Introduction

The interlaminar shear strength is often a limiting factor of fibrous-polymeric composites (Chandrasekaran et al. 2011). The in-plane properties of the laminate depend primarily on the fibres whereas the out-of-plane (through the thickness) properties such as SBS, historically referred as interlaminar shear strength (ILSS) depend largely on the polymeric constituents of the composite (Hull 1994). The interfacial fibre-matrix properties are also a key factor due to the fact that load on the composite is transferred from the matrix to the fibres through the interface; hence fibre-matrix interfacial shear strength can affect the toughness and strength of the composite (Dirand et al. 1996; Zhang 2000). Therefore, moisture conditions will most likely result in changes on the mechanical properties of the matrix and/or the interfacial properties between the fibres and the matrix (Alam et al. 2018). A consistent and significant loss of SBS is seen and reported in the literature of this thesis for CFRP specimens after moisture exposure (Kafodya et al. 2015; Meng et al. 2015). Cysne Barbosa et al. (2017) reported that there was a drop in CFRP composites' SBS values after water absorption and the aged specimens showed a sharp drop in applied load from the load-versus-displacement graphs, followed by its further increase until the final failure is observed. The authors suggested that this behaviour to the potential formation of microcracks in the composites, this chapter further investigates this behaviour. In addition, this chapter studies the evolution of damage mechanisms in CFRP material following water immersion for increasing durations. It focuses on the matrix dominated property of interlaminar strength; additionally, examination of load history, in-test fracture imaging and representative AE features provided a detailed understanding of the change in failure behaviours that occur (Almudaihesh et al. 2021). Therefore, this work reflects on the understanding of the effects of gradual water absorption on the delamination resistance of fibrous/polymeric composites. It also explains, from a micro-scale perspective, the fracture mechanism observed prior to final fracture and provides an overall evaluation of the SBS testing method with the use of non-destructive test (NDT) techniques.

6.2 Methods

6.2.1 Materials and testing

The 15k unidirectional (UD) Pyrofil TR50S high strength carbon fibre 200gsm with 33% Skyflex K51 epoxy resin content was used in this study due to their current high usage in aerospace, energy, and automotive industries (Hexcel 2013). Large panels (110mm by 100mm) consisting of 30 plies (5.77mm thick) with a layup of $[0/90]_{15}$ were prepared. The stacking sequence was implemented to simplify the damage mechanism by excluding additional fibre directions and to avoid symmetric plies in the mid plane. For this study, and to understand the interlaminar damage mechanism and the role of moisture absorption, the SBS test was applied with the same method detailed in chapter 3 (3.6 Shear characterisation).

The handling of the water absorption testing in this section was exactly the same as that used for the water diffusion experiment chapter 4 (4.2.3 Water diffusion). In this study, specimens were only exposed for 43 days from which their fracture behaviour was monitored after 3, 9, 24, and 43 days of water immersion.

6.2.2 Optical measurement and AE approach

The methods of optical measurement and AE techniques used in this study are those detailed in chapter 3 (3.11 Optical measurement) and (3.12 Acoustic Emission), respectively.

For the VSG, in order to observe where the maximum shear strains are, the Imetrum 2D shear strain map function was employed (by monitoring the shear optical displacement) with the settings shown in Figure 78, which is found represent clear shear mappings for the selected test set up.

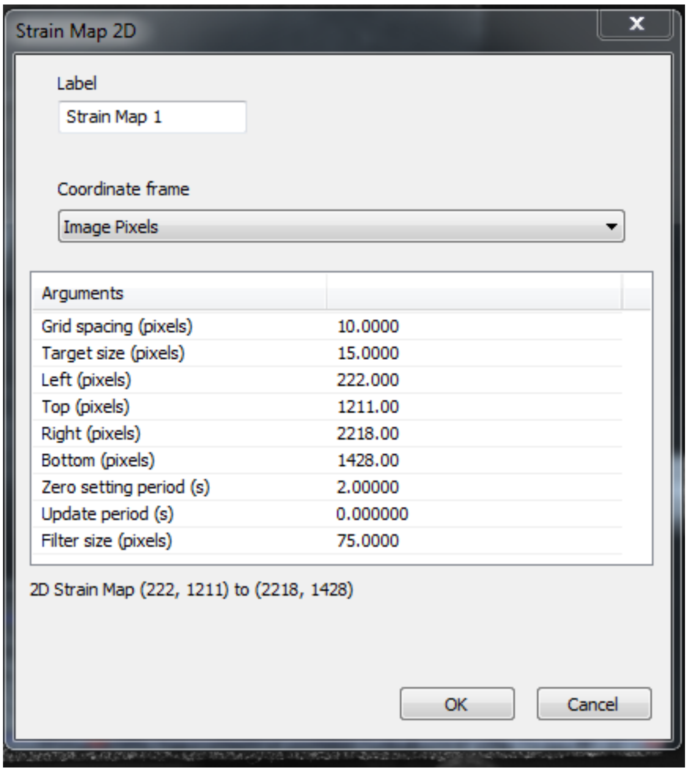

Label

Strain Map 1

Coordinate frame

Image Pixels

Arguments	
Grid spacing (pixels)	10.0000
Target size (pixels)	15.0000
Left (pixels)	222.000
Top (pixels)	1211.00
Right (pixels)	2218.00
Bottom (pixels)	1428.00
Zero setting period (s)	2.00000
Update period (s)	0.000000
Filter size (pixels)	75.0000

2D Strain Map (222, 1211) to (2218, 1428)

Figure 78: 2D shear strain mapping setting set up.

This was applied to all specimens used in this chapter in order to monitor the shear strain behaviour in the dry and after 3, 9, 24, and 43 days of water immersion.

6.3 Results and discussions

Figure 79 shows the mass gain resulting from water immersion and the consequential reduction in SBS. The mass change follows an expected trend of weight gain until a saturation state is reached after approximately 35 days, and the SBS is seen to correspondingly reduce with the increase of immersion times (Grammatikos et al. 2015; Cysne Barbosa et al. 2017). Carbon fibres in CFRP composites are very resistant to water swelling and do not absorb water (Vasiliev and Morozov 2007); thus, the reduction in SBS is believed to be due to plasticisation of the matrix, along with microcracking and interfacial degradation, induced by the moisture absorption process in the aged specimens, which, therefore, reduces the fibre supports, further demonstrating the role of polymers within the composite structure after aging (Selzer 1997; Vanlandingham et al. 1998; Li et al. 2003; Ray 2006; Vasiliev and Morozov 2007; Dao et al. 2010; Hunkley and Connell 2012).

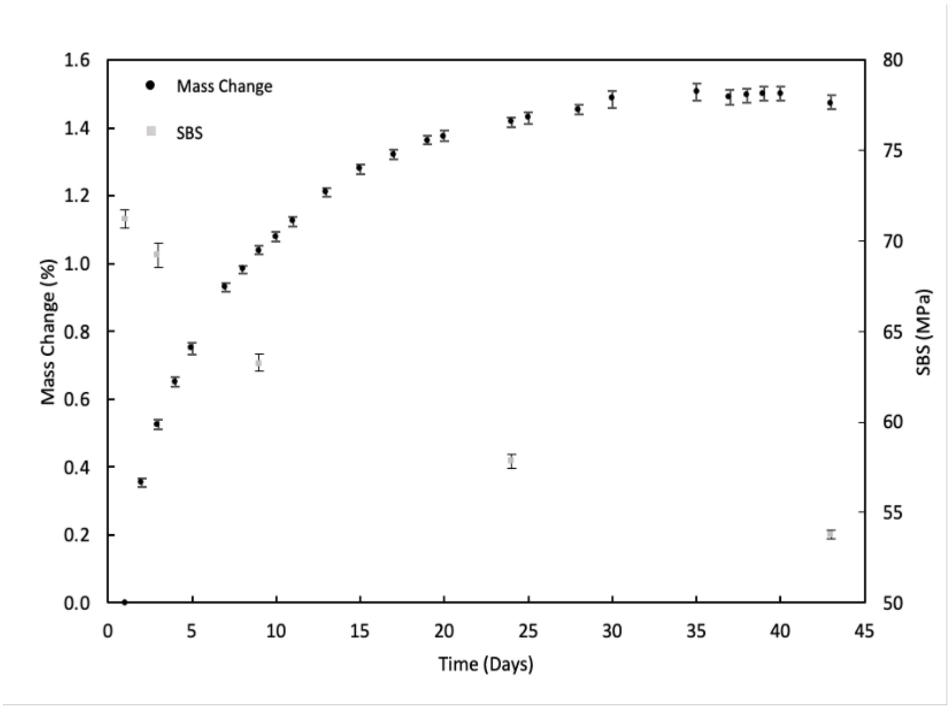

Figure 79. Water absorption versus SBS.

Figure 80 shows the SBS versus displacement curves for all specimens. As observed in the literature, two expected behaviours are seen: higher strain at lower SBS for aged specimens and a drop in the applied load from the load versus displacement followed by its further increase until the final failure. To further understand these two known findings, AE, optical measurements and microscopy will be used for the analysis.

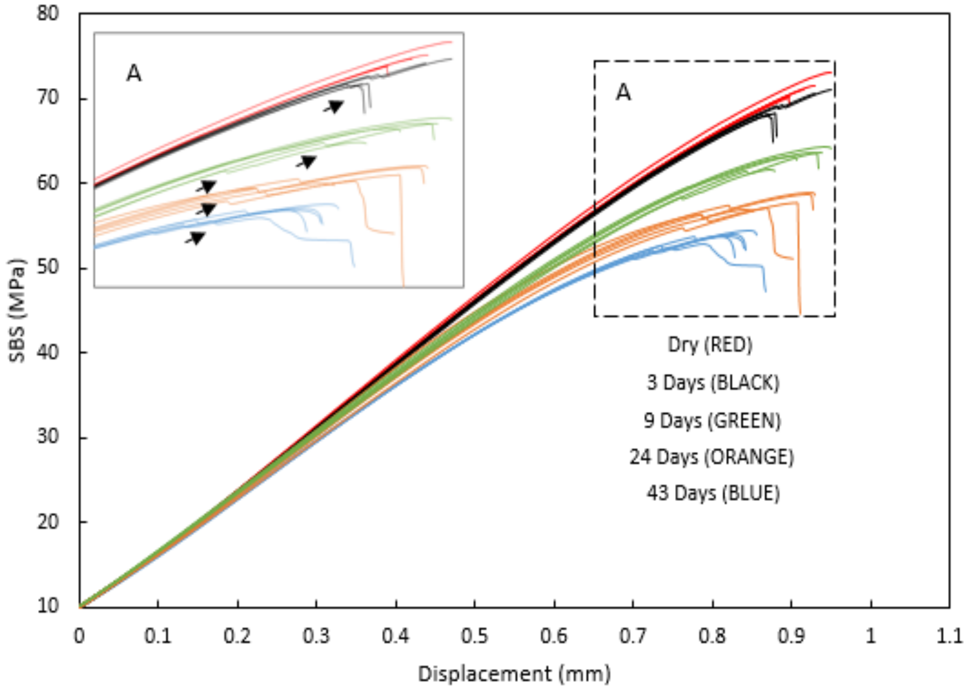

Figure 80. SBS versus displacement curves for all specimens.

In (Figure 80), the modulus is seen to reduce, and the curves become more non-linear (evidence of yielding in the matrix) as immersion time increases. As the carbon fibres are not affected by moisture, this confirms the plasticisation of the epoxy matrix due to moisture ingress, as expected. Figure 81 shows 2D DIC strain maps of a representative specimen at 40 MPa SBS. The colour contours represent shear strain, and a symmetric behaviour is seen in the specimen, with higher strains observed at the mid-plane. The shear strain is seen to increase with immersion time as the matrix properties degrade, which corresponds to the behaviour seen in the SBS versus deflection curve (Figure 80). Figure 82 shows the cumulative counts from the AE data versus time (one representative specimen is shown for each aging category, and AE results for all remaining specimens are presented in the appendix D). The higher shear strain seen in aged specimens (Figure 81) is believed to have led to more crack formation at this point, which is demonstrated by higher AE cumulative counts (Figure 82).

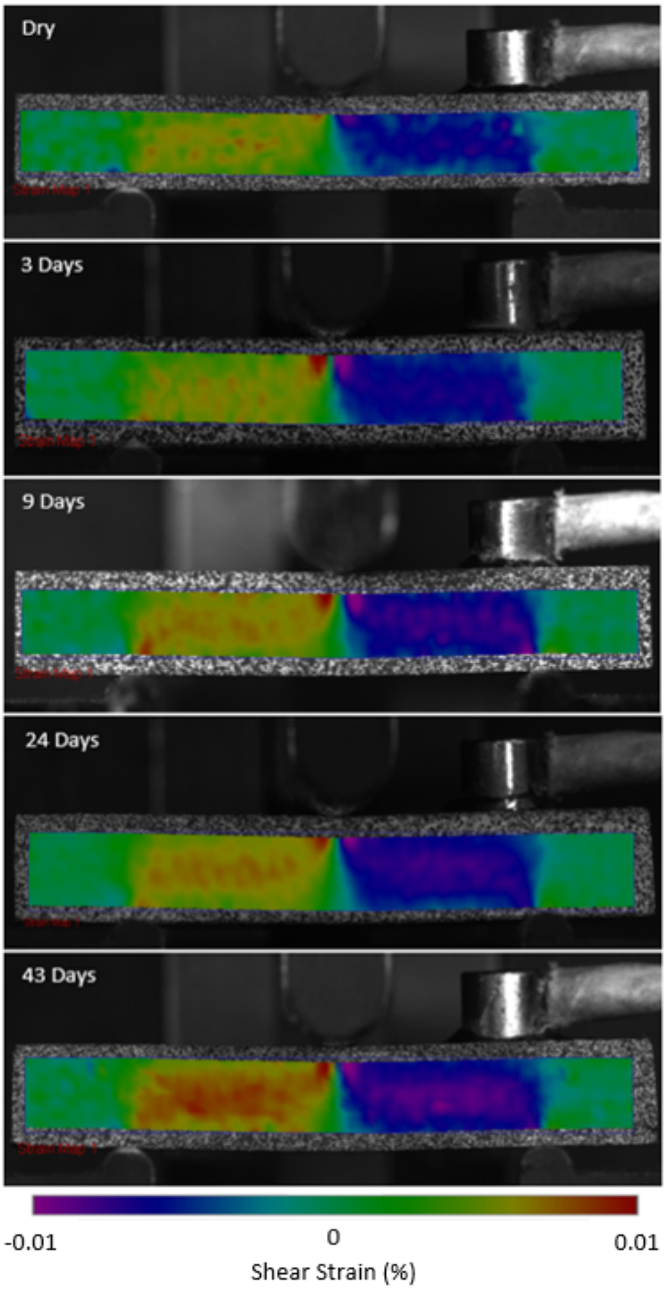

Figure 81. 2D shear strain maps observed at 40MPa SBS.

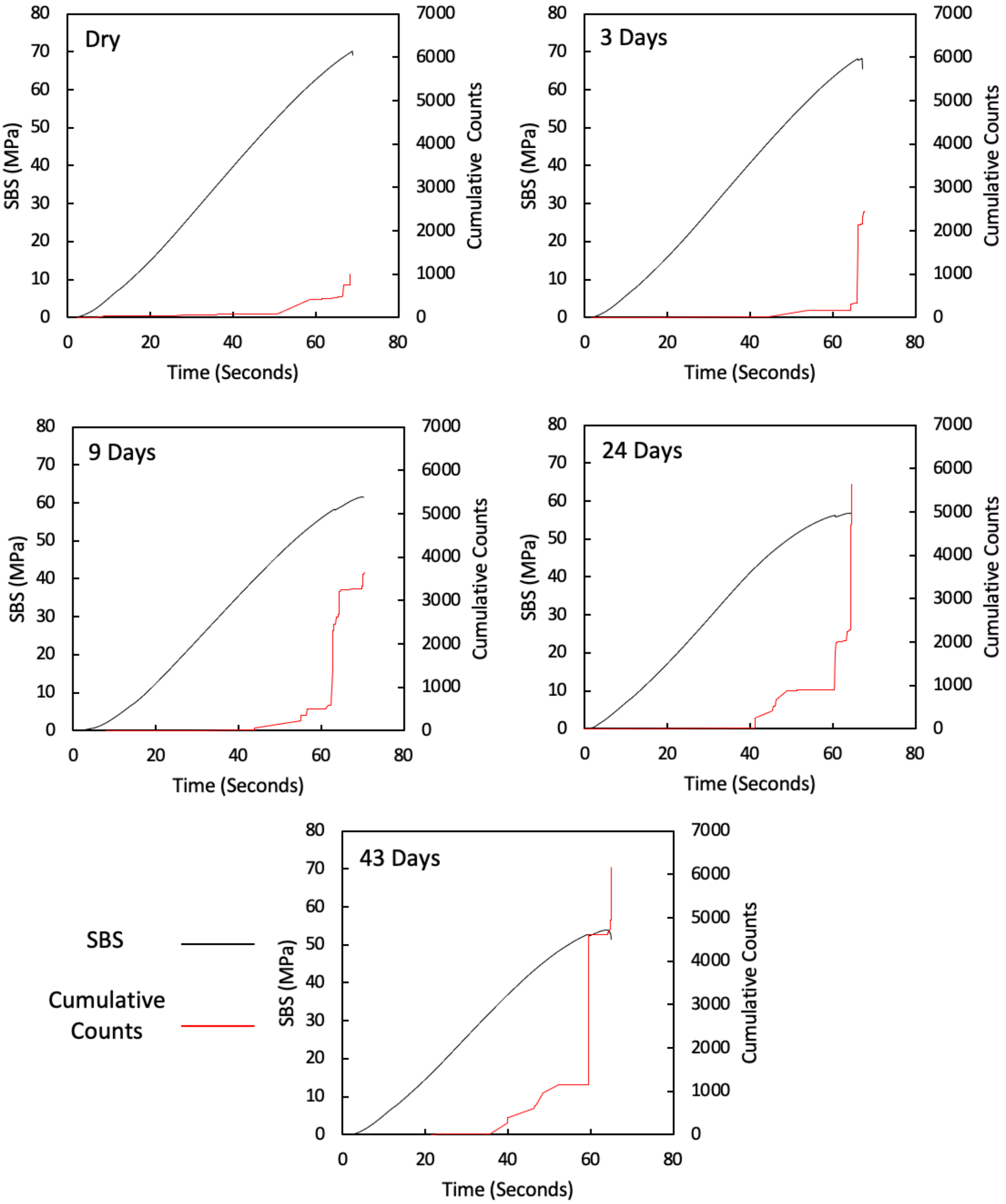

Figure 82. AE cumulative counts versus time for dry, 3-day, 9-day, 24-day and 43-day water-immersed specimens.

The sharp drop in the applied load from the load versus displacement, followed by its further increase until the final failure, as shown in section A of (Figure 80), is in agreement with the findings of Cysne Barbosa et al. (2017) who correlated this behaviour to the potential formation of microcracks in the composites. For this study, this behaviour was investigated further in order to understand any influence on failure mechanics and therefore on the interlaminar properties determined.

Figure 83 shows the AE absolute energy versus time for all specimens with a maximum absolute-energy scale bar of 1.0E+07 in order to show the significant AE signals associated with high energy, which increases with an increase in water immersion time, and this signal also correlates well in with the drop in applied load versus time prior to final fracture, which suggests that there are significant damage mechanisms taking place at this point. Figure 84 is similar to Figure 83, but with a maximum absolute-energy scale bar that show all absolute energy signals detected prior to final fracture. The drop in applied load and its association with the high absolute energy observed in aged specimens is clearly seen in (Figure 84), particularly in the 24-day and 43-day aged specimens.

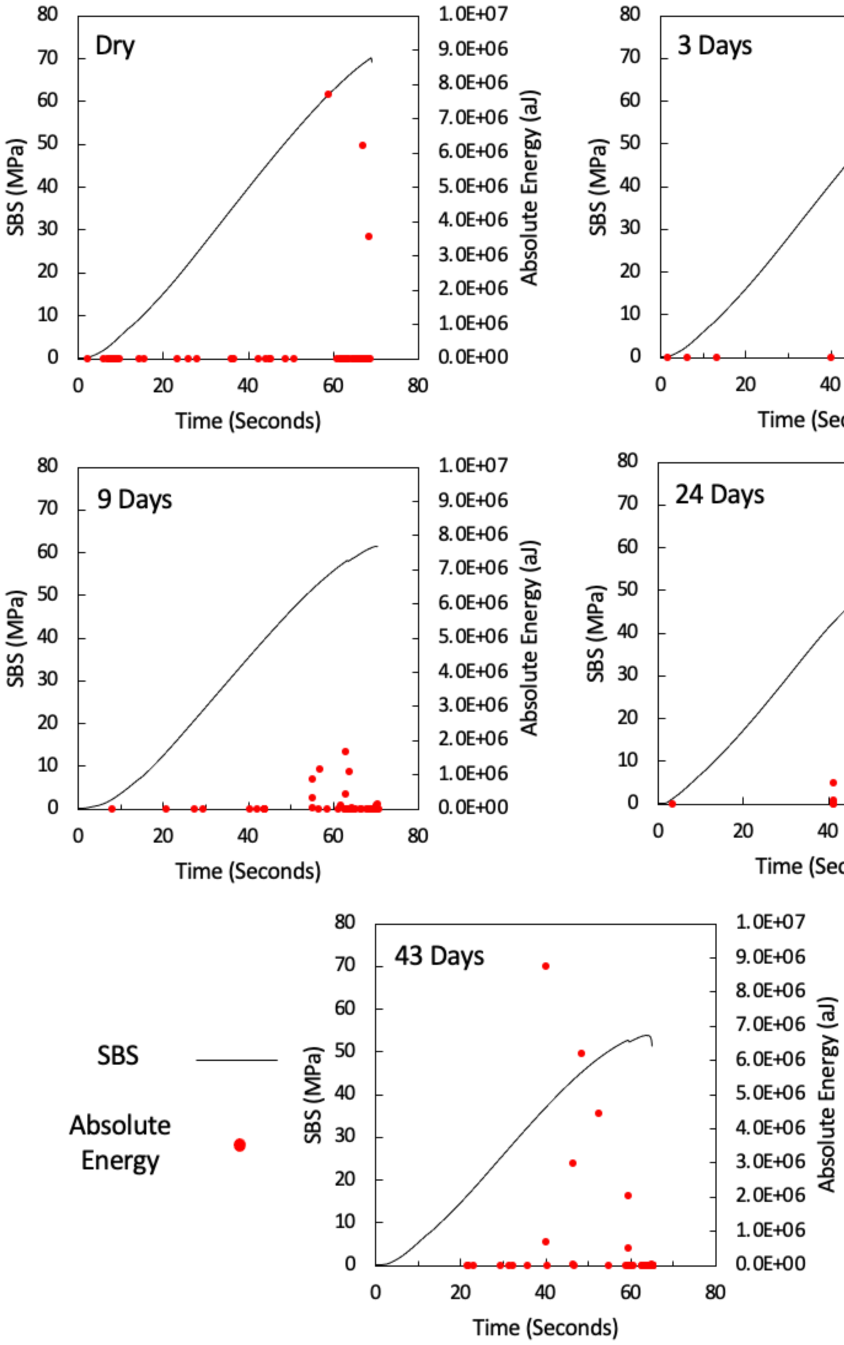

Figure 83. AE absolute energy versus time for dry, 3-day, 9-day, 24-day and 43-day water-immersed specimens with an absolute energy maximum scale of 1.0E+07.

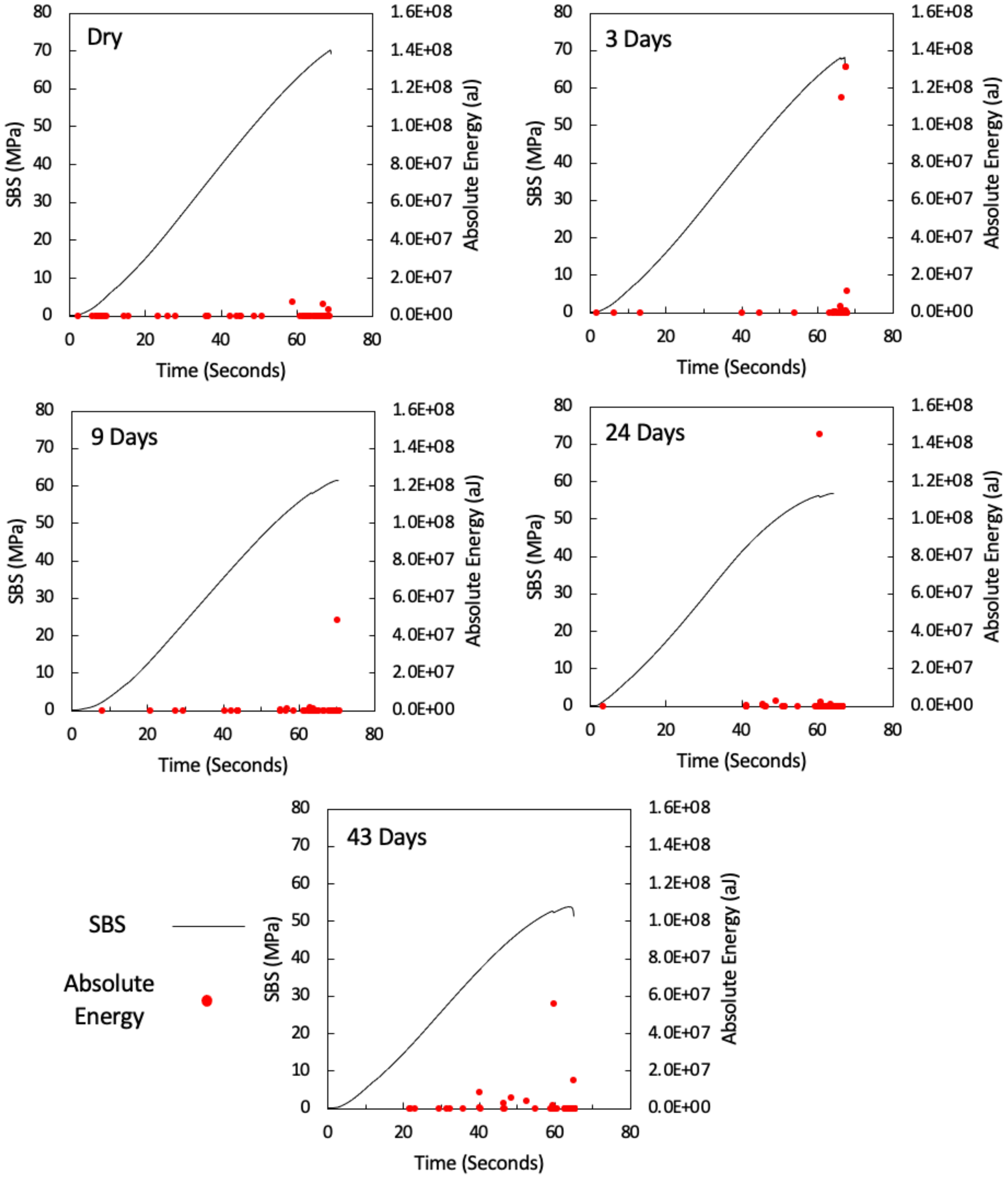

Figure 84. AE absolute energy versus time for dry, 3-day, 9-day, 24-day and 43-day water-immersed specimens with an absolute energy maximum scale of 1.6E+08.

From the AE absolute energy data, it is clear that there are significant AE signals that correspond to the drop in applied load prior to final failure. To understand this crack behaviour, the amplitude and duration of the AE signals observed from these specimens were used to investigate the physical damage mechanism associated with this behaviour. In order to do this, the findings in (Table 8), taken from the study by Pérez-Pacheco et al. (2013) were used. Their study correlated duration versus amplitude to the physical damage of CFRP. However, that study was conducted on tensile specimens, whereas the tests here were conducted under bending (SBS). To use their data as a reference, it is assumed that the AE activity released from fractures in composite samples is similar regardless of the load case. For instance, the release of AE activity when fibres break in a tensile test is similar in a shear test because in both cases reference is made to the energy from the fibre breakage. This is not necessarily an accurate assumption because a complex failure mechanism is expected under shear tests (Xie and Adams 1995). It is also assumed that the moisture effects on the attenuation is neglected due to samples being very small in this test. Never the less, classifying the signals in this way still provides a means of robust comparison between aged samples in this study. Recorded signals for each test have been classified using the ranges given in (Table 8) and the occurrence of signals from each class are plotted cumulatively against time of test in Figure 85. The occurrence of signals classified as microcracks is seen throughout all tests with a significant increase observed towards the end of the test. In the case of the un-aged and 3-day aged specimens very little activity is seen from other classes. In samples aged for 9 or more days other classes become more evident and their occurrence seems to be correlated to the load drops observed prior to final failure.

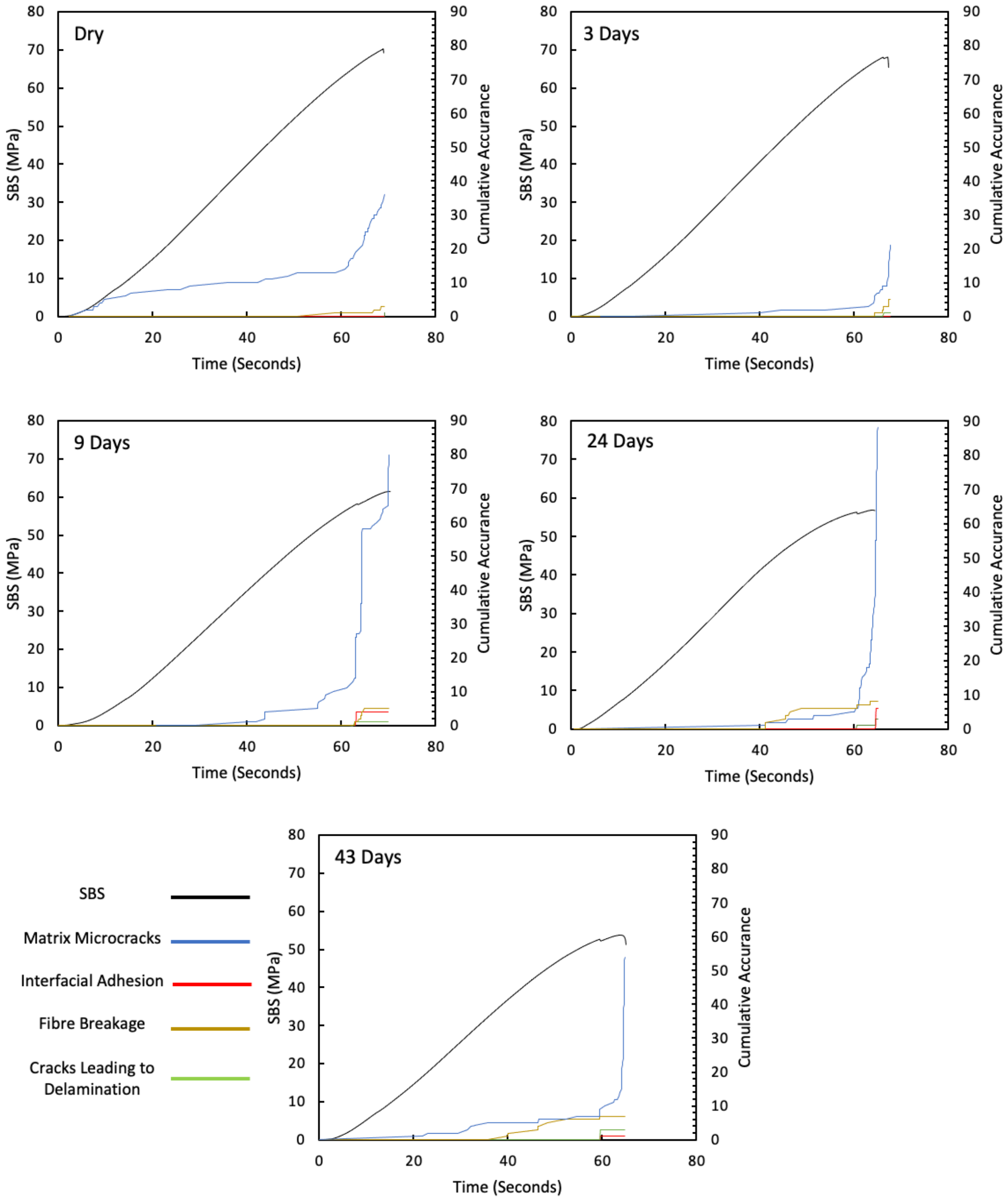

Figure 85. The representative damage mechanism based on the observed amplitude and duration data from the AE signals.

To investigate this change in damage behaviour, images taken from the VSG system and microscope images were used in order to visualise the damage in all aging groups and associate the groups with the observed AE data. A video clip for all fractures can be downloaded using this link (https://data.mendeley.com/datasets/7ngs8h9yv9/1) the small fractures under the load nose are really observable in the video along with crack formation and propagations for all specimens (Almudaihesh 2021).

For the dry (control) specimen, crushing in the upper 0° ply under the loading nose after 59 seconds is observed, as shown in Figure 86. The post-test microscopy images shown in Figure 87, confirms and shows that no further propagation of this damage occurred, and the applied load rose until the final failure of single delamination occurred, as expected (Cysne Barbosa et al. 2017). This shows that some damage has occurred prior to the final failure, which has led to the observed AE activity discussed above, but it is not significant enough to cause an observable drop in the load versus displacement/time curve.

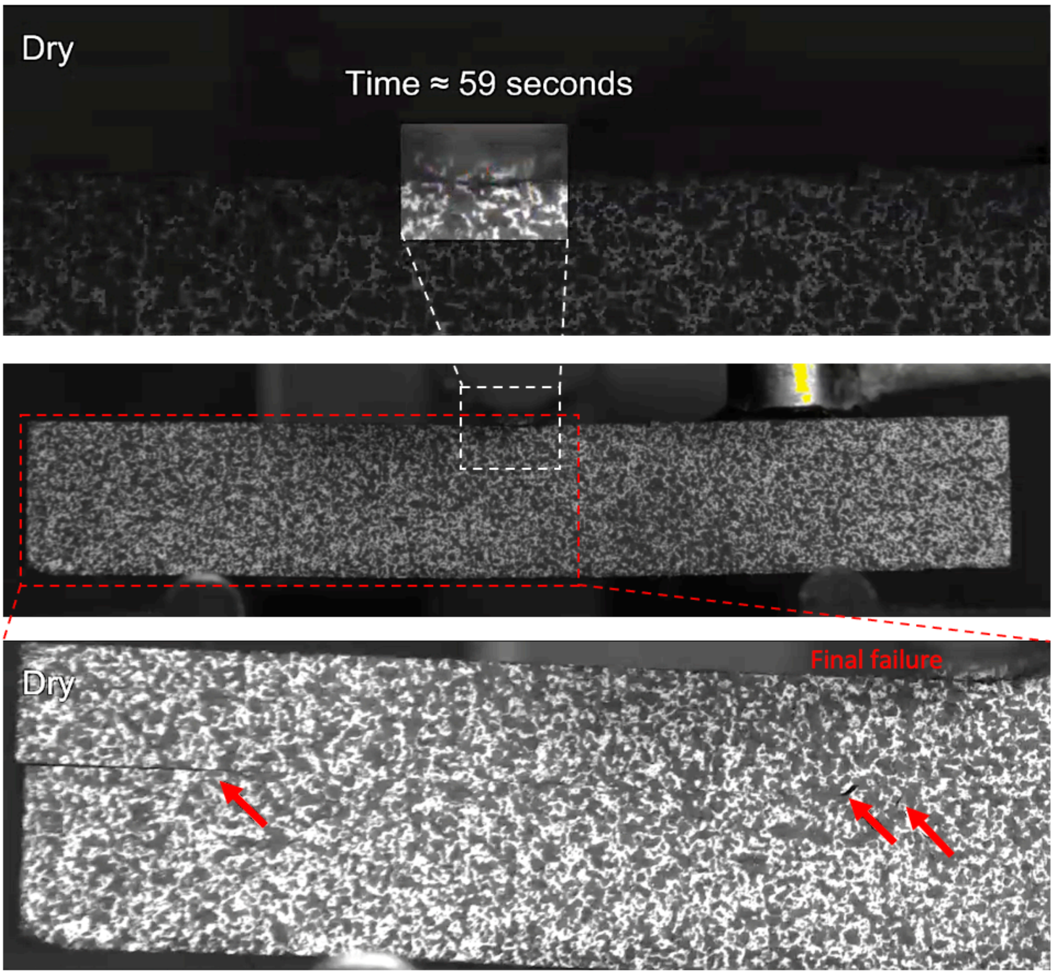

Figure 86. The damage observed in a dry specimen prior to final fracture. The final fracture is also seen.

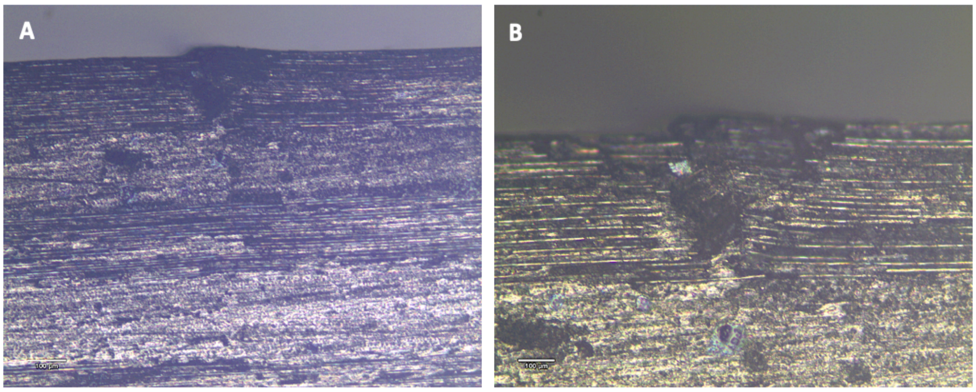

Figure 87. Optical microscopy of the region in contact with the loading nose for a dry specimen. A is x5 magnification and B is x10 magnification.

After three and nine days of water immersion, similar crushing of the upper 0° ply under the loading nose is seen after 65 and 64 seconds, as shown in Figure 88 and Figure 89, respectively. The post-test micrographs shown in Figure 90 for the three-day aged specimen and in Figure 91 for the nine-day aged specimen show that this damage propagated further in to the sample compared with the dry specimen, resulting in crushing of the second 0^{o} ply. This local damage did not propagate any further and a final failure of a single delamination still occurred. Therefore, the drops in applied load (observed prior to final failure) are believed to correlate to the crushing behaviour along with the compressive loads local to the loading nose, which is also associated with higher shear strain near the upper 0° ply with the same SBS (Figure 81) and increased cumulative counts observed at this drop in applied load versus displacement/time (Figure 82), as compared with their dry equivalent.

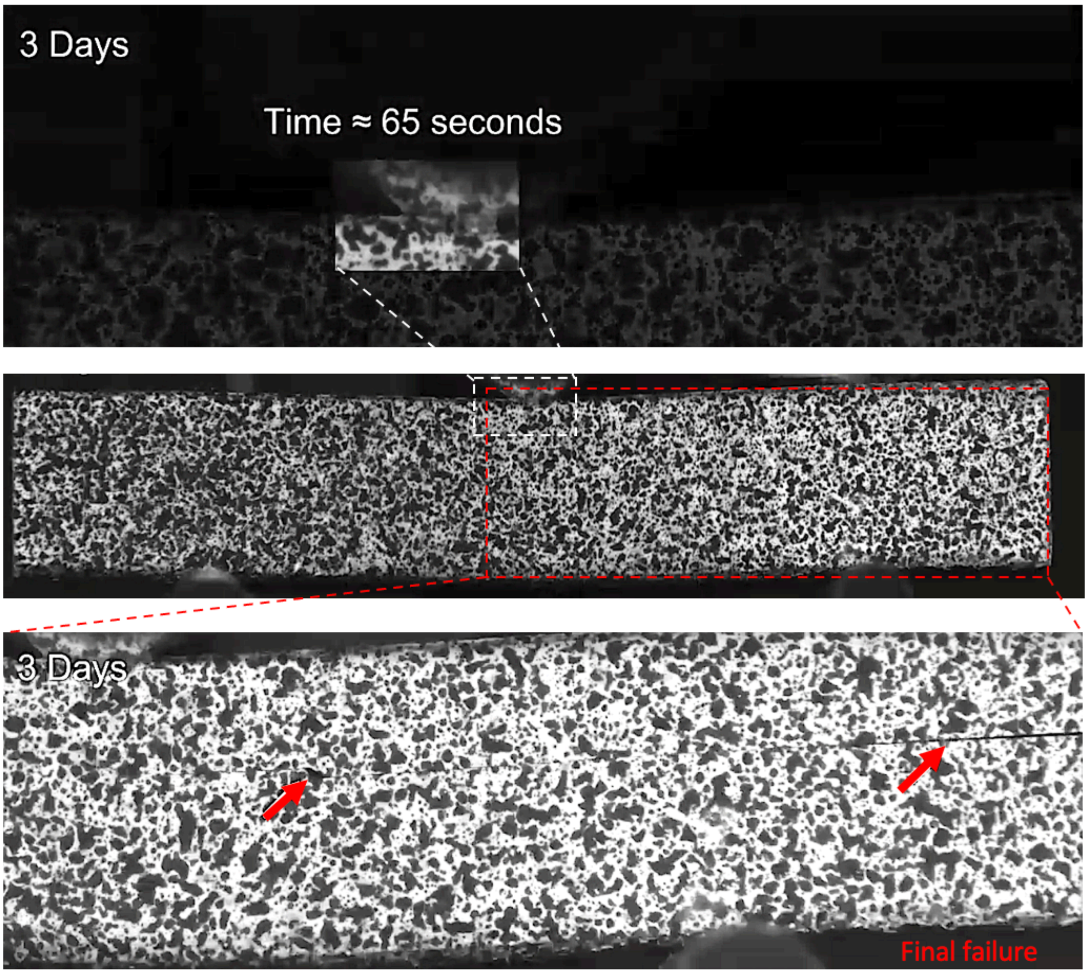

Figure 88. The damage observed for a 3-day water immersed specimen prior to final fracture. The final fracture is also seen.

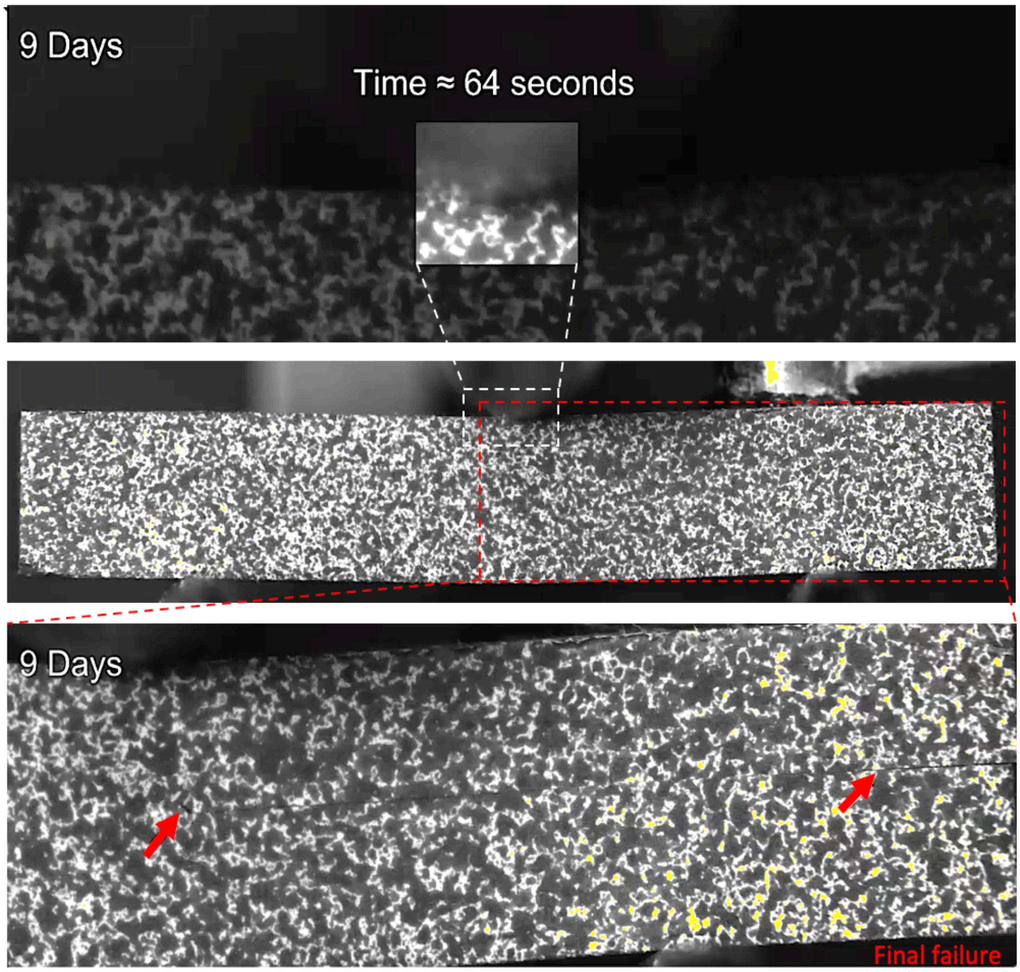

Figure 89. The damage observed for a 9-day water immersed specimen prior to final fracture. The final fracture is also seen.

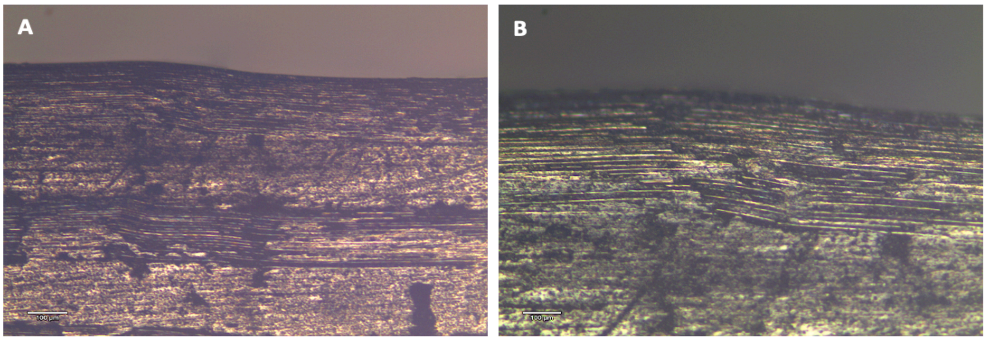

Figure 90. Optical microscopy of the region in contact with the loading nose for a 3-day water immersed specimen. A is x5 magnification and B is x10 magnification.

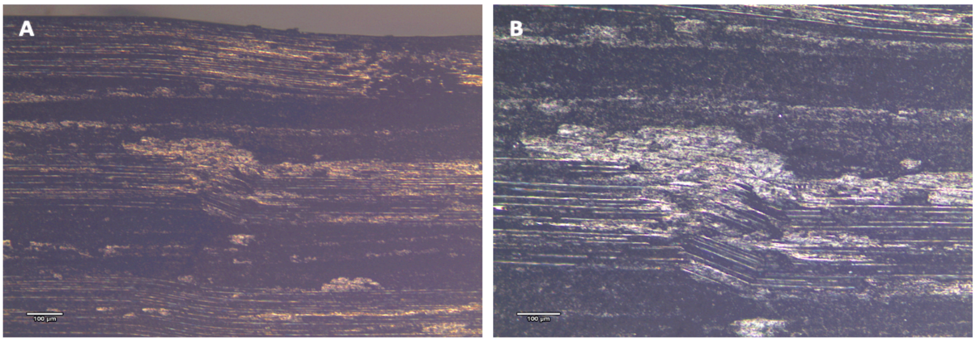

Figure 91. Optical microscopy of the region in contact with the loading nose for a 9-day water immersed specimen. A is x5 magnification and B is x10 magnification.

At longer exposure times (24 and 43 days), crushing is also seen directly under the loading nose at the upper 0° ply after 60 seconds and 58 seconds after 24 and 43 days of immersion, as seen in Figure 92 and Figure 93, respectively. There is some noticeably high AE activity at the point of crushing in the observed data (Figure 82, Figure 83, and Figure 85), which is well correlated with the drop in the applied load prior to the final failure. The post-test micrographs shown in Figure 94 for the 24 day aged specimen and in Figure 95 for the 43 day aged specimen confirm the significant development of the crack propagation of this damage occurred at the upper 0° ply, leading to the final failure of multiple transverse cracks and delaminations occurring throughout the thickness, but predominantly in the upper half of the specimens.

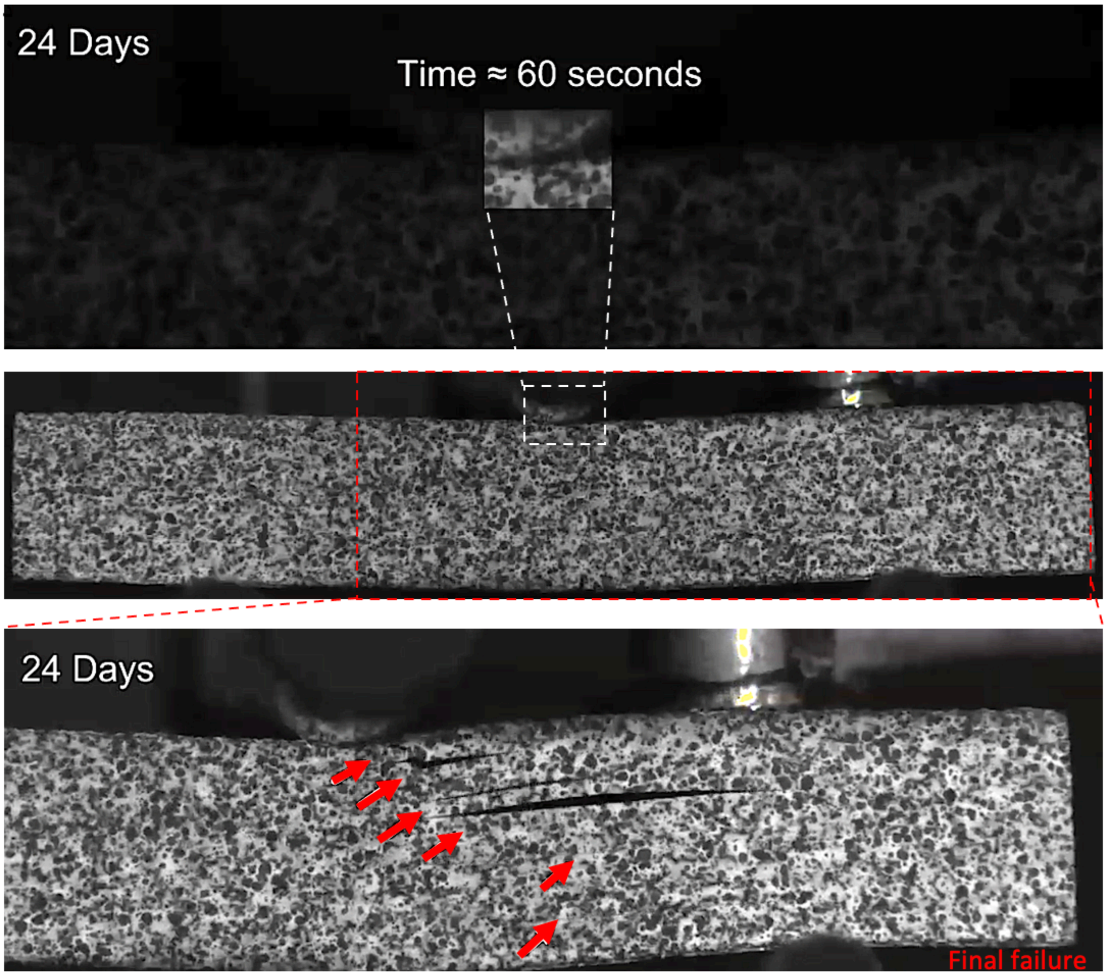

Figure 92. The damage observed for a 24-day water immersed specimen prior to final fracture. The final fracture is also seen.

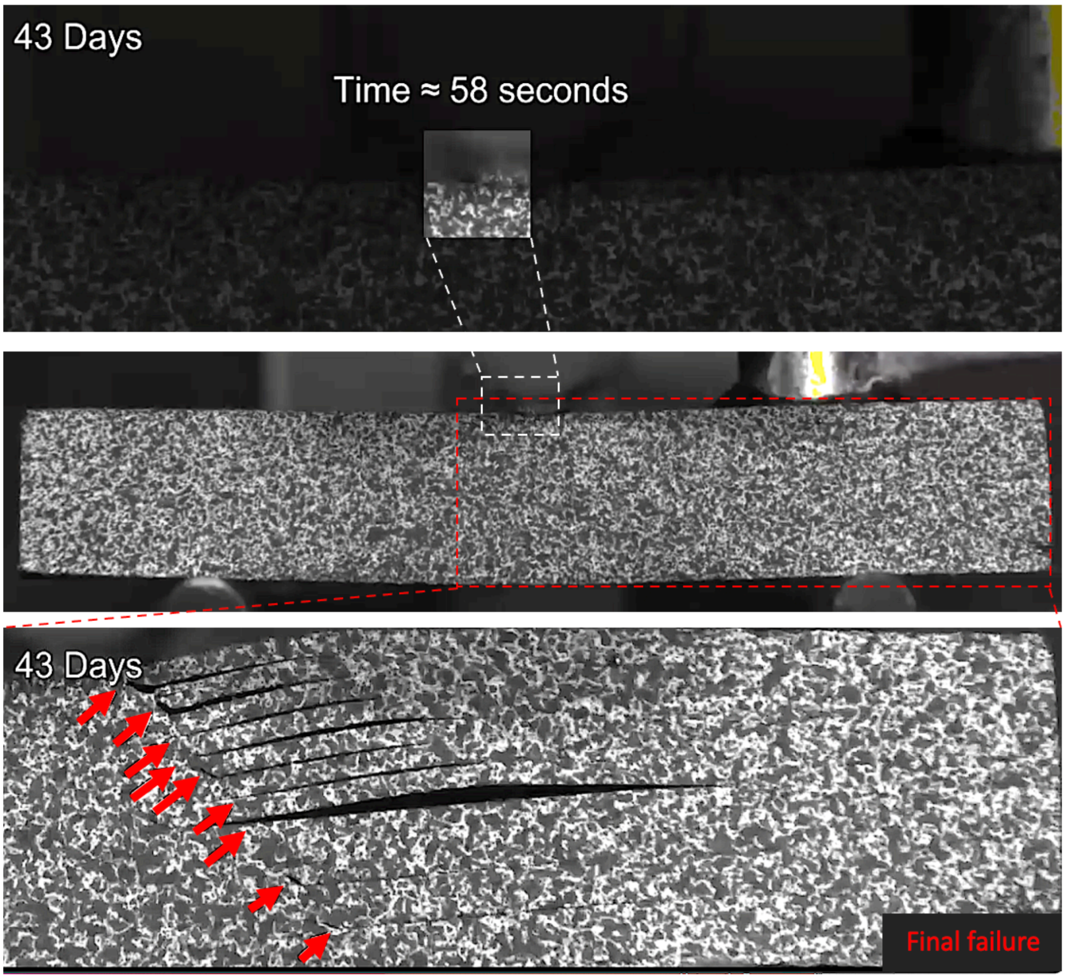

Figure 93. The damage observed for a 43-day water immersed specimen prior to final fracture. The final fracture is also seen.

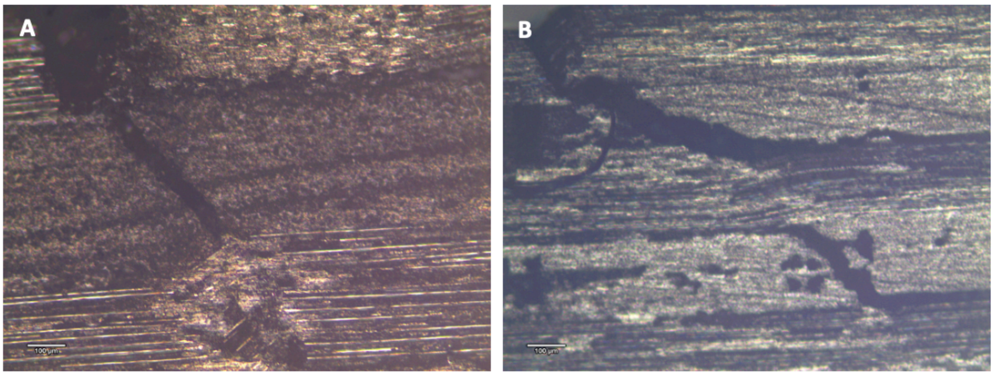

Figure 94. Optical microscopy of the region in contact with the loading nose for a 24-day water immersed specimen. A is x5 magnification and B is x10 magnification.

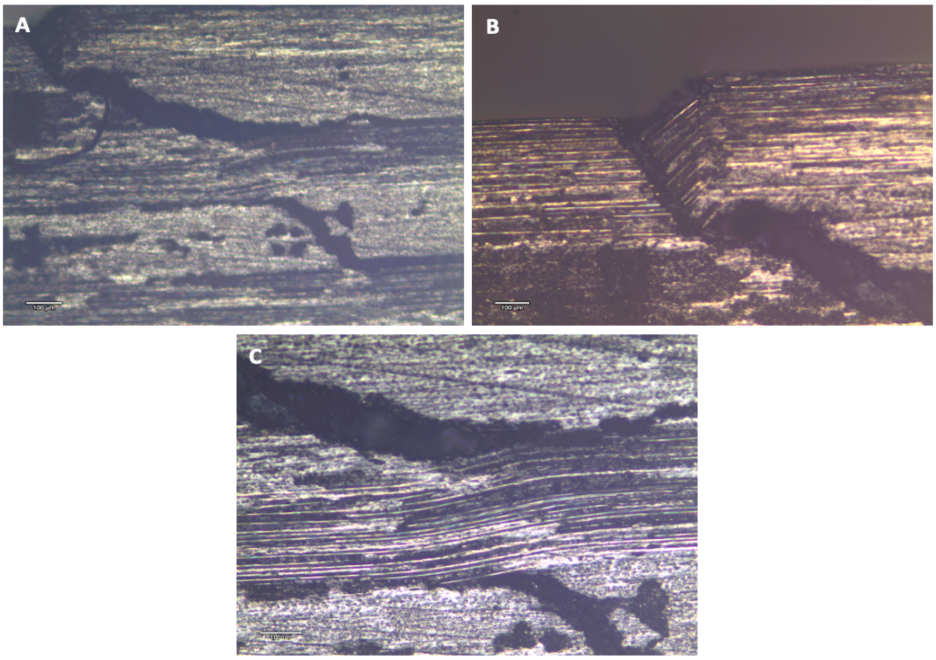

Figure 95. Optical microscopy of the region in contact with the loading nose for a 43-day water immersed specimen. A is x5 magnification, B is x10 magnification (surface in contact with the loading nose) and C is x10 magnification (into the second 0^{o} ply from the surface).

In Figure 96, the AE signals are presented in dots as peak frequency and their associated amplitude (scaled in grey for low and black for high). Unlike the other extracted AE parameters discussed in this chapter (i.e. counts, absolute energy, amplitude, and duration), it is difficult to observe clear distinction/trend between the different aging groups in this test with the use of peak frequency particularly at low peak frequencies which are bellow 200 kHz due to the PICO sensor being limited to operating frequency range of 200-750 kHz. It is established from the use of amplitude and duration (Figure 85) that the dominant cumulative failure mode is matrix cracking which therefore is represented by frequencies bellow 180 kHz from de Groot's (1995) study. This leads to the conclusion that the use of PICO sensor is not the ideal option for frequency analysis for this test; however, it was used due to its suitable size for the SBS specimen dimension.

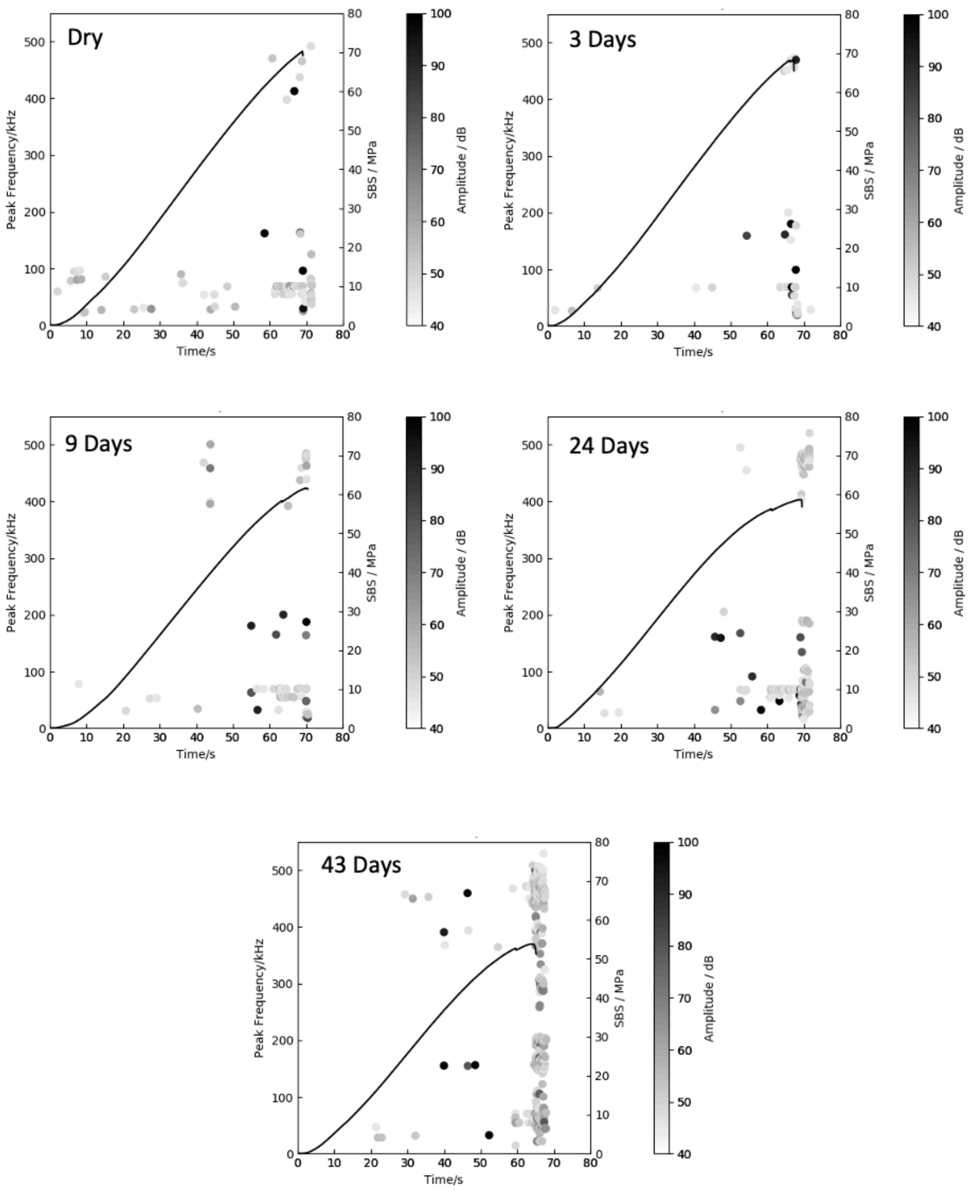

Figure 96: Peak frequency and their associated amplitude.

In the cases of the dry, 3-day and 9-day aged specimens, surface crushing does not appear to influence the final failure, which is by a single delamination at approximately the mid-plane. However, at longer exposure times of 24 and 43 days, surface crushing seems to be more important to the initiation of the final failure. It is suggested that this crushing leads to a buckling/peel up delamination at the first 90/0 interface, which transmits stresses into the second 0^{o} ply from the surface, resulting in further crushing and therefore further buckling/peel up at the next 90/0 interface. This repeats every two plies at the 90/0 interface until approximately the mid-plane of the specimen. The thickness of the material between the delaminations, shown in Figure 92 and Figure 93 is ≈0.4 mm, which corresponds to two ply thicknesses. Further evidence of this behaviour is seen in the optical microscope images (Figure 94 and Figure 95). Evidence of kink bands, commonly associated with in-plane compressive failure, can also be seen in these images. This suggests that the axial bending stresses could also be contributing to this failure behaviour. Given the larger deflections (therefore larger bending stresses) for a given SBS, seen in the 24- and 43-day aged specimens (Figure 80), this seems to be a reasonable possibility. The compressive strength of this material has also been shown to reduce by ≈15% in an aged condition (Figure 72), further increasing the likelihood of compressive failure due to these bending stresses. This is an important observation because the later tests (24- and 43-day aged) do not represent an interlaminar shear failure; therefore, they are not a true measure of the residual short beam shear strength in the aged specimens. Rather, they are indicative of a separate and more complex failure mode brought about by the local stresses induced by the loading nose. So, while the apparent SBS is seen to reduce with increased immersion time, it is not clear if this is actually the case. It also indicates that some of the large reductions in SBS reported in the literature (>20%) could potentially be an overestimation of the effect of moisture absorption. Other flexural tests associated with shear could be investigated, such as the 4-point bend test (Xie and Adams 1995) or evaluation of the suggestions (Adams and Busse 2004) where a proposal of modifying the SBS test by increasing the loading nose diameter is yet to be standardised. The validation of these tests, in terms of fracture behaviour, could perhaps be done with the same or similar methods used for this study in order to draw conclusions on the reductions in shear values after aging the polymers in CFRP composites.

6.4 Conclusion

Water absorption by polymers can cause irreversible changes in the physical and chemical properties of the material. This leads to substantial changes in the overall performance of fibrous/polymeric composites. This study investigates the effects of gradual change in the status of aged polymers on the overall performance of CFRP composites. The effects are noticeable at an early stage of accelerated ageing, where the SBS reduced by 2.8%, 11.14%, 18.78% and 24.47% after 3, 9, 24 and 43 days of water immersion, respectively, which correlates well with observed mass changes. Higher shear strains at lower SBS values with an increase in AE activity (presented in cumulative counts, absolute energy, amplitude and durations) are clearly seen in specimens that were immersed in water for longer. From literature, the drop in the applied load prior to the final fracture in aged specimens, are associated with crack formation in the matrix due to water absorption. In this study, this behaviour was further investigated with the use of AE and by associating the damage with the VSG and microscopy recordings, it is found that this behaviour is more complex; it is associated with crushing in the upper surface of the specimens in contact with the loading nose, leading to crack formation and propagation with more severe damage mechanisms taking place in aged specimens. It is crucial to emphasise that this change in behaviour in the overall fracture is due to physical changes taking place within the polymers due to water absorption. In conclusion, at longer exposure times, a pure interlaminar shear failure (seen as a single delamination in the control specimens) did not occur, and therefore, the true SBS was not determined. Therefore, this study supports proposals for further research, which is required in order to develop testing standards by which to evaluate the shear properties of CFRP composites, particularly after environmental aging since many CFRP structures in real-life applications are expected to operate in moist conditions.

7 Summary of Conclusions and Future Recommendations

7.1 Summary of conclusions

The high demands seen in several industry sectors for composite materials requires further attention in understating to ensure safer service life predictions and further development. The influence of water absorption on CFRP composites was investigated in this thesis taking in to consideration the role of key parameters such as fibre architecture, constituent contents, and the consequential effect of moisture on the mechanical properties. Many researchers have investigated the damage mechanism of water absorption (Saito and Kimpara 2009; Kim and Takemura 2011; Zafar et al. 2012; Arnold et al. 2013; Pérez-Pacheco et al. 2013; Grammatikos et al. 2015; Sethi and Ray 2015; Grammatikos et al. 2016; Masoumi and Valipour 2016; Cysne Barbosa et al. 2017; Davies et al. 2017). The literature carried out for this study has helped in drawing and presenting the theory of moisture ingress and damage mechanism in fibrous reinforced polymers composites (Almudaihesh et al. 2020). The diffusion coefficients were experimentally analysed and found to be in line with literature in that the diffusivities are higher through the edges of the samples ($D_{x/y}$) as compared with the through thickness (D_z) (Arao et al. 2008; Arnold et al. 2013; Grammatikos et al. 2015). The work of this study allowed the comparison of $D_{x/y}$, and D_z of different CFRP fibre architectures and better understand their role on the moisture diffusivities into the structure. In line with other literature, the fracture mechanisms are found to be significantly influenced after moisture absorption (Cysne Barbosa et al. 2017; Korkees et al. 2018b; Zhang et al. 2019). This work therefore highlights the role of fibre architecture on the water absorption ingress mechanism by studying their directional diffusivities, and somewhat more importantly the consequential reduction in strength that corresponds to each architecture and their fracture behaviour and brings into attention that the optimum material/design for an application may not be the most intuitive choice based on un-aged properties (Almudaihesh et al. 2020). It is also understood that the interlaminar shear strength is often a limiting factor of fibrous-polymeric composites (Chandrasekaran et al. 2011). The in-plane properties of the laminate depend primarily on the fibres whereas the out-of-plane properties such as SBS depend largely on the polymeric constituents of the composite (Hull 1994). An assessment of the effect of progressive water absorption on the interlaminar strength of unidirectional CFRP is further investigated in this work with the use of SBS test. The progressive damage evolution was monitored with the use of AE, VSG, and microscopy.

The concluding remarks of this study are presented in the following bullets:

- Moisture absorption in CFRP materials is found to take place within the early stage of water exposure, dominantly affecting the polymeric constituents of the CFRP structure. The water penetration process into the CFRP structure initiate from the micro-cracks and defects. The experimental work of this study shows sharp mass increases within the first stage followed by an equilibrium stage where saturation is present. The interfacial region is found to be a critical parameter where detachment of the interfacial fibre/matrix bonding is observed further demonstrating the potential effect of different fibre architecture in this region where the weave pattern in the woven specimens is believed to have slowed the capillary process in the interfacial region

- A critical reduction in the matrix dominant properties is found in CFRP composites after moisture absorption and is seen to be affected by the fibre architecture. The fibre architecture has been shown to influence how failure occurs and how the failure mechanisms change when the matrix degrades. Under compressive failures, the most linear fibres (the UD), showed a reduction of 14.6% after ageing, followed by the twill (the fibre architecture is more linear than plain) reduced by 7.5% whereas plain only reduced by 1.3% after ageing indicating that the weave pattern is providing more fibre support to the neighbouring ply when the epoxy is aged (plain and twill have identical constituent contents and the only difference is the weave patterns). The failure mechanisms observed from the microscopy also showed less changes observed in terms of final failure after compression for the plain weave as compared with UD (most affected) and twill architectures (less affected than UD but more than the plain weave). The UD fibre architecture is often considered superior in CFRP structures. In fact, the UD was superior only in the un-aged condition in this work whereas after exposure to moist conditions, the 2D woven fibre architecture (particularly the plain weave) outperformed the UD.
- The interlaminar shear strength of UD CFRP is a key property and the literature reported reductions of >20% under SBS tests after water absorption. In this study, with the use of NDT techniques such as AE, VSG, and microscopy, it is found that a pure delamination (representation of a true interlaminar failure) is

only present when the samples are un-aged, or at their early stages of ageing. After longer duration of water exposure, more complex failure mechanisms are involved and does not necessarily reflect the condition of the interlaminar strength and could potentially be overestimating the influence of moisture absorption for this particular test. This leads to the conclusion that the use of SBS test is valid method that could represent the interlaminar strength of un-aged specimens, or at their early stage of ageing. However, the test is believed to not be a true measure of the interlaminar strength after longer exposure of water absorption and this was evident by the NDT analysis

7.2 Future recommendations

This work has highlighted areas of interest for further investigation. The following bullet point summarise the areas where further investigations are desired:

- The low void content observed by the CFRP specimens manufacturing process used in this study featured small amounts of void content which resulted in minimal changes on the behaviour of moisture uptake. It is essential to understand the void content limit to which CFRP composite structures can maintain the same behaviour. This is a particularly important key factor when other manufacturing processes for instance are used which may produce more structural defects as compared with the autoclave process
- The pure influence of carbon fibre architecture on the moisture penetration mechanism can be studied with producing specimens that features the exact constituent contents and geometrical aspects. This will further demonstrate the

role of fibre architecture on the moisture penetration mechanism, which will enable a better weave pattern design optimisation to develop both the mechanical properties and moisture absorption resistance capabilities

- The sizing of carbon fibres is believed to play an essential role in the interfacial region and further studies on understanding the influence of different sizing agents and levels on the bonding capabilities under hydrothermal/hygrothermal conditions are essential for safer and better optimised CFRP composites structure under moist conditions
- At longer exposure times, a pure interlaminar shear failure (seen as a single delamination in the control specimens) did not occur with the use of SBS test, and therefore, the true interlaminar strength was not determined. Other shear testing standards exist such as the V-Notched Beam Method (ASTM D5379-19), In-Plane Shear Strength (ASTM D3846-15), V-Notched Rail Shear Method (ASTM D7078-20); however, they involve more complex sample/fixture preparation. Therefore, this study supports proposals for further research, which is required in order to develop testing standards by which to evaluate the shear properties of CFRP composites, particularly after environmental aging since many CFRP structures in real-life applications are expected to operate in moist conditions

References

Adams, D.F. and Busse, J.M. 2004. Suggested Modifications of the Short Beam Shear Test Method. In: *49th international SAMPE symposium and exhibition*. Long Beach, CA: Society for the Advancement of Material and Process Engineering

Agarwal, B.D., Broutman, L.J. and Chandrashekhara, K. 2006. *Analysis and Performance of Fibre Composites*. 3rd ed. John Wiley & Sons, Inc.

Alam, P., Robert, C. and Ó Brádaigh, C.M. 2018. Tidal turbine blade composites - A review on the effects of hygrothermal aging on the properties of CFRP. *Composites Part B: Engineering* 149(February), pp. 248–259. Available at: https://doi.org/10.1016/j.compositesb.2018.05.003.

Almeida, J.H.S., Souza, S.D.B., Botelho, E.C. and Amico, S.C. 2016. Carbon fiber-reinforced epoxy filament-wound composite laminates exposed to hygrothermal conditioning. *Journal of Materials Science* 51(9), pp. 1–12. doi: 10.1007/s10853-016-9787-9.

Almudaihesh, F. 2021. Fracture of unidirectional CFRP under short-beam test, before and after water absorption. doi: 10.17632/7ngs8h9yv9.1.

Almudaihesh, F., Grigg, S., Holford, K., Pullin, R. and Eaton, M. 2021. An Assessment of the Effect of Progressive Water Absorption on the Interlaminar Strength of Unidirectional Carbon/Epoxy Composites Using Acoustic Emission. *Sensors 2021, Vol. 21, Page 4351* 21(13), p. 4351. Available at: https://www.mdpi.com/1164564 [Accessed: 25 June 2021].

Almudaihesh, F., Holford, K., Pullin, R. and Eaton, M. 2020. The influence of water absorption on unidirectional and 2D woven CFRP composites and their mechanical performance. *Composites Part B: Engineering* 182(September), p. 107626. Available at: https://doi.org/10.1016/j.compositesb.2019.107626.

Arao, Y., Koyanagi, J., Hatta, H. and Kawada, H. 2008. Analysis of time-dependent deformation of CFRP considering the anisotropy of moisture diffusion. *Advanced Composite Materials* 17(4), pp. 359–372. doi: 10.1163/156855108X385276.

Arhamnamazi, S.A., Arab, N.B.M., Oskouei, A.R. and Aymerich, F. 2019. Accuracy assessment of ultrasonic C-scan and X-ray radiography methods for impact damage detection in glass fiber reinforced polyester composites. *Journal of Applied and Computational Mechanics* 5(2), pp. 258–268. doi: 10.22055/JACM.2018.26297.1318.

Arnold, J.C., Alston, S.M. and Korkees, F. 2013. An assessment of methods to determine the directional moisture diffusion coefficients of composite materials. *Composites Part A: Applied Science and Manufacturing* 55, pp. 120–128. Available at: http://dx.doi.org/10.1016/j.compositesa.2013.08.012.

Asmatulu, E., Twomey, J. and Overcash, M. 2014. Recycling of fiber-reinforced composites and direct structural composite recycling concept. *Journal of Composite Materials* 48(5), pp. 593–608. Available at: http://journals.sagepub.com/doi/10.1177/0021998313476325.

ASTM 1989. E610-82 Standard Definitions of Terms Relating to Acoustic Emission. ASTM International

Azwa, Z.N., Yousif, B.F., Manalo, A.C. and Karunasena, W. 2013. A review on the degradability of polymeric composites based on natural fibres. *Materials & Design* 47, pp. 424–442. Available at: https://linkinghub.elsevier.com/retrieve/pii/S0261306912007832.

Baley, C., Davies, P., Grohens, Y. and Dolto, G. 2004. Application of Interlaminar Tests to Marine Composites. A Literature Review. *Applied Composite Materials* 11(2), pp. 99–126. doi: 10.1023/B:ACMA.0000012902.93986.bf.

Bank, L., Gentry, T.R. and Barkatt, A. 1995. Accelerated Test Methods to Determine the Long-Term Behavior of FRP Composite Structures: Environmental Effects. *Journal of Reinforced Plastics and Composites* 14(6), pp. 559–587.

Bao, L.R. and Yee, A.F. 2002. Moisture diffusion and hygrothermal aging in bismaleimide matrix carbon fiber composites: Part II-woven and hybrid composites. *Composites Science and Technology* 62(16), pp. 2111–2119. doi: 10.1016/S0266-3538(02)00162-8.

Barbero, E.J. 2017. *ntroduction to Composite Materials Design*. 3rd ed. CRC Press.

Bogdanovic, A.E. and Pastore, C.M. 1996. *Mechanics of Textile and Laminated Composites: With Applications to Structural Analysis*. London.

Broughton, W. 2012. Assessing the moisture resistance of adhesives for marine environments. In: *Adhesives in Marine Engineering*. Elsevier, pp. 155–186. Available at: https://linkinghub.elsevier.com/retrieve/pii/B9781845694524500072.

Brown, L.P. and Long, A.C. 2021. Modeling the geometry of textile reinforcements for composites: TexGen. In: *Composite Reinforcements for Optimum Performance*. Elsevier, pp. 237–265. Available at: https://linkinghub.elsevier.com/retrieve/pii/B9780128190050000083.

Brown, R.P., Kockott, D., Trubiroha, P., Ketola, W. and Shorthouse, J. 1995. *A Review of Accelerated Durability Tests*. Available at: http://www.vamas.org/documents/twa12/vamas_twa12_report_18.pdf.

Buxton, A. and Baillie, C. 1994. A study of the influence of the environment on the measurement of interfacial properties of carbon fibre/epoxy resin composites. *Composites* 25(7), pp. 604–608. Available at: https://linkinghub.elsevier.com/retrieve/pii/0010436194901902.

Campbell, F.C. 2004. *Manufacturing Processes for Advanced Composites*. Oxford: Elsevier Advanced Technology.

Cao, S., Wu, Z. and Wang, X. 2009. Tensile properties of CFRP and hybrid FRP composites at elevated temperatures. *Journal of Composite Materials* 43(4), pp. 315–330. doi: 10.1177/0021998308099224.

Capiel, G., Miccio, L.A., Montemartini, P.E. and Schwartz, G.A. 2017. Water diffusion and hydrolysis effect on the structure and dynamics of epoxy-anhydride networks. *Polymer Degradation and Stability* 143, pp. 57–63. Available at: http://dx.doi.org/10.1016/j.polymdegradstab.2017.06.010.

Capiel, G., Uicich, J., Fasce, D. and Montemartini, P.E. 2018. Diffusion and hydrolysis effects during water aging on an epoxy-anhydride system. *Polymer Degradation and*

Stability 153, pp. 165–171. Available at: https://linkinghub.elsevier.com/retrieve/pii/S014139101830140X.

Carmi, R. et al. 2015. Acoustic Emission and Digital Image Correlation as Complementary Techniques for Laboratory and Field Research., pp. 605–622. Available at: http://link.springer.com/10.1007/978-1-4939-1239-1_56.

Carter, H.G. and Kibler, K.G. 1978. Langmuir-Type Model for Anomalous Moisture Diffusion In Composite Resins. *Journal of Composite Materials* 12(2), pp. 118–131. Available at: http://journals.sagepub.com/doi/10.1177/002199837801200201.

Cauich-Cupul, J.I., Pérez-Pacheco, E., Valadez-González, A. and Herrera-Franco, P.J. 2011a. Effect of moisture absorption on the micromechanical behavior of carbon fiber/epoxy matrix composites. *Journal of Materials Science* 46(20), pp. 6664–6672. doi: 10.1007/s10853-011-5619-0.

Cauich-Cupul, J.I., Pérez-Pacheco, E., Valadez-González, A. and Herrera-Franco, P.J. 2011b. Effect of moisture absorption on the micromechanical behavior of carbon fiber/epoxy matrix composites. *Journal of Materials Science* 46(20), pp. 6664–6672. Available at: http://link.springer.com/10.1007/s10853-011-5619-0.

Chandrasekaran, V.C.S., Advani, S.G. and Santare, M.H. 2011. Influence of resin properties on interlaminar shear strength of glass/epoxy/MWNT hybrid composites. *Composites Part A: Applied Science and Manufacturing* 42(8), pp. 1007–1016. Available at: http://dx.doi.org/10.1016/j.compositesa.2011.04.004.

Chang, B.P., Mohanty, A.K. and Misra, M. 2020. Studies on durability of sustainable biobased composites: a review. *RSC Advances* 10(31), pp. 17955–17999. Available at: http://xlink.rsc.org/?DOI=C9RA09554C.

Chateauminois, A., Chabert, B., Soulier, J.P. and Vincent, L. 1995. Dynamic mechanical analysis of epoxy composites plasticized by water: Artifact and reality. *Polymer Composites* 16(4), pp. 288–296. Available at: http://doi.wiley.com/10.1002/pc.750160405.

Cheng, X., Baig, Y. and Li, Z. 2011. Effects of hygrothermal environmental conditions on compressive strength of CFRP stitched laminates. *Journal of Reinforced Plastics and Composites* 30(2), pp. 110–122. doi: 10.1177/0731684410384894.

Choi, H.S., Ahn, K.J., Nam, J. and Chun, H.J. 2001. Hygroscopic aspects of epoxy / carbon fiber composite laminates in aircraft environments. *Composites Part A: Applied Science and Manufacturing* 32, pp. 709–720.

Costa, M.L., Rezende, M.C. and de Almeida, S.F.M. 2006. Effect of void content on the moisture absorption in polymeric composites. *Polymer - Plastics Technology and Engineering* 45(6), pp. 691–698. doi: 10.1080/03602550600609549.

Crank, J. 1975. *The Mathematics of Diffusion*. Second. Clarendon Press.

Cree, D., Gamaniouk, T., Loong, M.L. and Green, M.F. 2015. Tensile and lap-splice shear strength properties of CFRP composites at high temperatures. *Journal of Composites for Construction* 19(2), pp. 1–12. doi: 10.1061/(ASCE)CC.1943-5614.0000508.

Cysne Barbosa, A.P., P. Fulco, A.P., S.S. Guerra, E., K. Arakaki, F., Tosatto, M., B. Costa, M.C. and D. Melo, J.D. 2017. Accelerated aging effects on carbon fiber/epoxy composites. *Composites Part B: Engineering* 110, pp. 298–306. Available at: https://www.sciencedirect.com/science/article/pii/S1359836816313579#fig2 [Accessed: 9 March 2018].

Dao, B., Hodgkin, J., Krstina, J., Mardel, J. and Tian, W. 2010. Accelerated aging versus realistic aging in aerospace composite materials. V. The effects of hot/wet aging in a structural epoxy composite. *Journal of Applied Polymer Science* 115(2), pp. 901–910. Available at: http://doi.wiley.com/10.1002/app.31029 [Accessed: 9 March 2018].

Davies, P., Le Gac, P.-Y. and Le Gall, M. 2017. Influence of Sea Water Aging on the Mechanical Behaviour of Acrylic Matrix Composites. *Applied Composite Materials* 24(1), pp. 97–111. Available at: https://doi.org/10.1007/s10443-016-9516-1.

Dell'Anno, G. and Lees, R. 2012. Effect of water immersion on the interlaminar and flexural performance of low cost liquid resin infused carbon fabric composites. *Composites Part B: Engineering* 43(3), pp. 1368–1373. doi: 10.1016/j.compositesb.2011.08.037.

Dirand, X., Hilaire, B., Soulier, J.P. and Nardin, M. 1996. Interfacial shear strength in glass-fiber/vinylester-resin composites. *Composites Science and Technology* 56(5), pp. 533–539. doi: 10.1016/0266-3538(96)00040-1.

Duann, Y.F., Liu, T.M., Cheng, K.C. and Su, W.F. 2004. Thermal stability of some naphthalene- and phenyl-based epoxy resins. *Polymer Degradation and Stability* 84(2), pp. 305–310. doi: 10.1016/j.polymdegradstab.2004.01.016.

Dutta, S.S. 2008. *Water absorption and dielectric properties of Epoxy insulation*.

Norwegian University of Science and Technology. Available at: http://hdl.handle.net/11250/256588.

Eaton, M. 2007. *Acoustic Emission (AE) monitoring of buckling and failure in carbon fibre composite structures*. Cardiff University.

Espert, A., Vilaplana, F. and Karlsson, S. 2004. Comparison of water absorption in natural cellulosic fibres from wood and one-year crops in polypropylene composites and its influence on their mechanical properties. *Composites Part A: Applied Science and Manufacturing* 35(11), pp. 1267–1276. doi: 10.1016/j.compositesa.2004.04.004.

Fard, M.Y., Raji, B., Woodward, J. and Chattopadhyay, A. 2019. Characterization of interlaminar fracture modes I, II, and I-II of carbon/epoxy composites including in-service related bonding quality conditions. *Polymer Testing* 77(March), p. 105894. Available at: https://doi.org/10.1016/j.polymertesting.2019.05.010.

Feih, S., Boiocchi, E., Kandare, E., Mathys, Z., Gibson, A.G. and Mouritz, A.P. 2009. Strength Degradation of Glass and Carbon Fibres at High Temperature. In: *ICCM17.*, p. 10.

Field, S.Y. and Ashbee, K.H.G. 1972. Weathering of fibre reinforced plastics. Progress of dbonding detected in model systems by using fibres as light pipes. *Polymer Engineering and Science* 12(1), pp. 30–33. Available at: http://doi.wiley.com/10.1002/pen.760120105.

Frigione, M. and Lettieri, M. 2018. Durability Issues and Challenges for Material Advancements in FRP Employed in the Construction Industry. *Polymers* 10(3), p. 247.

Available at: http://www.mdpi.com/2073-4360/10/3/247.

Le Gac, P.Y., Arhant, M., Le Gall, M. and Davies, P. 2017. Yield stress changes induced by water in polyamide 6: Characterization and modeling. *Polymer Degradation and Stability* 137, pp. 272–280. Available at: http://dx.doi.org/10.1016/j.polymdegradstab.2017.02.003.

Gao, S.L., Mäder, E. and Zhandarov, S.F. 2004. Carbon fibers and composites with epoxy resins: Topography, fractography and interphases. *Carbon* 42(3), pp. 515–529. doi: 10.1016/j.carbon.2003.12.085.

González, C. and LLorca, J. 2007. Mechanical behavior of unidirectional fiber-reinforced polymers under transverse compression: Microscopic mechanisms and modeling. *Composites Science and Technology* 67(13), pp. 2795–2806. Available at: https://citeseerx.ist.psu.edu/viewdoc/download?doi=10.1.1.575.4236&rep=rep1&type=pdf.

Gorman, M.R. and Prosser, W.H. 1990. AE source orientation by plate wave analysis. *Journal of Acoustic Emission(USA)* 9(4), pp. 282–288.

Grammatikos, S.A., Evernden, M., Mitchels, J., Zafari, B., Mottram, J.T. and Papanicolaou, G.C. 2016. On the response to hygrothermal aging of pultruded FRPs used in the civil engineering sector. *Materials and Design* 96, pp. 283–295. Available at: http://dx.doi.org/10.1016/j.matdes.2016.02.026.

Grammatikos, S.A., Zafari, B., Evernden, M.C., Mottram, J.T. and Mitchels, J.M. 2015. Moisture uptake characteristics of a pultruded fibre reinforced polymer flat sheet subjected to hot/wet aging. *Polymer Degradation and Stability* 121, pp. 407–419. Available at: http://dx.doi.org/10.1016/j.polymdegradstab.2015.10.001.

de Groot, P.J., Wijnen, P.A.M. and Janssen, R.B.F. 1995. Real-time frequency determination of acoustic emission for different fracture mechanisms in carbon/epoxy composites. *Composites Science and Technology* 55, pp. 405–412.

Hasiotis, T., Badogiannis, E. and Tsouvalis, N.G. 2007. Application of Ultrasonic C-Scan Techniques for Tracing Defects in Laminated Composite Materials. In: *4th International Conference on NDT*. Chania

Herakovich, C.T. 1998. Mechanics of Fibrous Composites., p. 480.

Hexcel 2013. HexPly Prepreg. Available at: https://www.hexcel.com/Resources/Technology-Manuals.

Hughes, J.D.H. 1991. The carbon fibre/epoxy interface—A review. *Composites Science and Technology* 41(1), pp. 13–45. Available at: https://linkinghub.elsevier.com/retrieve/pii/026635389190050Y.

Hull, D. 1994. Matrix-dominated properties of polymer matrix composite materials. *Materials Science and Engineering: A* 184(2), pp. 173–183. Available at: https://linkinghub.elsevier.com/retrieve/pii/0921509394910308.

Hunkley, J.A. and Connell, J.W. 2012. Resin Systems and Chemistry: Degradation Mechanisms and Durability. In: Pochiraju, K. V, Tandon, G., and Schoeppner, G. A. eds. *Long-Term Durability of Polymeric Matrix Composites*.

Imetrum Limited 2016. *Video Gauge User Manual - Version 5.0.1*.

Imoisili, P.E. and Jen, T.-C. 2020. Mechanical and water absorption behaviour of potassium permanganate (KMnO4) treated plantain (Musa Paradisiacal) fibre/epoxy bio-composites. *Journal of Materials Research and Technology* 9(4), pp. 8705–8713. Available at: https://linkinghub.elsevier.com/retrieve/pii/S2238785420313910.

Johncock, P. and Tudgey, G.F. 1986. Some Effects of Structure, Composition and Cure on the Water Absorption and Glass Transition Temperature of Amine-cured Epoxies. *British Polymer Journal* 18(5), pp. 292–302. Available at: http://doi.wiley.com/10.1002/pi.4980180504.

Kafodya, I., Xian, G. and Li, H. 2015. Durability study of pultruded CFRP plates immersed in water and seawater under sustained bending: Water uptake and effects on the mechanical properties. *Composites Part B: Engineering* 70, pp. 138–148. Available at: https://www.sciencedirect.com/science/article/pii/S1359836814004909 [Accessed: 19 April 2018].

Kahraman, R. and Al-Harthi, M. 2005. Moisture diffusion into aluminum powder-filled epoxy adhesive in sodium chloride solutions. *International Journal of Adhesion and Adhesives* 25(4), pp. 337–341. Available at: https://linkinghub.elsevier.com/retrieve/pii/S0143749604001241.

Karbhari, V.M. and Xian, G. 2009. Hygrothermal effects on high VF pultruded unidirectional carbon/epoxy composites: Moisture uptake. *Composites Part B: Engineering* 40(1), pp. 41–49. Available at: http://dx.doi.org/10.1016/j.compositesb.2008.07.003.

Karmaker, A.C. 1997. Effect of water absorption on dimensional stability and impact energy of jute fibre reinforced polypropylene. *Journal of Materials Science Letters* 16(6), pp. 462–464. doi: 10.1023/A:1018508209022.

Kawai, M., Yagihashi, Y., Hoshi, H. and Iwahori, Y. 2013. Anisomorphic constant fatigue life diagrams for quasi-isotropic woven fabric carbon/epoxy laminates under different hygro-thermal environments. *Advanced Composite Materials* 22(2), pp. 79–98. doi: 10.1080/09243046.2013.777172.

Kentish, S.E. 2011. Polymeric membranes for natural gas processing. In: *Advanced Membrane Science and Technology for Sustainable Energy and Environmental Applications*. Elsevier, pp. 339–360. Available at: https://linkinghub.elsevier.com/retrieve/pii/B9781845699697500114.

Kersemans, M., Verboven, E., Segers, J., Hedayatrasa, S. and Paepegem, W. Van 2018. Non-Destructive Testing of Composites by Ultrasound, Local Defect Resonance and Thermography. *Proceedings* 2(8), p. 554. doi: 10.3390/icem18-05464.

Kim, H. and Takemura, K. 2011. Influence of water absorption on creep behaviour of carbon fiber/epoxy laminates. *Procedia Engineering* 10, pp. 2731–2736. Available at: http://dx.doi.org/10.1016/j.proeng.2011.04.455.

Kondo, K. and Taki, T. 1982. Moisture diffusivity of unidirectional composites. *Journal of Composite Materials* 16(2), pp. 82–93.

Korkees, F., Alston, S. and Arnold, C. 2018a. Directional diffusion of moisture into unidirectional carbon fiber/epoxy Composites: Experiments and modeling. *Polymer Composites* 39(S4), pp. E2305–E2315. Available at:

http://doi.wiley.com/10.1002/pc.24626.

Korkees, F., Arnold, C. and Alston, S. 2018b. An investigation of the long-term water uptake behavior and mechanisms of carbon fiber/977-2 epoxy composites. *Polymer Engineering & Science* 58(12), pp. 2175–2184. Available at: http://doi.wiley.com/10.1002/pen.24830.

Korkees, F., Arnold, C. and Alston, S. 2018c. Water absorption and low-energy impact and their role in the failure of ±45° carbon fibre composites. *Polymer Composites* 39(8), pp. 2771–2782. Available at: http://doi.wiley.com/10.1002/pc.24269.

Krauklis, A.E., Gagani, A.I. and Echtermeyer, A.T. 2018. Hygrothermal aging of amine epoxy: Reversible static and fatigue properties. *Open Engineering* 8(1), pp. 447–454. doi: 10.1515/eng-2018-0050.

Kumosa, M. 1987. Acoustic emission monitoring of stress corrosion cracks in aligned GRP. *Journal of Physics D: Applied Physics* 20(1)

Ladizesky, N.H. and Ward, I.M. 1983. A study of the adhesion of drawn polyethylene fibre/polymeric resin systems. *Journal of Materials Science* 18(2), pp. 533–544. Available at: http://link.springer.com/10.1007/BF00560643.

Lahouari, H.T., Allel, M., Belkaid, N., Boutaous, A. and Bouamrane, R. 2013. Study of the Effect of Water Intake by the Matrix on the Optimization of the Fiber Matrix Interface Damage for a Composite Material by Genetic Algorithms. *Strength of Materials* 45(6), pp. 739–747. Available at: http://link.springer.com/10.1007/s11223-013-9509-3.

Li, Y., Cordovez, M. and Karbhari, V.M. 2003. Dielectric and mechanical characterization of processing and moisture uptake effects in E-glass / epoxy composites. 34, pp. 383–390.

Liu, L. et al. 2015. Interfacial characterization, control and modification of carbon fiber reinforced polymer composites. *Composites Science and Technology* 121, pp. 56–72. Available at: https://linkinghub.elsevier.com/retrieve/pii/S0266353815300506.

Liu, L., Zhao, Z., Chen, W., Shuang, C. and Luo, G. 2018. An experimental investigation on high velocity impact behavior of hygrothermal aged CFRP composites. *Composite Structures* 204, pp. 645–657. Available at: https://linkinghub.elsevier.com/retrieve/pii/S026382231830816X.

Liu, P.F., Chu, J.K., Liu, Y.L. and Zheng, J.Y. 2012. A study on the failure mechanisms of carbon fiber/epoxy composite laminates using acoustic emission. *Materials and Design* 37, pp. 228–235. Available at: http://dx.doi.org/10.1016/j.matdes.2011.12.015.

Liu, P.F., Yang, J. and Peng, X.Q. 2017. Delamination analysis of carbon fiber composites under hygrothermal environment using acoustic emission. *Journal of Composite Materials* 51(11), pp. 1557–1571. doi: 10.1177/0021998316661043.

Luke, S., Canning, L., Collins, S., Knudsen, E., Brown, P., Taljsten, B. and Olofsson, I. 2002. Advanced Composite Bridge Decking System—Project ASSET. *Structural Engineering International* 12(2), pp. 76–79. Available at: https://www.tandfonline.com/doi/full/10.2749/101686602777965522.

Ma, L. et al. 2014. Interfacial enhancement of carbon fiber composites by generation

1-3 dendritic hexamethylenetetramine functionalization. *Applied Surface Science* 296, pp. 61–68. Available at: http://dx.doi.org/10.1016/j.apsusc.2014.01.039.

Marsh, G. 2002. Finding flaws in composites. *Reinforced Plastics* 46(12), pp. 42–46. Available at: https://linkinghub.elsevier.com/retrieve/pii/S0034361702802272.

Martin, K. 2008. *Analysis of Failure in Fibre Polymer Laminates The theory of Alfred Puck*. New York: Springer.

Masoumi, S. and Valipour, H. 2016. Effects of moisture exposure on the crosslinked epoxy system: An atomistic study. *Modelling and Simulation in Materials Science and Engineering* 24(3), p. 035011. Available at: http://stacks.iop.org/0965-0393/24/i=3/a=035011?key=crossref.9f00859d063d0b80497ec812578ae14e.

Maxwell, A.S., Broughton, W.R., Dean, G. and Sims, G.D. 2005. *Review of Accelerated Ageing Methods and Lifetime Prediction Techniques for Polymeric Materials*.

Mazor, A., Broutman, L.J. and Eckstein, B.H. 1978. Effect of long-term water exposure on properties of carbon and graphite fiber reinforced epoxies. *Polymer Engineering and Science* 18(5), pp. 341–349. Available at: http://doi.wiley.com/10.1002/pen.760180502.

McCrory, J. 2016. *dvanced Acoustic Emission (AE) monitoring techniques for aerospace structures*. Cardiff Univeristy. Available at: http://orca.cf.ac.uk/id/eprint/89212.

Megiatto, J.D., Ramires, E.C. and Frollini, E. 2010. Phenolic matrices and sisal fibers modified with hydroxy terminated polybutadiene rubber: Impact strength, water absorption, and morphological aspects of thermosets and composites. *Industrial Crops* *and Products* 31(1), pp. 178–184. Available at: https://linkinghub.elsevier.com/retrieve/pii/S0926669009001897.

Melo, R.Q.C., Santos, W.R.G., Barbosa de Lima, A.G., Lima, W.M.P.B., Silva, J. V. and Farias, R.P. 2018. Water Absorption Process in Polymer Composites: Theory Analysis and Applications., pp. 219–249. Available at: http://link.springer.com/10.1007/978-3-319-91062-8_7.

Meng, M., Rizvi, M.J., Grove, S.M. and Le, H.R. 2015. Effects of hygrothermal stress on the failure of CFRP composites. *Composite Structures* 133, pp. 1024–1035. doi: 10.1016/j.compstruct.2015.08.016.

Meng, M., Rizvi, M.J., Le, H.R. and Grove, S.M. 2016. Multi-scale modelling of moisture diffusion coupled with stress distribution in CFRP laminated composites. *Composite Structures* 138, pp. 295–304. doi: 10.1016/j.compstruct.2015.11.028.

Meredith, J., Bilson, E., Powe, R., Collings, E. and Kirwan, K. 2015. A performance versus cost analysis of prepreg carbon fibre epoxy energy absorption structures. *Composite Structures* 124, pp. 206–213. Available at: https://www.sciencedirect.com/science/article/pii/S0263822315000343 [Accessed: 9 March 2018].

Miller, R.K., Hill, E. v. K. and Moore, P.O. eds. 2005. *Acoustic Emission Testing, Nondestructive Testing Handbook, Third Edition, Volume 6 of Nondestructive testing handbook*. 3rd ed. American Society for Nondestructive Testing, 2005.

Miller, R.K. and McIntire, P. eds. 1987. *Nondestructive testing handbook. Vol. 5,* *Acoustic emission testing*. 2nd ed. Columbus, OH : American Society for Nondestructive Testing.

Mrad, H., Alix, S., Migneault, S., Koubaa, A. and Perré, P. 2018. Numerical and experimental assessment of water absorption of wood-polymer composites. *Measurement* 115, pp. 197–203. Available at: https://linkinghub.elsevier.com/retrieve/pii/S0263224117306358.

Muñoz, E. and García-Manrique, J.A. 2015. Water Absorption Behaviour and Its Effect on the Mechanical Properties of Flax Fibre Reinforced Bioepoxy Composites. *International Journal of Polymer Science* 2015, pp. 1–10. Available at: http://www.hindawi.com/journals/ijps/2015/390275/.

Otaluka, E.P., Arnold, C. and Alston, S. 2015. THE LONG TERM EFFECTS OF WATER ABSORPTION, DESORPTION AND RE-ABSORPTION IN CARBON-FIBRE / EPOXY COMPOSITES. In: *10th International Conference on Composite Science and Technology*. Lisboa. Available at: http://www.dem.ist.utl.pt/iccst10/files/ICCST10_Proceedings/pdf/WEB_PAPERS/ICCST10_Upload_208.pdf.

Papa, I., Lopresto, V. and Langella, A. 2021. Ultrasonic inspection of composites materials: Application to detect impact damage. *International Journal of Lightweight Materials and Manufacture* 4(1), pp. 37–42. Available at: https://doi.org/10.1016/j.ijlmm.2020.04.002.

Pastore, C. and Gowayed, Y. 2008. Structure and mechanics of 2D and 3D textile composites. In: *Structure and Mechanics of Textile Fibre Assemblies*. Elsevier, pp. 145–

190. Available at: https://linkinghub.elsevier.com/retrieve/pii/B9780081026199000055.

Pérez-Pacheco, E., Cauich-Cupul, J.I., Valadez-González, A. and Herrera-Franco, P.J. 2013. Effect of moisture absorption on the mechanical behavior of carbon fiber/epoxy matrix composites. *Journal of Materials Science* 48(5), pp. 1873–1882. Available at: https://link.springer.com/article/10.1007/s10853-012-6947-4#citeas.

Perrier, A., Touchard, F., Chocinski-Arnault, L. and Mellier, D. 2016. Mechanical behaviour analysis of the interface in single hemp yarn composites: DIC measurements and FEM calculations. *Polymer Testing* 52, pp. 1–8. doi: 10.1016/j.polymertesting.2016.03.019.

Perrier, A., Touchard, F., Chocinski-Arnault, L. and Mellier, D. 2017. Influence of water on damage and mechanical behaviour of single hemp yarn composites. *Polymer Testing* 57, pp. 17–25. doi: 10.1016/j.polymertesting.2016.10.035.

Peters, P.W.M. and Andersen, S.I. 1989. The Influence of Matrix Fracture Strain and Interface Strength on Cross-Ply Cracking in CFRP in the Temperature Range of -100°C to +100°C. *Journal of Composite Materials* 23(9), pp. 944–960. doi: 10.1177/002199838902300905.

Peters, W.H. and Ranson, W.F. 1982. Digital Imaging Techniques In Experimental Stress Analysis. *Optical Engineering* 21(3). Available at: http://opticalengineering.spiedigitallibrary.org/article.aspx?doi=10.1117/12.7972925.

Physical Acoustics Corporation 2004. *PCI-2 Baed AE System*.

Pollock, A.A. 1986. Classical wave theory in practical AE testing. *Progress in Acoustic Emission III-JAP Society of Non-Destructive Testing* , pp. 708–721.

Post, N.L., Riebel, F., Zhou, A., Keller, T., Case, S.W. and Lesko, J.J. 2009. Investigation of 3D moisture diffusion coefficients and damage in a pultruded E-glass/Polyester structural composite. *Journal of Composite Materials* 43(1), pp. 75–96. doi: 10.1177/0021998308098152.

Pullin, R., Eaton, M.J., Hensman, J.J., Holford, K.M., Worden, K. and Evans, S.L. 2010. Validation of Acoustic Emission (AE) Crack Detection in Aerospace Grade Steel Using Digital Image Correlation. *Applied Mechanics and Materials* 24–25, pp. 221–226. Available at: https://www.scientific.net/AMM.24-25.221.

Rao, R.M.V.G.K., Balasubramanian, N. and Chanda, M. 1984a. Factors Affecting Moisture Absorption in Polymer Composites Part I: Influence of Internal Factors. *Journal of Reinforced Plastics and Composites* 3(3), pp. 232–245. Available at: http://journals.sagepub.com/doi/10.1177/073168448400300304.

Rao, R.M.V.G.K., Chanda, M. and Balasubramanian, N. 1984b. Factors Affecting Moisture Absorption in Polymer Composites Part II: Influence of External Factors. *Journal of Reinforced Plastics and Composites* 3(3), pp. 246–253. Available at: http://journals.sagepub.com/doi/10.1177/073168448400300305.

Ray, B.C. 2006. Temperature effect during humid ageing on interfaces of glass and carbon fibers reinforced epoxy composites. *Journal of Colloid and Interface Science* 298(1), pp. 111–117. Available at: https://www.sciencedirect.com/science/article/pii/S0021979705012701 [Accessed: 19

April 2018].

Ren, P., Liang, G. and Zhang, Z. 2006. Influence of epoxy sizing of carbon-fiber on the properties of carbon fiber/cyanate ester composites. *Polymer Composites* 27(5), pp. 591–598. Available at: http://doi.wiley.com/10.1002/pc.20230.

Rindorf, H.J. 1981. *Acoustic emission source location in theory and in practice*. Brüel & Kjær.

Ríos-Soberanis, C.R. 2011. Acoustic Emission Technique, an Overview as a Characterization Tool in Materials Science. *Journal of Applied Research and Technology* 9(03). Available at: http://www.jart.icat.unam.mx/index.php/jart/article/view/431.

Rueden, C.T., Schindelin, J., Hiner, M.C., Dezonia, B.E., Walter, A.E., Arena, E.T. and Eliceiri, K.W. 2017. ImageJ2 : ImageJ for the next generation of scientific image data., pp. 1–26. doi: 10.1186/s12859-017-1934-z.

Saeed, M.U., Chen, Z., Chen, Z. and Li, B. 2014. Compression behavior of laminated composites subjected to damage induced by low velocity impact and drilling. *Composites Part B: Engineering* 56, pp. 815–820. Available at: https://www.sciencedirect.com/science/article/pii/S1359836813005301 [Accessed: 9 March 2018].

Saito, H. and Kimpara, I. 2009. Damage evolution behavior of CFRP laminates under post-impact fatigue with water absorption environment. *Composites Science and Technology* 69(6), pp. 847–855. Available at: https://www.sciencedirect.com/science/article/pii/S0266353808001188 [Accessed: 19

April 2018].

Sales, R., Thim, G. and Brunelli, D. 2017. Understanding the water uptake in F-161 glass-epoxy composites using the techniques of luminescence spectroscopy and FT-NIR. *Polímeros* 27(2), pp. 171–182. Available at: http://www.scielo.br/scielo.php?script=sci_arttext&pid=S0104-14282017000200171&lng=en&tlng=en.

Schreier, H., Orteu, J.-J. and Sutton, M.A. 2009. *Image Correlation for Shape, Motion and Deformation Measurements*. Boston, MA: Springer US. Available at: http://link.springer.com/10.1007/978-0-387-78747-3.

Schwartz, P. 2008. *Structure and Mechanics of Textile Fibre Assemblies*. Woodhead: Woodhead Publishing.

Selzer, R. 1997. Mechanical properties and failure behaviour of carbon fibre-reinforced polymer composites under the influence of moisture. (96), pp. 595–604.

Seo, H., Jang, H. and Lee, I. 2017. Experimental investigation of salt fog effect on the CFRP laminates. *Advanced Composite Materials* 26(4), pp. 321–334. Available at: http://dx.doi.org/10.1080/09243046.2016.1187822.

Sethi, S. and Ray, B.C. 2015. Environmental effects on fibre reinforced polymeric composites: Evolving reasons and remarks on interfacial strength and stability. *Advances in Colloid and Interface Science* 217, pp. 43–67. Available at: http://dx.doi.org/10.1016/j.cis.2014.12.005.

Shen, C.-H. and S. Springer, G. 1976. Moisture Absorption and Desorption of

Composite Materials. *Journal of Composite Materials* 10(1), pp. 2–20. Available at: https://doi.org/10.1177/002199837601000101.

Shenoi, R A and Wellicome, J.F. 1993. *Composite Materials in Maritime Structures, Volume 1, Fundamental Aspects*. New York: Cambridge University Press.

Shi, S.Q. 2007. Diffusion model based on Fick's second law for the moisture absorption process in wood fiber-based composites: is it suitable or not? *Wood Science and Technology* 41(8), pp. 645–658. Available at: http://link.springer.com/10.1007/s00226-006-0123-4.

Silberschmidt, V. V 2016. *Dynamic Deformation, Damage and Fracture in Composite Materials and Structures*. Cambridge: Woodhead Publishing.

Smith, R., Jones, L., Zeqiri, B. and Hodnett, M. 1998a. Ultrasonic C-scan standardisation for fibre-reinforced polymer composites - minimising the uncertainties in attenuation measurements. *Insight: Non-Destructive Testing and Condition Monitoring* 40, pp. 34–43.

SMITH, R.A., JONES, L.D., WILLSHER, S.J. and MARRIOTT, A.B. 1998. Diffraction and shadowing errors in -6 dB defect sizing of delaminations in composites. *Insight: Non-Destructive Testing and Condition Monitoring* 40(1), pp. 44–49.

Smith, R.A., Zeqiri, B., Jones, L.D. and Hodnett, M. 1998b. Nonlinear Propagation in Water and its Effect on Ultrasonic C-scanning. *Insight: Non- Destructive Testing and Condition Monitoring* 40(1), pp. 12–19.

Spragg, C.J., Drzal, L.T. and Composites, A.C.D.-30 on H.M.F. and T. 1996. *Fiber, Matrix,* *and Interface Properties*. ASTM. Available at: https://books.google.co.uk/books?id=1DQ5LZG-hQ0C.

Sun, P., Zhao, Y., Luo, Y. and Sun, L. 2011. Effect of temperature and cyclic hygrothermal aging on the interlaminar shear strength of carbon fiber/bismaleimide (BMI) composite. *Materials and Design* 32(8–9), pp. 4341–4347. Available at: http://dx.doi.org/10.1016/j.matdes.2011.04.007.

Surathi, P. and Karbhari, V.M. 2006. *Hygrothermal Effects on Durability and Moisture Kinetics of Fiber-reinforced Polymer Composites*. San Diego. Available at: https://rosap.ntl.bts.gov/view/dot/27688.

Takeda, S.I., Tsukada, T., Sugimoto, S. and Iwahori, Y. 2014. Monitoring of water absorption in CFRP laminates using embedded fiber Bragg grating sensors. *Composites Part A: Applied Science and Manufacturing* 61, pp. 163–171. Available at: http://dx.doi.org/10.1016/j.compositesa.2014.02.018.

Torres, A., Abad, M.J., Cano, J., Lo, J., Lo, I., Nogueira, P. and Rami, C. 2000. Effect of Water Sorption on the Structure and Mechanical Properties of an Epoxy Resin System. *Journal of Applied Polymer Science* 80, pp. 71–80.

Tranchard, P., Duquesne, S., Samyn, F., Estèbe, B. and Bourbigot, S. 2017. Kinetic analysis of the thermal decomposition of a carbon fibre-reinforced epoxy resin laminate. *Journal of Analytical and Applied Pyrolysis* 126(July), pp. 14–21. Available at: http://dx.doi.org/10.1016/j.jaap.2017.07.002.

Tsenoglou, C.J., Pavlidou, S. and Papaspyrides, C.D. 2006. Evaluation of interfacial relaxation due to water absorption in fiber–polymer composites. *Composites Science and Technology* 66(15), pp. 2855–2864. Available at: https://linkinghub.elsevier.com/retrieve/pii/S0266353806000698.

Vanlandingham, M.R., Eduljee, R.F. and Gillespie, J.W. 1998. Moisture Diffusion in Epoxy Systems. (July), pp. 787–798.

Vasiliev, V. V and Morozov, E. V 2007. *Advanced Mechanics of Composite Materials*. 2nd ed. Oxford: Elsevier.

Wong, T.C. and Broutman, L.J. 1985. Water in epoxy resins Part II. Diffusion mechanism. *Polymer Engineering and Science* 25(9), pp. 529–534. Available at: http://doi.wiley.com/10.1002/pen.760250904.

Wright, W.W. 1981. The effect of diffusion of water into epoxy resins and their carbon-fibre reinforced composites. *Composites* 12(3), pp. 201–205. Available at: https://linkinghub.elsevier.com/retrieve/pii/001043618190505X.

Wróbel, G. and Pawlak, S. 2007. A comparison study of the pulse-echo and through-transmission ultrasonics in glass / epoxy composites. *Journal of Achievements in Materials and Manufacturing Engineering* 22(2), pp. 51–54.

Xiao, S., Wang, P., Soulat, D. and Legrand, X. 2019. Structure and mechanics of braided fabrics. In: *Structure and Mechanics of Textile Fibre Assemblies*. Elsevier, pp. 217–263. Available at: https://linkinghub.elsevier.com/retrieve/pii/B9780081026199000079.

Xie, M. and Adams, D.F. 1995. Study of three- and four-point shear testing of unidirectional composite materials. *Composites* 26(9), pp. 653–659. Available at:

https://linkinghub.elsevier.com/retrieve/pii/0010436195989147.

El Yagoubi, J., Lubineau, G., Traidia, A. and Verdu, J. 2015. Monitoring and simulations of hydrolysis in epoxy matrix composites during hygrothermal aging. *Composites Part A: Applied Science and Manufacturing* 68, pp. 184–192. Available at: https://linkinghub.elsevier.com/retrieve/pii/S1359835X14003121.

Youssef, G., Fréour, S. and Jacquemin, F. 2009. Stress-dependent Moisture Diffusion in Composite Materials. *Journal of Composite Materials* 43(15), pp. 1621–1637. doi: 10.1177/0021998309339222.

Zafar, A., Bertocco, F., Schjødt-Thomsen, J. and Rauhe, J.C. 2012. Investigation of the long term effects of moisture on carbon fibre and epoxy matrix composites. *Composites Science and Technology* 72(6), pp. 656–666. Available at: http://dx.doi.org/10.1016/j.compscitech.2012.01.010.

Zeqiri, B. and Hodnett, M. 1998. A Systematic Investigation of the Effects of Collimators on the Characteristics of Ultrasonic NDT Transducers. *Insight: Non-Destructive Testing and Condition Monitoring* 40(1), pp. 28–33.

Zeqiri, B., Hodnett, M., Smith, R.A. and Scudder, L.P. 1998. An Assessment of Pulse-Echo and Hydrophone Methods for Charactersing Ultrasonic NDT Transducers. *Insight: Non-Destructive Testing and Condition Monitoring Monitoring* 40(1), pp. 20–27.

Zhang, D., Heider, D. and Jr, J.W.G. 2017. Void reduction of high-performance thermoplastic composites via oven vacuum bag processing. *Journal of Composite Materials* 51(30), pp. 4219–4230. doi: 10.1177/0021998317700700.

Zhang, S.Y. 2000. A simple approach to the evaluation of fiber/matrix interfacial shear strength and fracture toughness. *Composites Science and Technology* 60(1), pp. 145–148. doi: 10.1016/S0266-3538(99)00098-6.

Zhang, X., Wang, Y., Wan, B., Cai, G. and Qu, Y. 2019. Effect of specimen thicknesses on water absorption and flexural strength of CFRP laminates subjected to water or alkaline solution immersion. *Construction and Building Materials* 208, pp. 314–325. Available at: https://doi.org/10.1016/j.conbuildmat.2019.03.009.

Zhang, Z. and Richardson, M. 2011. Nondestructive Testing of Composite Materials. In: *Handbook of Multiphase Polymer Systems*. Chichester, UK: John Wiley & Sons, Ltd, pp. 777–796. Available at: http://doi.wiley.com/10.1002/9781119972020.ch20.

Zhuang, X. and Yan, X. 2005. Investigation of damage mechanisms in self-reinforced polyethylene composites by acoustic emission. *Composites Science and Technology* 66(3), pp. 444–449. doi: 10.1016/j.compscitech.2005.07.013.

Appendices

Appendix A (data sheets)

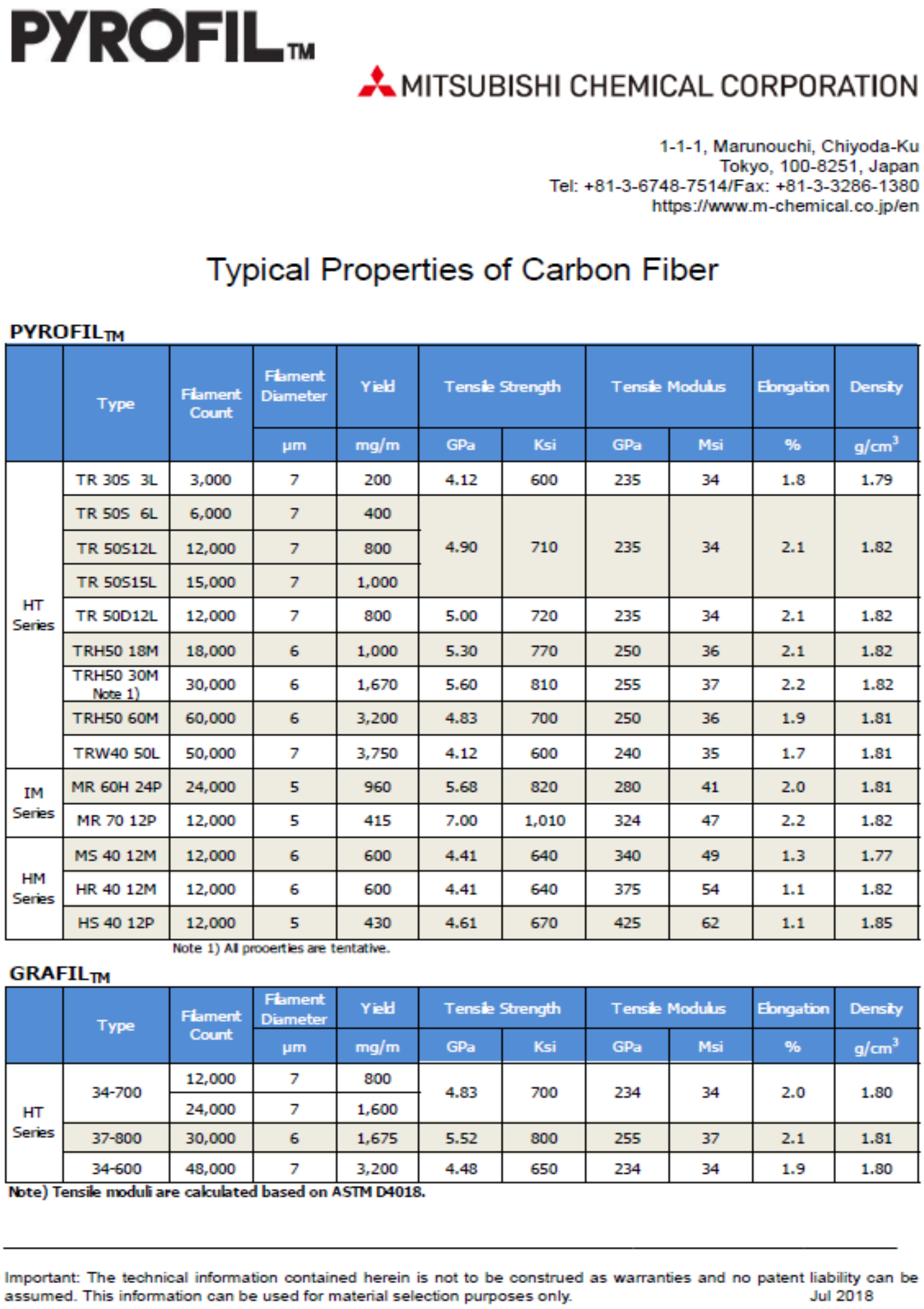

PYROFIL™

MITSUBISHI CHEMICAL CORPORATION

1-1-1, Marunouchi, Chiyoda-Ku
Tokyo, 100-8251, Japan
Tel: +81-3-6748-7514/Fax: +81-3-3286-1380
https://www.m-chemical.co.jp/en

Typical Properties of Carbon Fiber

PYROFIL™

	Type	Filament Count	Filament Diameter	Yield	Tensile Strength		Tensile Modulus		Elongation	Density
			µm	mg/m	GPa	Ksi	GPa	Msi	%	g/cm^3
HT Series	TR 30S 3L	3,000	7	200	4.12	600	235	34	1.8	1.79
	TR 50S 6L	6,000	7	400	4.90	710	235	34	2.1	1.82
	TR 50S12L	12,000	7	800						
	TR 50S15L	15,000	7	1,000						
	TR 50D12L	12,000	7	800	5.00	720	235	34	2.1	1.82
	TRH50 18M	18,000	6	1,000	5.30	770	250	36	2.1	1.82
	TRH50 30M Note 1)	30,000	6	1,670	5.60	810	255	37	2.2	1.82
	TRH50 60M	60,000	6	3,200	4.83	700	250	36	1.9	1.81
	TRW40 50L	50,000	7	3,750	4.12	600	240	35	1.7	1.81
IM Series	MR 60H 24P	24,000	5	960	5.68	820	280	41	2.0	1.81
	MR 70 12P	12,000	5	415	7.00	1,010	324	47	2.2	1.82
HM Series	MS 40 12M	12,000	6	600	4.41	640	340	49	1.3	1.77
	HR 40 12M	12,000	6	600	4.41	640	375	54	1.1	1.82
	HS 40 12P	12,000	5	430	4.61	670	425	62	1.1	1.85

Note 1) All prooerties are tentative.

GRAFIL™

	Type	Filament Count	Filament Diameter	Yield	Tensile Strength		Tensile Modulus		Elongation	Density
			µm	mg/m	GPa	Ksi	GPa	Msi	%	g/cm^3
HT Series	34-700	12,000	7	800	4.83	700	234	34	2.0	1.80
		24,000	7	1,600						
	37-800	30,000	6	1,675	5.52	800	255	37	2.1	1.81
	34-600	48,000	7	3,200	4.48	650	234	34	1.9	1.80

Note) Tensile moduli are calculated based on ASTM D4018.

Important: The technical information contained herein is not to be construed as warranties and no patent liability can be assumed. This information can be used for material selection purposes only.

Jul 2018

Figure 97: Data sheet for Pyrofil TR50S 15 (UD) and Pyrofil TR30S 3L (plain and twill) used in this study.

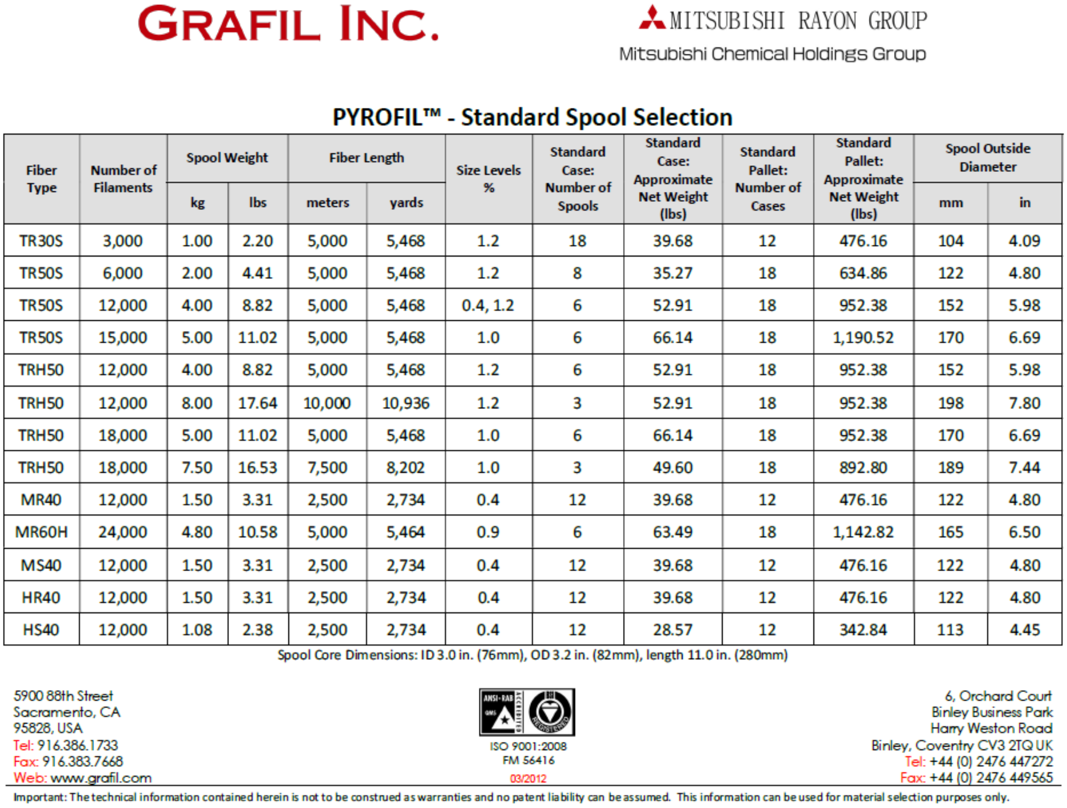

GRAFIL INC.

MITSUBISHI RAYON GROUP
Mitsubishi Chemical Holdings Group

PYROFIL™ - Standard Spool Selection

Fiber Type	Number of Filaments	Spool Weight		Fiber Length		Size Levels %	Standard Case: Number of Spools	Standard Case: Approximate Net Weight (lbs)	Standard Pallet: Number of Cases	Standard Pallet: Approximate Net Weight (lbs)	Spool Outside Diameter	
		kg	lbs	meters	yards						mm	in
TR30S	3,000	1.00	2.20	5,000	5,468	1.2	18	39.68	12	476.16	104	4.09
TR50S	6,000	2.00	4.41	5,000	5,468	1.2	8	35.27	18	634.86	122	4.80
TR50S	12,000	4.00	8.82	5,000	5,468	0.4, 1.2	6	52.91	18	952.38	152	5.98
TR50S	15,000	5.00	11.02	5,000	5,468	1.0	6	66.14	18	1,190.52	170	6.69
TRH50	12,000	4.00	8.82	5,000	5,468	1.2	6	52.91	18	952.38	152	5.98
TRH50	12,000	8.00	17.64	10,000	10,936	1.2	3	52.91	18	952.38	198	7.80
TRH50	18,000	5.00	11.02	5,000	5,468	1.0	6	66.14	18	952.38	170	6.69
TRH50	18,000	7.50	16.53	7,500	8,202	1.0	3	49.60	18	892.80	189	7.44
MR40	12,000	1.50	3.31	2,500	2,734	0.4	12	39.68	12	476.16	122	4.80
MR60H	24,000	4.80	10.58	5,000	5,464	0.9	6	63.49	18	1,142.82	165	6.50
MS40	12,000	1.50	3.31	2,500	2,734	0.4	12	39.68	12	476.16	122	4.80
HR40	12,000	1.50	3.31	2,500	2,734	0.4	12	39.68	12	476.16	122	4.80
HS40	12,000	1.08	2.38	2,500	2,734	0.4	12	28.57	12	342.84	113	4.45

Spool Core Dimensions: ID 3.0 in. (76mm), OD 3.2 in. (82mm), length 11.0 in. (280mm)

5900 88th Street
Sacramento, CA
95828, USA
Tel: 916.386.1733
Fax: 916.383.7668
Web: www.grafil.com

ISO 9001:2008
FM 56416
03/2012

6, Orchard Court
Binley Business Park
Harry Weston Road
Binley, Coventry CV3 2TQ UK
Tel: +44 (0) 2476 447272
Fax: +44 (0) 2476 449565

Important: The technical information contained herein is not to be construed as warranties and no patent liability can be assumed. This information can be used for material selection purposes only.

Figure 98: A technical report for Pyrofil TR50S 15 (UD) and Pyrofil TR30S 3L (plain and twill) used in this study.

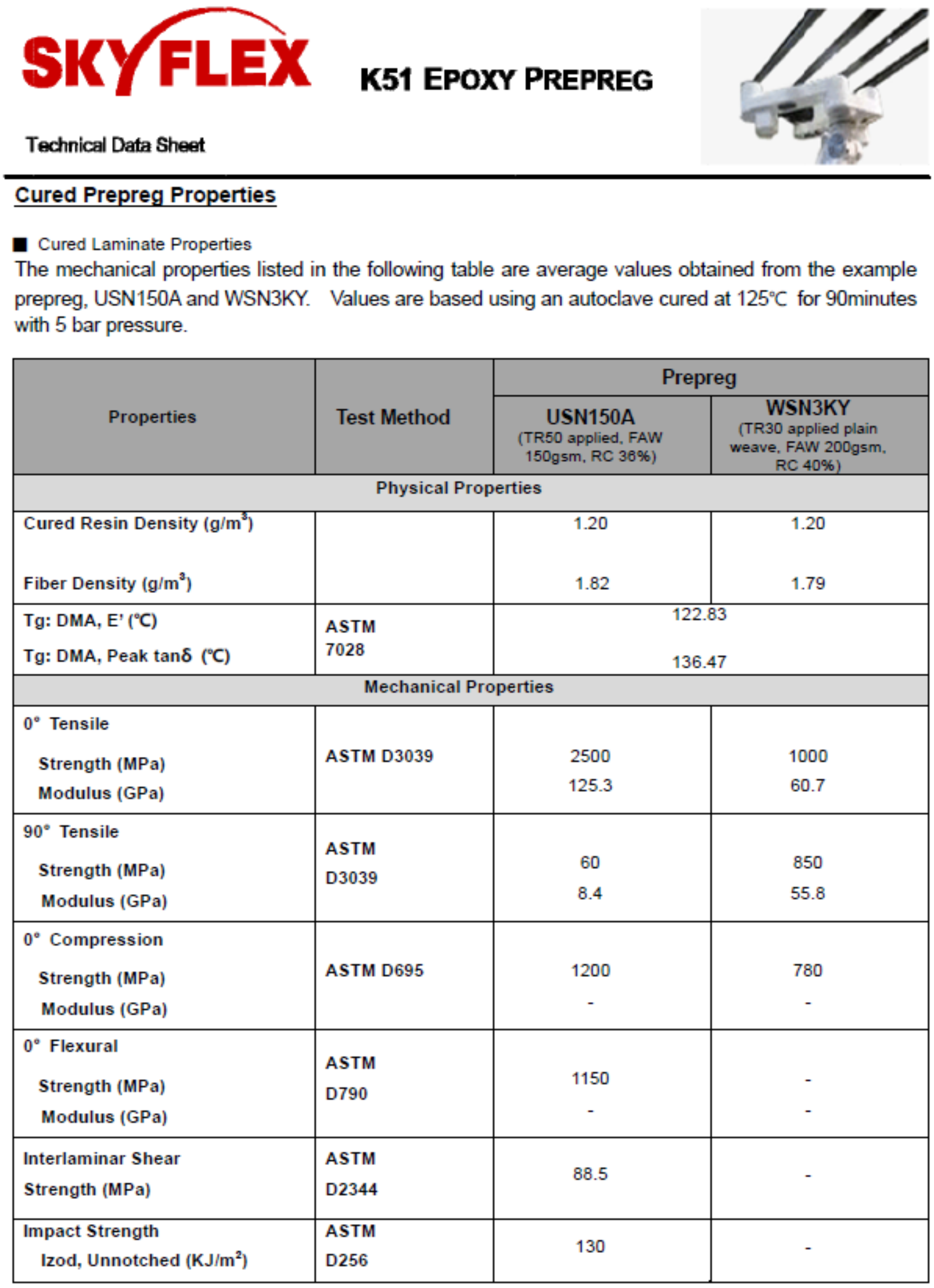

SKYFLEX

K51 EPOXY PREPREG

Technical Data Sheet

Cured Prepreg Properties

- Cured Laminate Properties

The mechanical properties listed in the following table are average values obtained from the example prepreg, USN150A and WSN3KY. Values are based using an autoclave cured at 125℃ for 90minutes with 5 bar pressure.

Properties	Test Method	Prepreg	
		USN150A (TR50 applied, FAW 150gsm, RC 36%)	**WSN3KY** (TR30 applied plain weave, FAW 200gsm, RC 40%)
Physical Properties			
Cured Resin Density (g/m^3) **Fiber Density (g/m^3)**		1.20 1.82	1.20 1.79
Tg: DMA, E' (℃) **Tg: DMA, Peak tanδ (℃)**	**ASTM 7028**	122.83 136.47	
Mechanical Properties			
0° Tensile **Strength (MPa)** **Modulus (GPa)**	**ASTM D3039**	2500 125.3	1000 60.7
90° Tensile **Strength (MPa)** **Modulus (GPa)**	**ASTM D3039**	60 8.4	850 55.8
0° Compression **Strength (MPa)** **Modulus (GPa)**	**ASTM D695**	1200 -	780 -
0° Flexural **Strength (MPa)** **Modulus (GPa)**	**ASTM D790**	1150 -	- -
Interlaminar Shear Strength (MPa)	**ASTM D2344**	88.5	-
Impact Strength **Izod, Unnotched (KJ/m^2)**	**ASTM D256**	130	-

Figure 99: Data sheet for Skyflex K51 epoxy resin used in this study.

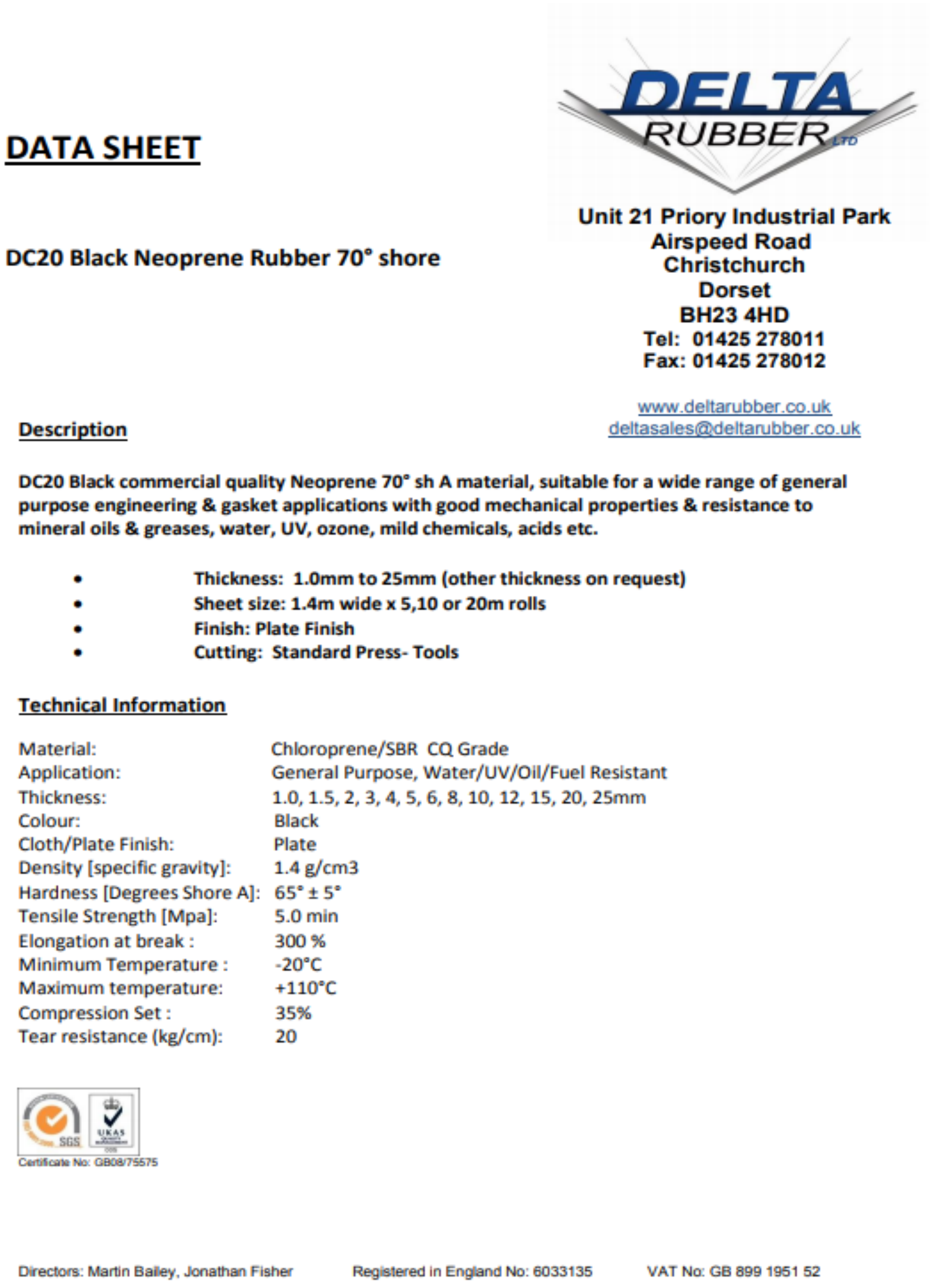

DATA SHEET

DELTA RUBBER LTD

Unit 21 Priory Industrial Park
Airspeed Road
Christchurch
Dorset
BH23 4HD
Tel: 01425 278011
Fax: 01425 278012

www.deltarubber.co.uk
deltasales@deltarubber.co.uk

DC20 Black Neoprene Rubber 70° shore

Description

DC20 Black commercial quality Neoprene 70° sh A material, suitable for a wide range of general purpose engineering & gasket applications with good mechanical properties & resistance to mineral oils & greases, water, UV, ozone, mild chemicals, acids etc.

- **Thickness: 1.0mm to 25mm (other thickness on request)**
- **Sheet size: 1.4m wide x 5,10 or 20m rolls**
- **Finish: Plate Finish**
- **Cutting: Standard Press- Tools**

Technical Information

Material:	Chloroprene/SBR CQ Grade
Application:	General Purpose, Water/UV/Oil/Fuel Resistant
Thickness:	1.0, 1.5, 2, 3, 4, 5, 6, 8, 10, 12, 15, 20, 25mm
Colour:	Black
Cloth/Plate Finish:	Plate
Density [specific gravity]:	1.4 g/cm3
Hardness [Degrees Shore A]:	65° ± 5°
Tensile Strength [Mpa]:	5.0 min
Elongation at break :	300 %
Minimum Temperature :	-20°C
Maximum temperature:	+110°C
Compression Set :	35%
Tear resistance (kg/cm):	20

Certificate No: GB08/75575

Directors: Martin Bailey, Jonathan Fisher   Registered in England No: 6033135   VAT No: GB 899 1951 52

Figure 100: Technical details for the neoprene rubber used in the diffusion test set up in this study.

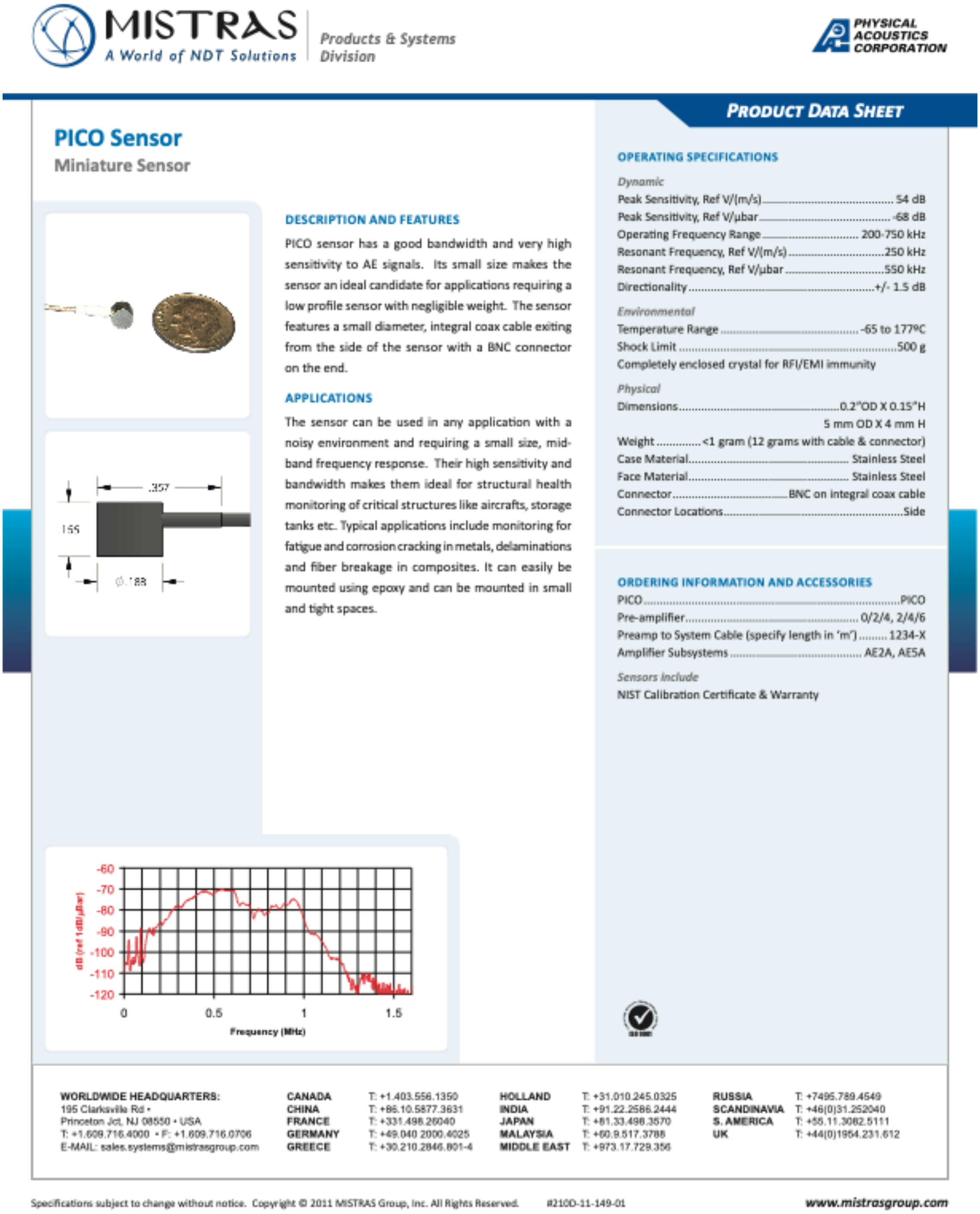

MISTRAS
A World of NDT Solutions
Products & Systems Division

PHYSICAL ACOUSTICS CORPORATION

PRODUCT DATA SHEET

PICO Sensor

Miniature Sensor

DESCRIPTION AND FEATURES

PICO sensor has a good bandwidth and very high sensitivity to AE signals. Its small size makes the sensor an ideal candidate for applications requiring a low profile sensor with negligible weight. The sensor features a small diameter, integral coax cable exiting from the side of the sensor with a BNC connector on the end.

APPLICATIONS

The sensor can be used in any application with a noisy environment and requiring a small size, mid-band frequency response. Their high sensitivity and bandwidth makes them ideal for structural health monitoring of critical structures like aircrafts, storage tanks etc. Typical applications include monitoring for fatigue and corrosion cracking in metals, delaminations and fiber breakage in composites. It can easily be mounted using epoxy and can be mounted in small and tight spaces.

OPERATING SPECIFICATIONS

Dynamic

Peak Sensitivity, Ref V/(m/s)	54 dB
Peak Sensitivity, Ref V/µbar	-68 dB
Operating Frequency Range	200-750 kHz
Resonant Frequency, Ref V/(m/s)	250 kHz
Resonant Frequency, Ref V/µbar	550 kHz
Directionality	+/- 1.5 dB

Environmental

Temperature Range	-65 to 177ºC
Shock Limit	500 g

Completely enclosed crystal for RFI/EMI immunity

Physical

Dimensions	0.2"OD X 0.15"H 5 mm OD X 4 mm H
Weight	<1 gram (12 grams with cable & connector)
Case Material	Stainless Steel
Face Material	Stainless Steel
Connector	BNC on integral coax cable
Connector Locations	Side

ORDERING INFORMATION AND ACCESSORIES

PICO	PICO
Pre-amplifier	0/2/4, 2/4/6
Preamp to System Cable (specify length in 'm')	1234-X
Amplifier Subsystems	AE2A, AE5A

Sensors include

NIST Calibration Certificate & Warranty

WORLDWIDE HEADQUARTERS:
195 Clarksville Rd •
Princeton Jct, NJ 08550 • USA
T: +1.609.716.4000 • F: +1.609.716.0706
E-MAIL: sales.systems@mistrasgroup.com

CANADA	T: +1.403.556.1350
CHINA	T: +86.10.5877.3631
FRANCE	T: +331.498.26040
GERMANY	T: +49.040 2000.4025
GREECE	T: +30.210.2846.801-4
HOLLAND	T: +31.010.245.0325
INDIA	T: +91.22.2586.2444
JAPAN	T: +81.33.498.3570
MALAYSIA	T: +60.9.517.3788
MIDDLE EAST	T: +973.17.729.356
RUSSIA	T: +7495.789.4549
SCANDINAVIA	T: +46(0)31.252040
S. AMERICA	T: +55.11.3082.5111
UK	T: +44(0)1954.231.612

Specifications subject to change without notice. Copyright © 2011 MISTRAS Group, Inc. All Rights Reserved. #210D-11-149-01

www.mistrasgroup.com

Figure 101: Technical details for PICO sensor.

Appendix B (all water absorption testing data)

Table 15: Weight record for all CLC specimens.

ID	Day (weight change, %)											
	1	2	3	4	5	10	15	20	25	30	35	40
UD 1	0	0.240	0.354	0.411	0.480	0.776	0.925	1.062	1.130	1.199	1.256	1.267
UD 2	0	0.217	0.434	0.456	0.570	0.901	1.072	1.198	1.278	1.335	1.403	1.403
UD 3	0	0.193	0.410	0.455	0.546	0.842	1.001	1.104	1.206	1.274	1.342	1.342
UD 4	0	0.148	0.388	0.434	0.468	0.787	0.936	1.027	1.118	1.187	1.255	1.278
UD 5	0	0.182	0.421	0.490	0.501	0.797	0.979	1.059	1.138	1.230	1.252	1.286
Ave. UD	0	0.196	0.401	0.449	0.513	0.821	0.983	1.090	1.174	1.245	1.302	1.316
Plain 1	0	0.178	0.456	0.495	0.515	0.728	0.881	0.990	1.080	1.129	1.159	1.218
Plain 2	0	0.189	0.446	0.476	0.496	0.764	0.943	1.022	1.121	1.141	1.210	1.240
Plain 3	0	0.178	0.406	0.456	0.486	0.793	0.941	1.021	1.090	1.169	1.199	1.229
Plain 4	0	0.188	0.416	0.456	0.466	0.733	0.902	0.981	1.060	1.120	1.189	1.209
Plain 5	0	0.218	0.396	0.446	0.466	0.743	0.842	0.981	1.060	1.120	1.169	1.189
Ave. Plain	0	0.190	0.424	0.466	0.486	0.763	0.902	0.999	1.082	1.136	1.185	1.217
Twill 1	0	0.193	0.427	0.457	0.498	0.802	0.955	1.046	1.137	1.198	1.259	1.269
Twill 2	0	0.234	0.437	0.498	0.508	0.822	0.944	1.046	1.168	1.198	1.249	1.310
Twill 3	0	0.183	0.457	0.467	0.487	0.822	0.985	1.066	1.147	1.198	1.269	1.320
Twill 4	0	0.233	0.445	0.466	0.536	0.830	0.982	1.083	1.184	1.255	1.285	1.306
Twill 5	0	0.213	0.446	0.446	0.507	0.800	0.922	1.043	1.094	1.165	1.195	1.266
Ave. Twill	0	0.211	0.442	0.467	0.507	0.815	0.957	1.057	1.146	1.203	1.252	1.294

Table 16: Weight record for all SBS specimens.

ID	Day (weight change, %)											
	1	2	3	4	5	10	15	20	25	30	35	40
UD 1	0	0.333	0.384	0.384	0.410	0.563	0.640	0.717	0.793	0.845	0.921	0.998
UD 2	0	0.307	0333	0.333	0358	0.563	0.640	0.742	0.870	0.896	0.998	1.024
UD 3	0	0.333	0.384	0.384	0.410	0.563	0.614	0.742	0.794	0.896	0.947	0.998
UD 4	0	0.282	0.436	0.436	0.461	0.564	0.641	0.743	0.846	0.897	0.974	0.974
UD 5	0	0.307	0.358	0.384	0.384	0.538	0.640	0.691	0.768	0.870	0.896	0.998
Ave. UD	0	0.312	0.379	0.384	0.405	0.558	0.635	0.727	0.814	0.881	0.947	0.998
Plain 1	0	0.224	0.267	0.267	0.289	0.467	0.556	0.645	0.733	0.822	0.845	0.911
Plain 2	0	0.298	0.321	0.321	0.321	0.458	0.596	0.687	0.733	0.802	0.847	0.916
Plain 3	0	0.255	0.278	0.301	0.301	0.463	0.556	0.649	0.672	0.811	0.811	0.904
Plain 4	0	0.267	0.311	0.311	0.311	0.467	0.578	0.690	0.756	0.778	0.867	1.001
Plain 5	0	0.296	0.319	0.319	0.319	0.433	0.592	0.615	0.706	0.751	0.865	0.956
Ave. Plain	0	0.272	0.299	0.304	0.308	0.458	0.576	0.657	0.720	0.793	0.847	0.938
Twill 1	0	0.255	0.255	0.255	0.278	0.441	0.580	0.673	0.742	0.766	0.882	0.998
Twill 2	0	0.272	0.295	0.295	0.317	0.431	0.567	0.703	0.726	0.794	0.884	0.975
Twill 3	0	0.252	0.252	0.321	0.344	0.413	0.551	0.619	0.780	0.826	0.895	1.009
Twill 4	0	0.257	0.257	0.257	0.350	0.421	0.561	0.654	0.724	0.794	0.888	0.981
Twill 5	0	0.274	0.297	0.297	0.343	0.434	0.594	0.685	0.685	0.799	0.891	0.982
Ave. Twill	0	0.262	0.271	0.285	0.327	0.428	0.570	0.667	0.731	0.796	0.888	0.989

Table 17: Weight record for all undamaged IDR specimens.

ID	Day (weight change, %)										
	1	2	3	4	5	10	15	20	25	30	35	40
UD 1	0	0.091	0.142	0.187	0.222	0.382	0.479	0.594	0.674	0.745	0.806	0.861
UD 2	0	0.087	0.141	0.182	0.216	0.373	0.473	0.586	0.664	0.738	0.799	0.852
UD 3	0	0.087	0.141	0.182	0.216	0.373	0.473	0.586	0.664	0.738	0.799	0.852
UD 4	0	0.083	0.134	0.171	0.214	0.368	0.467	0.579	0.661	0.733	0.790	0.850
UD 5	0	0.081	0.132	0.177	0.215	0.369	0.470	0.585	0.662	0.732	0.793	0.850
Ave. UD	0	0.087	0.138	0.179	0.217	0.374	0.473	0.587	0.667	0.738	0.799	0.854
Plain 1	0	0.101	0.150	0.187	0.229	0.377	0.457	0.544	0.623	0.688	0.720	0.786
Plain 2	0	0.085	0.128	0.163	0.197	0.330	0.417	0.511	0.575	0.644	0.688	0.733
Plain 3	0	0.092	0.123	0.160	0.194	0.326	0.410	0.504	0.570	0.639	0.681	0.724
Plain 4	0	0.086	0.124	0.161	0.192	0.324	0.410	0.500	0.566	0.630	0.657	0.723
Plain 5	0	0.084	0.122	0.157	0.191	0.322	0.412	0.504	0.567	0.622	0.677	0.720
Ave. Plain	0	0.090	0.130	0.166	0.201	0.336	0.421	0.513	0.580	0.645	0.688	0.737
Twill 1	0	0.103	0.128	0.163	0.189	0.329	0.415	0.516	0.577	0.635	0.684	0.731
Twill 2	0	0.092	0.121	0.155	0.193	0.327	0.412	0.512	0.579	0.631	0.682	0.728
Twill 3	0	0.086	0.125	0.157	0.190	0.325	0.408	0.511	0.577	0.634	0.682	0.721
Twill 4	0	0.089	0.119	0.158	0.196	0.324	0.411	0.509	0.567	0.634	0.677	0.720
Twill 5	0	0.089	0.129	0.159	0.193	0.325	0.412	0.511	0.571	0.636	0.680	0.723
Ave. Twill	0	0.092	0.124	0.158	0.192	0.326	0.411	0.512	0.574	0.634	0.681	0.724

Table 18: Weight record for all 20 joules IDR specimens.

ID	Day (weight change, %)										
	1	2	3	4	5	10	15	20	25	30	35	40
UD 1	0	0.095	0.155	0.198	0.239	0.401	0.506	0.623	0.699	0.776	0.831	0.882
UD 2	0	0.093	0.147	0.197	0.238	0.402	0.511	0.628	0.707	0.778	0.842	0.892
UD 3	0	0.092	0.151	0.197	0.235	0.407	0.507	0.632	0.709	0.782	0.837	0.892
UD 4	0	0.094	0.156	0.206	0.248	0.423	0.533	0.644	0.711	0.794	0.848	0.899
UD 5	0	0.093	0.154	0.205	0.247	0.421	0.530	0.644	0.720	0.788	0.848	0.894
Ave. UD	0	0.093	0.153	0.201	0.241	0.411	0.518	0.634	0.709	0.784	0.841	0.892
Plain 1	0	0.108	0.147	0.184	0.218	0.356	0.447	0.537	0.603	0.654	0.709	0.755
Plain 2	0	0.105	0.144	0.181	0.219	0.357	0.439	0.539	0.595	0.657	0.707	0.748
Plain 3	0	0.114	0.153	0.194	0.231	0.376	0.460	0.555	0.631	0.679	0.728	0.780
Plain 4	0	0.114	0.151	0.188	0.227	0.360	0.451	0.545	0.610	0.667	0.718	0.764
Plain 5	0	0.107	0.149	0.185	0.222	0.360	0.449	0.542	0.608	0.665	0.717	0.755
Ave. Plain	0	0.110	0.149	0.186	0.223	0.362	0.449	0.554	0.609	0.664	0.716	0.760
Twill 1	0	0.113	0.145	0.201	0.228	0.357	0.445	0.545	0.613	0.671	0.713	0.762
Twill 2	0	0.108	0.148	0.194	0.220	0.358	0.441	0.545	0.615	0.663	0.705	0.751
Twill 3	0	0.109	0.138	0.197	0.218	0.357	0.449	0.546	0.600	0.670	0.709	0.751
Twill 4	0	0.109	0.146	0.196	0.226	0.357	0.454	0.542	0.601	0.667	0.707	0.754
Twill 5	0	0.105	0.144	0.197	0.225	0.359	0.449	0.543	0.600	0.663	0.707	0.748
Ave. Twill	0	0.109	0.144	0.197	0.224	0.358	0.448	0.544	0.606	0.667	0.708	0.753

Table 19: Weight record for all 70 joules IDR specimens.

ID	Day (weight change, %)											
	1	2	3	4	5	10	15	20	25	30	35	40
UD 1	0	0.262	0.351	0.440	0.493	0.731	0.833	0.931	1.013	1.082	1.107	1.158
UD 2	0	0.128	0.198	0.257	0.310	0.508	0.622	0.735	0.813	0.883	0.936	0.980
UD 3	0	0.112	0.164	0.223	0.276	0.477	0.592	0.711	0.784	0.850	0.906	0.952
UD 4	0	0.125	0.189	0.239	0.286	0.467	0.576	0.693	0.770	0.837	0.894	0.942
UD 5	0	0.112	0.177	0.225	0.273	0.466	0.579	0.700	0.778	0.845	0.903	0.950
Ave. UD	0	0.087	0.138	0.179	0.217	0.374	0.473	0.587	0.667	0.738	0.799	0.854
Plain 1	0	0.392	0.420	0.488	0.516	0.669	0.769	0.886	0.994	0.936	1.071	1.135
Plain 2	0	0.366	0.419	0.488	0.489	0.662	0.756	0.841	0.990	1.017	1.071	1.139
Plain 3	0	0.327	0.396	0.423	0.461	0.626	0.702	0.816	0.839	0.889	0.954	1.056
Plain 4	0	0.394	0.422	0.415	0.548	0.650	0.708	0.883	0.878	0.997	1.104	1.147
Plain 5	0	0.291	0.355	0.360	0.414	0.563	0.645	0.728	0.838	0.872	0.946	0.999
Ave. Plain	0	0.354	0.402	0.435	0.486	0.634	0.716	0.831	0.908	0.942	1.029	1.095
Twill 1	0	0.259	0.310	0.381	0.428	0.567	0.656	0.764	0.846	0.919	0.947	0.984
Twill 2	0	0.303	0.410	0.423	0.449	0.631	0.710	0.839	0.905	0.957	1.017	1.052
Twill 3	0	0.266	0.294	0.402	0.425	0.575	0.685	0.770	0.849	0.925	0.959	1.017
Twill 4	0	0.279	0.358	0.399	0.453	0.595	0.696	0.781	0.829	0.930	0.969	1.016
Twill 5	0	0.252	0.310	0.375	0.439	0.571	0.677	0.765	0.815	0.894	0.962	0.984
Ave. Twill	0	0.272	0.336	0.396	0.439	0.588	0.685	0.784	0.849	0.925	0.971	1.011

Table 20: Weight record for all water diffusion specimens (1/2).

ID	Day (weight change, %)											
	1	2	3	5	6	7	8	9	10	14	15	16
UD 1	0	0.434	0.723	1.000	1.105	1.184	1.223	1.302	1.329	1.421	1.394	1.434
UD 2	0	0.405	0.628	0.954	1.020	1.098	1.164	1.229	1.242	1.334	1.347	1.347
UD 3	0	0.409	0.673	0.977	1.043	1.122	1.201	1.254	1.294	1.386	1.373	1.400
UD 4	0	0.433	0.683	0.985	1.050	1.142	1.208	1.234	1.313	1.379	1.366	1.392
UD 5	0	0.380	0.654	0.929	1.047	1.099	1.191	1.230	1.270	1.335	1.348	1.348
Ave. UD	0	0.412	0.672	0.969	1.053	1.129	1.197	1.250	1.289	1.371	1.366	1.384
Plain 1	0	0.418	0.621	0.836	0.944	1.016	1.063	1.135	1.147	1.255	1.267	1.279
Plain 2	0	0.411	0.605	0.883	0.944	1.004	1.101	1.125	1.173	1.234	1.246	1.270
Plain 3	0	0.356	0.557	0.806	0.878	0.996	1.032	1.103	1.150	1.198	1.198	1.233
Plain 4	0	0.386	0.596	0.865	0.946	1.017	1.087	1.145	1.180	1.262	1.274	1.297
Plain 5	0	0.379	0.598	0.851	0.943	1.012	1.069	1.150	1.184	1.288	1.299	1.310
Ave. Plain	0	0.390	0.595	0.848	0.931	1.009	1.070	1.132	1.167	1.247	1.257	1.278
Twill 1	0	0.474	0.648	0.947	1.010	1.059	1.122	1.209	1.209	1.271	1.296	1.284
Twill 2	0	0.423	0.641	0.931	1.016	1.088	1.125	1.197	1.221	1.306	1.306	1.306
Twill 3	0	0.470	0.668	0.928	1.027	1.089	1.151	1.188	1.225	1.324	1.287	1.324
Twill 4	0	0.466	0.667	0.907	0.995	1.070	1.133	1.159	1.196	1.272	1.272	1.297
Twill 5	0	0.447	0.695	0.966	1.036	1.107	1.189	1.272	1.295	1.354	1.354	1.401
Ave. Twill	0	0.456	0.664	0.936	1.017	1.083	1.144	1.205	1.229	1.306	1.303	1.322
ID	Day (weight change, %)											
	17	20	22	23	24	27	29	31	34	36	38	41
UD 1	1.421	1.460	1.421	1.421	1.421	1.434	1.473	1.473	1.447	1.473	1.460	1.447
UD 2	1.373	1.386	1.399	1.373	1.360	1.386	1.399	1.399	1.373	1.360	1.386	1.347
UD 3	1.386	1.400	1.360	1.386	1.400	1.413	1.400	1.413	1.400	1.386	1.400	1.400
UD 4	1.405	1.431	1.379	1.418	1.392	1.366	1.418	1.418	1.418	1.405	1.418	1.405
UD 5	1.374	1.374	1.374	1.401	1.414	1.387	1.361	1.387	1.335	1.374	1.361	1.374
Ave. UD	1.392	1.410	1.386	1.400	1.397	1.397	1.410	1.418	1.394	1.400	1.405	1.394
Plain 1	1.314	1.326	1.314	1.326	1.314	1.326	1.314	1.350	1.326	1.326	1.338	1.326
Plain 2	1.282	1.294	1.318	1.294	1.294	1.294	1.318	1.306	1.331	1.343	1.306	1.282
Plain 3	1.281	1.305	1.316	1.305	1.281	1.293	1.281	1.305	1.293	1.316	1.305	1.269
Plain 4	1.332	1.344	1.320	1.332	1.309	1.320	1.367	1.355	1.379	1.344	1.344	1.367
Plain 5	1.333	1.379	1.356	1.333	1.322	1.322	1.356	1.368	1.379	1.345	1.379	1.356
Ave. Plain	1.309	1.330	1.325	1.318	1.304	1.311	1.327	1.337	1.342	1.335	1.334	1.320
Twill 1	1.296	1.334	1.321	1.309	1.334	1.346	1.321	1.359	1.334	1.346	1.346	1.346
Twill 2	1.354	1.379	1.367	1.342	1.367	1.379	1.367	1.379	1.403	1.379	1.391	1.367
Twill 3	1.324	1.361	1.324	1.349	1.349	1.349	1.349	1.374	1.361	1.349	1.374	1.349
Twill 4	1.272	1.310	1.322	1.310	1.310	1.297	1.297	1.310	1.347	1.310	1.310	1.322
Twill 5	1.437	1.413	1.437	1.437	1.413	1.413	1.413	1.425	1.448	1.401	1.413	1.448
Ave. Twill	1.337	1.359	1.354	1.349	1.354	1.357	1.349	1.369	1.379	1.357	1.367	1.366

Table 21: Weight record for all water diffusion specimens (2/2).

ID	Day (weight change, %)											
	43	45	48	50	52	55	57	59	62	66	69	72
UD 1	1.421	1.460	1.408	1.408	1.447	1.434	1.421	1.421	1.394	1.408	1.394	1.408
UD 2	1.360	1.373	1.360	1.347	1.347	1.360	1.347	1.334	1.307	1.334	1.320	1.334
UD 3	1.373	1.400	1.373	1.386	1.386	1.400	1.386	1.373	1.347	1.373	1.386	1.373
UD 4	1.379	1.392	1.392	1.405	1.379	1.392	1.366	1.366	1.352	1.366	1.366	1.366
UD 5	1.361	1.374	1.361	1.374	1.348	1.348	1.335	1.348	1.322	1.348	1.348	1.335
Ave. UD	1.379	1.400	1.379	1.384	1.381	1.387	1.371	1.368	1.345	1.366	1.363	1.363
Plain 1	1.326	1.326	1.326	1.326	1.350	1.290	1.350	1.326	1.314	1.314	1.326	1.326
Plain 2	1.306	1.318	1.306	1.306	1.318	1.294	1.306	1.282	1.331	1.306	1.318	1.306
Plain 3	1.293	1.316	1.316	1.316	1.305	1.328	1.316	1.316	1.293	1.316	1.316	1.293
Plain 4	1.344	1.367	1.367	1.355	1.355	1.379	1.355	1.332	1.355	1.367	1.367	1.355
Plain 5	1.368	1.414	1.368	1.368	1.356	1.356	1.356	1.356	1.368	1.379	1.379	1.368
Ave. Plain	1.327	1.348	1.337	1.335	1.337	1.330	1.337	1.323	1.332	1.337	1.342	1.330
Twill 1	1.371	1.334	1.321	1.334	1.346	1.359	1.346	1.346	1.371	1.359	1.346	1.359
Twill 2	1.379	1.391	1.367	1.391	1.379	1.379	1.391	1.354	1.354	1.379	1.391	1.367
Twill 3	1.361	1.349	1.361	1.386	1.349	1.361	1.374	1.349	1.374	1.374	1.374	1.386
Twill 4	1.347	1.322	1.335	1.335	1.347	1.310	1.347	1.347	1.335	1.310	1.335	1.335
Twill 5	1.448	1.437	1.460	1.460	1.437	1.448	1.425	1.425	1.425	1.437	1.437	1.448
Ave. Twill	1.381	1.366	1.369	1.381	1.372	1.371	1.377	1.364	1.372	1.371	1.376	1.379

ID	Day (weight change, %)										
	76	80	83	87	90	94	97	100	Dry 105	Dry 110	Dry 115
UD 1	1.381	1.381	1.408	1.381	1.368	1.368	1.368	1.368	0.250	-0.013	-0.013
UD 2	1.347	1.347	1.320	1.320	1.307	1.307	1.307	1.307	0.235	-0.065	-0.078
UD 3	1.386	1.347	1.347	1.360	1.347	1.347	1.347	1.320	0.277	0.053	0.013
UD 4	1.366	1.339	1.366	1.352	1.352	1.339	1.339	1.326	0.289	0.013	0
UD 5	1.335	1.348	1.361	1.309	1.322	1.296	1.309	1.309	0.249	0	-0.039
Ave. UD	1.363	1.352	1.360	1.345	1.339	1.331	1.334	1.326	0.260	-0.003	-0.024
Plain 1	1.326	1.338	1.362	1.326	1.350	1.338	1.338	1.338	0.239	-0.024	-0.036
Plain 2	1.331	1.306	1.306	1.331	1.318	1.306	1.306	1.306	0.242	0.012	-0.024
Plain 3	1.340	1.340	1.340	1.316	1.316	1.316	1.316	1.316	0.285	0.012	-0.059
Plain 4	1.344	1.320	1.344	1.355	1.320	1.355	1.344	1.355	0.315	0.012	-0.023
Plain 5	1.368	1.356	1.379	1.356	1.356	1.379	1.368	1.368	0.322	0.034	-0.023
Ave. Plain	1.342	1.332	1.346	1.337	1.332	1.339	1.335	1.337	0.281	0.009	-0.033
Twill 1	1.334	1.346	1.371	1.334	1.334	1.359	1.346	1.346	0.212	0	-0.037
Twill 2	1.391	1.379	1.367	1.367	1.379	1.379	1.367	1.367	0.181	-0.048	-0.085
Twill 3	1.398	1.374	1.374	1.374	1.386	1.349	1.374	1.386	0.210	-0.012	-0.049
Twill 4	1.347	1.335	1.335	1.335	1.335	1.335	1.322	1.335	0.239	0.025	-0.025
Twill 5	1.437	1.448	1.448	1.460	1.460	1.484	1.460	1.425	0.330	0.035	0.012
Ave. Twill	1.381	1.376	1.379	1.374	1.379	1.381	1.374	1.372	0.235	0	-0.037

Table 22: Weight record for all samples used for the effects of moisture absorption on the interlaminar damage mechanism of UD CFRP.

ID	Day (weight change, %)											
	1	2	3	4	5	7	8	9	10	11	13	15	17
UD 1	0		0.678		Tested after 3 days of water immersion								
UD 2	0		0.682										
UD 3	0		0.630										
UD 4	0		0.679										
UD 5	0		0.605										
UD 6	0	0.406	0.684	0.760	0.811	0989	1.065	1.141	Tested after 9 days of water immersion				
UD 7	0	0.329	0.455	0.557	0.582	0.860	0.962	0.987					
UD 8	0	0.353	0.453	0.605	0.705	0.856	0.957	0.982					
UD 9	0	0.383	0.510	0.689	0.766	0.919	0.995	1.072					
UD 10	0	0.355	0.507	0.634	0.710	0.913	0.964	1.015					
UD 11	0	0.437	0.566	0.720	0.797	1.003	1.054	1.131	1.106	1.209	1.260	1.311	1.363
UD 12	0	0.425	0.600	0.650	0.800	0.950	0.975	1.050	1.100	1.125	1.200	1.300	1.350
UD 13	0	0.305	0.432	0.635	0.762	0.914	0.965	0.990	1.066	1.092	1.193	1.295	1.195
UD 14	0	0.300	0.476	0.601	0.726	0.901	0.951	1.002	1.027	1.052	1.152	1.227	1.252
UD 15	0	0.303	0.531	0.607	0.759	0.910	0.961	1.037	1.088	1.138	1.214	1.265	1.315
UD 16	0	0.354	0.531	0.657	0.783	0.960	0.985	1.061	1.112	1.162	1.238	1.263	1.339
UD 17	0	0.352	0.528	0.679	0.754	0.955	0.981	1.056	1.106	1.106	1.207	1.282	1.333
UD 18	0	0.330	0.559	0.686	0.737	0.940	0.965	1.042	1.067	1.118	1.194	1.296	1.347
UD 19	0	0.407	0.611	0.712	0.865	1.018	1.043	1.068	1.145	1.170	1.272	1.348	1.374
UD 20	0	0.280	0.458	0.586	0.688	0.866	0.891	0.968	0.993	1.070	1.172	1.197	1.248

ID	Day (weight change, %)											
	19	20	24	25	28	30	35	37	38	39	40	43
UD 11	1.414	1.466	1.491	Tested after 24 days of water immersion								
UD 12	1.375	1.400	1.450									
UD 13	1.346	1.346	1.396									
UD 14	1.327	1.327	1.377									
UD 15	1.340	1.366	1.416									
UD 16	1.390	1.390	1.415	1.415	1.465	1.465	1.541	1.516	1.541	1.516	1.516	1.491
UD 17	1.383	1.383	1.433	1.433	1.458	1.509	1.484	1.484	1.484	1.509	1.506	1.484
UD 18	1.347	1.347	1.423	1.448	1.474	1.499	1.499	1.474	1.499	1.499	1.499	1.474
UD 19	1.425	1.450	1.450	1.475	1.475	1.552	1.577	1.552	1.526	1.552	1.552	1.526
UD 20	1.299	1.299	1.325	1.375	1.401	1.401	1.426	1.426	1.426	1.426	1.426	1.401

Appendix C (all individual mechanical properties data)

Table 23: Compressive strength results for all CLC specimens.

ID	Compressive strength (MPa)		
	UD	Plain	Twill
Dry 1	656.72	584.03	644.77
Dry 2	637.79	570.22	644.76
Dry 3	593.53	626.91	659.06
Dry 4	687.92	623..33	623.33
Dry 5	664.83	615.47	605.71
Ave. dry	648.16	603.99	635.53
Wet 1	608.04	574.5	598.32
Wet 2	555.91	619.99	570.69
Wet 3	516.08	582.13	584.03
Wet 4	592.05	602.37	599.28
Wet 5	497.64	600.71	586.18
Ave. wet	553.94	595.94	587.7

Table 24: Short-beam strength results for all SBS specimens.

ID	Short-beam strength (MPa)		
	UD	Plain	Twill
Dry 1	67.957	65.29	66.302
Dry 2	66.886	59.964	60.885
Dry 3	68.219	64.48	63.401
Dry 4	69.28	64.27	65.312
Dry 5	69.977	65.257	68.544
Ave. dry	68.464	63.852	64.888
Wet 1	61.626	61.294	59.161
Wet 2	64.39	57.469	61.436
Wet 3	63.463	57.906	61.523
Wet 4	63.008	62.352	59.36
Wet 5	64.177	59.363	62.54
Ave. wet	63.333	59.677	60.804

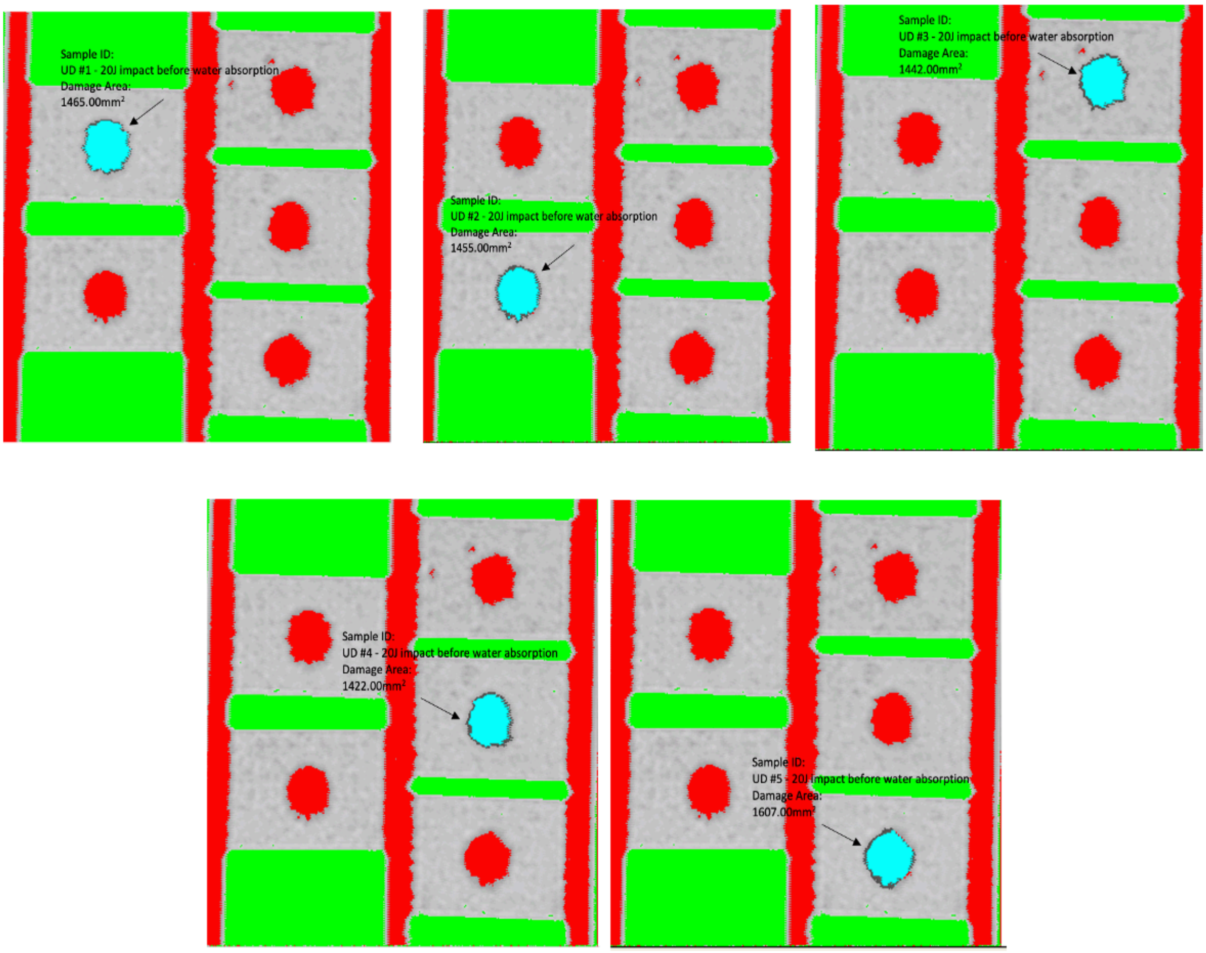

Figure 102: Damage area observed for UD specimens impacted with 20J before water absorption.

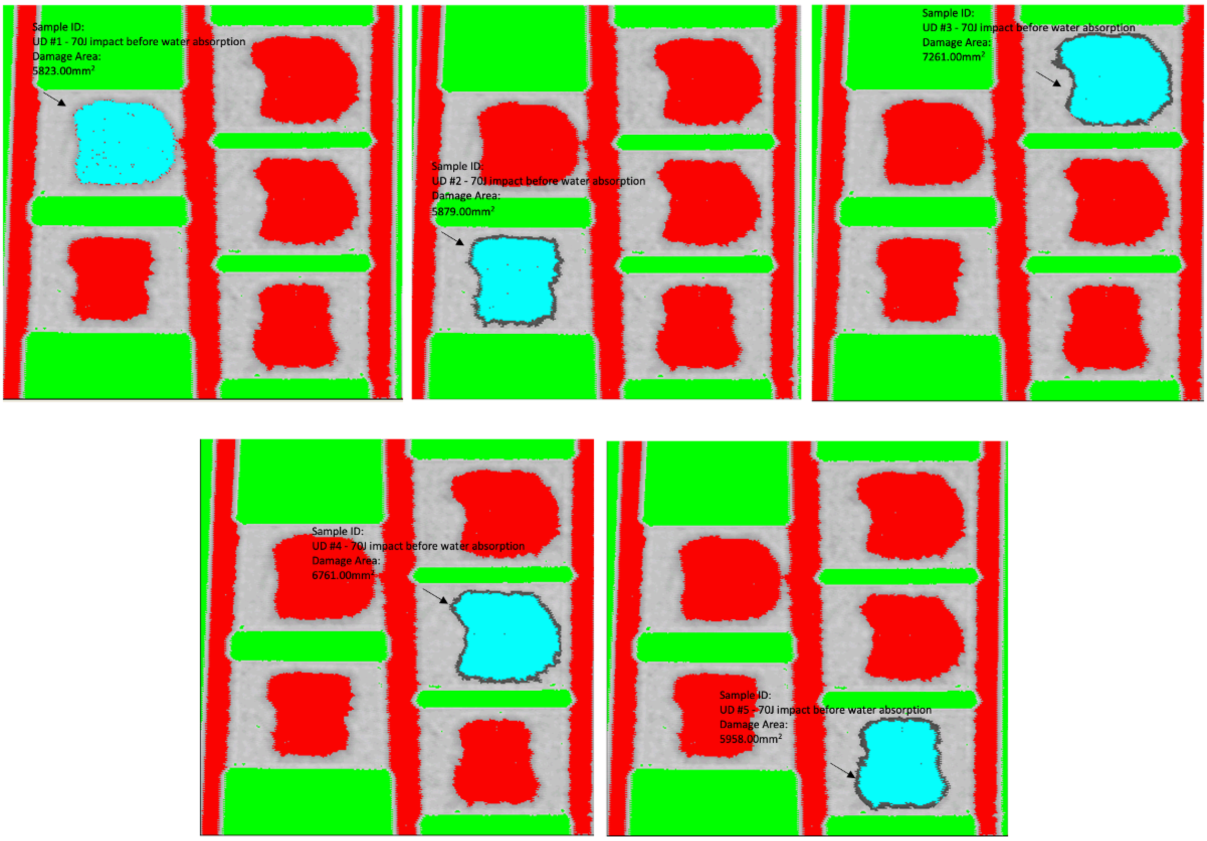

Figure 103: Damage area observed for UD specimens impacted with 70J before water absorption.

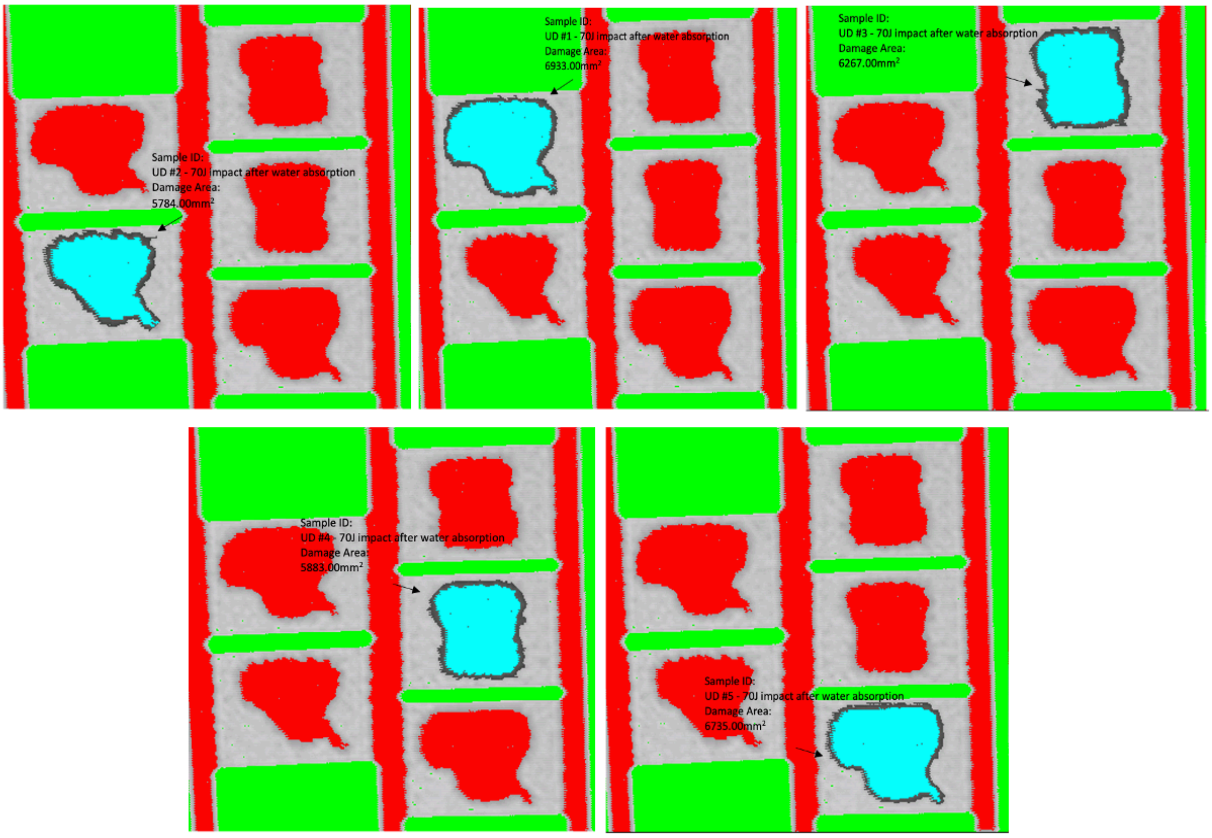

Figure 104: Damage area observed for UD specimens impacted with 70J after water absorption.

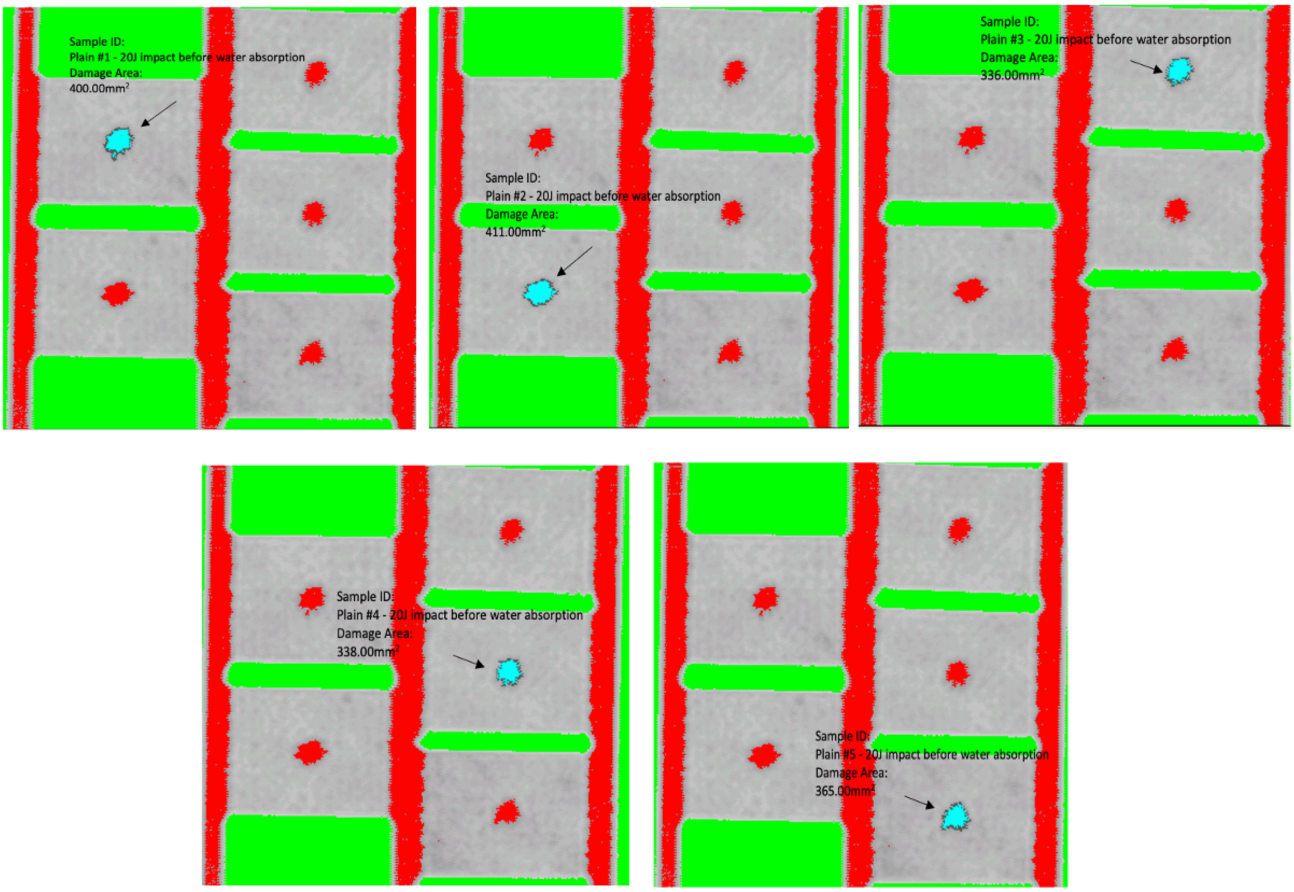

Figure 105: Damage area observed for plain specimens impacted with 20J before water absorption.

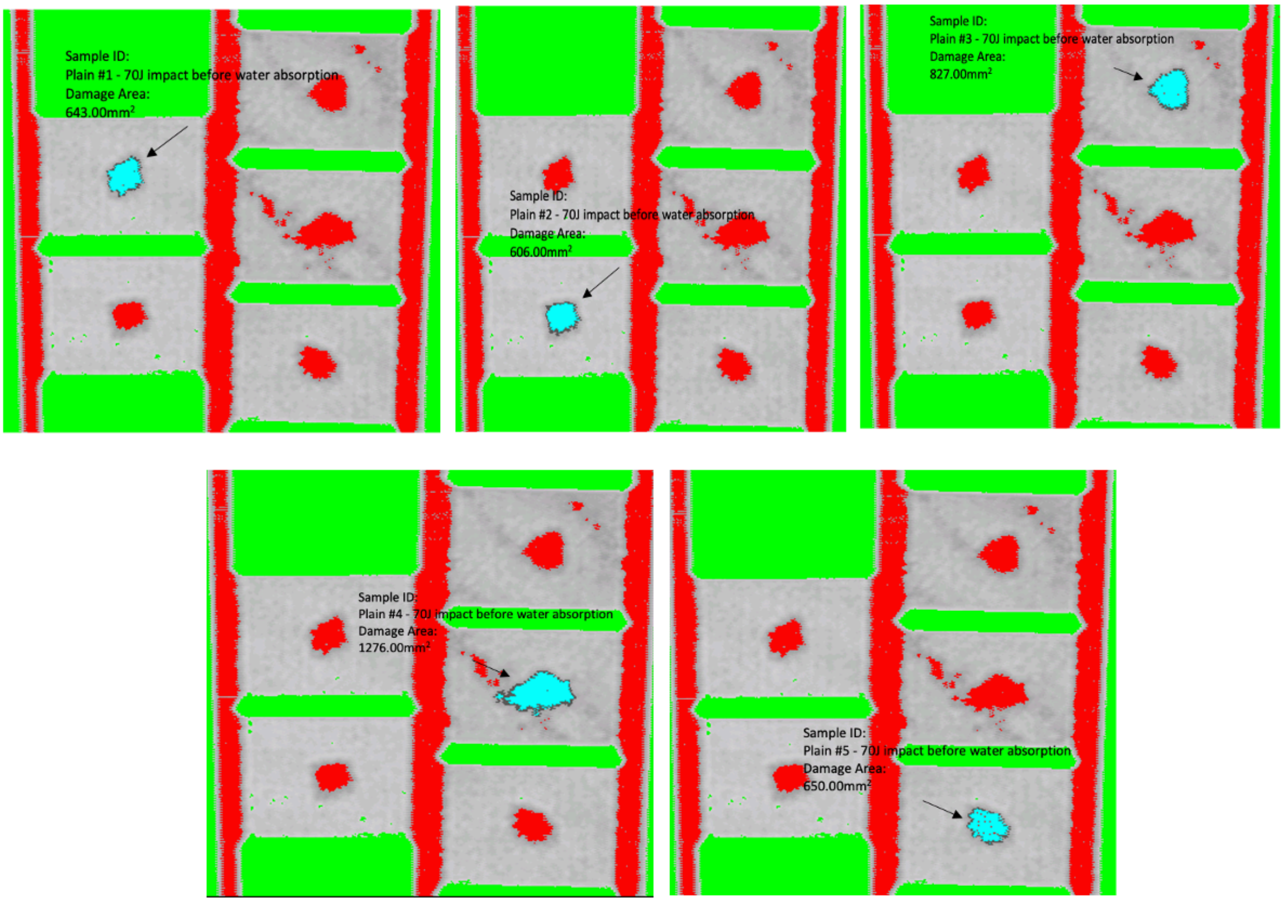

Figure 106: Damage area observed for plain specimens impacted with 70J before water absorption.

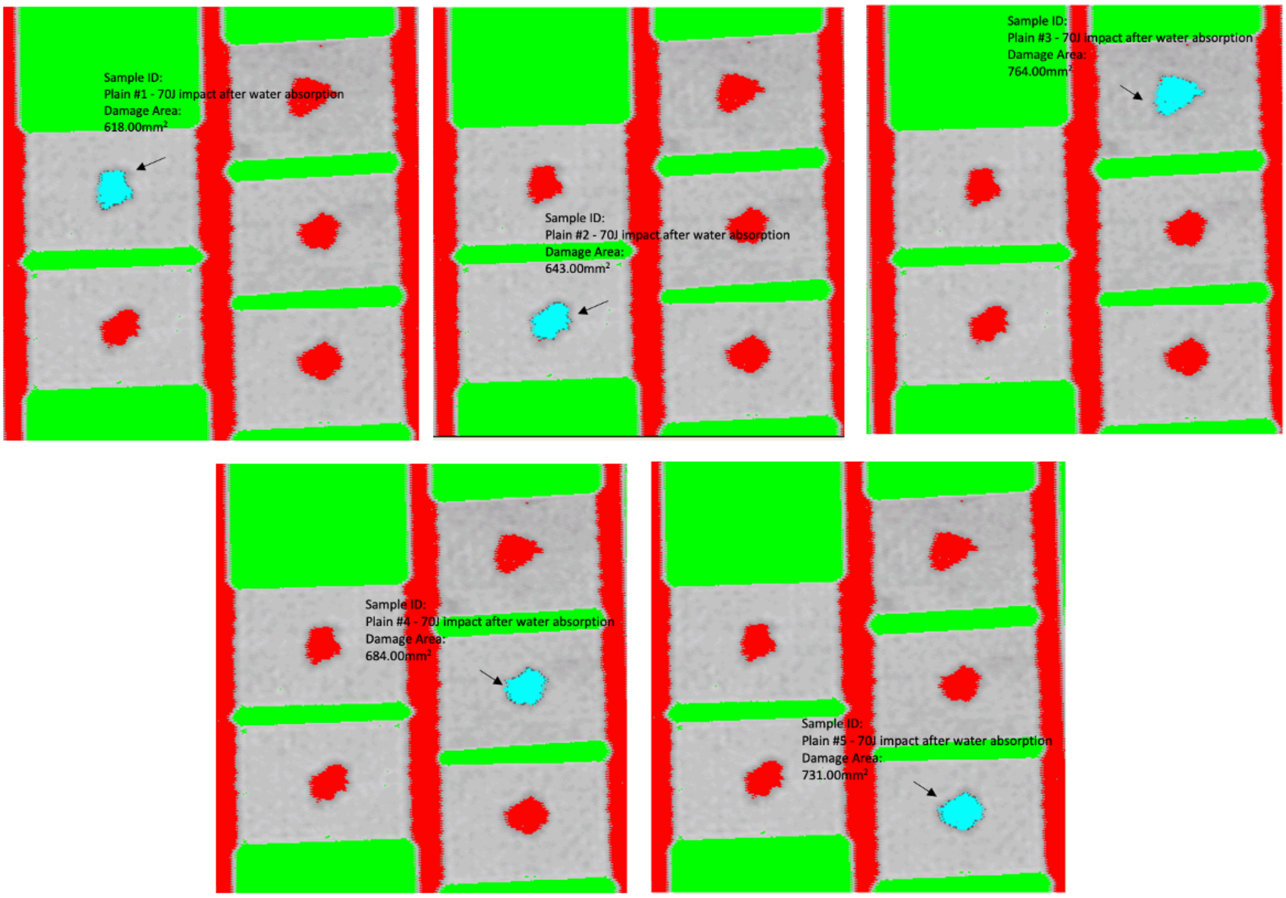

Figure 107: Damage area observed for plain specimens impacted with 70J after water absorption.

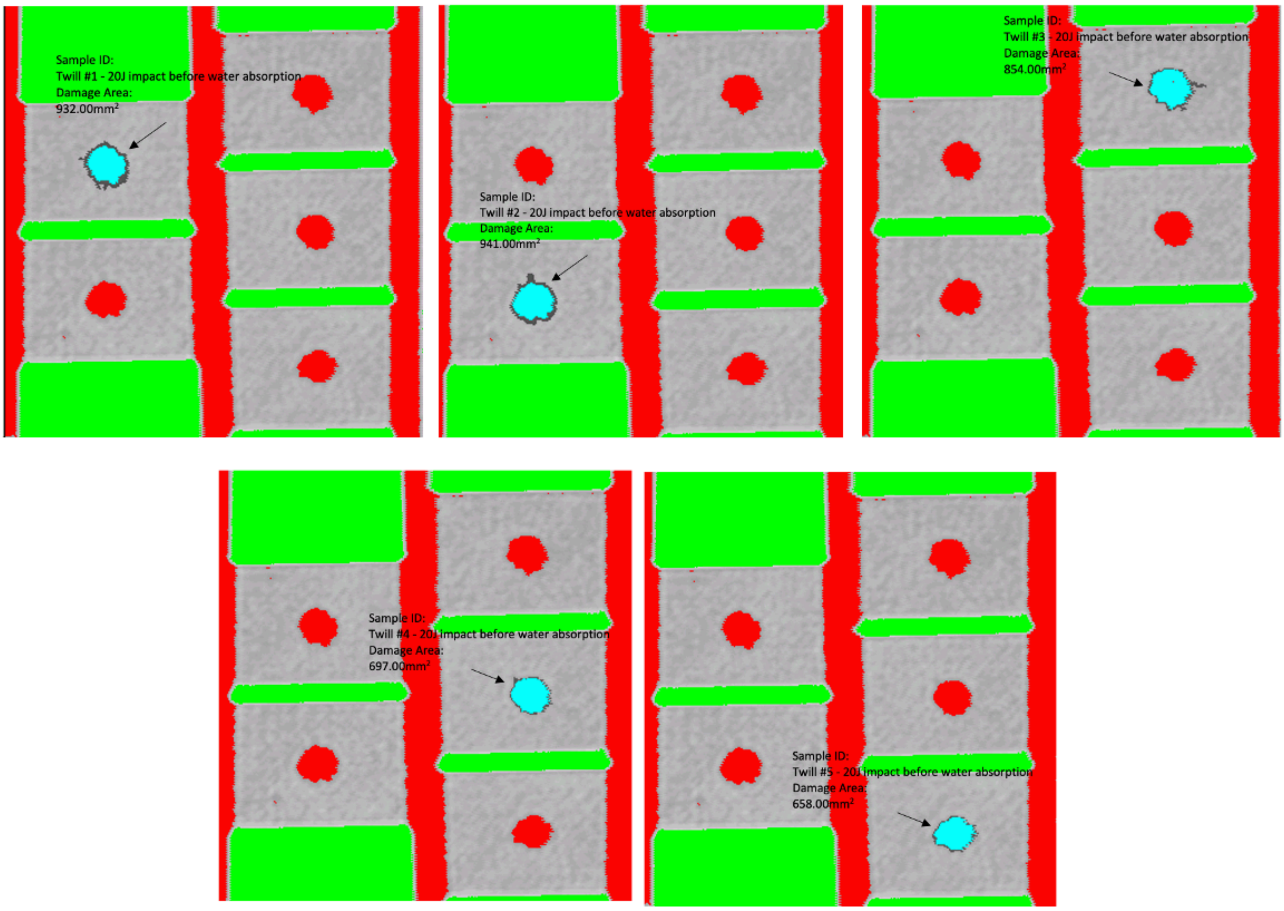

Figure 108: Damage area observed for twill specimens impacted with 20J before water absorption.

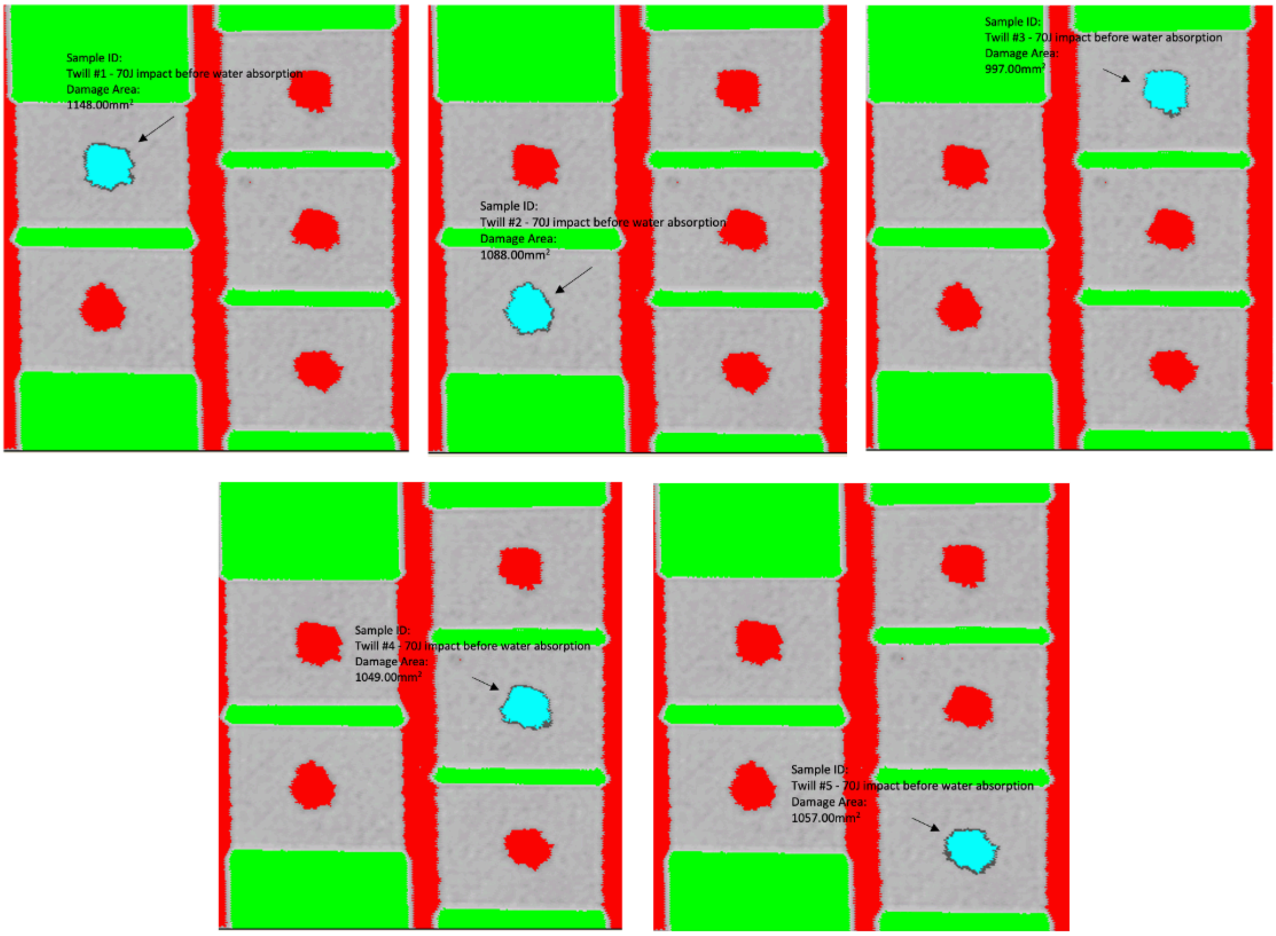

Figure 109: Damage area observed for twill specimens impacted with 70J before water absorption.

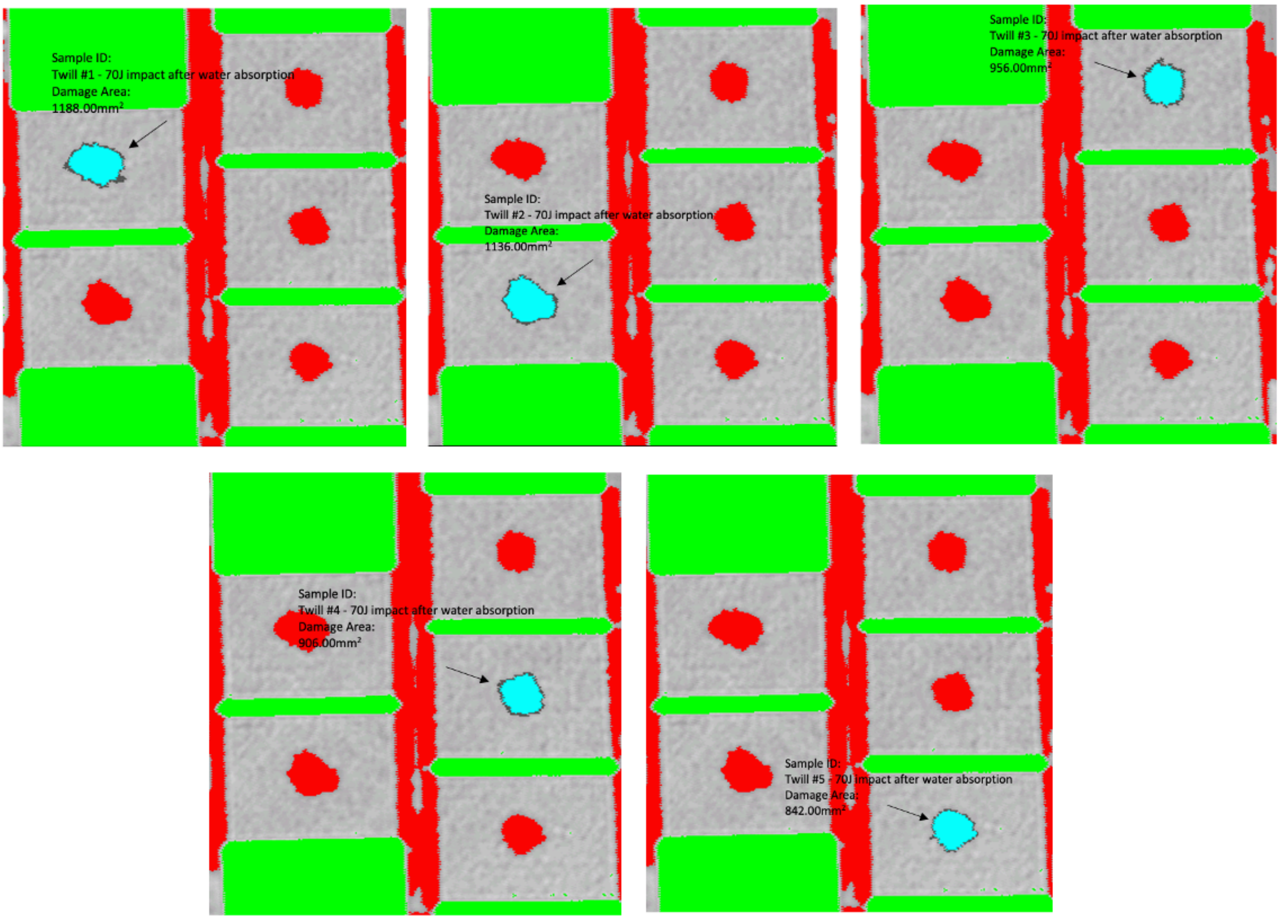

Figure 110: Damage area observed for twill specimens impacted with 70J after water absorption.

Appendix D (all AE data)

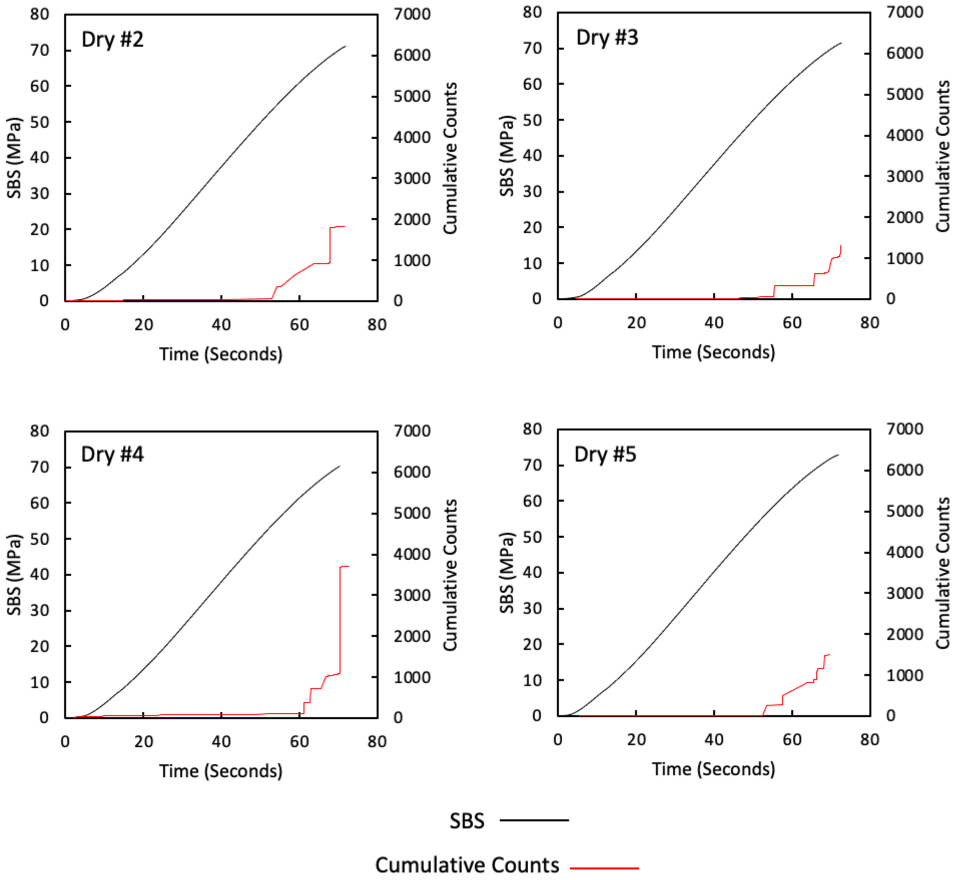

Figure 111: AE cumulative counts versus time for all remaining dry specimens.

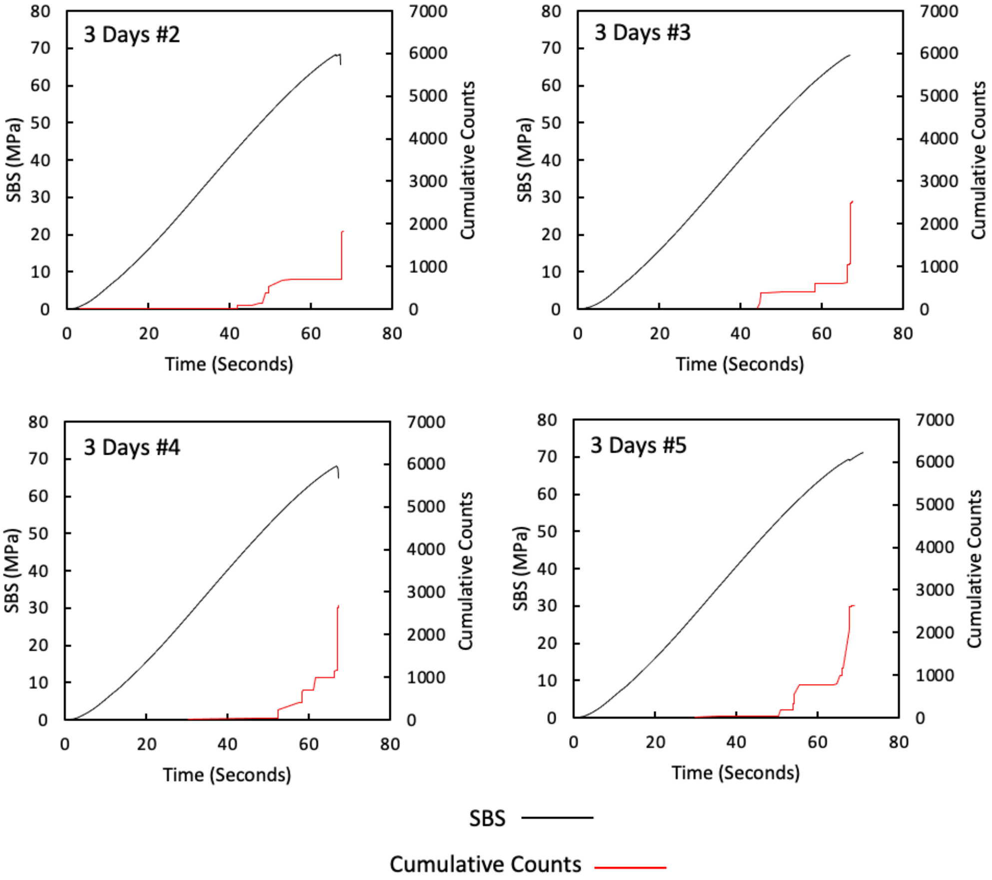

Figure 112: AE cumulative counts versus time for all remaining 3-day water immersed specimens.

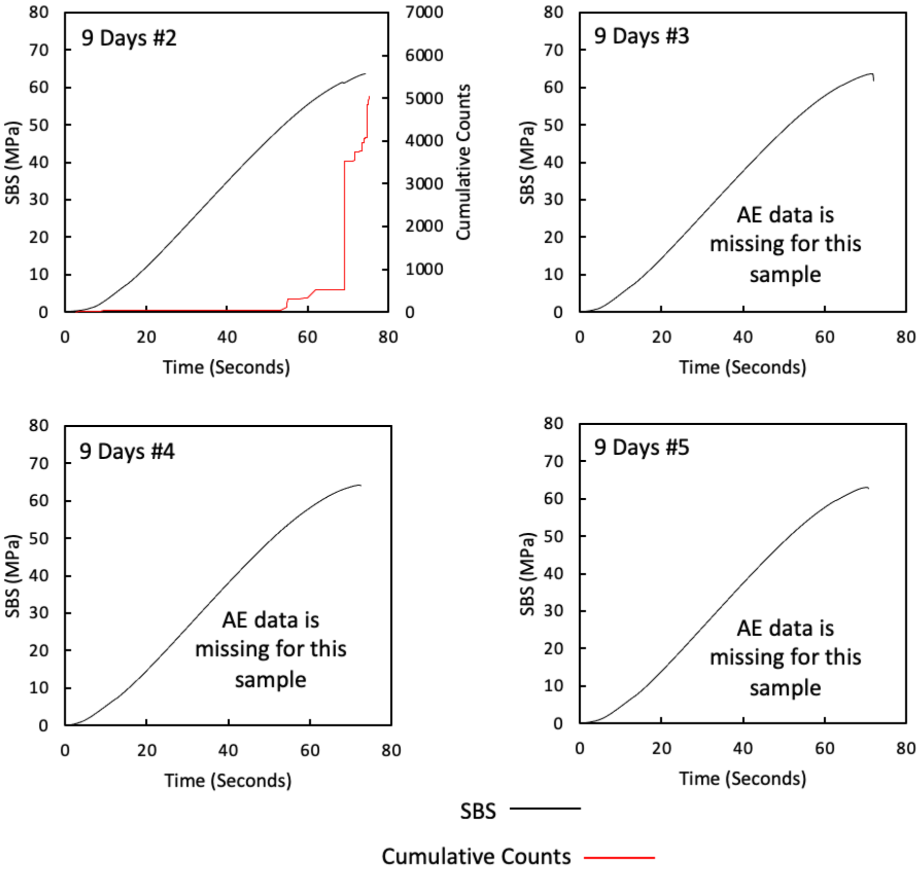

Figure 113: AE cumulative counts versus time for all remaining 9-day water immersed specimens.

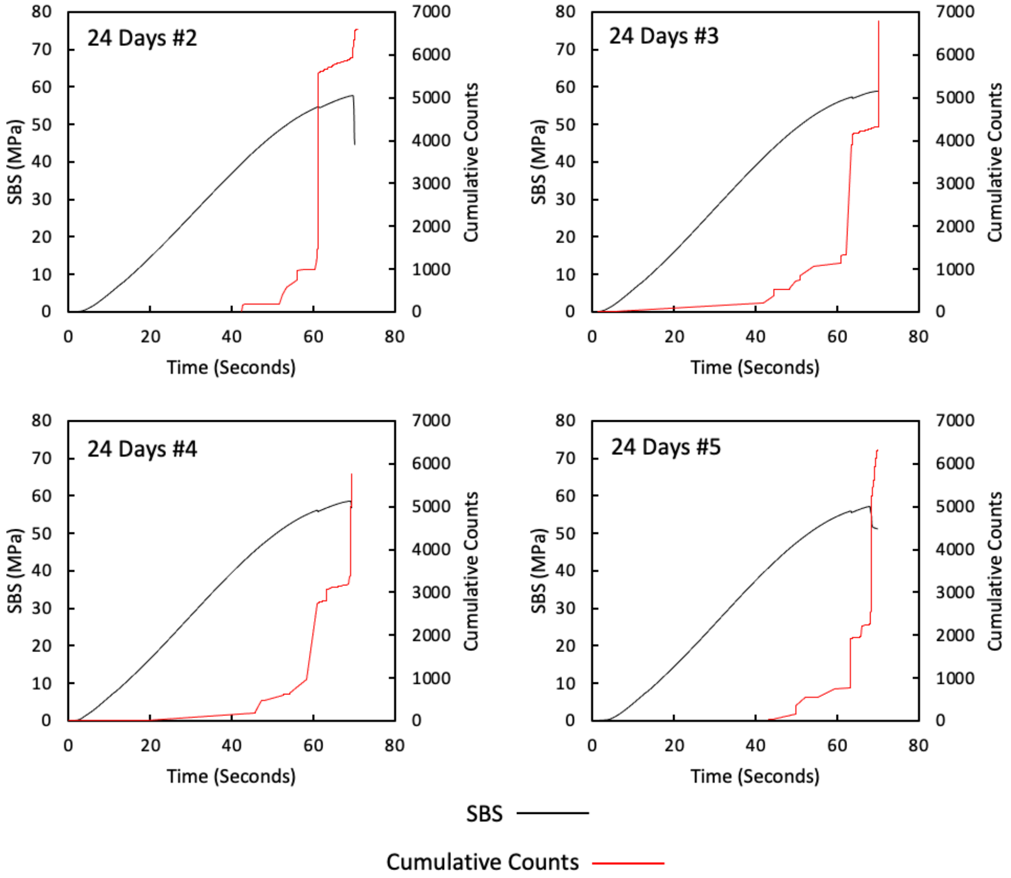

Figure 114: AE cumulative counts versus time for all remaining 24-day water immersed specimens.

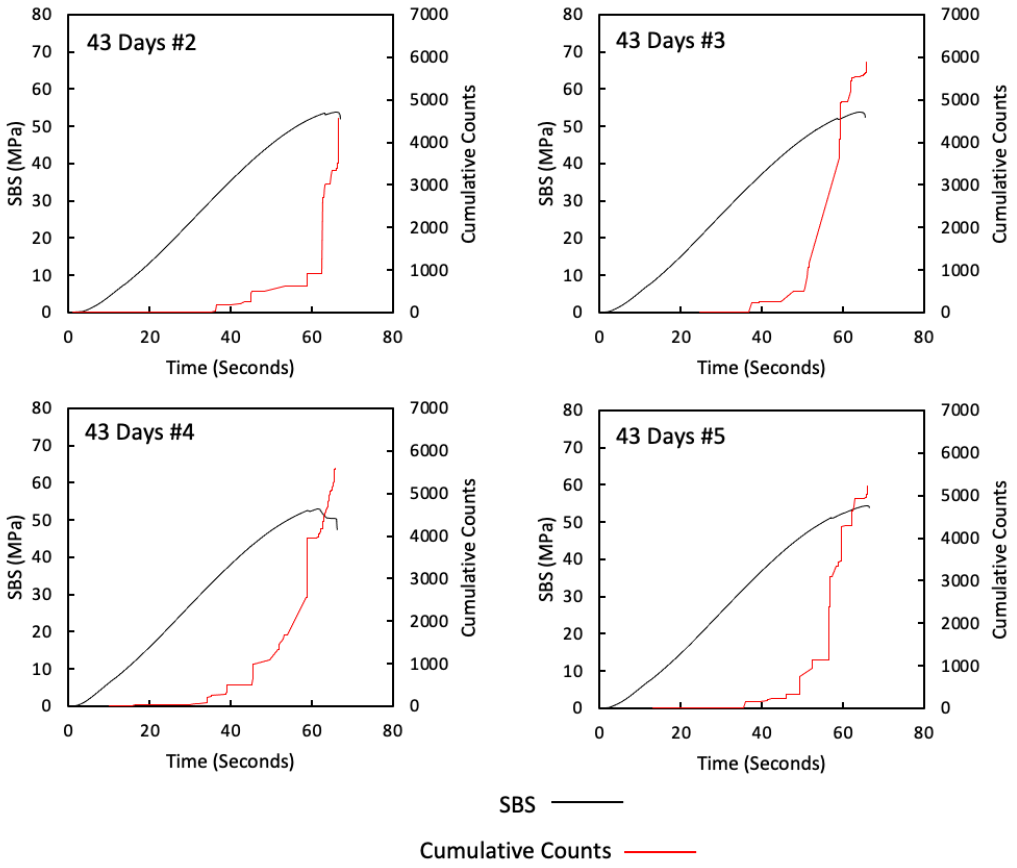

Figure 115: AE cumulative counts versus time for all remaining 43-day water immersed specimens.

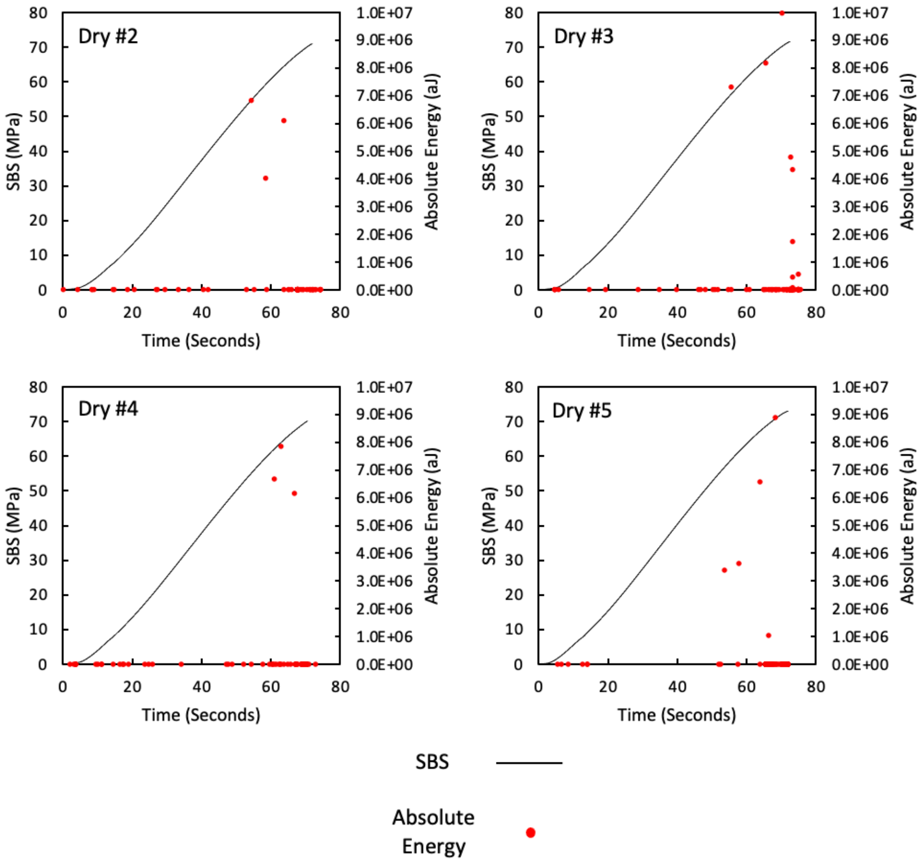

Figure 116: AE absolute energy versus time for all remaining dry specimens with absolute energy maximum scale bar of 1.0E+07.

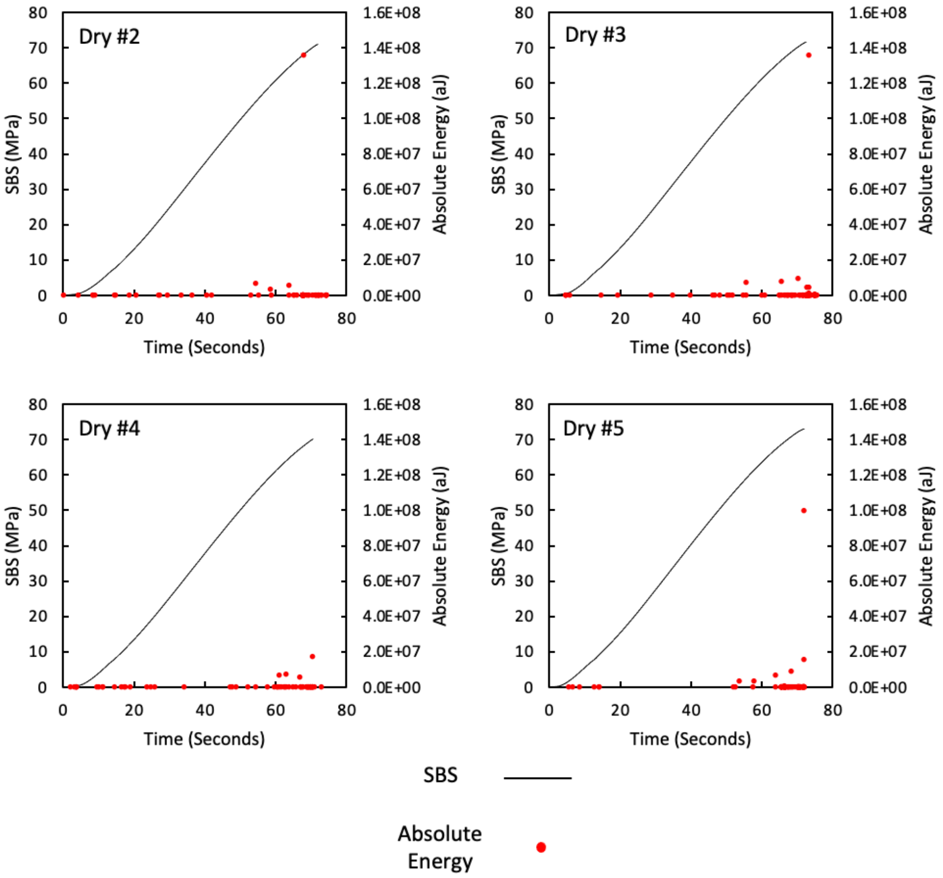

Figure 117: AE absolute energy versus time for all remaining dry specimens with absolute energy maximum scale bar of 1.6E+08.

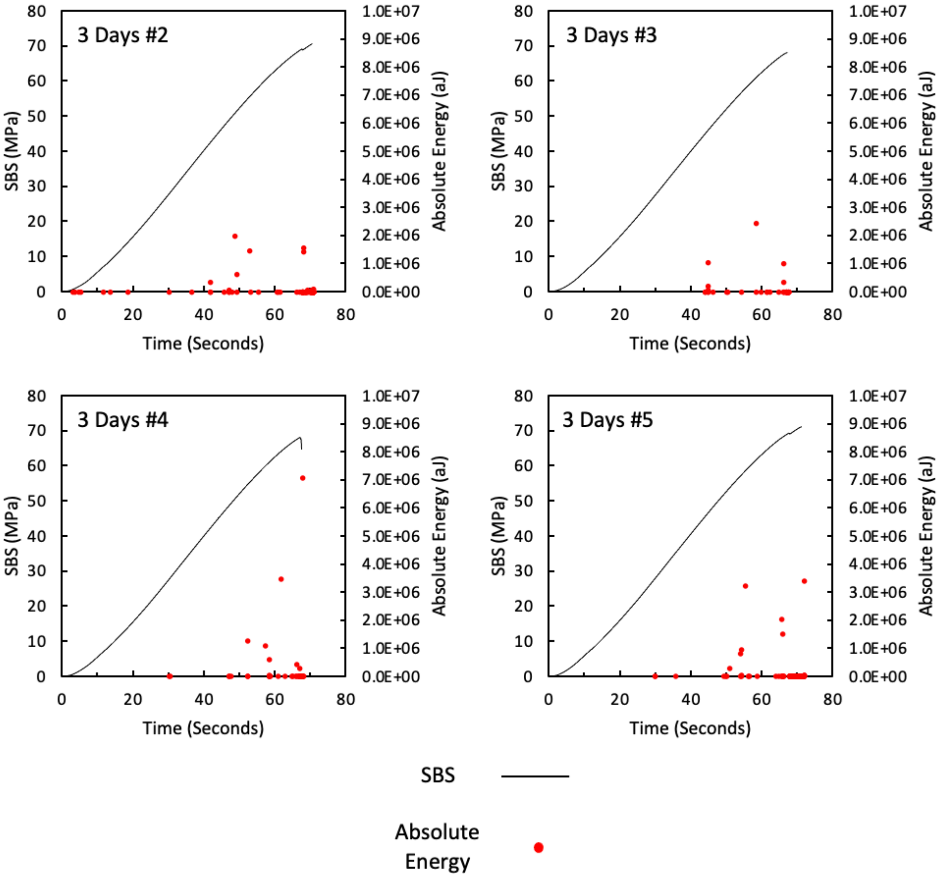

Figure 118: AE absolute energy versus time for all remaining 3-day water immersed specimens with absolute energy maximum scale bar of 1.0E+07.

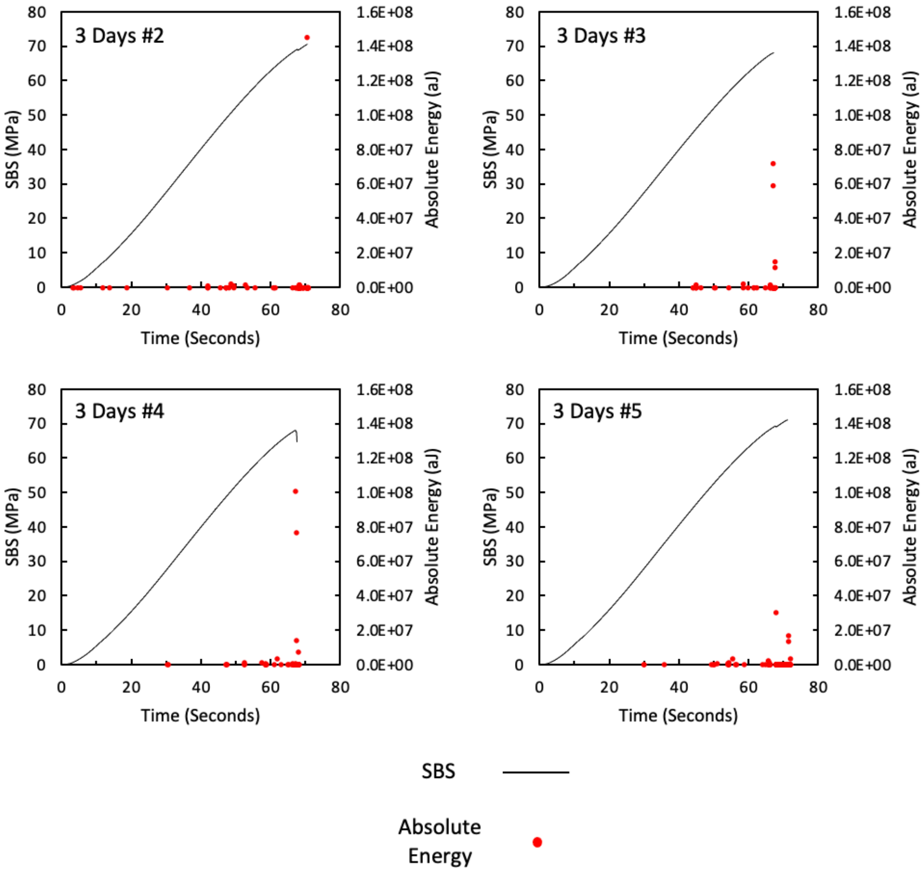

Figure 119: AE absolute energy versus time for all remaining 3-day water immersed specimens with absolute energy maximum scale bar of 1.6E+08.

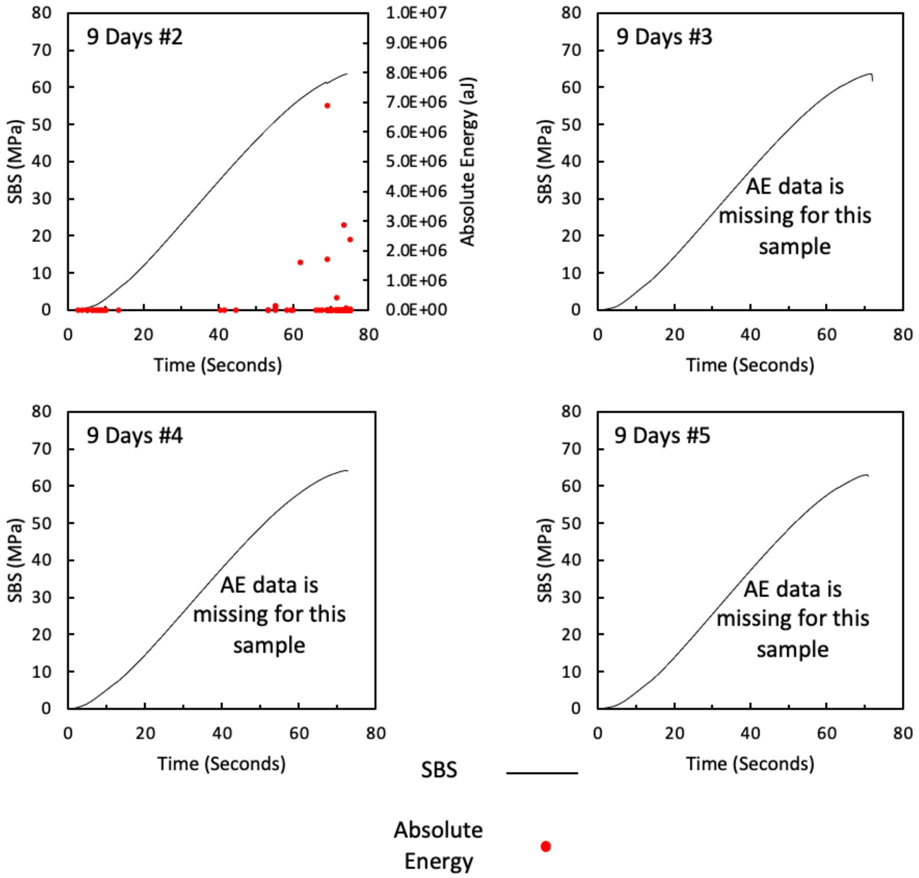

Figure 120: AE absolute energy versus time for all remaining 9-day water immersed specimens with absolute energy maximum scale bar of 1.0E+07.

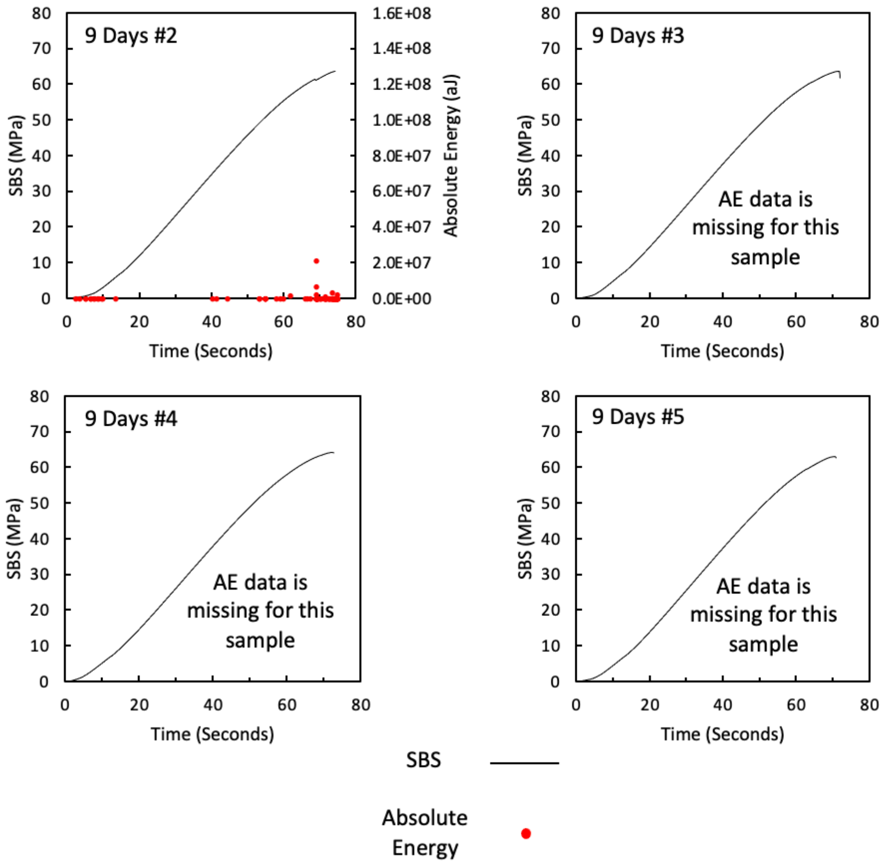

Figure 121: AE absolute energy versus time for all remaining 9-day water immersed specimens with absolute energy maximum scale bar of 1.6E+08.

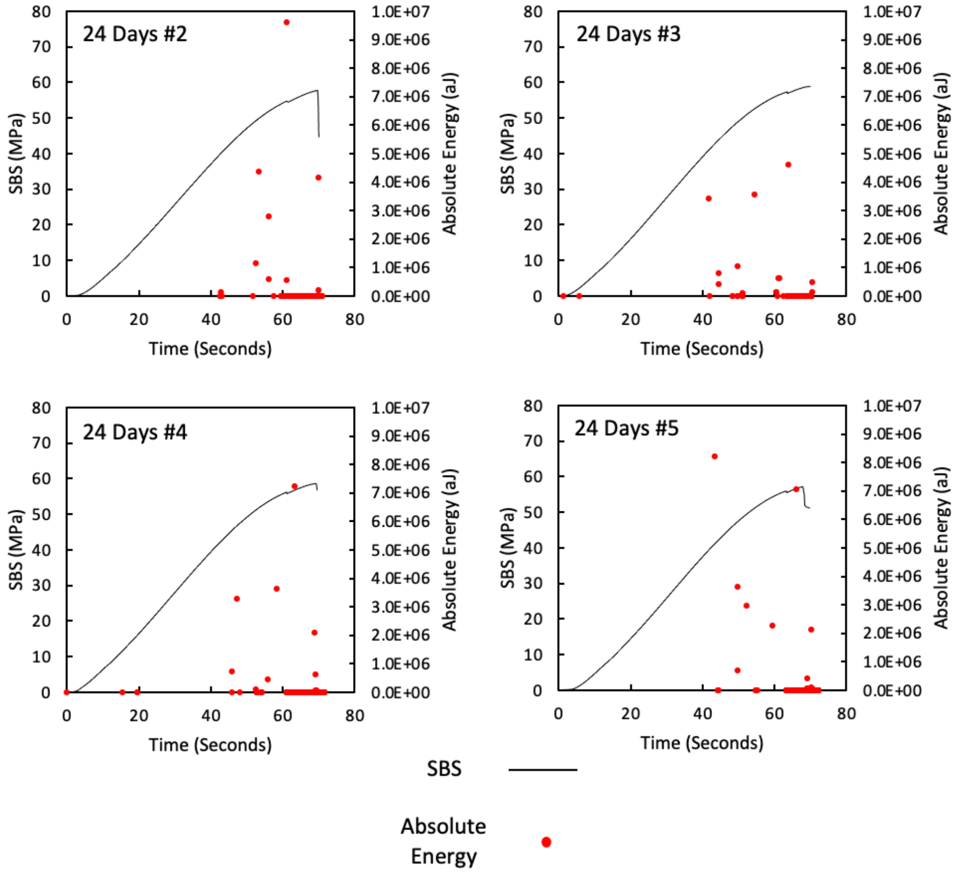

Figure 122: AE absolute energy versus time for all remaining 24-day water immersed specimens with absolute energy maximum scale bar of 1.0E+07.

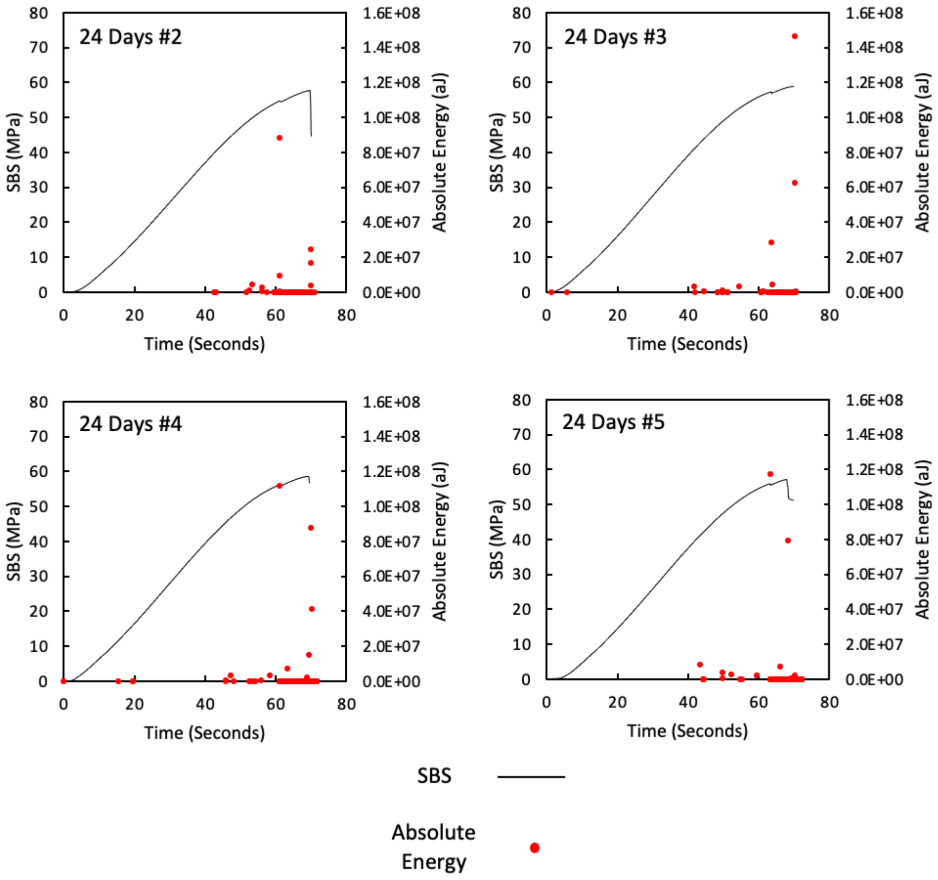

Figure 123: AE absolute energy versus time for all remaining 24-day water immersed specimens with absolute energy maximum scale bar of 1.6E+08.

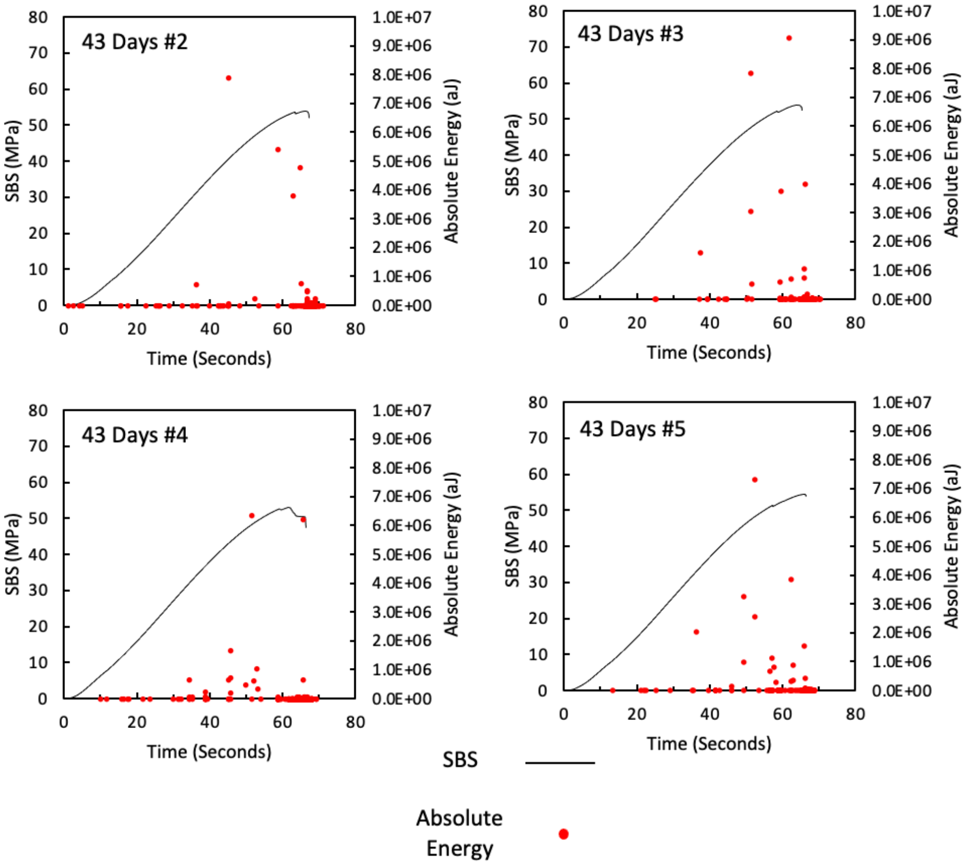

Figure 124: AE absolute energy versus time for all remaining 43-day water immersed specimens with absolute energy maximum scale bar of 1.0E+07.

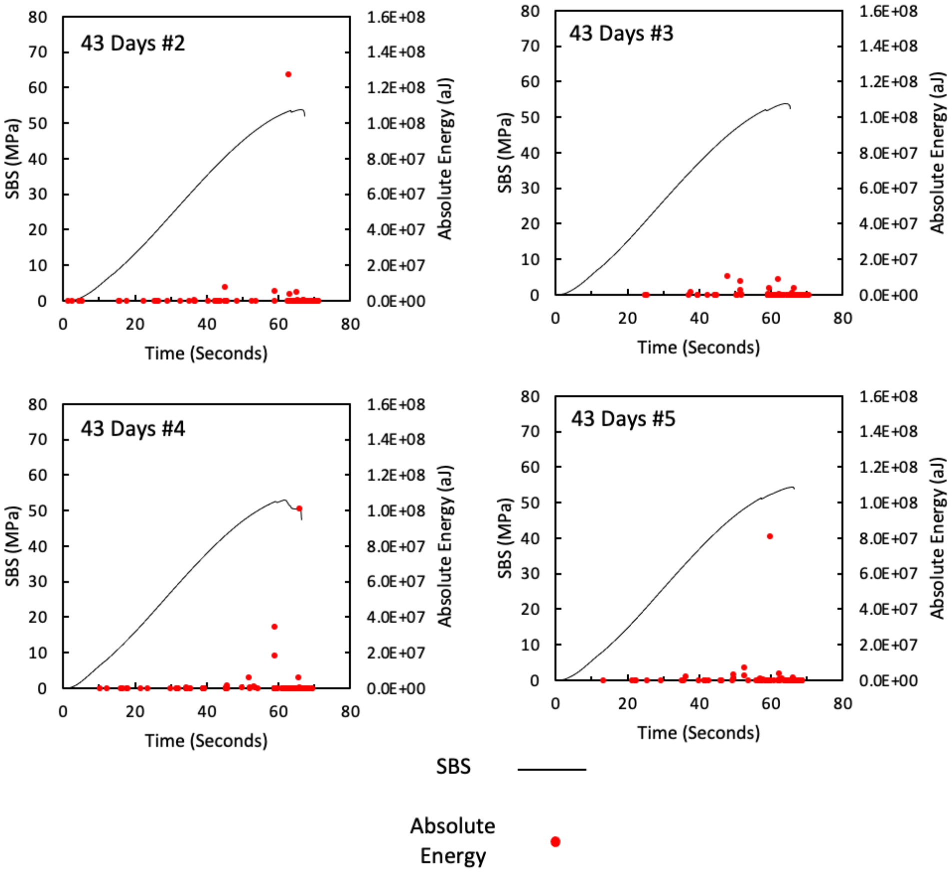

Figure 125: AE absolute energy versus time for all remaining 43-day water immersed specimens with absolute energy maximum scale bar of 1.6E+08.

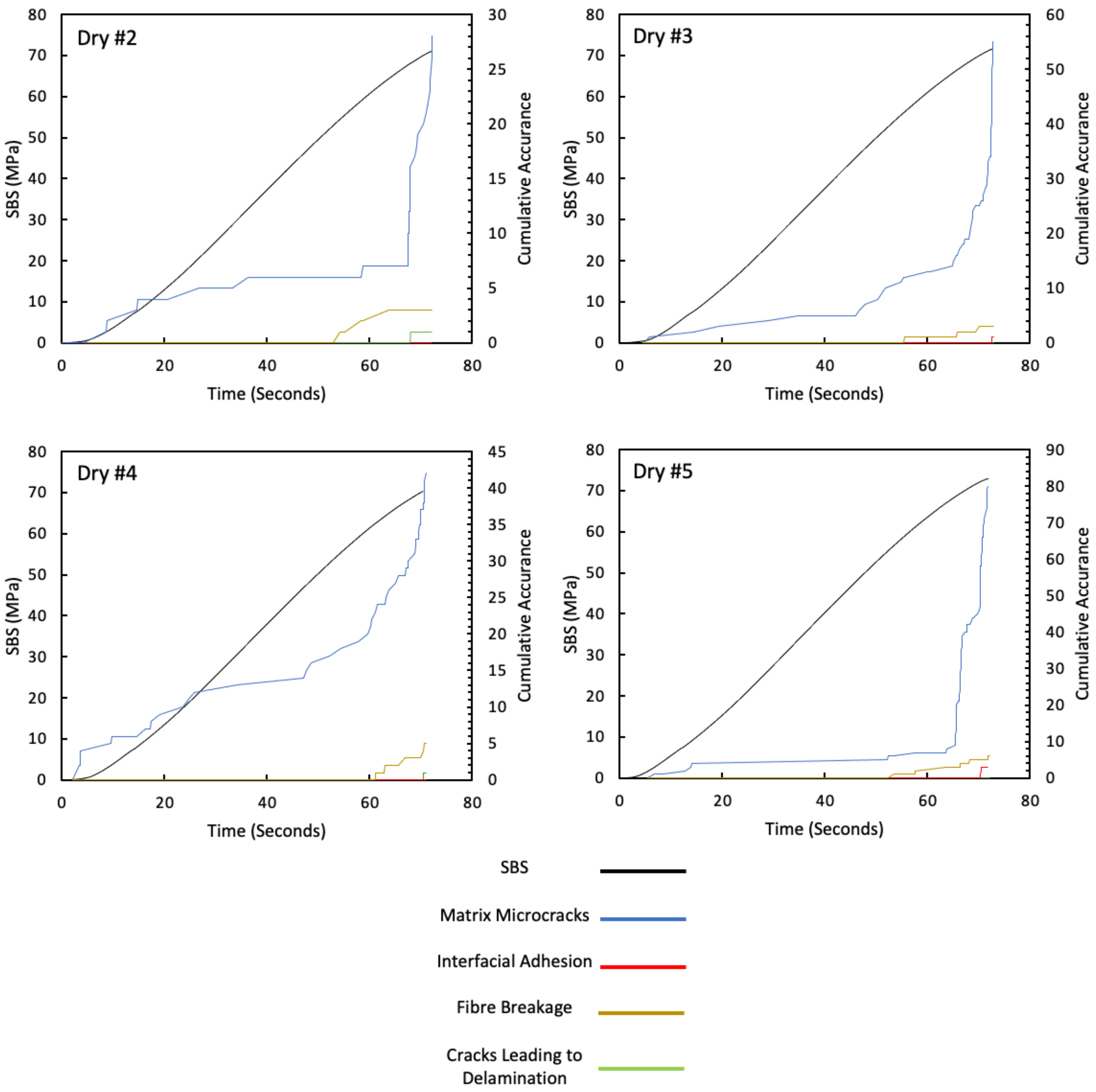

Figure 126: The representative damage mechanism based on the observed amplitude and duration data from the AE signals for all remaining dry specimens.

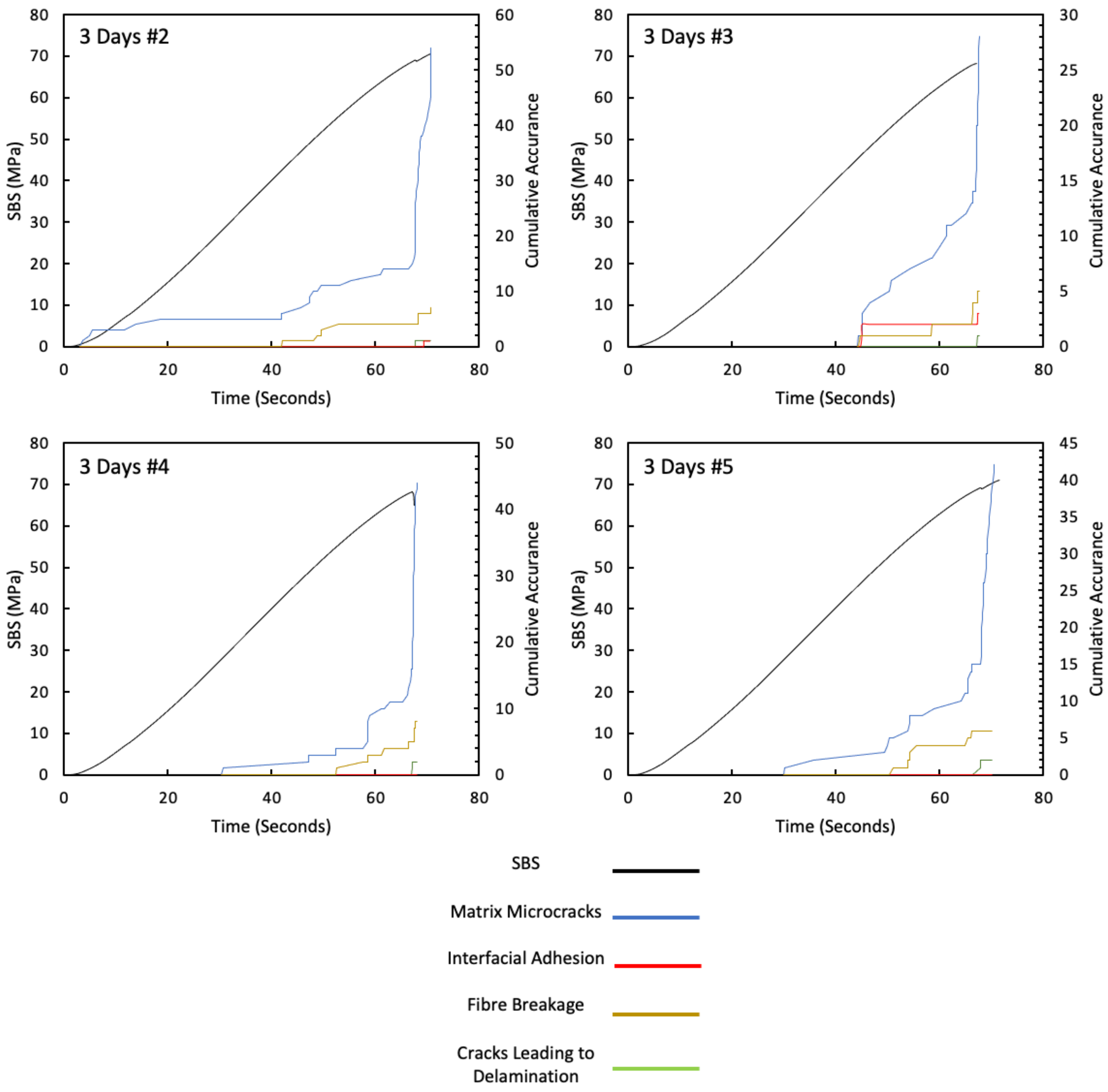

Figure 127: The representative damage mechanism based on the observed amplitude and duration data from the AE signals for all remaining 3-day water immersed specimens.

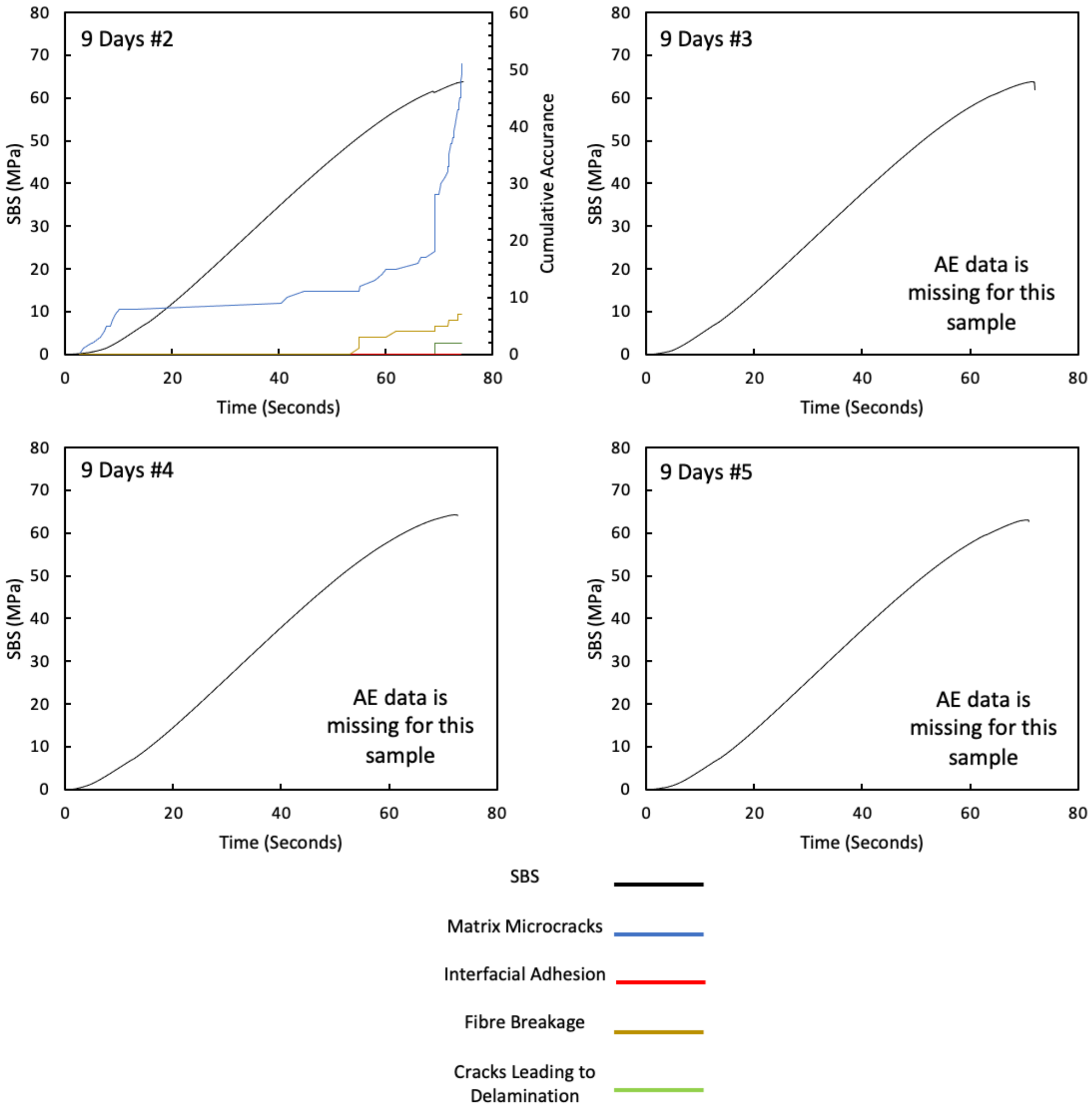

Figure 128: The representative damage mechanism based on the observed amplitude and duration data from the AE signals for all remaining 9-day water immersed specimens.

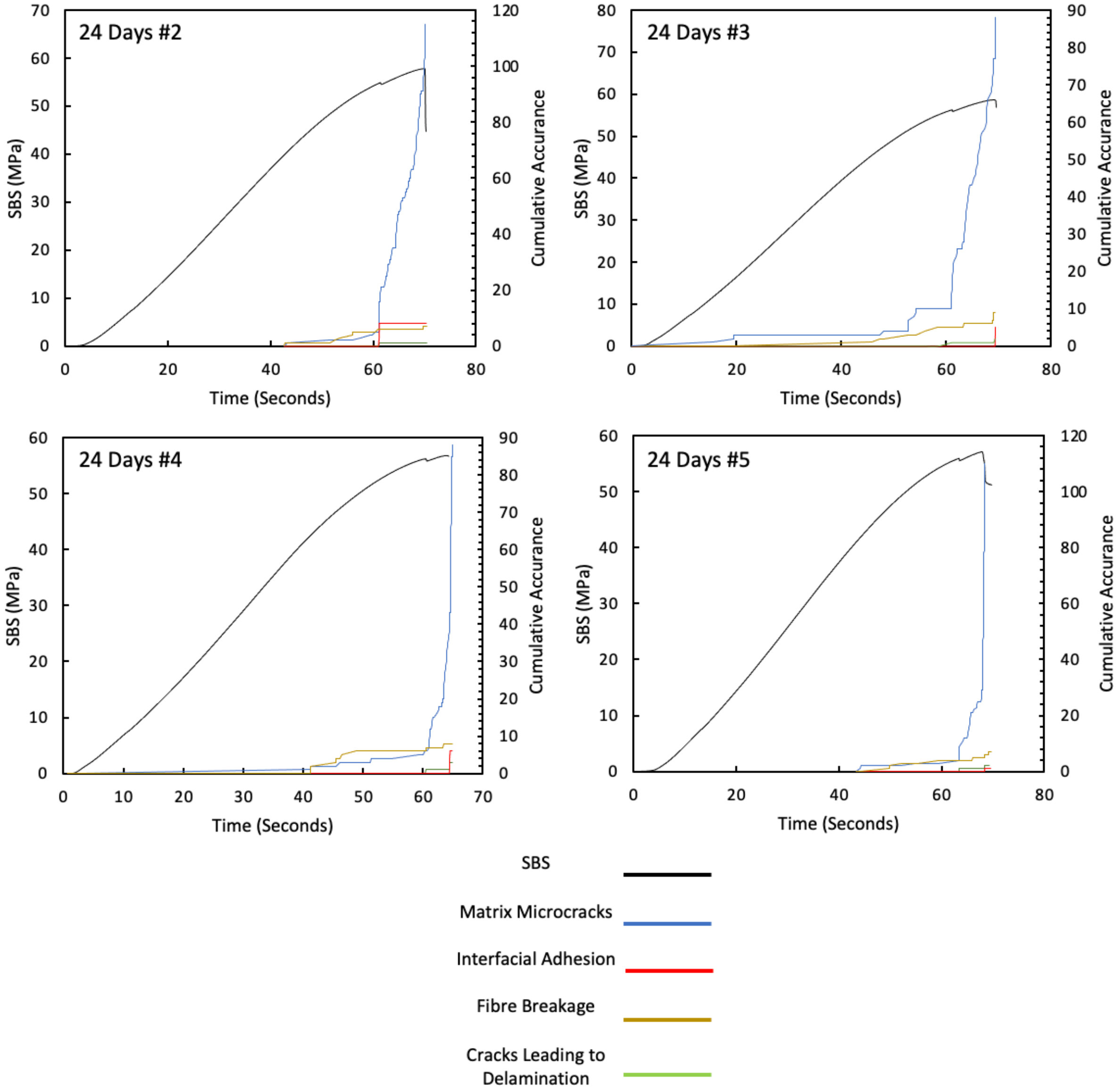

Figure 129: The representative damage mechanism based on the observed amplitude and duration data from the AE signals for all remaining 24-day water immersed specimens.

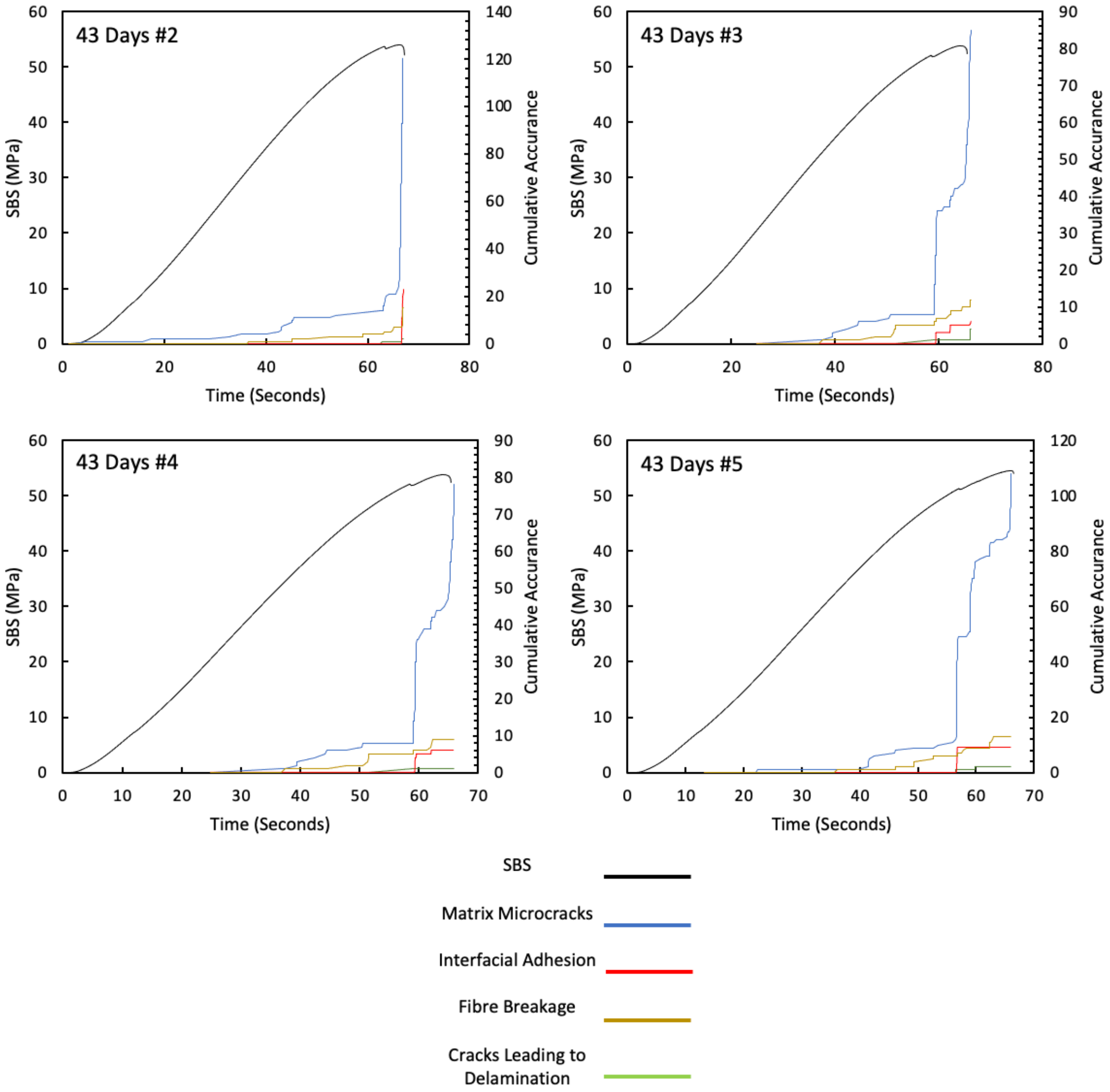

Figure 130: The representative damage mechanism based on the observed amplitude and duration data from the AE signals for all remaining 43-day water immersed specimens.

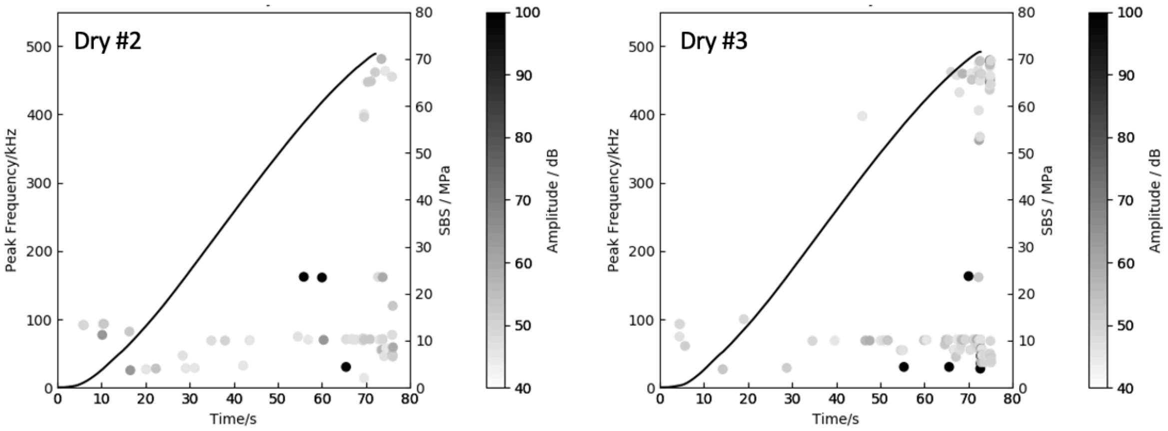

Figure 131: Peak frequency and their associated amplitude for all remaining dry specimens.

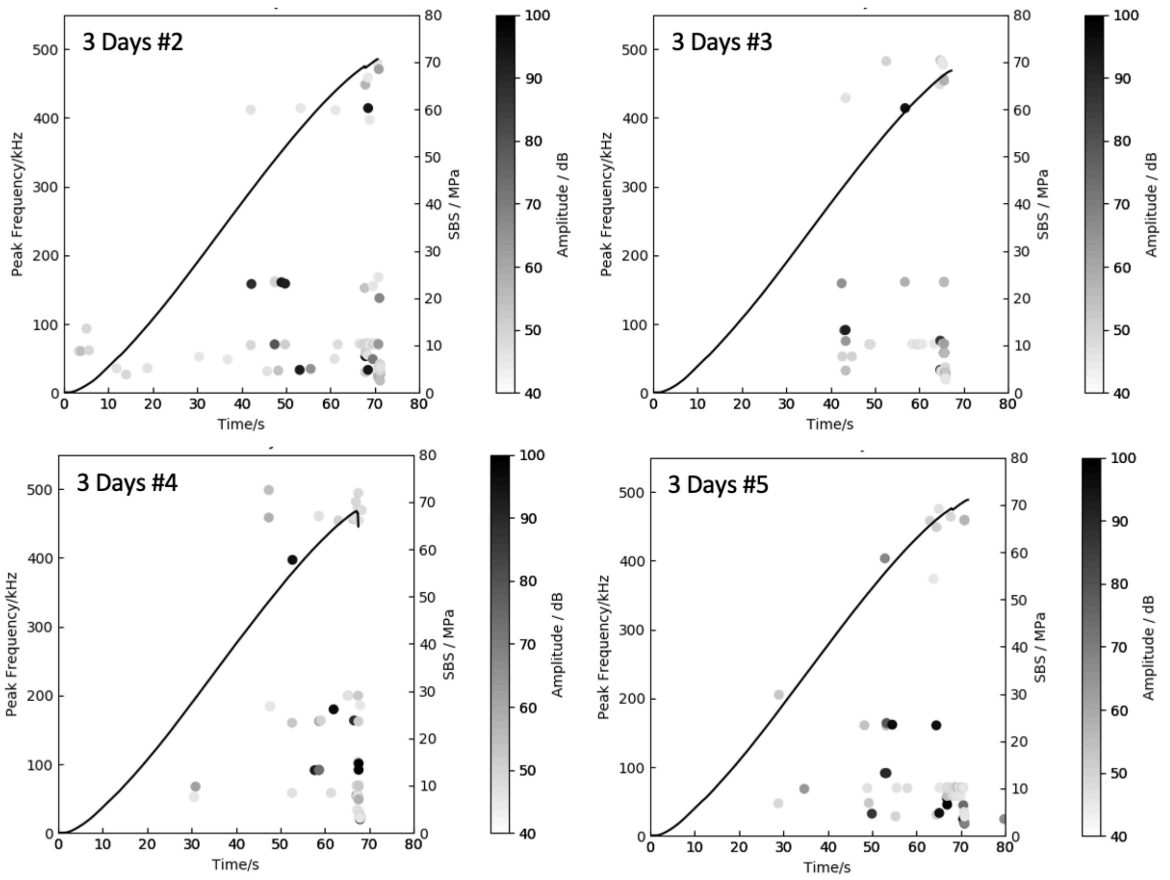

Figure 132: Peak frequency and their associated amplitude for all remaining 3-day water immersed specimens.

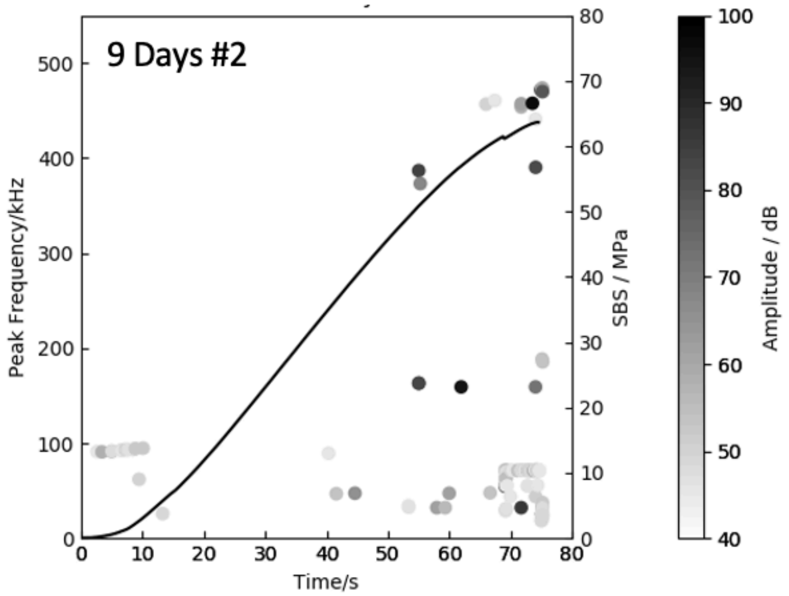

Figure 133: Peak frequency and their associated amplitude for all remaining 9-day water immersed specimens (AE data for other remaining specimens is missing).

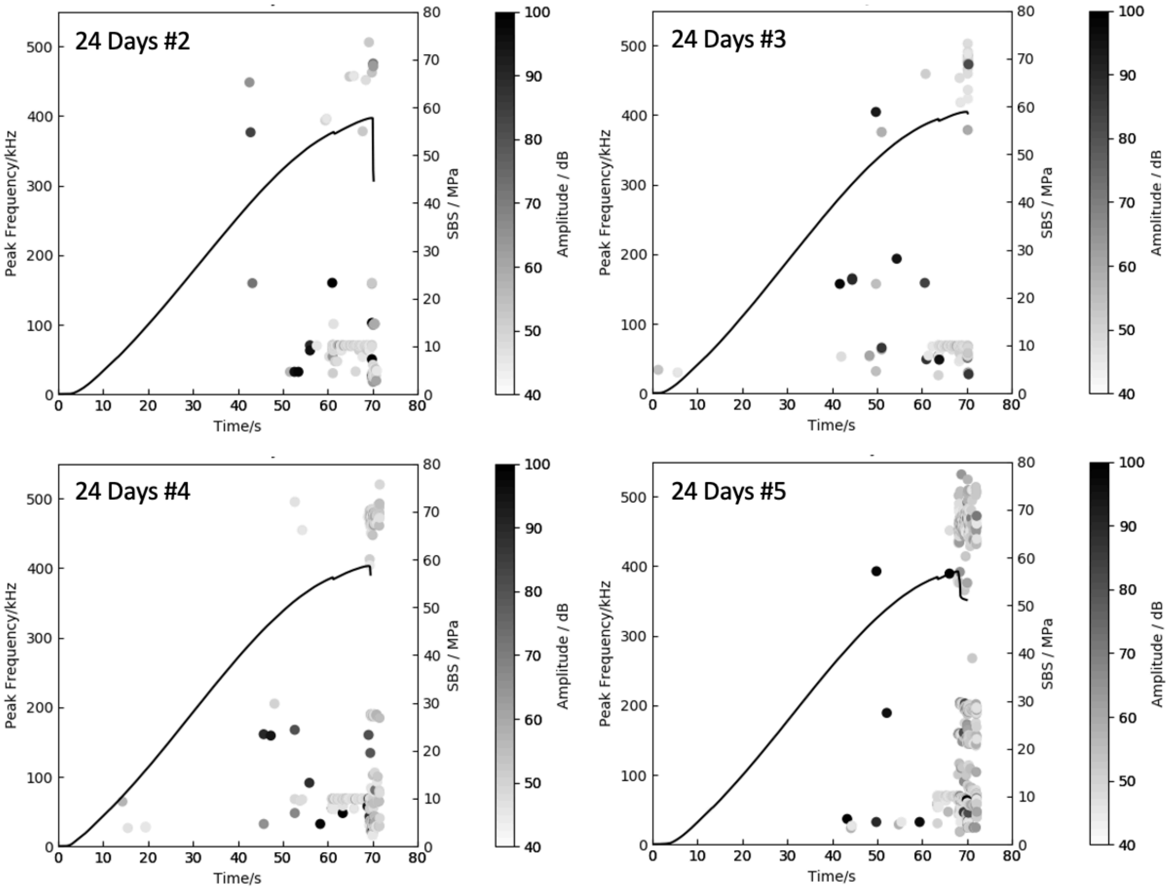

Figure 134: Peak frequency and their associated amplitude for all remaining 24-day water immersed specimens.

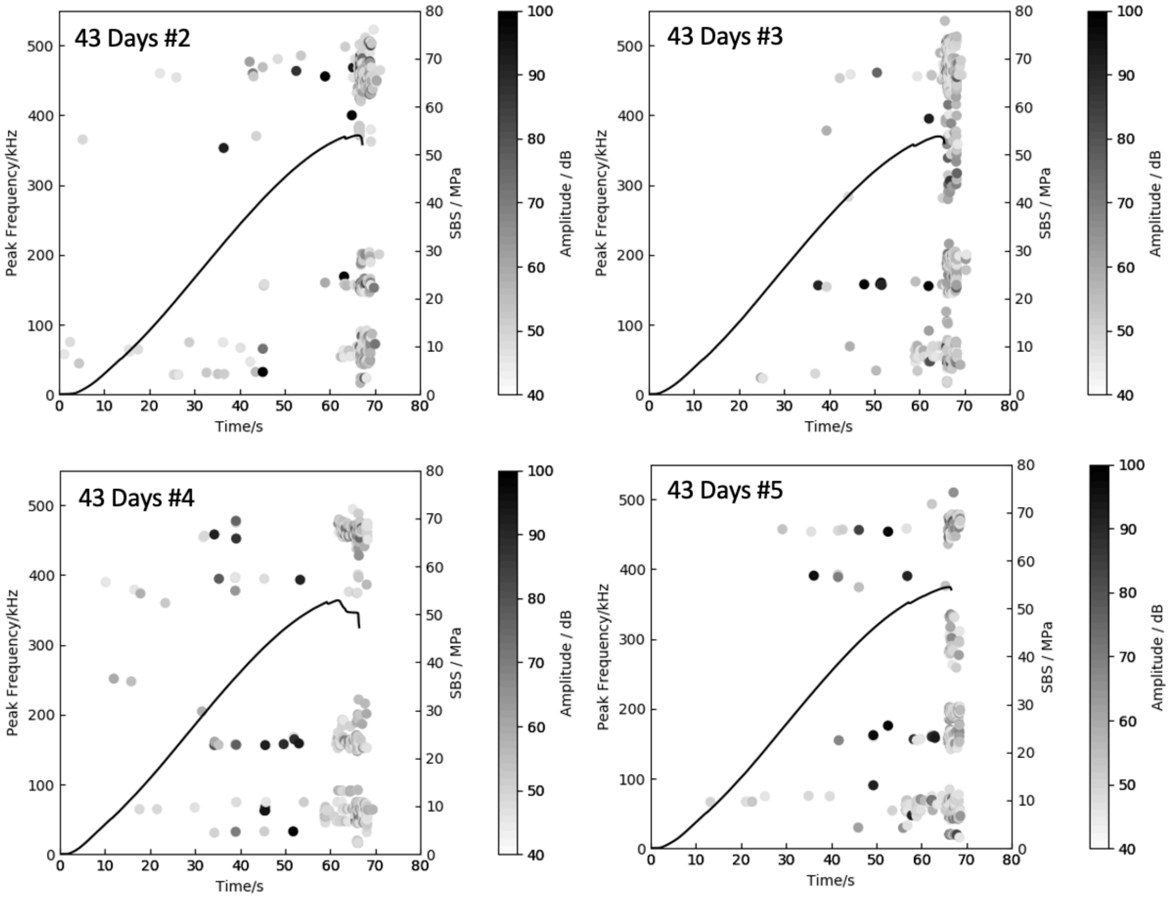

Figure 135: Peak frequency and their associated amplitude for all remaining 43-day water immersed specimens.